

CONVECTION AND SEGREGATION PHENOMENA
IN LOW PRANDTL NUMBER MELT GROWTH SYSTEMS:
A QUANTITATIVE EXPERIMENTAL AND THEORETICAL APPROACH

by

EDWARD PAUL MARTIN JR.

B.S., Boston College
(1970)

SUBMITTED IN PARTIAL FULFILLMENT
OF THE REQUIREMENTS FOR THE
DEGREE OF

DOCTOR OF PHILOSOPHY

at the

MASSACHUSETTS INSTITUTE OF TECHNOLOGY

(June 1977)

Signature redacted

Signature of Author.....
Department of Materials Science and Engineering
May 5, 1977

Signature redacted

Certified by.....
Thesis Supervisor

Signature redacted

Accepted by.....
Chairman, Departmental Committee on Graduate Students



ABSTRACT

Convection and Segregation Phenomena in Low Prandtl Number Melt Growth Systems: A Quantitative Experimental and Numerical Approach

by

Edward Paul Martin Jr.

Submitted to the Department of Materials Science and Engineering on May 5, 1977, in partial fulfillment of the requirements for the degree of Doctor of Philosophy.

A quantitative approach to the study of thermohydrodynamic and segregation phenomena in low Prandtl number melt growth systems has been developed and applied to Czochralski growth of Ga doped Ge crystals. The approach combines a quantitative segregation analysis (employing interface demarcation and spreading resistance measurements), thermal characterization of the growth system, and numerical analysis of the thermal convection equations for boundary conditions determined by the thermal characterization study. Its application required the development of a computer program stable at high Grashof numbers and the establishment of controlled thermal boundary conditions which was achieved by modification of the hot zone of a Czochralski puller through the installation of a coaxial heat pipe.

This modification of the hot zone was found to have a pronounced effect on the thermal and segregation behavior during Czochralski growth. In particular, it was observed that longitudinal and radial segregation inhomogeneities always associated with rotational crystal pulling are drastically reduced. Thermal asymmetry inherent to conventional Czochralski systems was, thus, virtually eliminated. Random melt temperature fluctuations were observed in the absence and presence of the heat pipe; their frequency, however, is increased in the modified system with a correspondingly decreased adverse effect on growth and segregation.

Numerical solutions of thermal convection in the modified growth configuration were found to be in semi-quantitative agreement with measured temperature profiles and revealed the existence of vigorous thermal convective flows in the melt. A comparison of calculated solute boundary layer thicknesses and convective melt flow rates determined from these solutions and other theoretical and experimental approaches indicated that both forced and thermal convection may simultaneously affect

dopant segregation during crystal growth with seed rotation.

As a result of the virtual elimination of thermal asymmetry in the hot zone through the installation of a heat pipe, crystal rotation can now be used during Czochralski growth to obtain a uniform solute boundary layer thickness and, thus, obtain radial dopant homogeneity without the simultaneous generation of adverse longitudinal dopant heterogeneities.

Thesis Supervisor: A.F. Witt

Title: Professor of Materials Sciences

TABLE OF CONTENTS

Chapter Number		Page Number
	ABSTRACT	2
	TABLE OF CONTENTS	4
	LIST OF FIGURES	9
	LIST OF TABLES	14
	ACKNOWLEDGEMENTS	16
I.	INTRODUCTION	19
II.	OUTLINE OF OBJECTIVES, APPROACH AND STRUCTURE	21
	A. Objectives of the Present Work	21
	B. Experimental and Theoretical Approach	21
	C. Structure of the Thesis	23
III.	BACKGROUND AND PREVIOUS WORK ON THERMAL CONVECTION	24
	A. General Reviews	24
	B. Horizontal Layer Heated From Below	25
	1. Horizontal Layer Heated From Below With Infinite Lateral Extent	25
	2. Horizontal Layer Heated From Below With Lateral Confinement	30
	C. Rectangular Enclosure Heated From the Side	32
	D. Vertical Cylindrical Enclosure With Horizontal and Vertical Heat Flow	36
	E. Control of Thermal Convection	40
IV.	APPARATUS AND EXPERIMENTAL PROCEDURES	42
	A. Crystal Growth System and Related Equipment	42

Chapter Number		Page Number
	1. Crystal Growth Apparatus	43
	a. Growth Chamber	43
	b. Heater System	43
	c. Heat Pipe and Heat Pipe Support	47
	d. Crucible	47
	e. Current Pulsing System	47
	2. Thermal Characterization Equipment	49
	a. Thermocouple Probe Assembly	49
	b. Thermocouple Manipulator	52
	c. Temperature Measure Equipment	54
	B. Experimental Procedures	55
	1. Heat Pipe Alignment	55
	2. Charge Preparation	56
	3. Melt Down Procedure	56
	4. Temperature Measurement Procedure	57
V.	THERMAL CHARACTERIZATION OF THE CZOCHRALSKI CRYSTAL GROWTH SYSTEM	59
	A. Comments on Temperature Measurement	59
	B. Thermal Characterization of the Hot Zone in the Czochralski System	62
	1. Time Dependent Temperature Behavior of the Hot Zone	63
	2. Spatially Dependent Temperature Behavior of the Hot Zone	68
VI.	NUMERICAL TREATMENT OF THERMAL CONVECTION	87
	A. Development of the Quantitative Theoretical Approach to Convection in Melt Growth Configurations	88

Chapter Number		Page Number
	1. Thermal Convection Equations	89
	2. Application to Crystal Growth Geometries	90
	a. Horizontal Bridgman Configuration	91
	b. Czochralski Configuration	93
	B. Numerical Solution of Thermal Convection in the Horizontal Bridgman Geometry	95
	1. Dependence of Computed Flows on the Grashof Number	97
	2. Dependence of the Flow Intensity on the Aspect Ratio	107
	3. Convective Oscillations	109
	C. Numerical Solution of Thermal Convection in the Czochralski Configuration	115
VII.	BASIC CONSIDERATIONS AND LITERATURE REVIEW ON FORCED CONVECTION AND SEGREGATION IN CZOCHRALSKI CRYSTAL GROWTH SYSTEMS	127
	A. Forced Convection	128
	B. Segregation	130
	1. Segregation Models	130
	2. Segregation Studies	131
VIII.	SEGREGATION BEHAVIOR IN CZOCHRALSKI CRYSTAL GROWTH SYSTEMS	137
	A. Crystal Growth and Characterization Procedures	139
	1. Growth Procedures	139
	a. Seed Preparation	139
	b. Seeding and Growth Procedure	140
	c. Interface Demarcation	141

Chapter Number		Page Number
	2. Specimen Preparation and Segregation Analysis	141
	a. Sample Preparation	141
	b. Microscopic Growth Rate Determination	142
	c. Spreading Resistance Measurement	147
	a. Calibration of the Spreading Resistance Probe	148
	b. Concentration Determination	149
	B. Comparative Segregation Analysis	151
	1. Segregation Analysis for Growth With Crystal Rotation	152
	2. Segregation Analysis for Growth With Crucible Rotation	156
	3. Segregation in Modified Growth System Without Rotation	158
IX.	DISCUSSION OF CONVECTION AND ITS EFFECTS ON SEGREGATION	164
	A. Solute Boundary Layer Thickness	164
	B. Fluid Flow Rates	173
	C. Sources of Convective Instabilities	177
	1. Models for Convective Temperature Oscillations	178
	2. Comparison of Theoretical and Experimental Periods	180
	D. Correlation of Growth Rate Variations With Convective Temperature Fluctuations and Crystal and Crucible Rotation Rate	185
X.	SUMMARY AND CONCLUSIONS	191
XI.	SUGGESTIONS FOR FURTHER WORK	194

Chapter Number		Page Number
XII.	APPENDICES	196
	A. Appendix 1 Materials Analysis and Properties	197
	B. Appendix 2 Analysis of Microsegregation Due to Fluctuation of Fluid Velocity and Temperature	200
	C. Appendix 3 Finite Difference Schemes for Numerical Integration of the Thermal Convection Equations	210
	D. Appendix 4 Computer Programs for Numerical Solution of the Thermal Convection Equations	252
	E. Appendix 5 Error Estimates of Solute Boundary Layer Thickness Calculations	282
	BIOGRAPHICAL NOTE	284
	REFERENCES	286

LIST OF FIGURES

Figure Number	Title	Page Number
1	Modified Czochralski Crystal Growth System	44
2	Schematic Drawing of Modified Crystal Growth Chamber	45
3	Modified Hot Zone Without Heat Shielding System	48
4	Interior of Modified Hot Zone	51
5	Schematic Drawing of Thermocouple Manipulator	53
6	Schematic Representation of Complications Associated With Temperature Measurement	61
7	Representative Temperature Fluctuation Spectra in a Standard Czochralski Puller	64
8	Representative Temperature Fluctuation Spectra in the Modified Czochralski System	65
9	Axial Melt Temperature Profile in a Standard Czochralski System	69
10	Axial Gas Temperature Profiles of the Heat Pipe With Crucible and Pedestal Removed	71
11	Gas Temperature Profiles of the Modified Hot Zone With an Empty Crucible at Position M	72
12	Vertical Temperature Profiles of the Melt and Crucible Wall (Crucible in Position H)	74

Figure Number	Title	Page Number
13	Vertical Temperature Profiles of Seeded Melt for a Crucible Located at Position H Within the Heat Pipe	75
14	Temperature Profiles of the Melt and the Gas Phase Within the Hot Zone of the Modified Growth System (Crucible in Position H)	76
15	Vertical Temperature Profiles of the Melt and Crucible Wall (Crucible in Position M)	77
16	Temperature Profiles of the Melt for a Crucible Located at Position M Within the Heat Pipe	78
17	Axial Temperature Profile of the Melt and Gas Phase Within the Modified Hot Zone (Crucible in Position L)	79
18	Axial Temperature Profiles of the Melt for a Crucible Located at Position L Within the Heat Pipe	80
19	Computed Contour Plots of Dimensionless Temperature, Vorticity, and Stream Function for Horizontal Bridgman Configuration; $Gr = 1 \times 10^4$, $A = 0.25$	98
20	Computed Contour Plots of Dimensionless Temperature, Vorticity, and Stream Function for Horizontal Bridgman Configuration; $Gr = 1 \times 10^5$, $A = 0.25$	99
21	Computed Contour Plots of Dimensionless Temperature, Vorticity, and Stream Function for Horizontal Bridgman Configuration; $Gr = 1 \times 10^6$, $A = 0.25$	100

Figure Number	Title	Page Number
22	Computed Contour Plots of Dimensionless Temperature, Vorticity, and Stream Function for Horizontal Bridgman Configuration; $Gr = 1 \times 10^7$, $A = 0.25$	101
23	Computed Contour Plots of Dimensionless Temperature, Stream Function, and Vorticity for Horizontal Bridgman Configuration; $Gr = 1 \times 10^6$, $A = 0.5$	104
24	Computed Contour Plots of Dimensionless Temperature, Stream Function, and Vorticity for Horizontal Bridgman Configuration; $Gr = 1 \times 10^5$, $A = 1.0$	105
25	Dependence of Main Vortex Intensity (I) on Grashof Number (Gr) for Constant Aspect Ratios (A)	106
26	Dependence of Main Vortex Intensity (I) on Aspect Ratio (A) for Constant Grashof Numbers (Gr)	108
27	Time Evolution of Dimensionless Temperature Field During One Convective Oscillation; $Gr = 1 \times 10^7$, $A = 0.25$	110
28	Time Evolution of Dimensionless Stream Function Field During One Convective Oscillation; $Gr = 1 \times 10^7$, $A = 0.25$	111
29	Time Evolution of Dimensionless Temperature and Stream Function Values at Center of Cavity; $Gr = 1 \times 10^7$, $A = 0.25$	113
30	Computed Contour Plots of Dimensionless Temperature and Stream Function for Czochralski Configuration (Run Number 20 in Table 9)	118

Figure Number	Title	Page Number
31	Computed Temperature Profiles for Czochralski Configuration (Run Number 20 in Table 9)	119
32	Computed Velocity Profiles for Czochralski Configuration (Run Number 20 in Table 9)	120
33	Computed Contour Plots of Dimensionless Temperature and Stream Function for Czochralski Configuration (Run Number 21 in Table 9)	122
34	Computed Temperature Profiles for Czochralski Configuration (Run Number 21 in Table 9)	123
35	Computed Velocity Profiles for Czochralski Configuration (Run Number 21 in Table 9)	124
36	Polished and Etched Sample Mounted on a Brass Disk with a Large Ohmic Back Contact	143
37	Impact Traces of Spreading Resistance Probe (10 μm spacings) and Interface Demarcation Lines on a Polished and Etched Ge Sample	143
38	Schematic Representation of Spreading Resistance Measurement Circuit	143
39	Assessment of Accuracy and Reproducibility of Microscopic Growth Rate Determination	146
40	Effect of Surface Preparation on Spreading Resistance (Ga Concentration) Measurements	150
41	Comparison of Longitudinal Segregation Associated with Growth Under Crystal Rotation	153

Figure Number	Title	Page Number
43	Comparison of Longitudinal Segregation Associated with Growth Under Crucible Rotation	157
44	Comparison of Radial Segregation Associated with Growth Under Crucible Rotation	159
45	Segregation in Modified Czochralski System Associated with Growth in the Absence of Rotation	161
46	Schematic Representation of a Non-Dimensional Finite Difference Grid	210
47	Horizontal Bridgman Configuration	214
48	Flow Chart of Numerical Solution	227
49	Czochralski Configuration	230
50	Flow Chart of Numerical Solution	251

LIST OF TABLES

Table Number	Title	Page Number
1	Values of the Critical Rayleigh Number for a Horizontal Layer of Infinite Extent Heated From Below	27
2	Temperature Fluctuation Components in the Standard Czochralski System	66
3	Temperature Fluctuation Components in the Modified Czochralski System	67
4	Selected Results From Vertical Temperature Profiles	81
5	Computer Runs for the Horizontal Bridgman Configuration	96
6	Positions and Intensities of the Main and Secondary Vortices During One Convective Oscillation of Computer Run Number 5	112
7	Experimental Convective Oscillation Periods	114
8	Theoretical Convective Oscillation Periods	115
9	Computer Runs for the Modified Czochralski Configuration	117
10	Summary of Comparative Segregation Behavior	162
11	Computed Values of the Solute Boundary Layer Thickness for a Ga Doped Ge Crystal Grown With Seed Rotation (17.1 rpm) in the Modified Czochralski Crystal Growth System	172
12	Fluid Velocities Due to Thermal and Forced Convection in the Modified Czochralski Crystal Growth System	177

Table Number	Title	Page Number
13	Measured and Calculated Periods of Convective Temperature Oscillations	181
14	Computed Periods of Momentum Bound- ary Layer Instabilities	182
15	Correlation of Growth Rate Varia- tions and Rotation Rate	189
16	Materials and Major Impurity Analysis	197
17	Selected Physical Properties of Liquid Germanium	198
18	Selected Physical Properties of Liquid Gallium and Silicone Oil	199

ACKNOWLEDGEMENTS

The author will be forever grateful to his thesis supervisor, Professor A.F. Witt, for introducing him to the fascinating field of convection and segregation phenomena in crystal growth systems. His constant support and timely advice throughout the period of the investigation and writing of this thesis are deeply appreciated.

A special thanks is extended to his co-advisor, Dr. J.R. Carruthers of Bell Telephone Laboratories, for lending his expertise to many enlightening discussions on thermal convection in crystal growth melts.

The author appreciated at all times the environment of scientific professionalism fostered within the Electronic Materials Group by Professor H.C. Gatos and acknowledges its profound influence on this work.

Gratitude is due the author's thesis review committee, Professors J.F. Elliott and T.B. King, in addition to Professor A.F. Witt and Dr. J.R. Carruthers, for their careful reading and criticism of the preliminary version of this document and their thoughtful suggestions for improvements.

The contributions of the staff, visiting scientists and postdoctoral fellows of the Electronic Materials Group are also gratefully acknowledged. In particular, discussions with Mr. C.J. Herman on crystal growth and equipment design, and with Mr. M. Lichtensteiger on spreading resistance

measurements were essential to the successful completion of this work. Furthermore, the aid and encouragement of Dr. L. Jastrezebski, Dr. K. Kim, Mr. W. Fitzgerald, Mr. J. Baker, and Ms. M. Cretella are greatly appreciated. In addition, the generous advice and assistance of Ms. G. Landahl and Ms. P. Merrick on procedural matters is cheerfully acknowledged.

The congenial interaction with fellow graduate students, including all the students in the Electronic Materials Group, in scientific discussions and social activities will be warmly remembered. The author is especially grateful to A. Muragi, D. Holmes, R. Gale, J. Thompson and M. Wargo for many thoughtful discussions on crystal growth and related topics; and to J. Vaughan for the many enjoyable discussions on philosophy and politics.

Thanks are due to Ms. D. Merritt for her careful preparation of the final text and tables and Ms. F. Lindon of Poly-Graphus for her skillful preparation of the figures.

Other individuals too numerous to mention individually have provided encouragement, advice, aid, and materials essential for the ultimate completion of this work. Each of these many contributions is gratefully acknowledged.

The author thanks God for whatever abilities he may have been given and for answering his numerous prayers for help during the course of this work.

The author's wife, Norine, has been a steadfast source of

love and encouragement throughout the course of this work and his son, Edward, has proved an inspiration during its completion.

Finally, much gratitude is extended to the John A. Lyons Fellowship and to the National Science Foundation (MRL) for financial support during the author's stay at MIT.

CHAPTER I

INTRODUCTION

Optimization of materials properties requires control of chemical composition and structural perfection. Deviation from specified composition, while inconsequential for some materials properties, may cause pronounced variations in the physical properties of others. Extreme sensitivity to chemical and structural homogeneity is, for example, encountered in the electronic properties of semiconductors.

Thus our inability to produce crystalline solids which achieve theoretical performance limits has in recent years been traced to a lack of adequate compositional and structural control during the processing of these materials. Specifically, compositional inhomogeneities in semiconductor crystals obtained by liquid-solid and gas-solid phase transformations could be correlated to adverse conditions at the growth interface resulting from hydrodynamic instabilities in the fluid phase. These instabilities take the form of temporal variations in growth rate and solute boundary layer thickness.

During melt growth, solute generally accumulates in a boundary layer region ahead of the solidification front. Convective processes within the melt will affect the distribution of solute whenever the diffusion distance D/R (where D is the liquid diffusion coefficient and R is the growth rate) exceeds the thickness of the solute boundary layer. Since crystal

growth from the melt requires the establishment of temperature gradients in the vicinity of the solid-liquid interface, heat flows are generated which invariably result in convective melt flows. The behavior of these flows and their influence on the phase transformation are complex and, as yet, not well understood. However, according to thermohydrodynamic theory, the nature of convective melt flows depends, among other things, on the magnitude of the temperature gradients (Rayleigh number), the nature of the molten material (Prandtl number), and the details of the imposed boundary conditions.

This work presents a quantitative approach to thermohydrodynamic and segregation phenomena in low Prandtl number crystal growth systems comprising a quantitative segregation analysis (employing interface demarcation and spreading resistance measurements), thermal characterization of the growth system, and a numerical analysis of the thermal convective flows. This approach has been applied to the Czochralski crystal growth system for which controlled thermal boundary conditions have been achieved.

CHAPTER II

OUTLINE OF OBJECTIVES, APPROACH, AND STRUCTURE

A. Objectives of Present Work

The present work was performed in an attempt to meet the following objectives: (a) development of a quantitative approach to the study of thermohydrodynamic and segregation phenomena in low Prandtl number crystal growth systems, (b) establishment of controlled thermal boundary conditions amenable to theoretical analysis of convective behavior and (c) reduction in the amplitude of compositional inhomogeneities in crystals grown.

B. Experimental and Theoretical Approach

To achieve these objectives a combined experimental and theoretical approach was developed and applied to a Czochralski crystal growth system. The experimental investigation involved (a) establishment of controlled thermal boundary conditions, (b) thermal characterization of the growth system, and (c) quantitative segregation analysis of grown crystals. The theoretical treatment required numerical solution of the equations appropriate to thermal convection in the Czochralski configuration.

Controlled thermal boundary conditions were to be achieved by exploiting the potential of a heat pipe for isothermal operation¹. This approach was taken since heat pipes have been

successfully used to establish uniform temperature distributions in horizontal vapor and solution growth systems. No attempts have, however, been made to use the heat pipe concept in the Czochralski growth configuration. Characterization of the resulting thermal environment was to be accomplished by mapping the temperature distribution in the hot zone (the crucible wall, the melt, and the protective gas phase) of the growth system. Quantitative segregation analysis was to be achieved through interface demarcation (for growth-rate determination) and spreading resistance measurements for the determination of composition on the micro-scale. Interface demarcation was further used to delineate the growth interface morphology and determine its changes during growth.

The theoretical analysis of thermal convection was to be pursued to establish the theoretical temperature distribution and flow pattern within the melt. This approach was necessitated by the lack of an experimental method of flow determination for high temperature, low Prandtl number melts in the Czochralski configuration. A computer program employing an explicit finite difference scheme was developed to solve for thermal convection within the crucible based on the measured thermal boundary conditions. The advection terms of the vorticity and energy equations were represented by quadratically conservative finite difference forms² which were expected to maintain numerical stability at high Grashof numbers. The

applicability of this analysis could be assessed by comparison of theoretical with experimental temperature profiles.

The indicated approach was applied to Czochralski growth of Ga doped Ge crystals. The choice of this binary system was based on the following considerations: (a) previous studies³ have indicated that the nature of thermal convection in Ge (937°C) melts is intermediate between the relative stability of InSb (527°C) melts and the thermal turbulence of Si (1410°C) melts, thus exhibiting all elements of convective behavior (laminar, oscillatory, and turbulent), (b) the Ge-Ga system has been shown to be amenable to quantitative segregation analysis⁴, and (c) the physical properties of Ge have been extensively investigated.

C. Structure of the Thesis

During the course of the present investigation, the study of thermal convection and that of growth and segregation were pursued separately. Therefore, this separation has been maintained in the structure of this thesis. The treatment of thermal convection is presented in chapters III through VI and that of growth and segregation in chapters VII and VIII. The results of these independently conducted studies are brought together and interrelated in chapter IX which presents a discussion and analysis of convection and its effects on segregation during Czochralski crystal growth.

CHAPTER III

BACKGROUND AND PREVIOUS WORK
ON THERMAL CONVECTION

This chapter reviews the literature pertaining to the factors which influence thermal convective phenomena in confined fluids and which are relevant to understanding such phenomena in crystal growth melts. For the readers convenience, several recent reviews of thermal convection in growth related configurations are presented first. (The previous work on forced convection and dopant segregation is presented in Chapter VII.)

A. General Reviews

The present state of knowledge of thermohydrodynamics in melt growth systems has been extensively reviewed in several recent papers^{5,6,7}. Carruthers⁵ discusses the factors which influence the stability and forms of thermal convective flow and presents the methods employed to control thermal convection; he emphasizes the importance of thermal and fluid boundary conditions and of the degree of confinement in determining the nature of thermal convective instabilities. Jakeman and Hurle⁶ treat temperature oscillations in the melt from both a theoretical and experimental point of view; they discuss the relationship between oscillations and solute striations in grown materials and consider methods of eliminating such oscillations in melt growth systems. Carruthers⁷, in another

review, considers various models for convective oscillations and develops expressions which relate the period of oscillation to the imposed boundary conditions with special emphasis on the distinction between low Prandtl number (Pr) fluids (liquid metals and semiconductors) and high Pr fluids (liquid oxides and nonmetallics).

B. Horizontal Layers Heated From Below

The study of a horizontal fluid layer heated from below and cooled from above is a fundamental model for the development of many important concepts in thermal convection which have direct application to complex systems including melt growth.

1. Horizontal Layers Heated From Below With Infinite Lateral Extent

The initial impetus for the study of convection associated with horizontal layers heated from below arose from observations of Benard⁸ which stimulated Lord Rayleigh⁹ to develop the linear theory of Benard instability. The complete linear theory for horizontal fluid layers of infinite lateral extent heated from below has been presented by Chandrasekhar¹⁰ in his treatise on hydrodynamic stability. Accordingly such systems are conveniently characterized by two dimensionless parameters, the Prandtl number, $Pr = \nu/\kappa$, (which is the ratio of momentum transfer due to kinematic viscosity, ν , to thermal transfer due to thermal diffusivity, κ) and the

Rayleigh number, $Ra = \alpha g \beta d^4 / \nu \kappa$, (which expresses the temperature gradient β in nondimensional form where α is the thermal expansion coefficient of the fluid, g is the acceleration due to gravity, and d is the thickness of the fluid layer). When the Rayleigh number exceeds a critical value (Ra^C), an initially stagnant fluid layer becomes unstable and subject to stationary cellular convection of dimensionless wave length, $a_c = \lambda_c / d$, where λ_c is the horizontal dimension of the convection cells. The principle of exchange of stabilities¹⁰ is said to apply to such systems meaning, the initial motion is not periodic in time.

It is important to recognize that the values of Ra^C and a_c depend on the nature of the horizontal bounding surfaces (Table 1). Thus systems with free surfaces which allow velocity perturbations are less stable than those with rigid surfaces as shown by the lower value of Ra^C . Similarly systems with insulating surfaces which allow temperature perturbations are less stable than those with isothermal surfaces.

TABLE 1

Values of the Critical Rayleigh Number for a Horizontal Fluid Layer of Infinite Extent Heated From Below⁵

Mechanical Boundary Conditions	Thermal Boundary Conditions		
	Both Conducting	Upper Insulating	Both Insulating
Both rigid	1708	1296	720
Upper free	1101	669	320
Both free	658	--	120

A number of experimental studies have been conducted at Rayleigh numbers in excess of the critical value. Schmidt and Milverton¹¹ developed a basic experimental approach which involves measurement of both the heat flux (Q) through the layer studied and the temperature difference (ΔT) across the layer. Their data were analyzed on the basis of a plot of Rayleigh number vs. Nusselt number, where the Nusselt number, $N = Q/(k\Delta T/d)$, is the ratio of the measured heat flux to that which would occur for pure conduction (k is the thermal conductivity of the fluid). On such a plot a transition from one mode of flow to another is indicated by a change of slope.

The most precise experiments of convection in the Benard geometry have been those conducted by Krishnamurti^{12,13,14}. Her studies included the range of Rayleigh numbers, $Ra^C < Ra < 10^6$, and the range of Prandtl numbers,

$2.5 \times 10^{-2} \leq Pr \leq 8.5 \times 10^3$. Krishnamurti^{12,13} identified in addition to Ra^C , four transitions at the critical Rayleigh numbers, Ra^{II} , Ra^{III} , Ra^{IV} , and Ra^V . Her studies showed steady flow ($Ra^C < Ra < Ra^{III}$) which, for $Ra < Ra^{II}$, took the form of two-dimensional rolls oriented such that a maximum number had their axes perpendicular to the lateral boundaries and, for $Ra > Ra^{II}$, took on a three-dimensional structure. Above Ra^{III} the flow became time dependent with full turbulence setting in at Ra^V . This development of turbulence through a series of flow transitions is a feature generally encountered in thermal convective flows.

Krishnamurti^{13,14} further revealed in high Prandtl number ($Pr > 1$) fluids the bimodal nature of time dependent flows through visual and thermal studies. One mode consists in a slow tilting of the convection cell walls with a period determined by the thermal diffusive time (d^2/κ); the second mode consists in the advection of a "knot" or region of high shear by the basic cellular flow. The temperature anomaly associated with the convective knot is recorded by a stationary thermocouple as a temperature oscillation, whose period depends on the cell dimensions and the flow velocity. The doubling of the oscillation frequency above Ra^{IV} has been correlated with a doubling of the number of convective knots. Krishnamurti suggests that, at very high Ra and Pr , Howard's¹⁵ model of periodic thermal boundary layer instability is likely to

apply. In this model, the thickness of the lower thermal boundary layer increases until the Rayleigh number, based on this thickness, exceeds a critical value (about 10^3) and a "blob" of warm fluid (a thermal) breaks away from the thermal boundary layer. This reduces the thermal boundary layer thickness (and the Rayleigh number) below the critical value and the process is repeated.

In low Prandtl number fluids, Krishnamurti¹⁴ observed a dramatic decrease in the critical Rayleigh numbers, Ra^{III} , Ra^{IV} , and Ra^V with decreasing Pr, while the transition at Ra^{II} could not be observed. She proposed that for such fluids shear instability is the likely mode of oscillation. Application of Busse's¹⁶ model for transverse wave instability of convective rolls ($\tau = (2/3)^{1/2} b / ((Ra - Ra^c) / Ra^{1/2})$ where b is the wave number and τ is the period in units of d^2/κ) resulted in good agreement with the data for air ($Pr = 0.71$) but poor agreement with data for mercury ($Pr = 2.5 \times 10^{-2}$) which instead exhibited periods on the order of the viscous diffusive time (d^2/ν). In this context it is worth noting that Carruthers⁷, most recently found good agreement between Busse's theory and experimental data reported in the literature.

A numerical study of the Bénard geometry has been conducted by Fromm¹⁷ using cyclic boundary conditions to simulate infinite horizontal extent. He found that, for $Ra \geq 10^6$, the fundamental mode exhibited an oscillation of period,

$\tau = 0.010 d^2/\kappa$, in the form of a pulsating growth and decay in tandem of adjacent vortices, causing a rising column of fluid to go alternatively left and right. This period is larger, by a factor of ten, than that observed by Krishnamurti for the same Rayleigh number and the calculated critical Rayleigh number (Ra^{III}) is larger by a factor of 10^2 .

2. Horizontal Layers Heated From Below With Lateral Confinement

The influence of lateral confinement on the stability and flow patterns of a fluid layer heated from below has been extensively discussed by Carruthers⁵. Analysis of this situation requires the specification of an additional dimensionless parameter, the aspect ratio, $A = d/L$, (where d is the layer thickness and L is the separation between the lateral bounding surfaces). The layer of infinite horizontal extent corresponds to the limit of vanishing aspect ratio.

It has been shown that the influence of lateral side walls on fluid stability through the action of viscous shear is proportional to the ratio of the total wetted surface area to the fluid volume. Heitz and Westwater¹⁸ have shown that, for a fluid in a box of square cross section, the surface area to volume ratio is $\Gamma = (2/L)(1/A + 2)$. They suggest that the influence of the side walls is important even at relatively low aspect ratios since the value of Γ at the aspect ratio of 5 is within 10% of its limit at large aspect ratios. This predicted

behavior has been confirmed by their experimental findings involving water confined in a rectangular region heated from below.

A two-dimensional numerical study of the confined Bénard geometry has been conducted by Samuels and Churchill¹⁹. Their calculations covered the range of parameters, $0.33 \leq A \leq 2.0$, $0.01 \leq Pr \leq 25$, and $1,000 \leq Ra \leq 40,000$. They found an increase in stability (larger critical Rayleigh number) with increasing fluid confinement (larger aspect ratio) and a decrease in stability with decreasing Prandtl number. Both of these findings are in agreement with the experiments conducted by Chiesa and Guthrie²⁰ involving mercury and lead contained in stainless steel tubes heated from below.

Several studies have been undertaken to determine the flow patterns in confined fluid layers. Ovchinnikov²¹ reported that flow in a water filled cube ($A = 1$) is initiated as a two-dimensional asymmetric roll at $Ra^C = 3650$ which exceeds that of the unbounded layer. The liquid undergoes a transition to three-dimensional flow with fluid rising in two diametrically opposite vertical quarters and descending in the other two at $Ra^{II} = 6000$. Harp and Hurle²² concluded the existence of this second convective mode in a container ($A = 2.8$) filled with liquid gallium from phase analysis of temperature oscillations with periods of 40 seconds measured across the upper surface.

The convective behavior of gases enclosed in a vertical cylindrical container heated from below has been reported by Mitchell and Quinn²³ for the range of parameters $10^4 < Ra < 10^5$ and $0.5 < A < 2.0$ where the aspect ratio is defined as $A = d/R$ (R is the cylinder radius). They found that, for large aspect ratios ($A > 1$), the flow consists of an asymmetric roll extending across the diameter of the cell. For $A < 1$, three different flow patterns extending across the radius were observed; (a) a symmetric toroidal roll, (b) a three-dimensional mode similar to the second mode of Ovchinnikov²¹, and (c) a mode with a mirror symmetry plane along one diameter. For Rayleigh numbers above a critical value the basic flow patterns developed an oscillatory character in the form of three-dimensional spirals rotating about the axes of the suboscillatory flow.

c. Rectangular Enclosure Heated From The Side

Studies conducted on thermal convection in a rectangular enclosure with imposed horizontal heat flow are of particular importance for horizontal crystal growth. The original theoretical treatment by Batchelor²⁴ demonstrated that, as opposed to the case of heating from below, no critical temperature difference need be exceeded to initiate thermal convective flow for horizontal heating. The nature of the temperature and flow fields were shown to depend on the values of three non-dimensional parameters, the aspect ratio ($A = H/L$), the Prandtl number (Pr), and the Rayleigh number ($Ra = g\alpha\Delta TL^3/\nu\kappa$)

(where T is the horizontal temperature difference imposed across the cavity of length L and height H). By power series expansion in terms of Ra , Batchelor determined that, for $A = 1$ and $Ra < 10^3$, to first order in Ra , the flow consisted in a circular roll with fluid ascending along the warm wall and descending along the cool wall. It is of interest to note that employing the technique of orthogonal polynomial expansion, Poots²⁵ obtained a more complicated solution which is in good agreement with Batchelor's for $Ra < 10^3$. Furthermore, Wilkes and Churchill²⁶ obtained a numerical solution for thermal convection in a square cavity ($A = 1$) filled with air ($Pr = 0.733$) which was in excellent agreement with the analytical solution of Poots for $Ra = 5 \times 10^3$.

An extensive numerical study of a square cavity ($A = 1$) was conducted by Stewart and Weinberg²⁷ for the range of parameters, $0.0127 \leq Pr \leq 10.0$ and $2 \times 10^3 \leq Gr \leq 2 \times 10^7$, where the Grashof number, $Gr = Ra/Pr$, is the customary nondimensional temperature difference used for horizontal heat flows. They found that, while the flow field depended on Gr and Pr separately, the thermal field depended only on Ra and was dominated by conduction for $Ra < 10^3$ with convection becoming increasingly important for $Ra > 10^3$ (as indicated by the Nusselt number). This observation has important consequences for thermal convection flows, since for identical thermal fields (same Ra), the velocity fields for high and low Pr fluids are

considerably different, while for similar flow rates, the temperature fields for high and low Pr fluids differ radically. High Pr fluids tend to develop a boundary layer structure with low flow rates, whereas the thermal and velocity fields extend further into the interior of low Pr fluids with higher rates of flow. Thus, flow simulations employing transparent high Pr fluids are of questionable value for modeling thermal convection in opaque, low Pr liquid metals and semiconductors.

Though most studies of thermal convection in rectangular enclosures have been conducted on high Pr fluids, a number of important investigations have been reported for liquid metals and semiconductors. Cole and Winegard²⁸ found that temperature fluctuations commenced in liquid tin when $H^3 \beta_H > 3.1 \text{ cm}^2 \cdot \text{C}$ (where β_H is the horizontal temperature gradient). Mueller and Wilhelm²⁹ found that the amplitude of temperature fluctuations, \bar{T} , increased with increasing L and β_H , and increased as liquid travelled along the upper free surface of indium antimonide melts. Using melts of liquid tin and aluminium, Utech and Flemings³⁰ observed an increase of both \bar{T} and frequency, ω , with increasing β_H and a decrease of \bar{T} with depth into the melt. In an extensive investigation on liquid gallium, Hurle and coworkers^{31,32,33} found that temperature oscillations commenced for $L\beta_H^C > 20^\circ\text{C}$ with a period which increases linearly with L and was independent of H (except for a mode change). From measured temperature distributions and time phase

correlations of the temperature oscillations, they determined that the basic unicellular roll was only slightly perturbed by the instability. Stewart and Weinberg³⁴, employing radioactive tracer techniques in liquid tin and lead, found an increase in flow rate with increasing temperature difference. MacAuley³⁵, also using radioactive tracer techniques, determined that, in liquid tin, the flow velocity is linearly dependent on the average β_H and independent of L. Employing the lead-thallium system in a series of quenching experiments, Carruthers and Winegard³⁶ determined a direct correlation between the amount of lateral (non-axial) heat flow and the intensity of thermal convection, as revealed by changes in the thermal and solute boundary layer structure near the solid-liquid interface. These experimental findings have been explained by Carruthers³⁷ on the premise that the basic unicellular thermal convective flow generated by the imposed horizontal temperature gradient, which produces a stable vertical temperature gradient (hotter fluid over cooler fluid) in the bulk liquid, is destabilized (cooler fluid over hotter fluid) in the vicinity of the horizontal surfaces by transverse vertical heat flow at these surfaces. When the fluid acceleration, generated within these regions of adverse vertical temperature gradient, is sufficiently large, boundary layer separation and associated vortex formation occurs along the horizontal end walls, which results in temperature fluctuations within the melt. Values of the

critical Rayleigh number ($Ra^C = \alpha g \beta_c H^3 L / \nu \kappa$) for the onset of temperature oscillations were computed to be 2940 and 1950 for the studies of Cole and Winegard²⁸ and Utech and Flemings³⁰, respectively. The close agreement of these values to those for confined fluid layers heated from below has been interpreted⁵ as an additional indication of the important role of vertical heat flow in determining fluid stability.

Carruthers⁵ has proposed that t_H , the length of time during which the fluid travels along horizontal surfaces where it is subject to the effect of vertical heat flows, is an important parameter. The increase in \bar{T} as the fluid travels along the horizontal surface is attributed to the increased time it has been affected by the adverse vertical temperature gradient. Since the axial flow velocity is independent of L and linearly dependent on β_H , t_H depends linearly on L and inversely on β_H . Thus the linear increase in the amplitude and period of the oscillation with L is interpreted as an increase in flow transit time along the horizontal surfaces, while the decrease of frequency with β_H is understood as a decrease of transit time.

C. Vertical Cylindrical Enclosure With Horizontal and Vertical Heat Flow

Investigation of thermal convection in vertical cylindrical enclosures with combined horizontal and vertical heat flows are of direct importance to crystal growth by the

Czochralski, vertical Bridgman, and other vertical solidification techniques. The rate of crystal growth is controlled by radial input of heat into the melt and axial withdrawal of heat through the solid-liquid interface. As discussed in the preceding section, the horizontal component of the heat flow will always generate a thermal convective flow. Several investigations of unstable thermal convection in Czochralski crystal growth from high Prandtl number oxide and fluoride melts have been reported. For both rotating and stationary CaF_2 melts, Wilcox and Fullmer³⁸ observed random temperature fluctuations with periods of 1 to 3 seconds and amplitude of 20 to 40°C which reached a maximum at a distance of a few millimeters below the upper surface and which could be reduced by reducing vertical heat losses. Brice and Whiffin³⁹ reported that regular thermal oscillations with 8 second periods and 0.5°C amplitudes in ZnWO_4 melts were related to growth rate induced solute striations in grown crystals.

Cockayne and Gates⁴⁰ have related temperature fluctuations in CaF_2 and CaWO_4 melts to solute striations in grown crystals; they also observed small angular movements of a radial spoke pattern on the surface of the melt produced by thermal convection and made visible by a temperature dependent emissivity; in non-rotating melts, thermal oscillations with periods of 10 to 15 seconds and amplitudes of 3 to 5°C appeared associated in grown crystals with solute striations and a displacement

(2 to 3mm) of the thermal center. More extensive meandering of the center of the spoke pattern was found to result in a longer period (1 to 3 minute) and larger amplitude temperature fluctuation (10 to 20°C, maximum at the crucible center). Small amplitude angular movements of the spoke pattern produced thermal oscillations with periods of less than 5 seconds and amplitudes of 2 to 3°C; these oscillations were associated with a finely spaced set of striations in the grown crystals. Reduction of heat loss from the melt surface by the use of after heaters eliminated the temperature oscillations and the spoke pattern, while application of crucible rotation enhanced them.

In studies on $\text{Ba}_2 \text{Na Nb}_5 \text{O}_{15}$ melts Cockayne et al.⁴¹ observed a reduction in the amplitude of temperature fluctuations (8 to 12 per minute in both the melt and the gas phase) and in the intensity of compositional growth striations with decreasing melt height. By extrapolation of this data to zero amplitude, Carruthers⁵ determined the critical Rayleigh number for the onset of temperature oscillations to be 3×10^4 , in good agreement with the minimum value (2×10^4) reported by Mitchell and Quinn²³. This value exceeds, however, the critical Rayleigh number (3.6×10^3) for the onset of thermal convection in a confined layer of equivalent aspect ratio (0.8) heated from below. The findings in oxide systems suggest that a steady cellular flow, driven by radial temperature gradients,

exists prior to the development of temperature oscillations.

Of direct importance for vertical crystal growth from low Pr melts is the series of experiments reported by Kim, Witt, and Gatos⁴² in which the thermohydrodynamics of completely confined InSb melts, heated radially and cooled axially, have been studied during growth for continuously varying aspect ratios ($0 < A < 4.5$) and Rayleigh numbers ($0 < Ra < 3 \times 10^5$). They report that, for $Ra > 4 \times 10^3$, random, high-frequency, temperature fluctuations (5°C) superposed on large (10°C) variations of the mean melt temperature with periods of 2 to 4 minutes which caused pronounced remelting alternately on the left and right side of the crystal; in the range, $3 \times 10^3 > Ra > 2 \times 10^3$, they observed highly periodic temperature oscillations and associated solute striations which, with decreasing Ra, undergo a mode change at $Ra = 2.6 \times 10^3$ from a frequency of 0.29/sec and amplitude 0.35°C to a frequency of 0.38/sec with the amplitude decreasing from 0.1°C to below measurement capability. Below $Ra = 2 \times 10^3$, neither thermal oscillations nor solute striations were observed.

These observations have been discussed by Carruthers⁵ who concluded that the long period thermal variations above $Ra = 4 \times 10^3$ are produced by meandering of the thermal center. He bases his conclusion on the similarity of measured amplitude and frequency to those reported by Cockayne and Gates⁴⁰.

The multitude of divergent observations concerning convective flow in growth systems reported in the literature^{40,41,43} have led Carruthers⁵ to the following conclusions: (a) the onset of oscillatory thermal convection occurs at Rayleigh numbers very close to the critical value (Ra^C) for heating from below; (b) the steady circulation due to radial temperature gradients is more effective in stabilizing high Pr fluids against such oscillatory behavior than in stabilizing low Pr fluids; (c) for low Pr fluids the destabilizing influence of fluid to container thermal conductivity ratio is more important than the stabilizing effect of the higher flow rates; and (d) due to the presence of the suboscillatory shear flow, the onset of oscillatory thermal convection does not violate the principle of exchange of stabilities for confined flows.

E. Control of Thermal Convection

The methods used to control thermal convection in the melt are based on an attempt to reduce the Rayleigh number.

Recently several methods for controlling thermal convection have been applied to Czochralski crystal growth systems. Cockayne and Gates⁴⁰ have successfully reduced the amplitude of thermal fluctuations by reducing the heat loss from the upper melt surface (and thereby the vertical temperature gradient in the melt) through the use of after heaters. This procedure, however also reduces the radial gradient in the melt making crystal diameter control difficult. Brice et al.⁴⁴

have employed a horizontal baffle in the melt to reduce the effective melt height and to minimize the amplitude of temperature oscillations in the melt.

Temperature oscillations (and associated solute striations in grown material) have been reported to be suppressed by application of a steady magnetic field^{30,32} to electrically conducting melts confined in a horizontal boat. The basis of this suppression is an increase in the effective melt viscosity through the action of the Lorentz force.

CHAPTER IV

APPARATUS AND EXPERIMENTAL PROCEDURE

The present chapter covers the apparatus and experimental procedures used for thermal characterization of the Czochralski crystal growth system. (The computational procedures employed in obtaining the numerical solution of thermal convection in this system are considered in Chapter VI and more completely in Appendix III. Apparatus and procedures required for analyzing growth and segregation phenomena are discussed in Chapter VIII.)

A. Crystal Growth System and Related Equipment

The experimental approach to the study and control of thermohydrodynamics and segregation required a crystal pulling facility with a well defined thermal configuration. Such a configuration was achieved by the installation of a sodium filled heat pipe located coaxially between the heating element and the crucible containing the germanium melt. Additionally, it required (a) the capability for performing thermal characterization of the melt system and (b) provisions for applying interface demarcation during crystal growth by current pulsing. The crystal growth facility modified to meet these requirements is hereafter referred to as the modified Czochralski crystal growth system.

1. Crystal Growth Apparatus

The study was carried out in a modified NRC crystal puller (Figure 1) with the following standard capabilities:

Furnace power:	4 kw
Temperature Control:	$\pm 0.05^{\circ}\text{C}$ (at growth temperature)
Pull Rate:	0 to 5.9 cm/hr
Seed Rotation Rate:	0 to 110 rpm
Crucible Rotation Rate:	0 to 40 rpm
Protective gas atmosphere:	argon

a. Growth Chamber

A detailed schematic of the crystal growth chamber is shown in Figure 2. The chamber has a double wall construction to permit water cooling and is capable of maintaining, at growth temperature, a vacuum lower than 5×10^{-2} torr. A feed-through ring permits access to the chamber interior for thermal characterization.

b. Heater System

The heater system consisted of a graphite ladder heater and heat shielding, a 40 volt, 100 amp power transformer (connected to the main line), and a Leeds and Northrup temperature control system. The controlling thermocouple was positioned below the crucible. The set point of temperature controller could be adjusted in units of 10 microvolts (0.25°C).

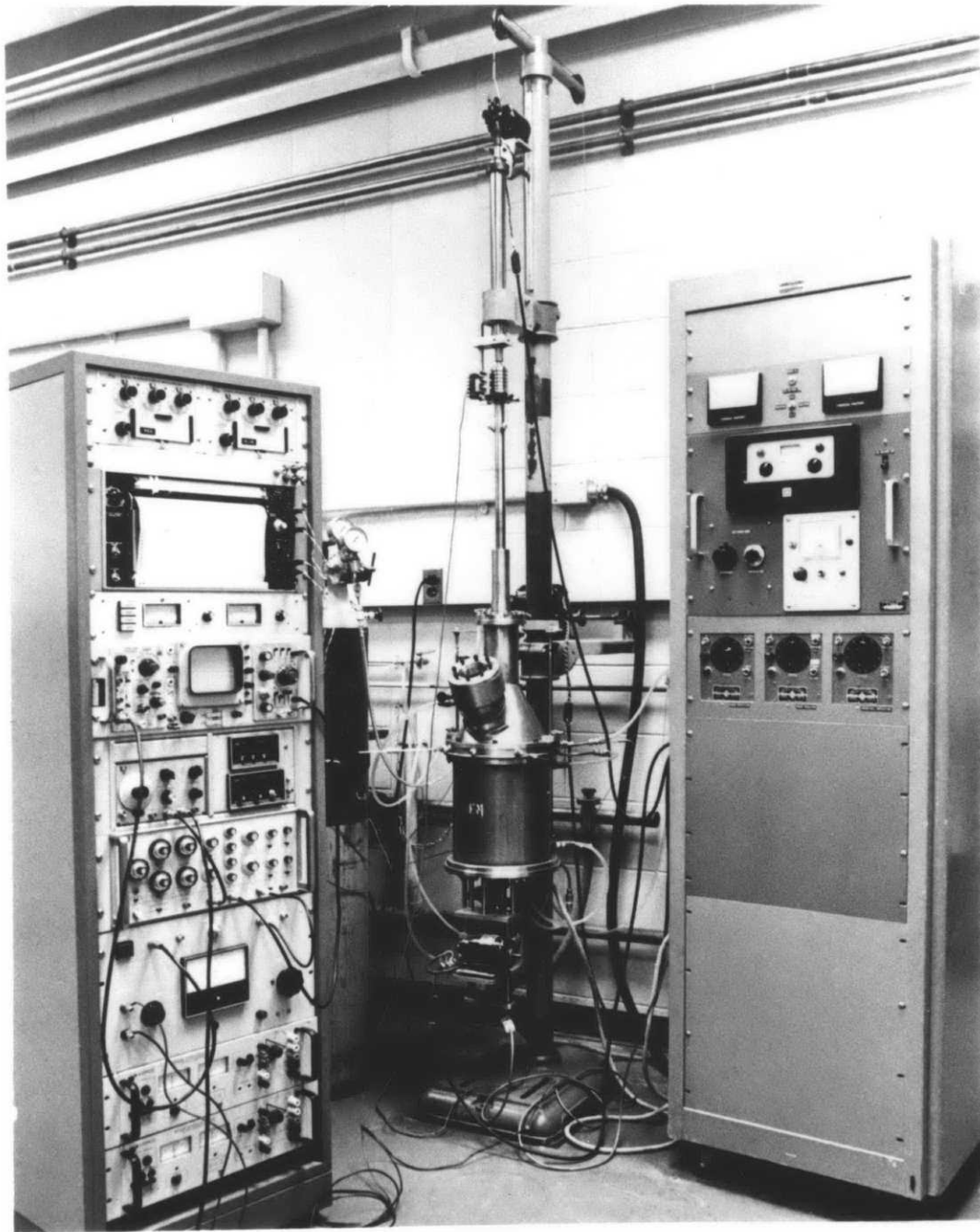


Figure 1. Modified Czochralski crystal growth system; current pulsing system and temperature recording instrumentation (left); modified NRC crystal puller (center); power supply and temperature controller (right).

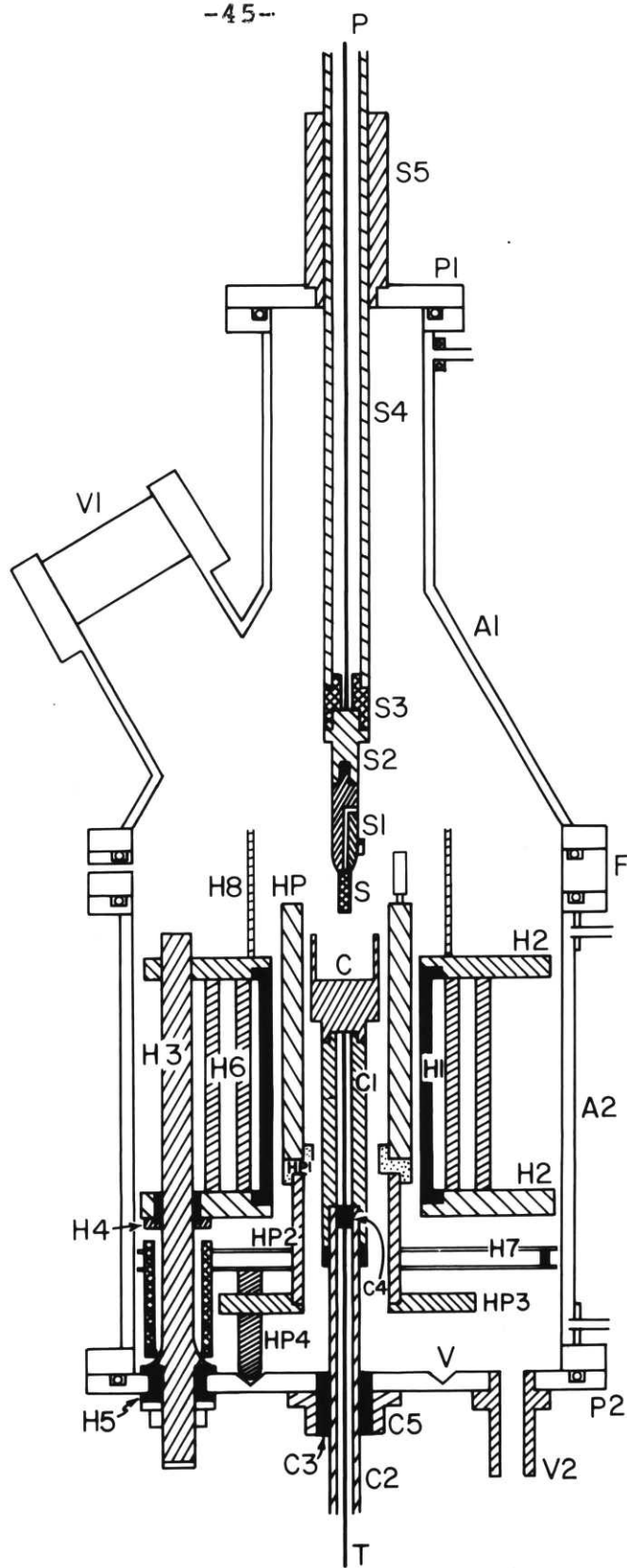


Figure 2. Schematic drawing of modified crystal growth chamber. (Explanation of various parts on next page.)

Figure 2. Schematic drawing of modified crystal growth chamber.
(Continued from preceding page).

Upper chamber section: chamber wall (A1), top plate (P1),
view port (V1).

Lower chamber section: chamber wall (A2), base plate (P2)
with V-groove (V) and vacuum port (V2),
feed-through ring (F).

Heater system: heater (H1), heater supports (H2),
electrode (H3), insulation (H4 and H5),
heat shields (H6, H7, and H8).

Heat pipe system: heat pipe (HP), heat pipe support (HP1,
HP2, HP3, and HP4).

Seed system: seed crystal (S), seed holder (S1),
seed holder bracket (S2),
insulation (S3), pull shaft (S4), pull
shaft bearing (S5), current lead (P).

Crucible system: crucible (C), pedestal (C1), crucible
shaft (C2), insulation (C3 and C4),
crucible shaft bearing (C5), control
thermocouple (T).

c. Heat Pipe and Heat Pipe Support

The heat pipe used in the present investigation was a sodium filled annular isothermal Inconel liner (Dynatherm 11-16-6) of length 15.24 cm, O.D. 7.32 cm and I.D. 4.14 cm. The heat pipe was installed with the fill tube oriented upward (see Figure 3) and operated in an argon atmosphere⁴⁵ (initial runs conducted in a hydrogen atmosphere resulted in swelling of the liner).

A heat pipe support (see Figures 2 and 3) was designed and constructed which allowed for positioning and alignment of the heat pipe. The threaded legs of the tripod base provided the capabilities of vertical positioning and angular adjustment and provided the means for coaxial alignment of the heat pipe with the crucible shaft.

d. Crucible

The crucibles (ATJ grade graphite) used in this study had the following dimensions: O.D. 3.81 cm, I.D. 3.20 cm, depth 1.90 cm. The capability for profiling the temperature of the side wall was provided for by two vertical holes (diameter 0.16 cm, depth 2.00 cm) at opposite ends of a crucible diameter into which thermocouple probes, could be inserted.

e. Current Pulsing System

A current pulsing system described by Lichtensteiger,

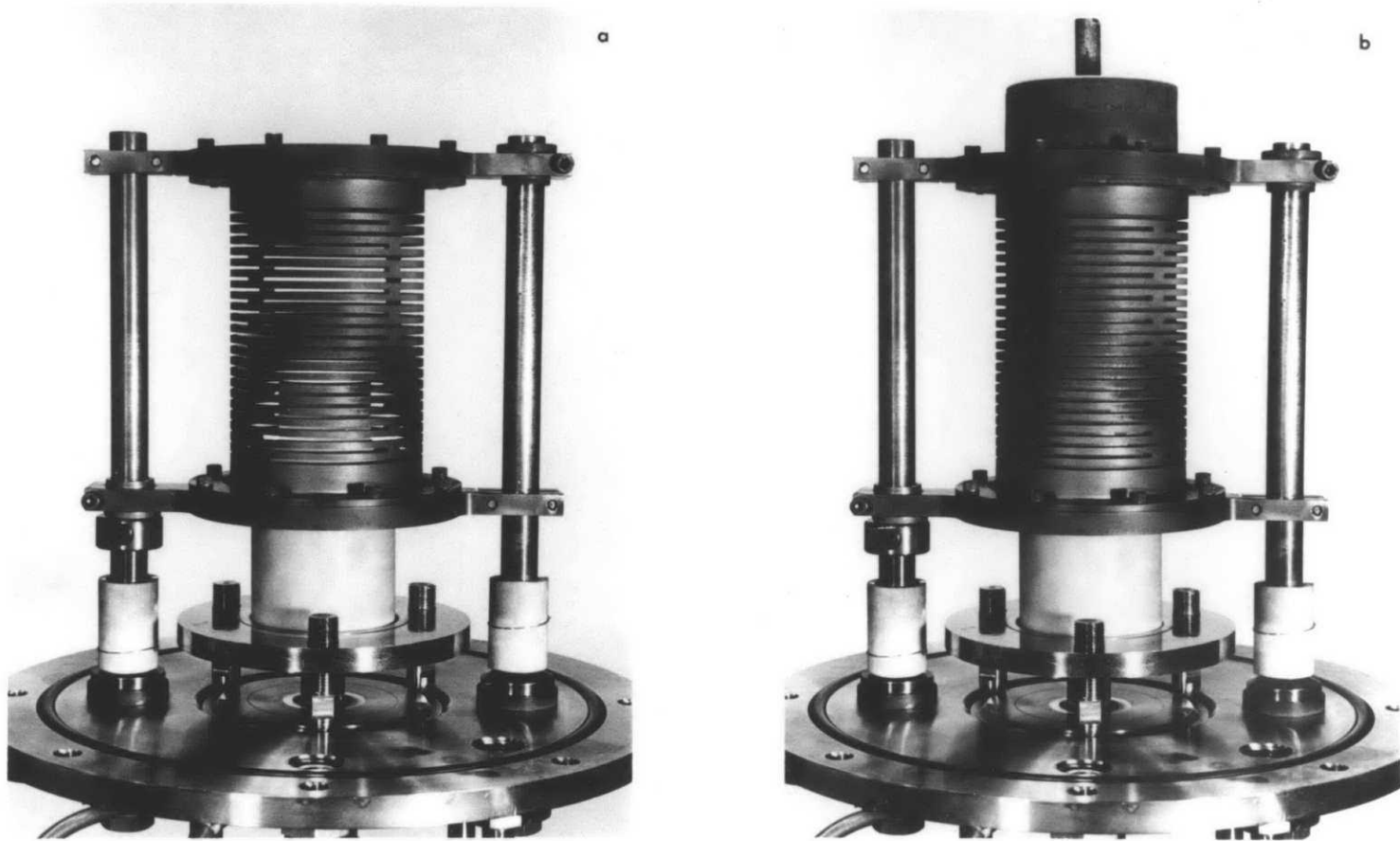


Figure 3. Modified hot zone without heat shielding system. (a) Hot zone without heat pipe. (b) Hot zone with heat pipe.

Witt, and Gatos⁴⁶ was used for interface demarcation: The output of a programmable power supply was controlled by a function generator which was triggered by a pulse generator; the resulting current pulses were monitored on a differential oscilloscope. The system was capable of introducing current pulses with the following characteristics: amplitude 0 to 36 amp, pulse width 10 nsec to 1 sec, repetition rate 0 to 10 MHz.

The current pulses were applied to the growth interface by means of an electrode system shown in Figure 2: The seed electrode system consisted of (1) a commutator ring, (2) a platinum current lead, (3) a stainless steel seed holder bracket, and (4) a molybdenum seed holder. The melt electrode system consisted of (1) a commutator ring, (2) a stainless steel crucible shaft, and (3) a graphite crucible with pedestal.

2. Thermal Characterization Equipment

Characterization of the thermal environment within the crystal growth system required the design and construction of a sensitive temperature measurement device, with the capability of positioning a temperature sensor throughout the hot zone.

a. Thermocouple Probe Assembly

The temperature measuring elements chosen for the present investigation were 76 μ m diameter bare wire chromel-alumel thermocouples (Omega Engineering Incorporated). The

choice of wire diameter was a compromise between the improved measurement accuracy and sensitivity of thinner wires and the improved service life of thicker wires. Wires of small diameter improve the accuracy of temperature measurement by reducing the heat conduction along the wire leads, reducing the time constant of the measuring junction (to permit the measurement of high frequency temperature oscillations), and also reducing the perturbing influence of the measurement device on the basic flow within the melt. The thermocouple probe assembly (diameter $D_p = 0.07$ cm) immersed in a Ge melt with a flow rate (V) of 0.1 cm/sec has a small Reynolds number ($Re = VD_p / \nu = 6$) and thus constitutes only a small perturbation to the basic flow⁴⁷. In a typical temperature measurement experiment, the thermocouple probe had to remain in the melt for a period of 12 hours which thus constitutes the shortest service life tolerable for the probe. Probes constructed with 76 μ m diameter chromel-alumel thermocouples and packaged as described below, were found to satisfy the above requirements.

The two thermocouple probe assemblies used during the course of this work are shown in Figure 4. The H-type assembly (left) was used to profile beneath the (seed) crystal and near the upper melt surface, while the S-type assembly was used to profile the crucible side wall and the vicinity of the crucible bottom.

The complete thermocouple probe assembly consisted of a

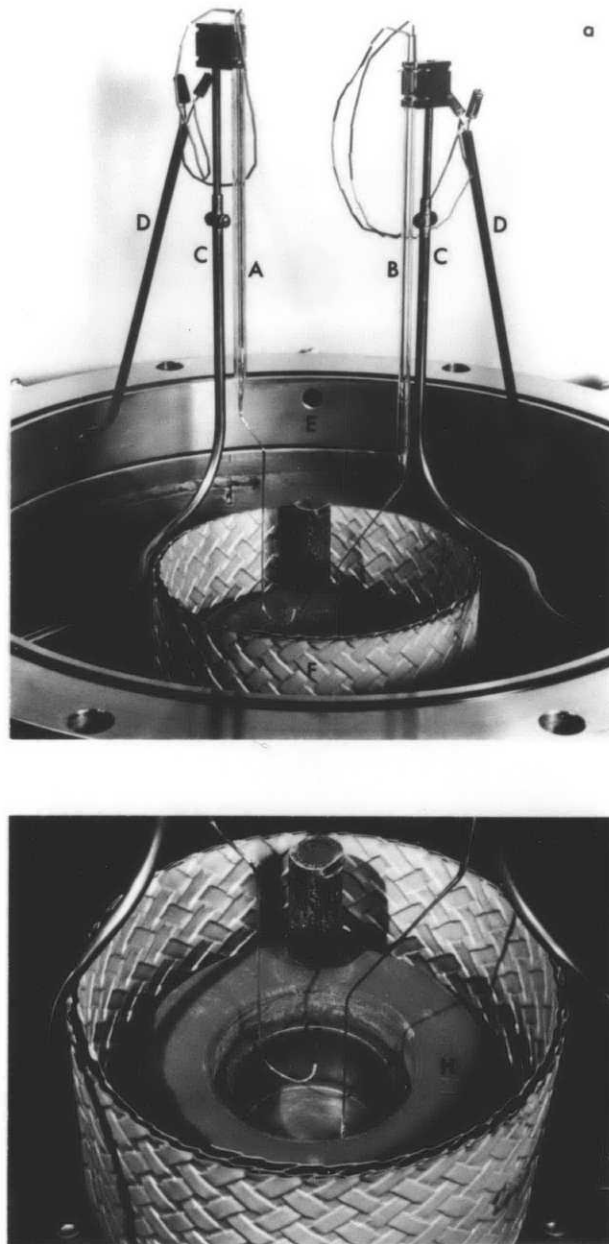


Figure 4. Interior of modified hot zone. (a) H-type thermocouple probe (A), S-type thermocouple probe (B), thermocouple manipulators (C), thermocouple feed-throughs (D), feed-through ring (E), heat shielding (F). (b) View showing H-type and S-type thermocouple probes positioned in the interior of the modified hot zone with crucible (G) at position M within the heat pipe (H).

thermocouple threaded through a thermocouple holder with a protective coating applied to the measurement junction and insulating beads applied to the lead wires. The thermocouple holder was fabricated by drawing one end of 3.5 mm diameter twin bore quartz tubes (General Electric Company) to a diameter of 0.5 mm³³ and shaping them as shown in Figure 4. Protective coatings of a dilute suspension of Ultra Bond 552 (Aremco Products), an alumina based adhesive, were applied in the following manner: The thermocouple assembly tip was immersed in the suspension, after briefly drying in a hot air stream, the assembly was further dried for 5 minutes at 90°C and baked for 10 minutes at 600°C. This procedure was repeated until the desired coating (0.15 to 0.25 mm) was achieved. The insulating beads were short (0.5 to 1.5 cm) broken pieces of 0.79 mm diameter two hole round (MgO) insulators (Omega Engineering Incorporated).

b. Thermocouple Manipulator

The thermocouple movement necessary for thermal profiling was provided by the thermocouple manipulator shown schematically in Figure 5 (see also Figure 4(a)). The outer tube (T) was shaped from thin wall stainless steel tubing (33 cm long, O.D. 0.32 cm). The inner push rod assembly consisted of two stainless steel rods ((P1) 23.5 cm long, O.D. 0.24 cm and (P3) 8.3 cm long, O.D. 0.24 cm) joined by a braided stainless steel cable ((P2) 17.1 cm long, O.D. 0.16 cm). This assembly was

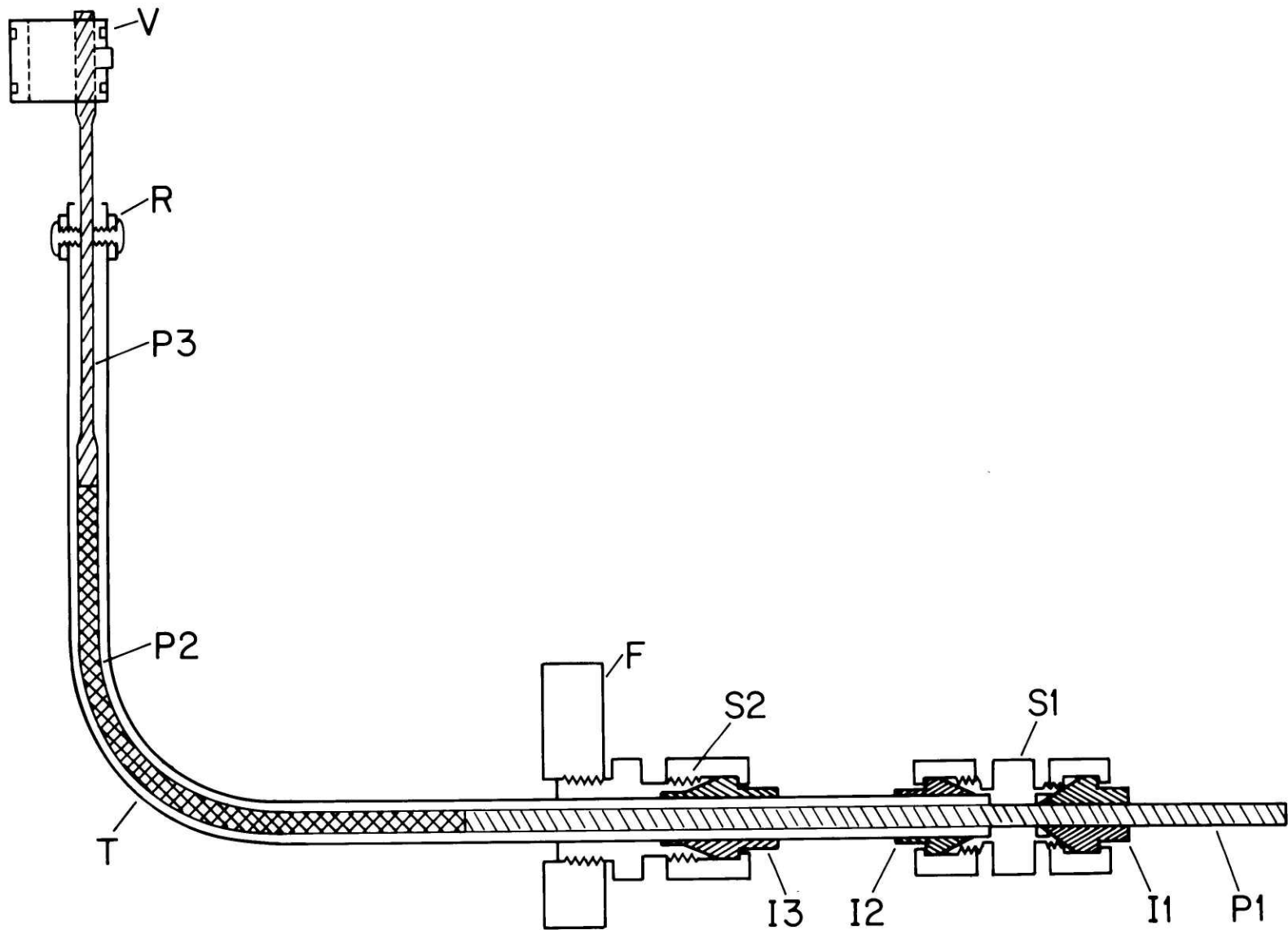


Figure 5. Schematic drawing of thermocouple manipulator (see text).

fastened by a Swagelok Union (200-6E) (S1) to T which was attached to the feed through ring (F) by a Swagelok Male Connector (S-300-1-2) (S2). The stainless steel ferrules of both fittings (S1 and S2) were replaced by teflon inserts (I1, I2, and I3) to provide vacuum tight ($<5 \times 10^{-2}$ torr) slip seals. The guide screws of the stainless steel guide ring assembly (R) were seated in grooves machined in P3 to prevent rotation of the push rod assembly. The stainless steel V-groove fastener (V) provided the means for attaching the thermocouple probe to the manipulator (see Figure 4 (a)).

The thermocouple manipulator provided both horizontal and vertical motion to the thermocouple probe. Controlled horizontal displacement was achieved by moving the outer tube (T) with respect to the feed through ring (F). Vertical movement was accomplished by moving the extended rod (P1) of the inner push rod assembly with respect to the outer tube. This movement was facilitated by lubricating the grooves in P3 with a suspension of graphite powder in methanol.

c. Temperature Measurement Equipment

The thermal emf generated by the thermocouple junction was brought outside the growth chamber by means of a thermal emf feed-through assembly. This assembly consisted of a sheathed chromel-alumel feed-through (Omega Engineering Incorporated TJ-36-CAIN-18E-12) inserted through a modified Swagelok Male Connector (S-300-1-2) (see S2 above) which was

mounted on the feed-through ring. The thermocouple lead wires were spot welded to those of the feed-through assembly.

Two temperature recording systems were used during the course of this investigation: (1) a Leeds and Northrup Speedo-max W/L Recorder with Calibrated Azar and (2) a Hewlett Packard Mosely Autograf Model 7100B Strip Chart Recorder augmented with a bucking voltage supply. Both recorders had the zero suppression capability necessary for recording the small variations in thermal emf encountered during the measurement of temperature profiles and temperature fluctuations. The Leeds and Northrup system had a maximum sensitivity of $0.8 \mu\text{v}$ (0.02°C) per mm of pen displacement, while that of the Hewlett Packard system is $4.0 \mu\text{v}$ (0.1°C) per mm of pen displacement.

All temperature measurements utilized an ice bath reference junction.

B. Experimental Procedures

1. Heat Pipe Alignment

To achieve symmetric heat input to the crucible containing the Ge melt, the heat pipe had to be aligned coaxially with the crucible shaft. Installation and alignment of the heat pipe and support assembly was performed with the bottom plate of the growth chamber isolated as shown in Figure 3. The base of the liner was positioned at the height of the lower heater ring. A procedure was adopted to insure alignment of the heat pipe coaxially with the crucible shaft and the alignment

was confirmed prior to each experiment.

2. Charge Preparation

A typical 64 g charge of Ge doped with Ga ($1 \times 10^{20}/\text{cm}^3$ in the melt) was prepared as follows. The desired quantity of Ge was cleaned in CP4 etchant (5 parts HNO_3 , 3 parts HF, 3 parts CH_3COOH , and a drop of Br), rinsed in distilled, de-ionized water, rinsed in acetone, and dried in a hot air stream. The amount of Ga required to achieve the initial melt concentration ($1 \times 10^{20}/\text{cm}^3$) was determined and placed in the crucible together with the Ge charge.

3. Melt Down Procedure

The seed holder with seed and the filled crucible were inserted into the crystal puller. After checking the alignment of the heat pipe, the crucible position was adjusted so that the upper rim of the crucible was below the top of the heat pipe at the desired depth 4, 9, or 14 cm. After closing, the chamber was evacuated ($< 5 \times 10^{-2}$ torr) and back filled with argon; this procedure was repeated three times. The cooling water was applied and a dynamic argon atmosphere (150 bubbles per minute) was established.

Because of the installation of the heat pipe, the system required a long heat-up period: to avoid damage to the thermal liner by excessive thermal stress prior to the onset of heat pipe action, the heat pipe was brought to its minimum operating temperature (500°C) within a period of one hour. After the

start of heat pipe action the temperature was raised at a more rapid rate. For a typical experiment the charge was melted after a heat-up period of three hours.

4. Temperature Measurement Procedure

Measurements of horizontal and vertical temperature profiles in the Ge melt and in the argon gas phase were performed with and without a seed crystal in contact with the melt. In addition, profiles were measured within the crucible wall (see Crucible above).

Data points were determined as follows: the position of the thermocouple probe was adjusted by means of the thermocouple manipulator. The length of tube T (see Figure 5) protruding from the fitting S2 determined the relative horizontal position of the thermocouple junction. Similarly the relative vertical position of the junction was obtained from the length of rod P1 protruding from the fitting S1. The effects of play in the push rod assembly (typically 0.5 mm) were minimized by performing all vertical displacements in the same direction during the determination of the profiles. Distances were measured with a metric scale with the estimated reading accuracy better than 0.25 mm. The time averaged temperature at each probe position was determined from the recorded thermocouple output with an estimated accuracy better than 0.25°C in the melt. The temperature measurement error was considerably larger in the gas phase due to the presence of large amplitude

temperature fluctuations.

Temperature fluctuations were recorded on the chart recorder during all temperature measurements. In several experiments, the temperature fluctuation spectra were recorded during crystal growth for correlation with transient segregation phenomena. In these experiments the thermocouple was positioned in the melt near the crucible side wall to minimize interference with the growing crystal; to avoid inductance effects, interface demarcation was not applied during these measurements.

CHAPTER V

THERMAL CHARACTERIZATION OF THE CZOCHRALSKI
CRYSTAL GROWTH SYSTEM

Control of the thermal environment within the hot zone of a Czochralski puller and of the time and spatial dependence of convective flows within the melt are prerequisites for the growth of high quality crystals. Such control can be established through proper attention to furnace and hot zone design.

In the present work the isothermal nature of heat pipe operation has been exploited to optimize the thermal configuration in the Czochralski system. The controlled temperature distribution established on the crucible wall was expected to (a) minimize the extent of thermal asymmetry within the melt and (b) reduce the intensity of thermohydrodynamic instability within the melt through a reduction of the adverse vertical temperature gradient (vertical Rayleigh number).

In this chapter the thermal behavior of the hot zone in the modified Czochralski crystal growth system is characterized and contrasted with the behavior found in a standard Czochralski system.

A. Comments on Temperature Measurement

This section discusses the problems of temperature measurement and interpretation arising from meniscus effects

and other sources of measurement error.

In the context of temperature measurements the problems of meniscus effects arise because molten Ge does not wet either the graphite crucible or the thermocouple probes used in the present investigation. This failure of the Ge melt (mass m and density ρ) to wet the crucible (radius R_c) results in a curved melt surface whose actual depth h (at the center) exceeds the depth $H(= m/\pi R_c^2 \rho)$ calculated for a flat melt surface (see Figure 6 (a) and Table 4). In addition both H-type and S-type thermocouple probes (discussed earlier) cause a local depression of the melt surface near the point of insertion (see Figure 6 (b) and (c)). As a result the measured temperature profiles will depart from the actual profiles in the vicinity of the melt surface (this error being largest for an S-type probe and smallest for an H-type probe approaching the surface from below).

Additional sources of error associated with temperature measurements include the effects of radiant energy exchange between the thermocouple and the surrounding surfaces and conductive heat loss along the thermocouple wires⁴⁸. Unavailability of the necessary heat transfer data and complexity of the thermal geometry prevented the determination of temperature corrections; however, the conduction error was minimized by using thermocouples with small wire diameter ($< 80 \mu\text{m}$),

Further uncertainties in the temperature measurements were associated with thermocouple calibration and temperature

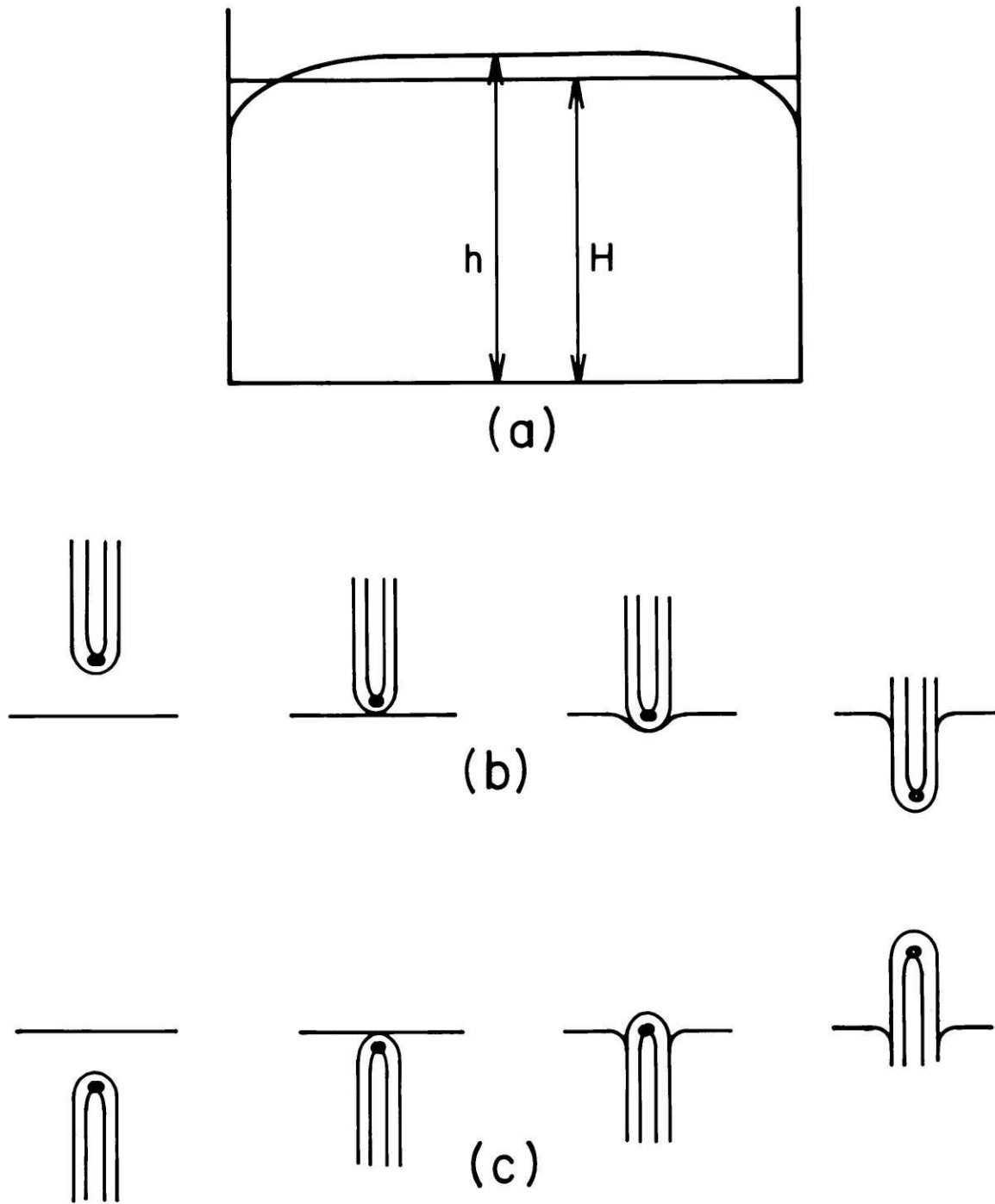


Figure 6. Schematic representation of complications associated with temperature measurement. (a) Curvature of the melt surface. (b) Deformation of melt surface by an S-type probe. (c) Deformation of melt surface by an H-type probe.

control. The purpose of this investigation was the determination of temperature profiles, temperature gradients, and temperature fluctuation amplitudes, none requiring absolute temperature measurement; thus the thermocouples (of reported⁴⁹ accuracy $\pm 7^\circ\text{C}$ at 940°C) were used without calibration.

B. Thermal Characterization of the Hot Zone in the Czochralski System

Measurements have been performed in order to determine the time dependence of temperature at fixed points and the distribution of temperature in the hot zone (the region within the heat pipe above the crucible bottom) of the modified Czochralski crystal growth system used in the current investigation. The thermal characterization of this region was accomplished both with and without the crucible present, with and without a Ge melt in the crucible, and with and without a seed crystal contacting the melt. For these measurements the crucible was located at either the "high" position (H), the "middle" position (M), or the "low" position (L) for which its upper rim was respectively 0.4 cm, 0.9 cm, and 1.4 cm below the upper rim of the heat pipe (see Figure 10 (a)). Additionally, measurements were performed to establish the comparative thermal behavior in the hot zone of a standard Czochralski puller with similar crucible geometry but without a heat pipe.

1. Time Dependent Temperature Behavior in the Hot Zone

During the course of this work all temperature measurements performed within the hot zones of both the standard and modified Czochralski systems were found to exhibit time dependent behavior in the form of random temperature fluctuations. These were characterized by their average period and root mean square amplitude which were determined in the following manner:

Within a specific time interval all the temperature maxima and minima (with variations larger than 1/2 division) were extracted from the temperature recording. From these data the (RMS) amplitude and the average period (the time interval divided by the number of maxima) were computed; longer period components were computed from the data exhibiting variations greater than twice the amplitude of the preceding component.

The time-dependent thermal behavior typical of the standard and modified Czochralski systems are shown in Figures 7 and 8, respectively; and the components of the observed temperature fluctuations are compiled in Tables 2 and 3. A study of these data reveals surprisingly that the amplitude of the convective temperature fluctuations in the melt is larger in the modified system (since the heat pipe was expected to reduce the intensity of thermohydrodynamic instabilities in this system). This finding is of interest in view of the significant reduction in microsegregation in crystals grown within a heat pipe over those grown in the standard configuration (see Chapter VIII). This apparent contradiction between

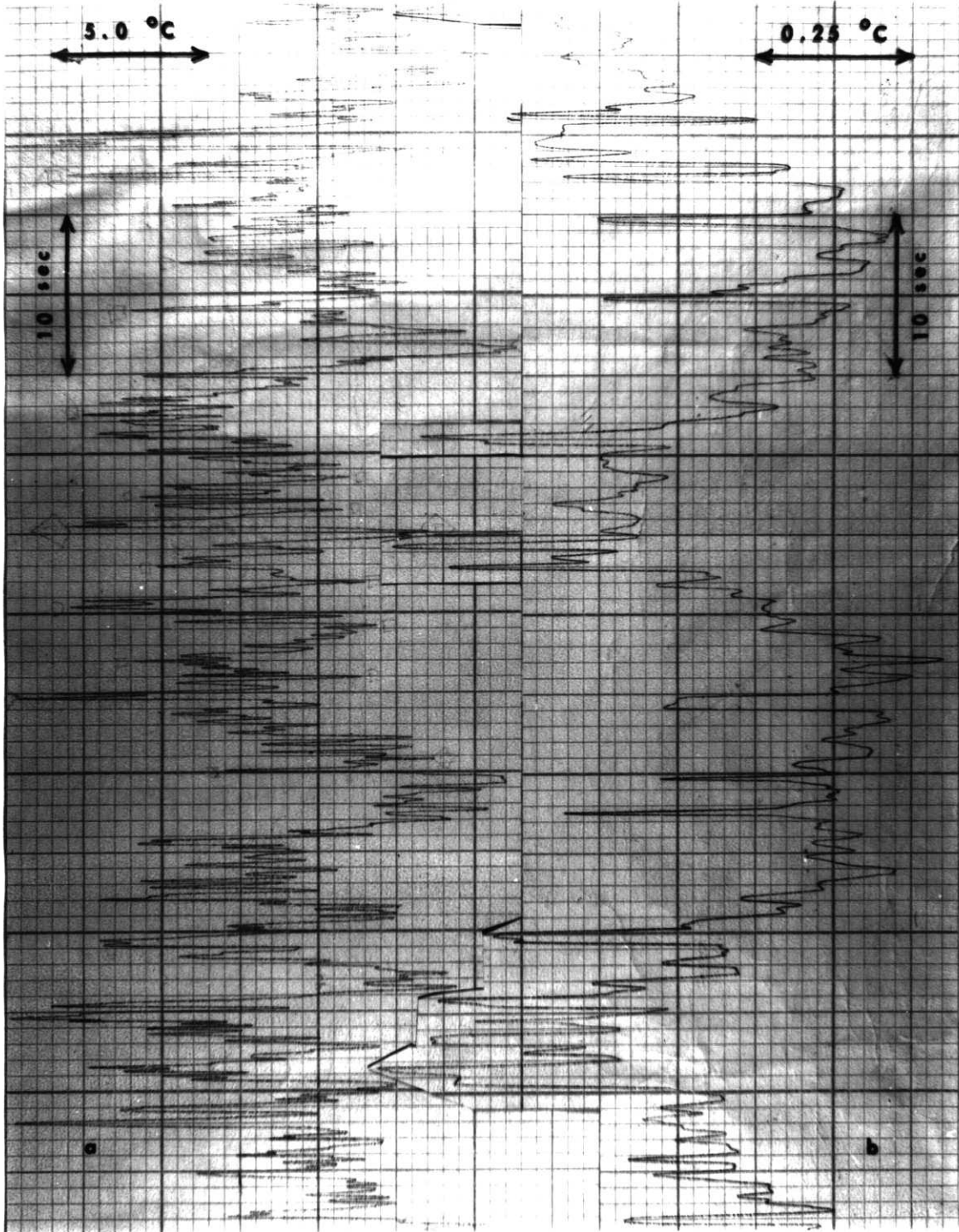


Figure 7. Representative temperature fluctuation spectra in a standard Czochralski puller. (a) Temperature fluctuation in gas phase. (b) Temperature fluctuations at bottom of melt.

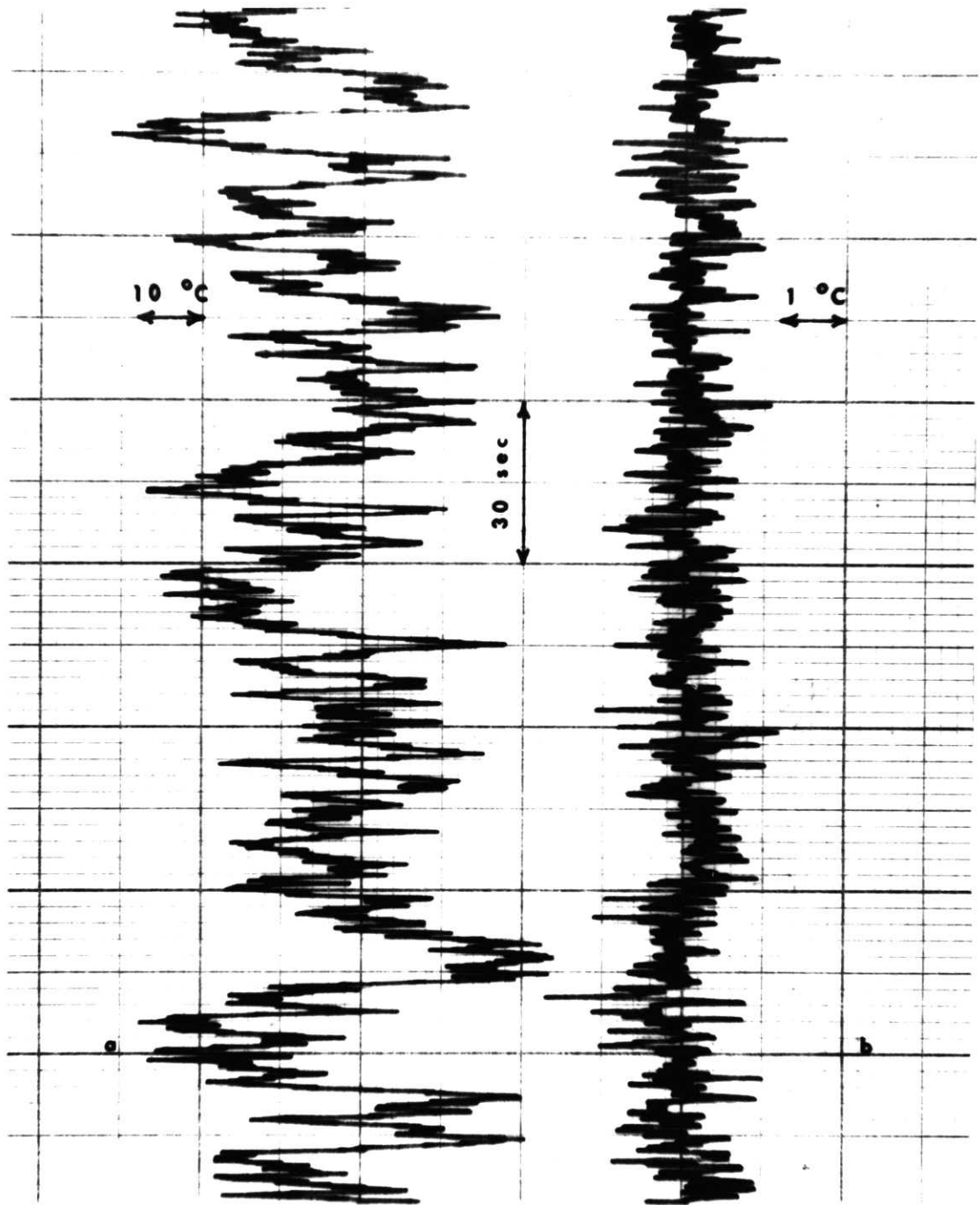


Figure 8. Representative temperature fluctuation spectra in the modified Czochralski system. (a) Temperature fluctuations in gas phase. (b) Temperature fluctuations at bottom of melt.

thermal and segregation behavior can be attributed to the fact that the standard puller exhibits a thermal perturbation of rather long period (30 sec), whereas, the longest dominant period in the modified configuration is 6.0 sec. Since the damping of a temperature oscillation as it passes through the thermal boundary layer from the bulk melt to the solid-liquid interface decreases with increasing oscillation period⁵⁰, the longer period components observed in the standard Czochralski system may be expected to have a more pronounced (adverse) effect on segregation than the corresponding shorter period components found in the modified system.

TABLE 2
TEMPERATURE FLUCTUATION COMPONENTS IN
THE STANDARD CZOCHRALSKI SYSTEM

Thermocouple Position	Components (Period(sec)-Amplitude(°C))
Hydrogen atmosphere	1.5-3.1, 11-4.8, 30-6.6
Top of Melt	1.3-0.24, 36-0.5
Bottom of Melt	1.3-0.24, 36-0.4

TABLE 3

TEMPERATURE FLUCTUATION COMPONENTS IN
THE MODIFIED CZOCHRALSKI SYSTEM

Crucible Position	Seed Rotation (RPM)	Thermocouple Position	Components (Period(sec)-Amplitude(°C))
H	--	Argon gas	1.9-14.7, 15.5-23.6, 37.2-28.8
H	0.0	Bottom of Melt	1.4-0.6, 6.0-0.9
H	10.7	Bottom of Melt	1.6-0.8, 6.0-1.1
M	0.0	Bottom of Melt	0.8-0.7, 2.0-0.9
M	10.7	Bottom of Melt	0.9-0.7, 2.2-1.0
L	0.0	Near Solid- Liquid Interface	1.8-0.3, 18.8-0.6
L	0.0	Bottom of Melt	0.6-0.5, 2.2-0.7

2. Spatially Dependent Temperature Behavior in the Hot Zone

The temperature profiles within the hot zone of the standard and modified Czochralski systems were determined to establish their correlation with growth and segregation phenomena. These profiles were furthermore determined to provide a data base for computational analysis of thermal convection in the Czochralski configuration.

In view of the time dependent thermal behavior discussed above, it was necessary to time average the temperature at each point for the construction of the horizontal and vertical temperature profiles which characterize the temperature distribution. The average temperature at each fixed point was determined in the following manner. The thermal emf was recorded for several minutes at each thermocouple probe position and, for each position, data were then extracted from the chart recording at fixed time intervals and used to determine the average temperature (thermal emf) at that position.

The characteristic vertical temperature profile within an unseeded melt contained in the hot zone of a standard Czochralski crystal puller (Figure 9) was primarily determined to establish the thermal conditions in a conventional system and to provide a basis of comparison for the conditions achieved in the modified Czochralski system. This profile was obtained by the continuous withdrawal (3.18 cm/hr) of a 127 μm diameter chromel-alumel thermocouple (protected by a 1.19 mm diameter twin bore alumina tube and a thin coating of "Aquadag")

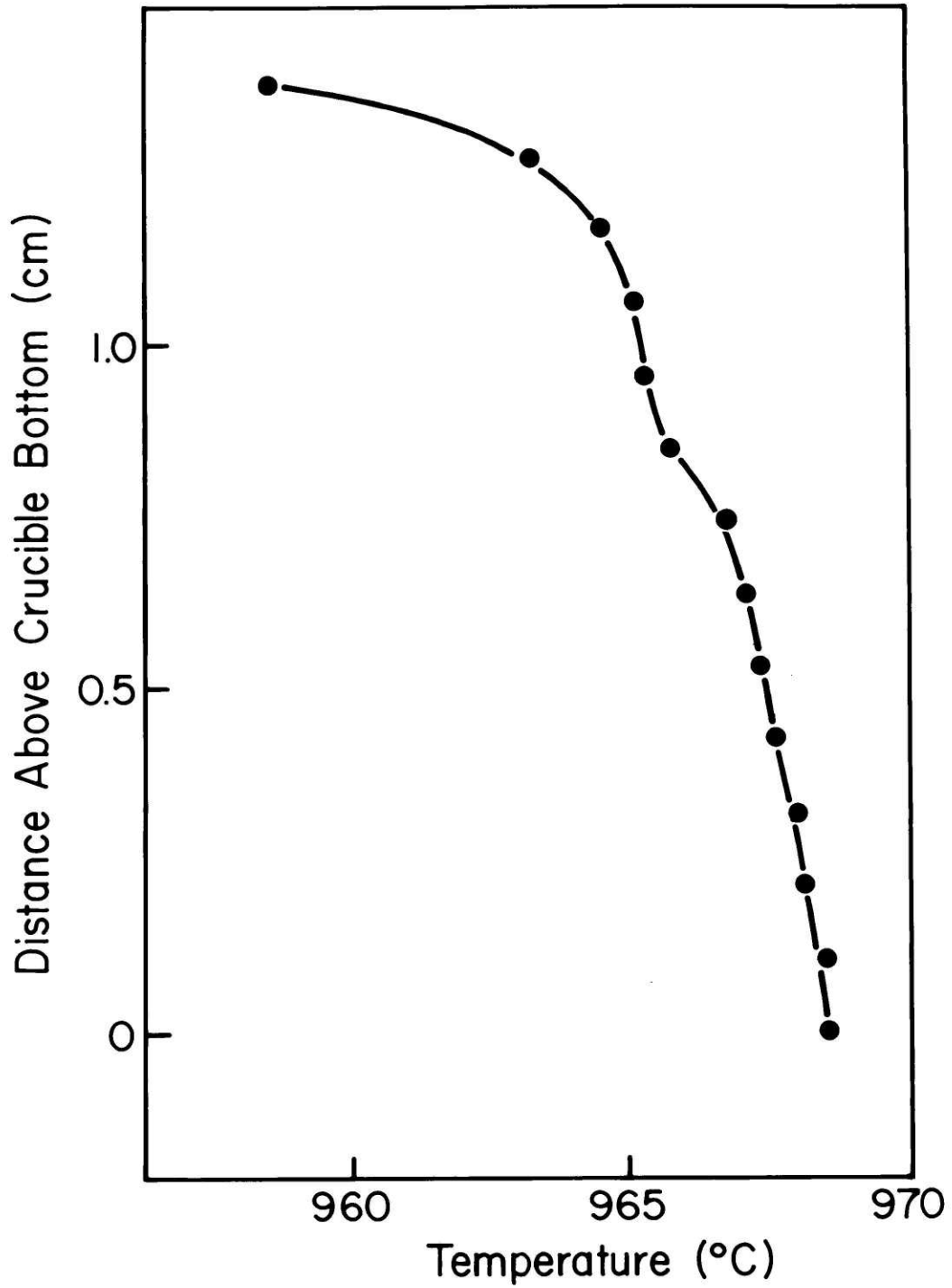


Figure 9. Axial melt temperature profile in a standard Czochralski system.

suitably attached to the crystal pull shaft. The temperature gradient is $29^{\circ}\text{C}/\text{dm}$ near the melt surface, goes through a minimum of $2^{\circ}\text{C}/\text{cm}$ near the 1 cm position, and increases to an average value of $3.7^{\circ}\text{C}/\text{cm}$ in the lower half of the melt. The surface temperature gradient computation neglected the uppermost data point since, at the surface, the measurement error of an S-type thermocouple is large (see Comments on Temperature Measurement).

The vertical temperature profiles measured in the argon gas along the centerline of the vertically oriented heat pipe (with the crucible and pedestal removed) for two similar operating temperatures (below the actual crystal growth temperature) shown in Figure 10 display a rapid decrease in temperature gradient with depth from $40^{\circ}\text{C}/\text{cm}$ at the top of the heat pipe to essentially $0^{\circ}\text{C}/\text{cm}$ at a depth of 5.5 cm (about one third the length of the heat pipe). By contrast, a vertically oriented zinc filled heat pipe (15 cm long quartz liner) exhibits an axial gradient decrease from the larger value of $190^{\circ}\text{C}/\text{cm}$ near its upper rim to a negligible value at a relatively larger depth of 7.5 cm (half the length of the heat pipe).

The average gas temperature profile along the heat pipe axis with an empty crucible located at position M (see Figure 11 (a)) taken below the growth temperature, exhibits four linear regions (based on a linear least square analysis): above the heat pipe ($30^{\circ}\text{C}/\text{cm}$), within the heat pipe above the

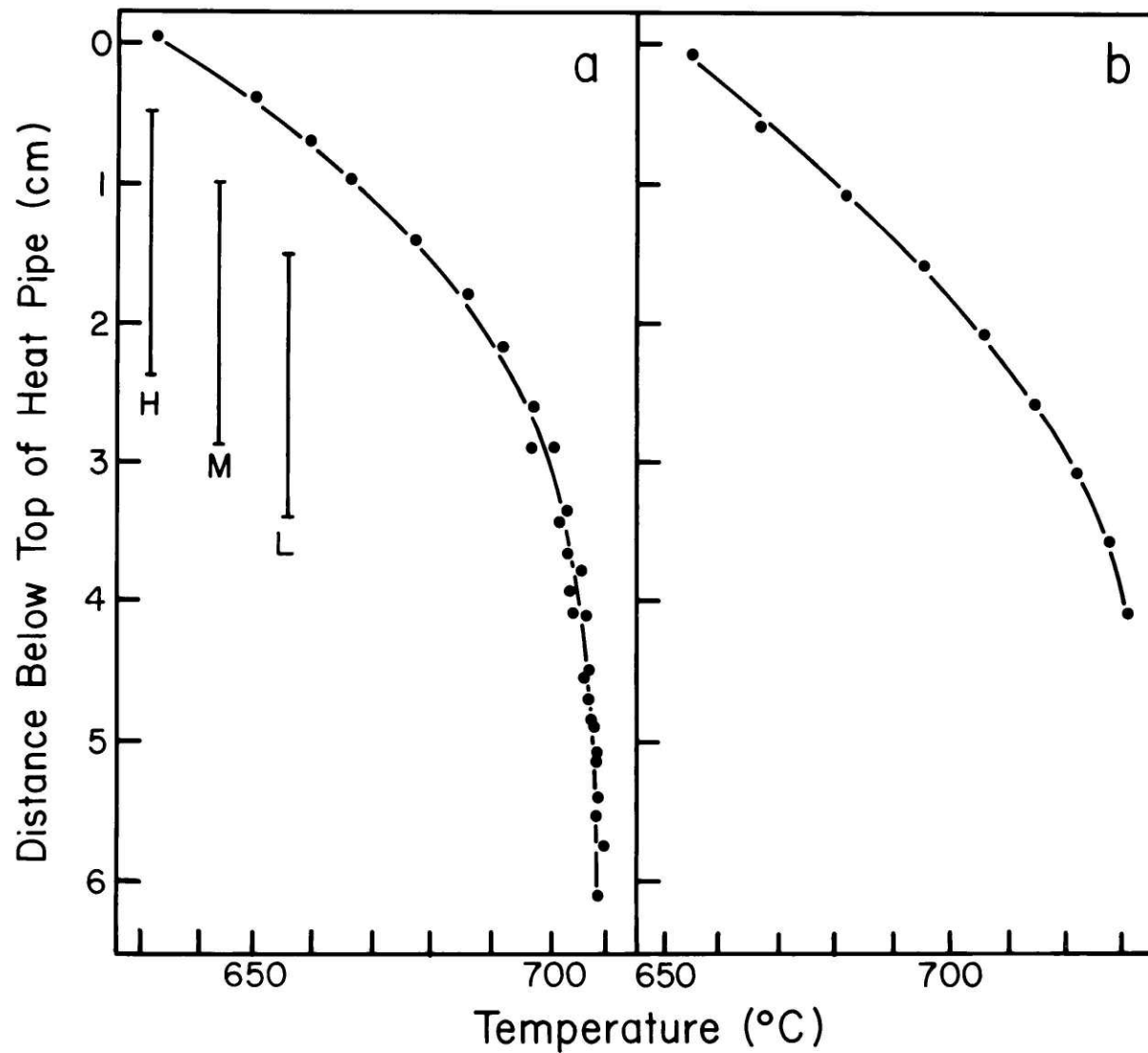


Figure 10. Axial gas temperature profiles of the heat pipe with crucible and pedestal removed (for details see text).

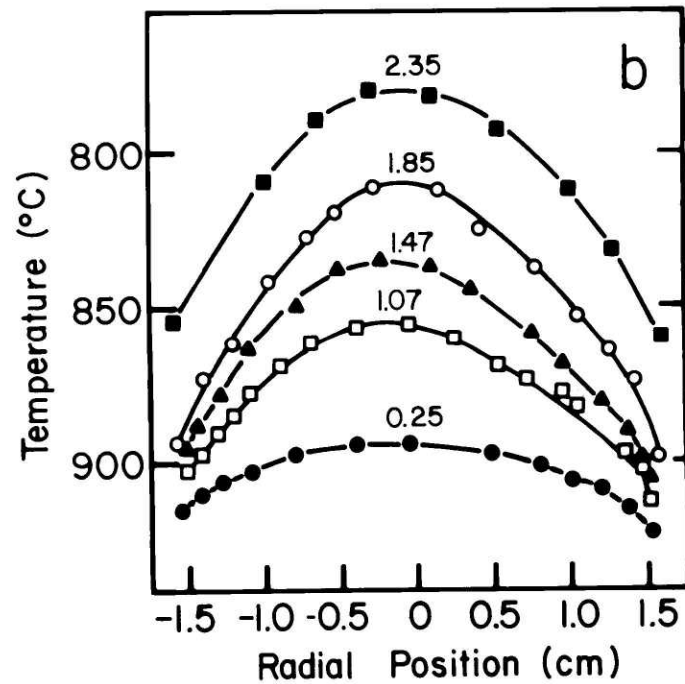
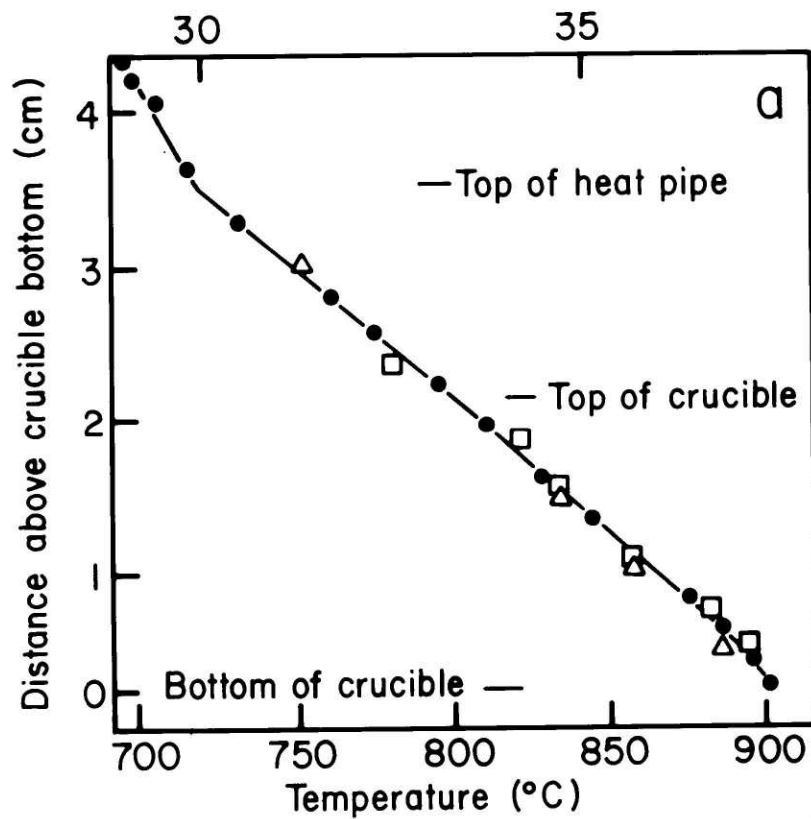


Figure 11. Gas temperature profiles of the modified hot zone with an empty crucible at position M. (a) Axial temperature profile (\bullet and Δ , results of independent scans and \square , temperature minima of horizontal profiles in (b)). (b) Horizontal temperature profiles taken at labeled distances above crucible bottom.

crucible rim ($62^{\circ}\text{C}/\text{cm}$), within the bulk of the crucible ($58^{\circ}\text{C}/\text{cm}$), and within the thermal boundary layer adjacent to the crucible bottom ($25^{\circ}\text{C}/\text{cm}$). The corresponding horizontal temperature profiles (see Figure 11 (b)) indicate that (based on a parabolic least square fit about each central temperature minimum) the thermal axis is displaced by 0.15 cm to the left of the geometric axis; thermal asymmetry is also reflected in a temperature difference of about 9°C between diagonally opposite positions adjacent to the crucible wall. It should be noted that visual observation of the hot zone during the heat up cycle revealed a noticeable (reversible) lateral movement of the graphite heater (displacement about 1 mm). Such a heater displacement while found to be inconsequential during operation with the coaxial heat pipe must be considered as highly detrimental to growth conditions in any conventional system.

The horizontal and vertical temperature profiles measured in the hot zone with a melt-filled crucible located in the previously defined positions H, M, and L are shown in Figures 12 to 14, 15 and 16, and 17 and 18, respectively. Selected temperature gradients determined from these profiles have been compiled in Table 4.

The temperature profiles within the crucible wall and in the melt along the axes of crucibles located in positions H and M, respectively, (see Figure 12 and 15) were measured with an S-type thermocouple probe. The wall profile (H9) exhibits a

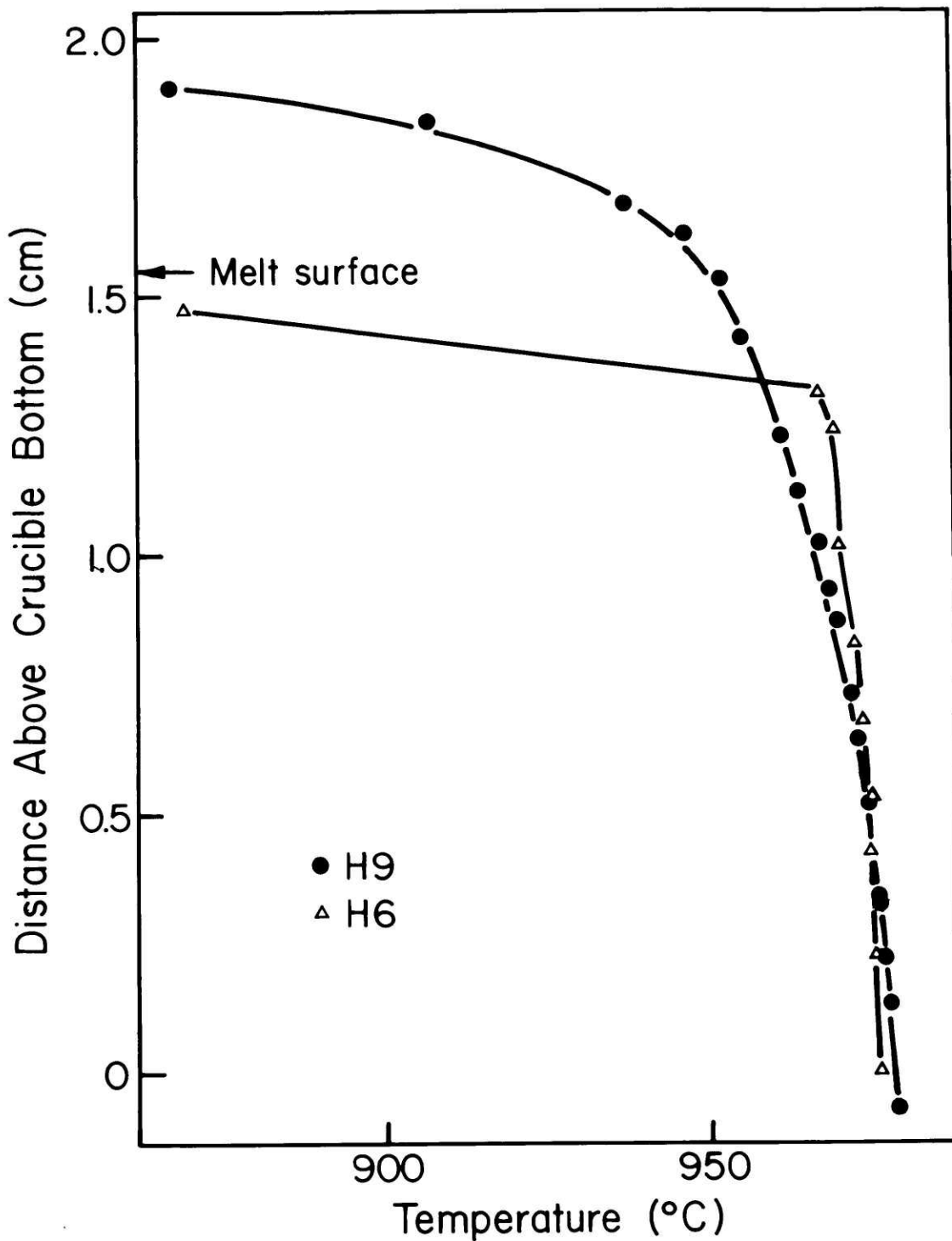


Figure 12. Vertical temperature profiles of the melt and crucible wall (crucible in position H). H9 data taken from thermocouple inserted within wall of crucible. H6 data obtained along axis of melt.

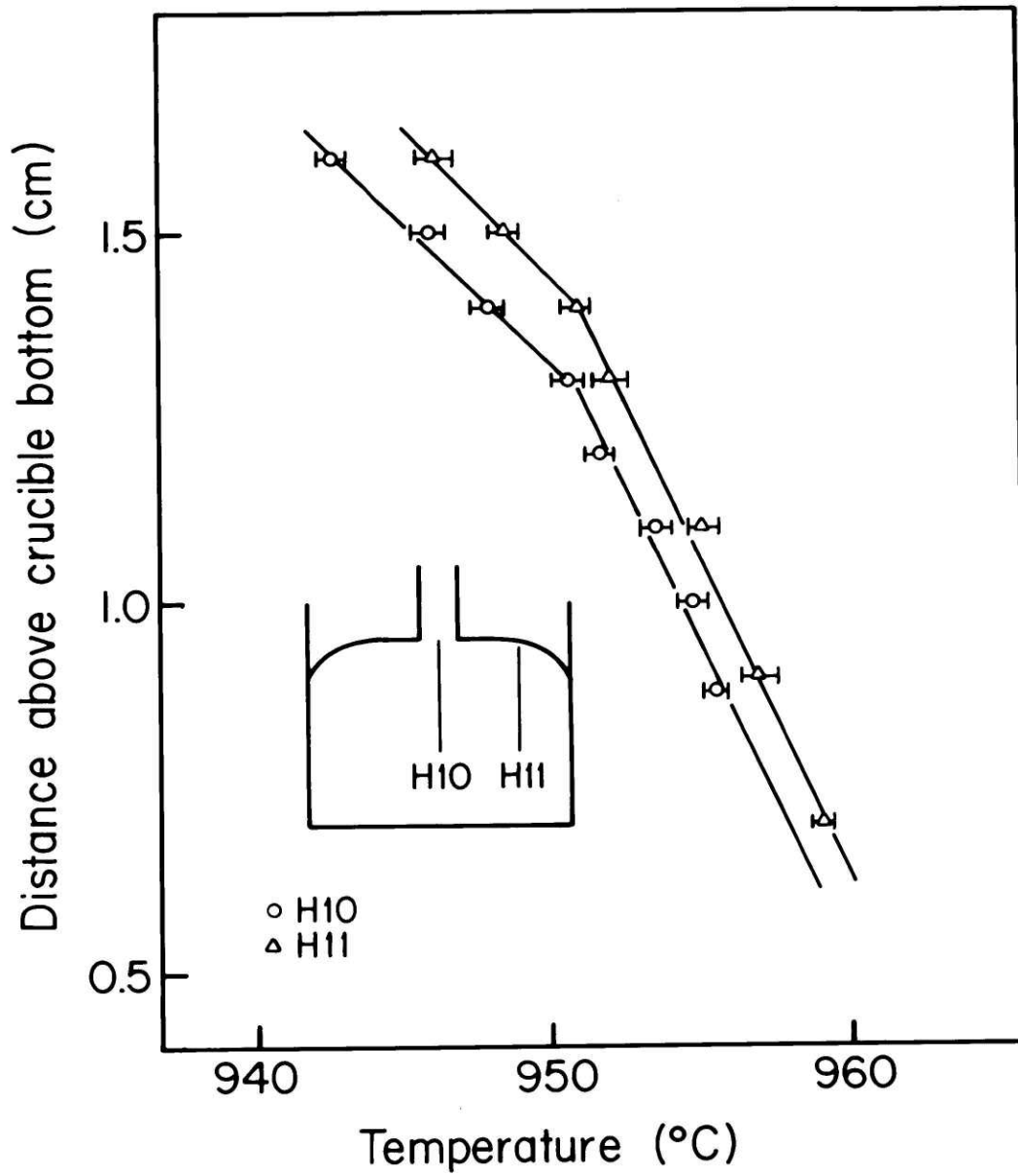
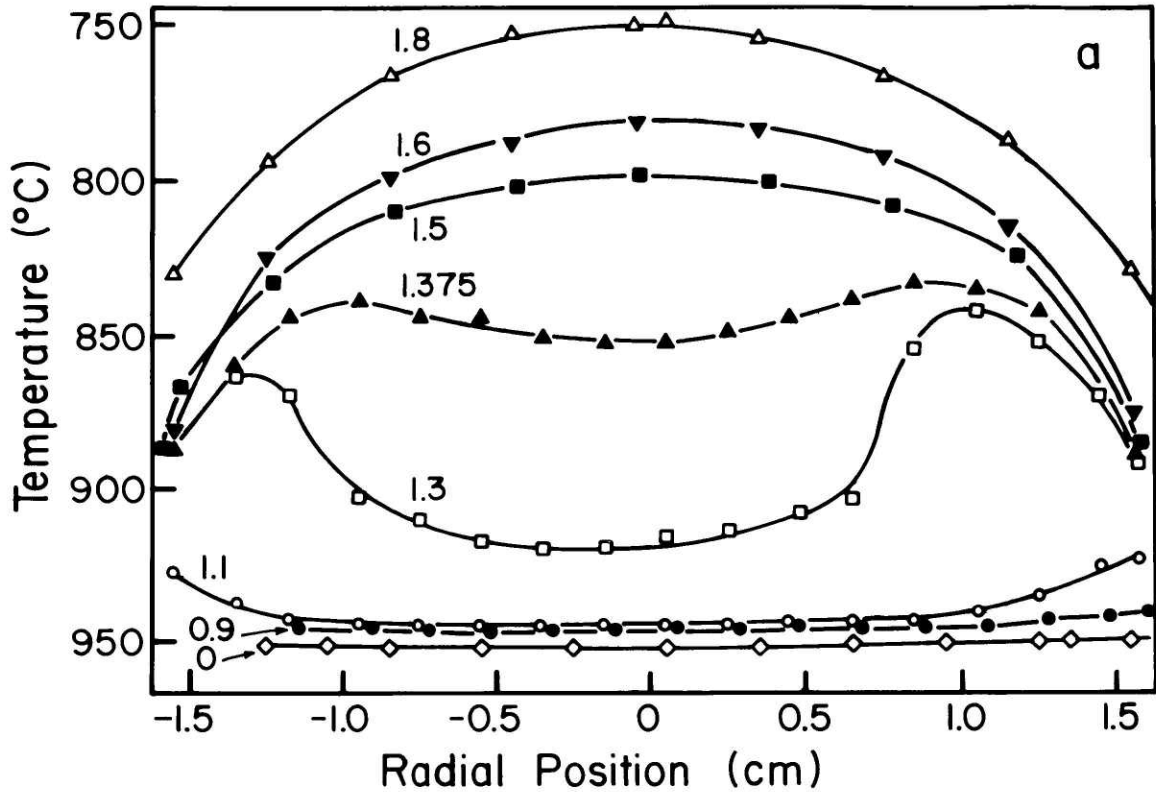
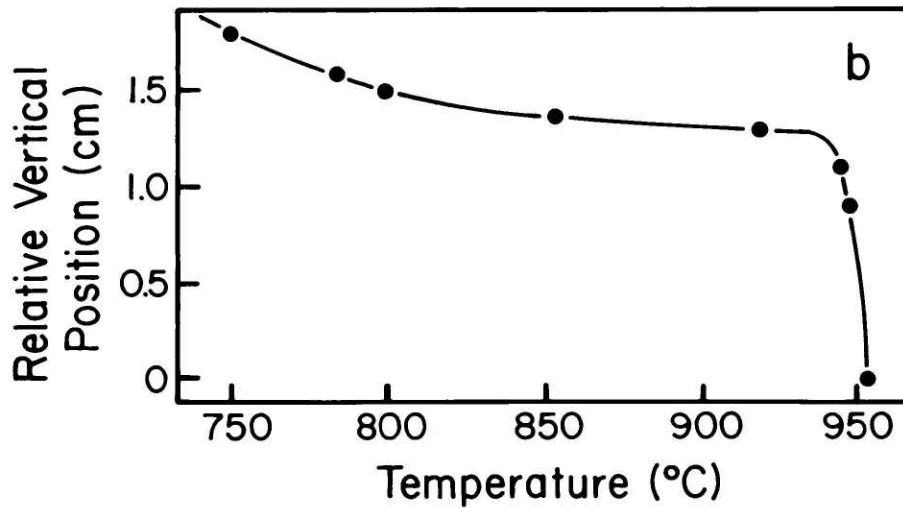


Figure 13. Vertical temperature profiles of seeded melt for a crucible located at position H within the heat pipe. Profiles were taken at locations identified by the insert; seed was rotated at 16.7 rpm.



(a) Horizontal temperature profiles taken at labeled relative vertical positions (cm). (Position 0.0 bottom of melt; position 1.375 highest point of melt surface.)



(b) Axial temperature profile; data points correspond to temperature at radial position 0 in (a).

Figure 14. Temperature profiles of the melt and the gas phase within the hot zone of the modified growth system (crucible in position H).

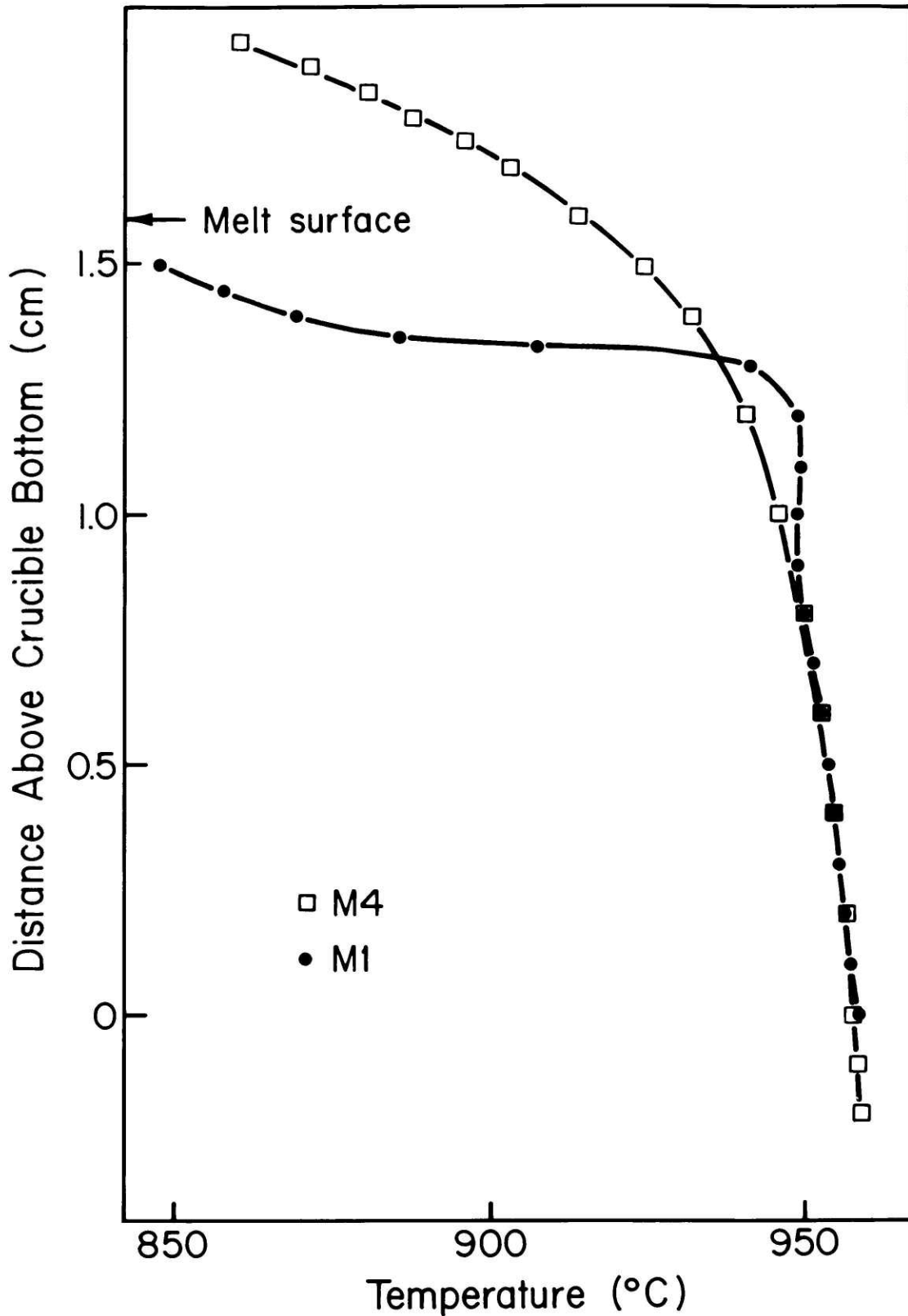
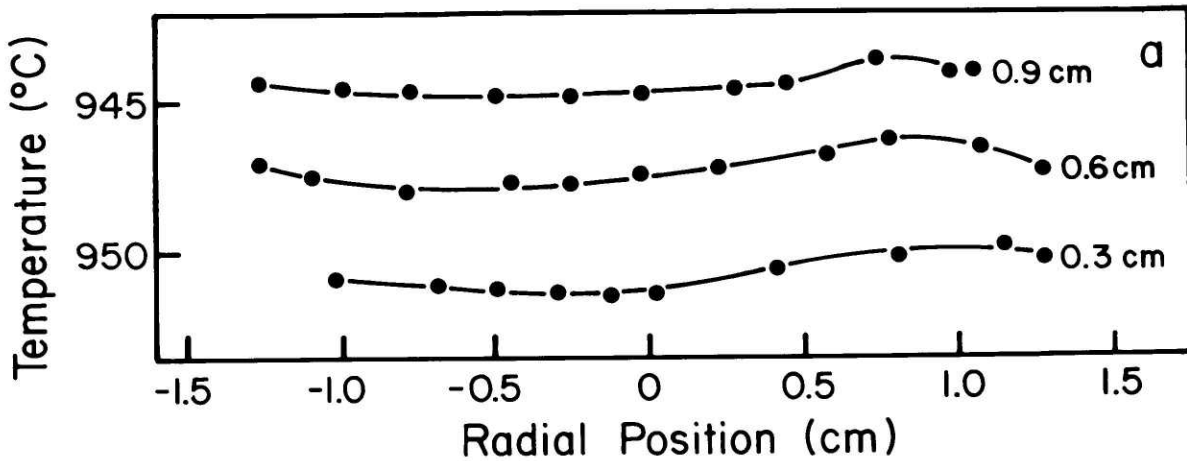
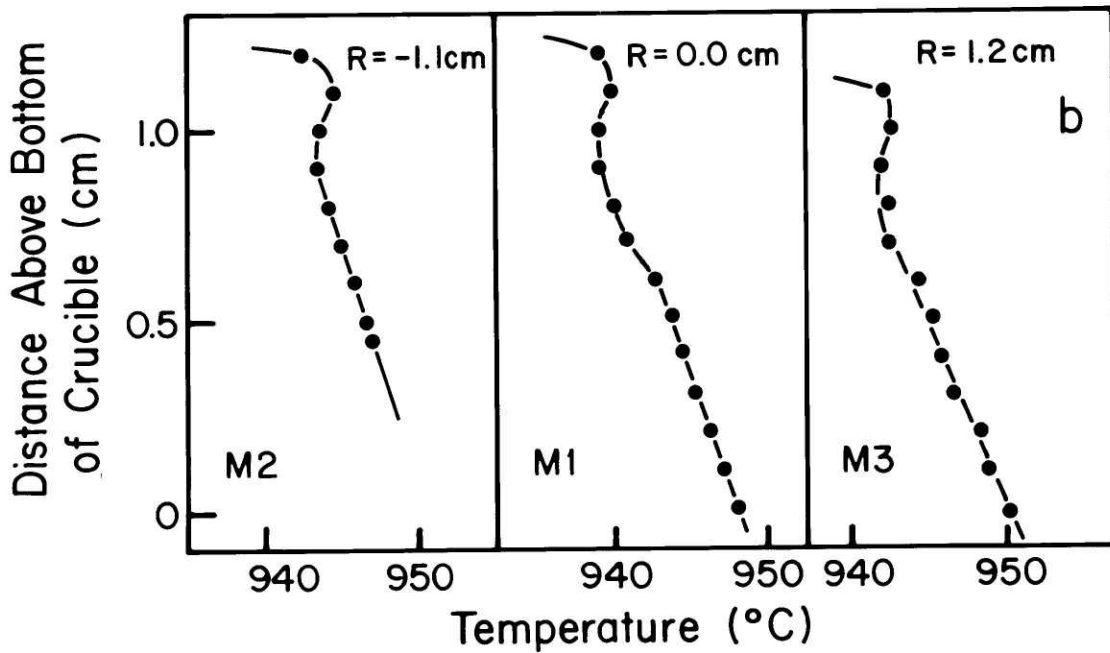


Figure 15. Vertical temperature profiles of the melt and crucible wall (crucible in position M). M1 data taken from thermocouple inserted within wall of crucible. M4 data obtained along axis of melt.



(a) Horizontal melt temperature profiles taken at labeled distances above the crucible bottom.



(b) Vertical melt temperature profiles measured at labeled radial positions.

Figure 16. Temperature profiles of the melt for a crucible located at position M within the heat pipe.

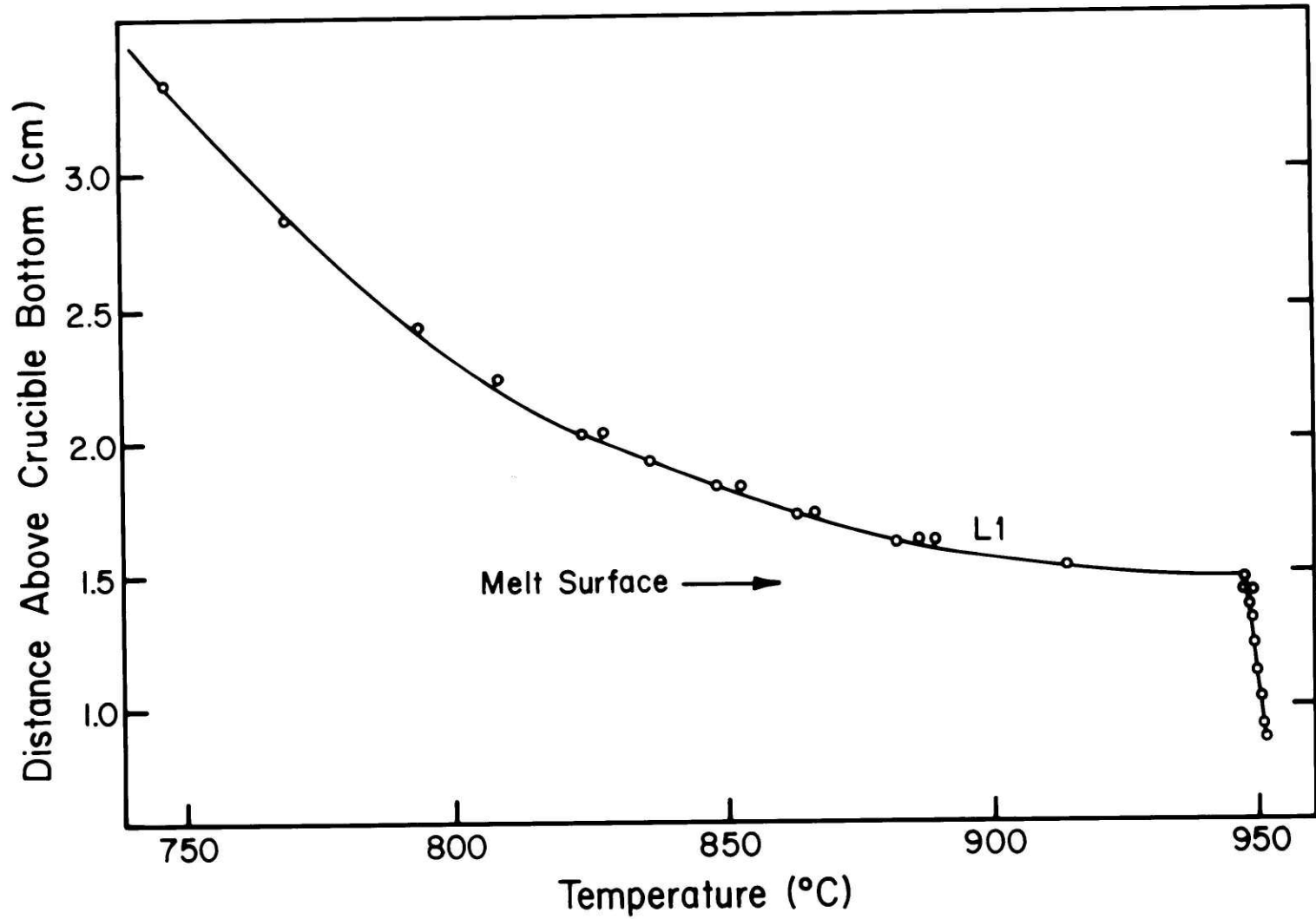


Figure 17. Axial temperature profile of the melt and gas phase within the modified hot zone (crucible in position L).

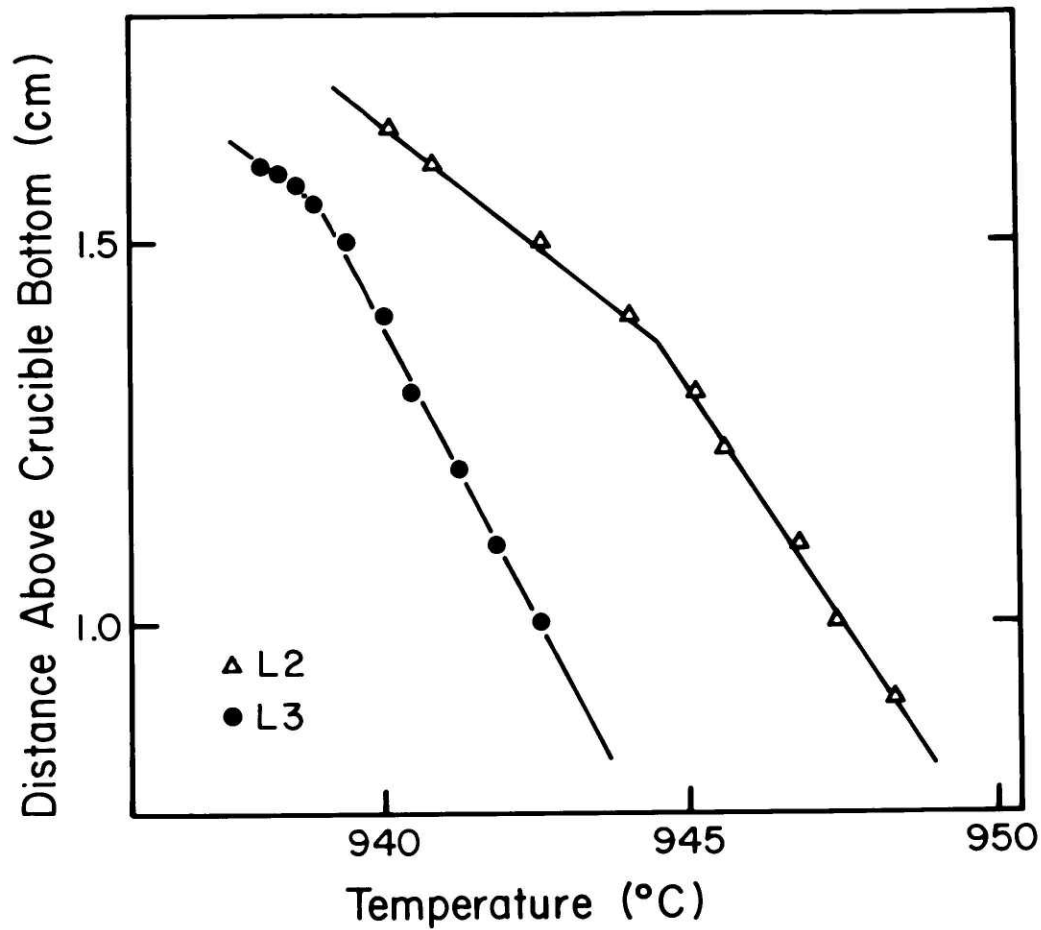


Figure 18. Axial temperature profiles of the melt for a crucible located at position L within the heat pipe. L2 data without seed crystal in contact with melt; L3 data with seed crystal in contact with melt.

TABLE 4

SELECTED RESULTS FROM VERTICAL TEMPERATURE PROFILES

Profile Number	Profile Position	Probe Type	Melt Depth (cm)		Temperature Surface	Gradient ($^{\circ}\text{C}/\text{cm}$)		Grashof Number
			\underline{h}	\underline{H}		Bulk		
H6	Center	S	1.55	1.43	24.7	4.4	2.2×10^6	
H9	Wall	S	--	--	270	5.2	--	
H10	Below Seed	H	1.60	1.46	15.2	5.6	2.8×10^6	
H11	1 cm from seed	H	--	--	10.7	4.5	--	
M1	Center	S	1.60	1.47	101.4	9.1	--	
M2	Half Radius	S	--	--	22.8	7.9	--	
M3	Half Radius	S	--	--	156.0	10.4	--	
M4	Wall	S	--	--	196.0	7.3	--	
L1	Center	H	1.60	1.46	--	6.0	--	
L2	Center	H	--	--	16.6	6.5	2.7×10^6	
L3	Below Seed	H	--	--	15.9	8.1	3.9×10^6	
Standard	Center	S	--	--	29.0	3.7	--	

gradient which is large ($270^{\circ}\text{C}/\text{cm}$) near the upper rim and diminishes ($5.2^{\circ}\text{C}/\text{cm}$) near the crucible bottom; the wall profile (M4) at the lower position M has corresponding gradients which are smaller ($196^{\circ}\text{C}/\text{cm}$) near the upper rim and larger ($7.3^{\circ}\text{C}/\text{cm}$) near the crucible bottom. The axial temperature profile (H6) shows a gradient which is maximum near the melt surface ($680^{\circ}\text{C}/\text{cm}$), decreases to a minimum ($3.1^{\circ}\text{C}/\text{cm}$), and becomes nearly constant ($4.4^{\circ}\text{C}/\text{cm}$) in the lower portion of the melt; the corresponding profile (M1) at position M displays a temperature gradient which is maximum near the surface ($1100^{\circ}\text{C}/\text{cm}$), exhibits an inversion ($5.0^{\circ}\text{C}/\text{cm}$), and likewise becomes nearly constant ($9.1^{\circ}\text{C}/\text{cm}$) in the lower portion of the melt. The inability to balance radiative heat flow to the chamber walls and conductive heat flow through the thermal boundary layers at the melt surface for these profiles is attributable to the meniscus limitation for S-type thermocouple probe temperature measurement discussed above (see Comments on Temperature Measurement). The temperature profile (L1) measured with an H-type probe along the axis of a melt-filled crucible located in position L (see Figure 17) shows that the steepest temperature gradient ($460^{\circ}\text{C}/\text{cm}$) actually occurs at the surface in the gas phase and not in the melt.

The horizontal profiles of gas and melt temperature shown in Figure 14 (a) were measured with an S-type thermocouple probe in a crucible located at position H. The profiles taken above the relative vertical position of 1.375 cm were

entirely in the argon gas phase and are similar in appearance to those in Figure 11 (b). The minima in the profiles taken at the vertical positions 1.375 and 1.3 cm result when the thermocouple detaches itself from the curved melt surface as its radial position is increased. The temperature distribution is seen to be slightly asymmetric, the temperature being higher on the left. The profiles completely within the melt are virtually flat in the center between the radial positions -1.0 and 1.0 cm; adjacent to the crucible wall the gradients are $40^{\circ}\text{C}/\text{cm}$, $2.5^{\circ}\text{C}/\text{cm}$, and $0.7^{\circ}\text{C}/\text{cm}$ for profiles at positions 1.1, 0.9, and 0.0 cm, respectively; at the same vertical positions the respective gradients in the bulk melt were 3.5, 1.6 and $0.7^{\circ}\text{C}/\text{cm}$. (The temperature profile shown in Figure 14 (b) is based on the horizontal profiles in Figure 14 (a).)

Further details of the temperature distribution for the crucible in position M are shown in Figure 16. The horizontal profiles (Figure 16 (a)) reveal a considerable asymmetry in which the average temperature of fluid on the left is 0.8°C higher than that on the right. This thermal asymmetry, attributed to some misalignment between the crucible and the heat pipe, can be expected to generate a thermal convective roll within the melt with fluid rising along the warm wall and descending along the cool wall. Such a flow pattern will result in the asymmetric melt temperature profiles observed. The axial temperature profiles M2 and M3 also display an inversion of the temperature gradient at about 1 cm above the

crucible bottom. Such behavior is indicative of a secondary convective mode existing near the melt surface and resulting from the observed thermal asymmetry.

Figure 18 shows the axial temperature profiles measured with an H-type probe with a melt filled crucible located in position L both without (L2) and with (L3) a seed crystal contacted to the melt surface. In the absence of a seed crystal, the average temperature gradient is 16.6°C/cm in the thin (0.5 mm) thermal boundary layer adjacent to the melt surface and 6.5°C/cm within the bulk of the melt. The apparent effect of the seed crystal is to increase by the action of viscosity, the thickness of the thermal boundary layer region (>3 mm) in which the temperature gradient is 15.9°C/cm and to increase the bulk temperature gradient to 8.1°C/cm. Extrapolation of this profile to the melting point of germanium indicates a meniscus rise of the interface (2.5 mm) which is in fair agreement with the value (1.8 mm) calculated from the approximate expression⁵¹

$$\Delta h = \Delta h_o \left\{ \left[1 + \left(\frac{\Delta h_o}{4R_s} \right)^2 \right]^{1/2} - \frac{\Delta h_o}{4R_s} \right\}$$

where $\Delta h_o = 2\sigma/\rho g$ and R_s is the radius of the seed crystal (2.26 mm).

The vertical temperature profiles shown in Figure 13 were taken with an H-type thermocouple probe with a melt-filled crucible located at position H and contacted with a rotating

(16.7 rpm) seed crystal. The profile beneath the seed (H10) indicates a temperature gradient of $15.2^{\circ}\text{C}/\text{cm}$ in the thermal boundary layer (> 3 mm) adjacent to the crystal and of $5.6^{\circ}\text{C}/\text{cm}$ in the bulk melt while the profile (H11) laterally displaced by 1 cm exhibits a gradient of $10.7^{\circ}\text{C}/\text{cm}$ in the boundary layer (2 mm) adjacent to the melt surface and $4.5^{\circ}\text{C}/\text{cm}$ in the bulk. Again, extrapolation of the temperature profile measured beneath the crystal indicates a meniscus rise of 2.5 mm.

Comparison of axial profiles measured with S-type thermocouple probes for the standard puller (Figure 9) and the modified Czochralski system (Figures 12 and 15) reveal similar reduction in the temperature gradient near the vertical position 1.0 cm. Thus it is quite likely that the flow pattern present in the standard system is asymmetric and is similar to that which produced the temperature distribution shown in Figure 16. While care was taken to minimize the extent of thermal asymmetry prior to performing axial profiles in the standard system, asymmetry appears to be inherent to the standard hot zone configuration and could not be eliminated. Thermal asymmetry in the modified puller (see Figure 16), however, could be attributed to misalignment of the heat pipe with the crucible axis and, under optimized conditions, can be significantly reduced (see Figure 14). In the light of this reduction in thermal asymmetry, crystals grown under seed rotation in the modified Czochralski system are expected to exhibit a significant reduction in the amplitude of rotational striations as compared to those grown in the standard system.

In summary, the time and spatial dependence of the temperature in the hot zones of the standard and modified Czochralski systems have been presented and compared. While the heat pipe was found to result in the expected decrease in thermal asymmetry, the increased intensity of thermohydrodynamic instability found in the modified system was contrary to expectations. The implications of these observations for segregation have been discussed.

The measured temperature profiles are used to establish the boundary conditions for the numerical analysis of thermal convection in the modified Czochralski configuration (see Chapter VI). Further, these profiles together with the computed component periods of the temperature fluctuations are used in Chapter IX to determine the mechanisms of convective instability operating in the Ge melt.

CHAPTER VI

NUMERICAL TREATMENT OF THERMAL CONVECTION

This chapter presents the results of a numerical study of thermal convection in crystal growth configurations. The computational analysis employs an explicit finite difference representation of the differential equations describing thermal convection in the stream function-vorticity formulation. The equations are developed in the Boussinesq approximation and their non-linear advection terms are represented by a quadratically conserving scheme to insure numerical stability at large Grashof numbers. The results are presented in the form of contour plots of fluid temperature (isotherms), stream function (stream lines), and vorticity (isodines).

The thermal convective melt flows in the modified Czochralski configuration were computed using thermal boundary conditions determined from the preceding thermal characterization study. The treatment was restricted to an analysis of melt flows for the following reasons: (a) Due to the low heat capacity of the gas, the large amplitude high frequency convective temperature fluctuations in the gas phase do not penetrate into the melt. (b) A previous investigation found no effect of H_2 pressure (over the range of 10^{-2} to 10^3 torr) on growth and segregation of Ga doped Ge⁵². Furthermore, since the computed temperature distributions were to be compared with those measured in unseeded Ge melts, the

computations were performed for this condition. It should be mentioned, however, that the computer program which was developed to treat thermal convection in Czochralski configurations has the capability of including a seed crystal as one of the boundary conditions and of treating forced convection due to crystal or crucible rotation. In addition to the contour plots mentioned above, the numerical results of this investigation are presented as temperature and fluid velocity profiles.

The computational approach to the study of thermal convection in melt growth systems was initially developed in the horizontal Bridgman configuration. The previous experimental work on this system provided the reference data necessary for assessing the applicability of this approach.

This chapter gives a brief development of the pertinent differential equations describing thermal convection in the stream function-vorticity formulation and presents the numerical results obtained. A detailed development of the finite difference equations and solution technique is presented in Appendix 3.

A. Development of the Quantitative Theoretical Approach to Convection in Melt Growth Configurations

Thermal convective flow in a fluid can be described in terms of the differential equations expressing conservation of mass, momentum, and energy within the fluid together with the

equation of state of the fluid. Provided the temperature variation within the fluid is not too large, a wide variety of fluids can be described by the simple equation of state⁷, $\rho = \rho_0(1-\alpha(T-T_0))$, where ρ is the fluid density at temperature T , ρ_0 is the density at the reference temperature T_0 , and α is the volume coefficient of thermal expansion of the fluid. Use was made of the Boussinesq approximation since the thermal expansion coefficients of low Prandtl number fluids (such as liquid Ga and Ge) are small.

Accordingly, the fluid may be treated as an incompressible medium with temperature independent properties except for the body force term in the equation of momentum conservation.

1. Thermal Convection Equations

Thermal convection within a fluid in the Boussinesq approximation is described by the following conservation equations⁷; The conservation of mass (continuity equation) is

$$\nabla \cdot \bar{V} = 0 \quad . \quad (1)$$

The conservation of momentum (Navier-Stokes equation) is

$$\frac{\partial \bar{V}}{\partial t} + \bar{V} \cdot \nabla \bar{V} = \frac{-1}{\rho_0} \nabla P' + \nu \nabla^2 \bar{V} - \alpha \bar{g}(T - T_0) \quad . \quad (2)$$

And the conservation of energy (Energy transport equation) is

$$\frac{\partial T}{\partial t} + \bar{V} \cdot \nabla T = \kappa \nabla^2 T \quad ; \quad (3)$$

where \bar{V} is the fluid velocity, $P' = P - \rho_0 \bar{g} \cdot \bar{r}$ is the reduced pressure, ν is the kinematic viscosity, \bar{g} is the acceleration of gravity, κ is the thermal diffusivity, P is the pressure, and \bar{r} is a position vector.

The pressure may be eliminated in favor of the vorticity, defined as

$$\bar{\Omega} = \nabla \chi \bar{V} \quad , \quad (4)$$

by taking the curl of equation (2) and utilizing the following vector identities⁵³:

$$\begin{aligned} \bar{A} \chi \nabla \chi \bar{A} &= (1/2 \nabla)(\bar{A} \cdot \bar{A}) - \bar{A} \cdot \nabla \bar{A} \quad , \\ \nabla \chi \nabla \chi \bar{A} &= \nabla(\nabla \cdot \bar{A}) - \nabla^2 \bar{A} \quad , \\ \nabla \chi (\bar{A} \chi \bar{B}) &= \bar{A} \nabla \cdot \bar{B} - \bar{A} \cdot \nabla \bar{B} - \bar{B} \nabla \cdot \bar{A} + \bar{B} \cdot \nabla \bar{A} \quad , \\ \nabla \chi \nabla \bar{A} &= 0 \quad , \\ \nabla \cdot \nabla \chi \bar{A} &= 0 \quad , \\ \nabla \chi (a \bar{A}) &= a \nabla \chi \bar{A} - \bar{A} \chi \nabla a \quad . \end{aligned}$$

This results in the following vorticity transport equation:

$$\frac{\partial \bar{\Omega}}{\partial t} + \bar{V} \cdot \nabla \bar{\Omega} - \bar{\Omega} \cdot \nabla \bar{V} = \nu \nabla^2 \bar{\Omega} + \alpha \bar{g} \chi \nabla T \quad . \quad (5)$$

2. Application to Crystal Growth Geometries

In the following two subsections the thermal convection equations will be presented in dimensionless form and

specialized to two-dimensional rectangular and axisymmetric cylindrical coordinates which are used for describing thermal convection in the horizontal Bridgman and modified Czochralski configurations, respectively.

a. Horizontal Bridgman Configuration

Thermal convection in the horizontal Bridgman geometry (see Figure 47(a)) is treated as a two-dimensional flow. The variables used for the computations in this geometry are non-dimensionalized by the following units: L for length, L^2/ν for time, ν/L for velocity, ν/L^2 for vorticity, ν for stream function, and $T_1 - T_0$ for temperature, where L is the length of the cavity (of depth H), T_1 is the temperature of the warm right wall, and T_0 is the temperature of the cool left wall. For this geometry, the velocity vector is

$$\bar{V} = \hat{i}V_x + \hat{j}V_y \quad ,$$

and from Equation (4) the vorticity vector is

$$\bar{\Omega} = \hat{k}\Omega \quad ,$$

where

$$\Omega = \frac{\partial V_y}{\partial x} - \frac{\partial V_x}{\partial y} \quad (6)$$

and \hat{i} , \hat{j} , and \hat{k} are unit vectors along the coordinate axes. The continuity equation is identically satisfied by defining the stream function Ψ so that the velocity components are

$$V_x = \frac{\partial \Psi}{\partial y} \quad (7)$$

$$V_y = - \frac{\partial \Psi}{\partial x} \quad . \quad (8)$$

In terms of the above definitions the energy transport equation (3) becomes

$$\frac{\partial T}{\partial t} + J(T, \Psi) = \frac{1}{Pr} \left(\frac{\partial^2 T}{\partial x^2} + \frac{\partial^2 T}{\partial y^2} \right) \quad (9)$$

and the vorticity transport Equation (5) becomes

$$\frac{\partial \Omega}{\partial t} + J(\Omega, \Psi) = \frac{\partial^2 \Omega}{\partial x^2} + \frac{\partial^2 \Omega}{\partial y^2} - Gr \frac{\partial T}{\partial x} \quad (10)$$

where the Jacobian, $J(A,B)$, is defined as

$$J(A,B) = \frac{\partial A}{\partial x} \frac{\partial B}{\partial y} - \frac{\partial A}{\partial y} \frac{\partial B}{\partial x} \quad . \quad (11)$$

The definition of vorticity (4) becomes

$$\frac{\partial^2 \Psi}{\partial x^2} + \frac{\partial^2 \Psi}{\partial y^2} = - \Omega \quad . \quad (12)$$

For this geometry, the Grashof number is $Gr = g\alpha(T_1 - T_0)L^3/\nu^2$ and the aspect ratio is $A = H/L$.

The finite difference representation of this problem is given in Appendix 3.b. and the program used for numerical integration is detailed in Appendix 4.a.

b. Czochralski Configuration

Fluid flow in the Czochralski geometry (see Figure 49(a)) is treated as an axisymmetric flow (no θ dependence). The variables used for computations in this geometry are non-dimensionalized by the following units: R_C for length, R_C^2/ν for time, ν/R_C for velocity, ν/R_C^2 for vorticity, νR_C for stream function, and $T_C - T_S$ for temperature, where R_C is the radius of the crucible (containing a melt of depth H), T_C is the highest temperature on the crucible wall, and T_S is the lowest temperature on the melt surface. For this geometry the velocity vector is

$$\bar{V} = \hat{r}V_r + \hat{\theta}V_\theta + \hat{z}V_z$$

and from Equation (4) the vorticity vector is

$$\bar{\Omega} = \hat{r} \frac{-\partial V_\theta}{\partial z} + \hat{\theta} \Omega + \hat{z} \frac{1}{r} \frac{\partial (rV_\theta)}{\partial r} ,$$

where the azimuthal vorticity component is

$$\Omega = \frac{\partial V_r}{\partial r} - \frac{\partial V_z}{\partial r} \quad (13)$$

and \hat{r} , $\hat{\theta}$, and \hat{z} are the unit vectors along the coordinate axes. The continuity equation can be solved identically by defining the Stokes stream function such that the radial and axial velocity components are

$$V_r = - \frac{1}{r} \frac{\partial \Psi}{\partial z} \quad (14)$$

$$V_z = \frac{1}{r} \frac{\partial \Psi}{\partial r} \quad . \quad (15)$$

In terms of the quantities defined above, the energy transport equation (3) becomes

$$\frac{\partial T}{\partial t} + \frac{1}{r} J(\Psi, T) = \frac{1}{Pr} \left(\frac{1}{r} \frac{\partial}{\partial r} \left(\frac{r \partial T}{\partial r} \right) + \frac{\partial^2 T}{\partial z^2} \right) \quad . \quad (16)$$

The zonal component of the momentum equation (2) becomes

$$\frac{\partial V_\theta}{\partial t} + \frac{1}{r} J(\Psi, V_\theta) - \frac{1}{r^2} V_\theta \frac{\partial \Psi}{\partial z} = \frac{\partial}{\partial r} \left(\frac{1}{r} \frac{\partial}{\partial r} (r V_\theta) \right) + \frac{\partial^2 V_\theta}{\partial z^2} \quad . \quad (17)$$

The zonal component of the vorticity transport equation (5) becomes

$$\frac{\partial \Omega}{\partial t} + J\left(\Psi, \frac{\Omega}{r}\right) + \frac{1}{r} \frac{\partial V_\theta^2}{\partial z} = \frac{\partial}{\partial r} \left(\frac{1}{r} \frac{\partial}{\partial r} (r \Omega) \right) + \frac{\partial^2 \Omega}{\partial z^2} + Gr \frac{\partial T}{\partial r} \quad . \quad (18)$$

The definition of zonal vorticity (13) becomes

$$\frac{\partial}{\partial r} \left(\frac{1}{r} \frac{\partial \Psi}{\partial r} \right) + \frac{1}{r} \frac{\partial^2 \Psi}{\partial z^2} = - \Omega \quad . \quad (19)$$

For this geometry, the Grashof number is $Gr = \alpha g (T_1 - T_0) R_c^3 / \nu^2$ and the aspect ratio is $A = H/R_c$.

The finite difference representation of this problem is given in Appendix 3.C. and the program used for numerical

integration is detailed in Appendix 4.b.

B. Numerical Solution of Thermal Convection in the Horizontal Bridgman Geometry

A detailed experimental study of convective temperature oscillations in molten gallium in the horizontal Bridgman geometry has been presented by Hurle et al.^{31,32,33}. These experiments were carried out in a rectangular boat heated on one end and cooled on the other; a thin layer of silicone oil was applied to the free melt surface to prevent oxidation of gallium and reduce vertical heat loss. The presently reported numerical results were obtained in order to understand the development of such convective instabilities in low Prandtl number melts where flows cannot be easily visualized.

The accuracy of the presently used finite difference scheme was verified by direct comparison with the numerical results of Stewart and Weinberg²⁷ for thermal convection in a square cavity heated from the side with $Gr = 2 \times 10^3$, $Pr = 0.0127$, and $A = 1$. The computation (with rigid insulating top and bottom surfaces) yielded a value for the volume flow rate about the vortex center (the maximum of the stream function field $\Psi_{max} = 2.80$) in good agreement with the value ($\Psi_{max} = 2.73$) found by Stewart and Weinberg²⁷.

The computer runs, summarized in Table 5, were conducted with a stress free boundary condition applied at the upper melt surface. The physical constants of molten gallium and

TABLE 5

COMPUTER RUNS FOR THE HORIZONTAL BRIDGMAN CONFIGURATION

Run Number	Aspect Ratio	Heat Flow		Grashof Number	Grid Size	Solution		Main Vortex	
		Biot Number	Gas Temperature			Condition	Time	Position	Intensity
1	0.25	0	-	1×10^4	33x9	SS	0.01693	0.500,0.094	2.19×10^{-1}
2	0.25	0	-	1×10^5	33x9	SS	0.01649	0.406,0.094	2.19×10^0
3	0.25	0	-	1×10^6	33x9	NS	0.00656	0.250,0.125	2.12×10^1
4	0.25	0	-	1×10^7	33x9	OS	0.00403	0.188,0.125	1.21×10^2
5	0.25	0	-	1×10^7	65x17	OS	0.00817	0.188,0.109	1.24×10^2
6	0.25	0	-	1×10^7	33x9	OS	0.01665	--	--
7	0.25	0.135	0.5	1×10^5	33x9	SS	0.01660	0.406,0.094	2.16×10^0
8	0.25	0.135	0.5	1×10^6	33x9	SS	0.01328	0.219,0.125	2.35×10^1
9	0.25	0.135	0.5	1×10^7	33x9	OS	0.01660	0.188,0.125	1.24×10^2
10	0.25	0.135	0.5	1×10^7	65x17	OS	0.02323	0.203,0.109	1.29×10^2
11	0.25	0.135	0.0	1×10^6	33x9	NS	0.01660	--	--
12	0.25	0.135	0.5	1×10^8	33x9	NU	--	--	--
13	0.5	0.135	0.5	1×10^4	33x17	NS	0.02656	0.469,0.219	2.65×10^0
14	0.5	0.135	0.5	1×10^5	33x17	NS	0.02188	0.406,0.219	2.24×10^1
15	0.5	0.135	0.5	1×10^6	33x17	OS	0.01992	0.312,0.219	1.19×10^2
16	0.5	0.135	0.5	1×10^7	33x17	NU	--	--	--
17	1.0	0.034	0.5	1×10^4	17x17	NS	0.05312	0.500,0.438	1.43×10^1
18	1.0	0.034	0.5	1×10^5	17x17	NS	0.05312	0.500,0.500	1.10×10^2
19	1.0	0.034	0.5	1×10^6	17x17	NU	--	--	--

SS=Steady State, N=Nearing Steady State, OS=Oscillatory State, NU=Numerically Unstable

silicone oil used in evaluating the dimensionless parameters are listed in Table 18. The numerical solutions are presented in the form of contour plots of the temperature (isotherms), vorticity (isodlines), and stream function (stream lines) fields in Figures 19 to 24. For the temperature and vorticity fields the minima are scaled to zero and the maxima are scaled to unity; for the stream function field, the zero level remains at zero and the minimum (which occurs at the main vortex center and is the volume flow rate between the vortex center and the upper surface referred to here as the intensity of the vortex) is scaled to minus one.

1. Dependence of Computed Flows on the Grashof Number

The solutions of the thermal convection equations, computed as part of the present study, show a marked dependence on Grashof number. This dependence is clearly illustrated in the sequence of solutions (runs number 1 to 4) with an insulating upper surface and constant aspect ratio ($A = 0.25$) presented in Figures 19 to 22. The analysis indicates a unicellular flow pattern at $Gr = 10^4$ (see Figure 19) which consists in a rising flow near the hot wall, a cross flow along the melt surface, a descending flow adjacent to the cold wall, and a return flow along the bottom of the enclosure. This convective cell is nearly symmetric about the vertical midplane. The vortex center is raised above the cavity mid-height to conserve volume flow (mass), since the flow rate

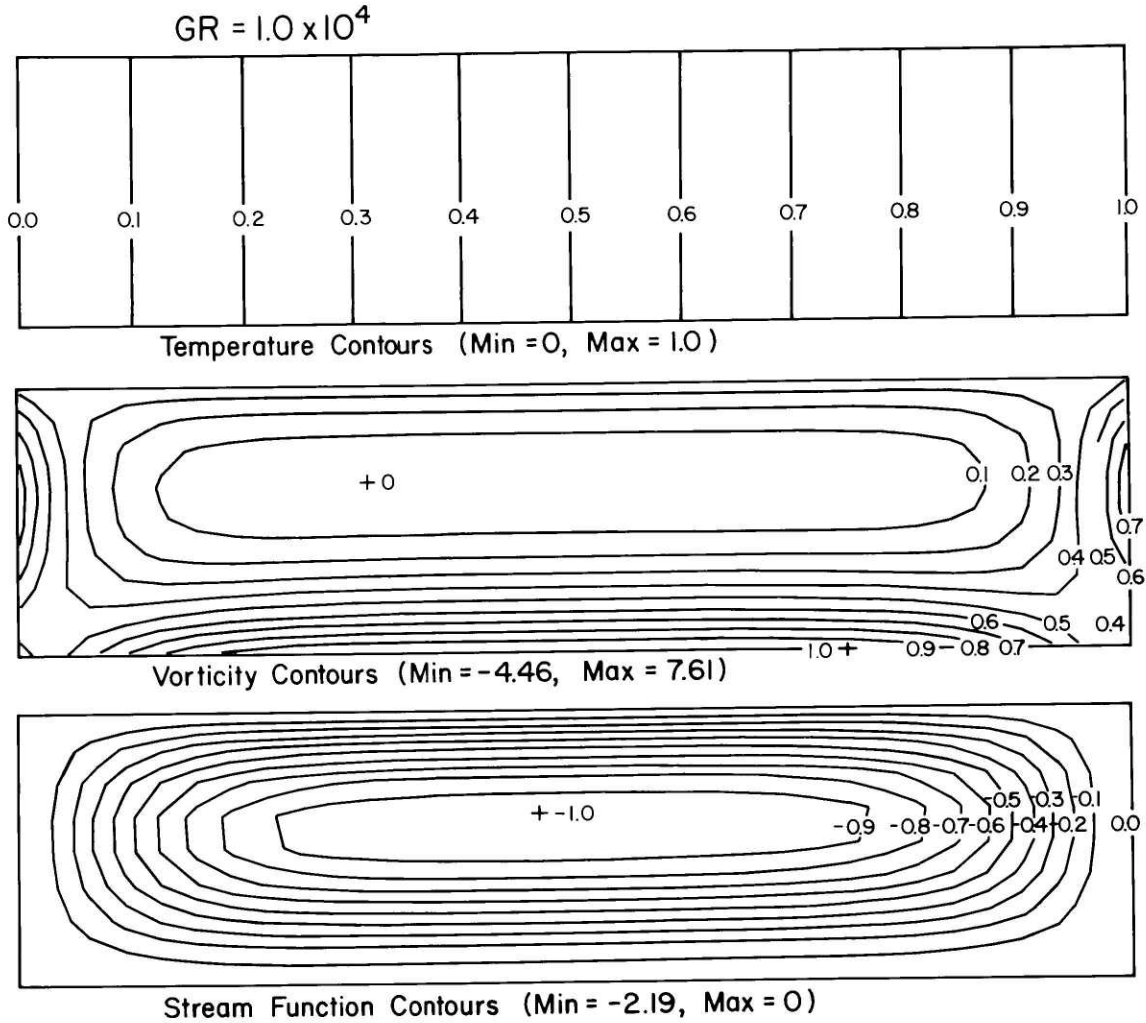


Figure 19. Computed contour plots of dimensionless temperature, vorticity, and stream function for horizontal Bridgman Configuration; $Gr = 1 \times 10^4$, $A = 0.25$. Run number 1 in Table 5.

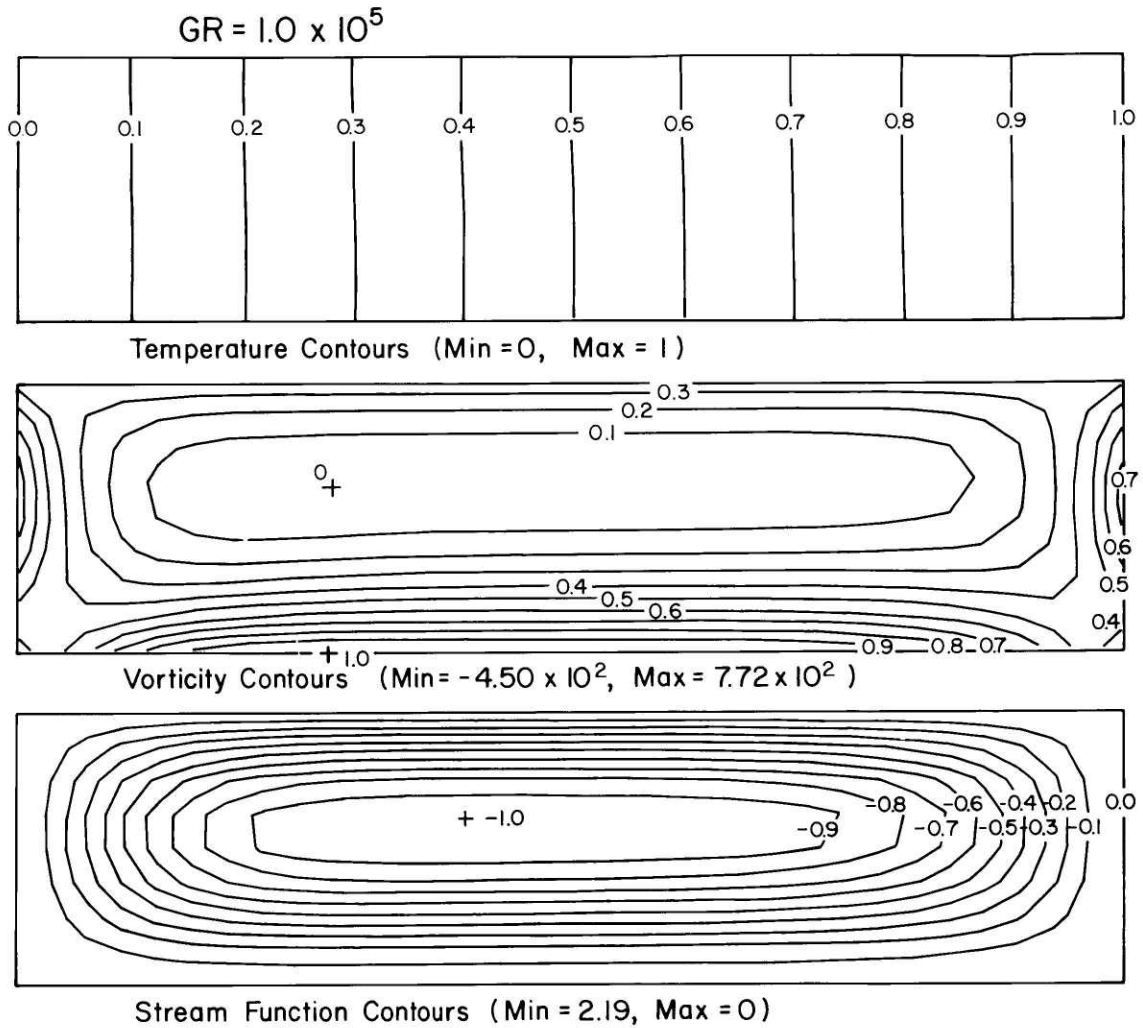


Figure 20. Computed contour plots of dimensionless temperature, vorticity, and stream function for horizontal Bridgman configuration; $Gr = 1 \times 10^5$, $A = 0.25$. Run number 2 in Table 5.

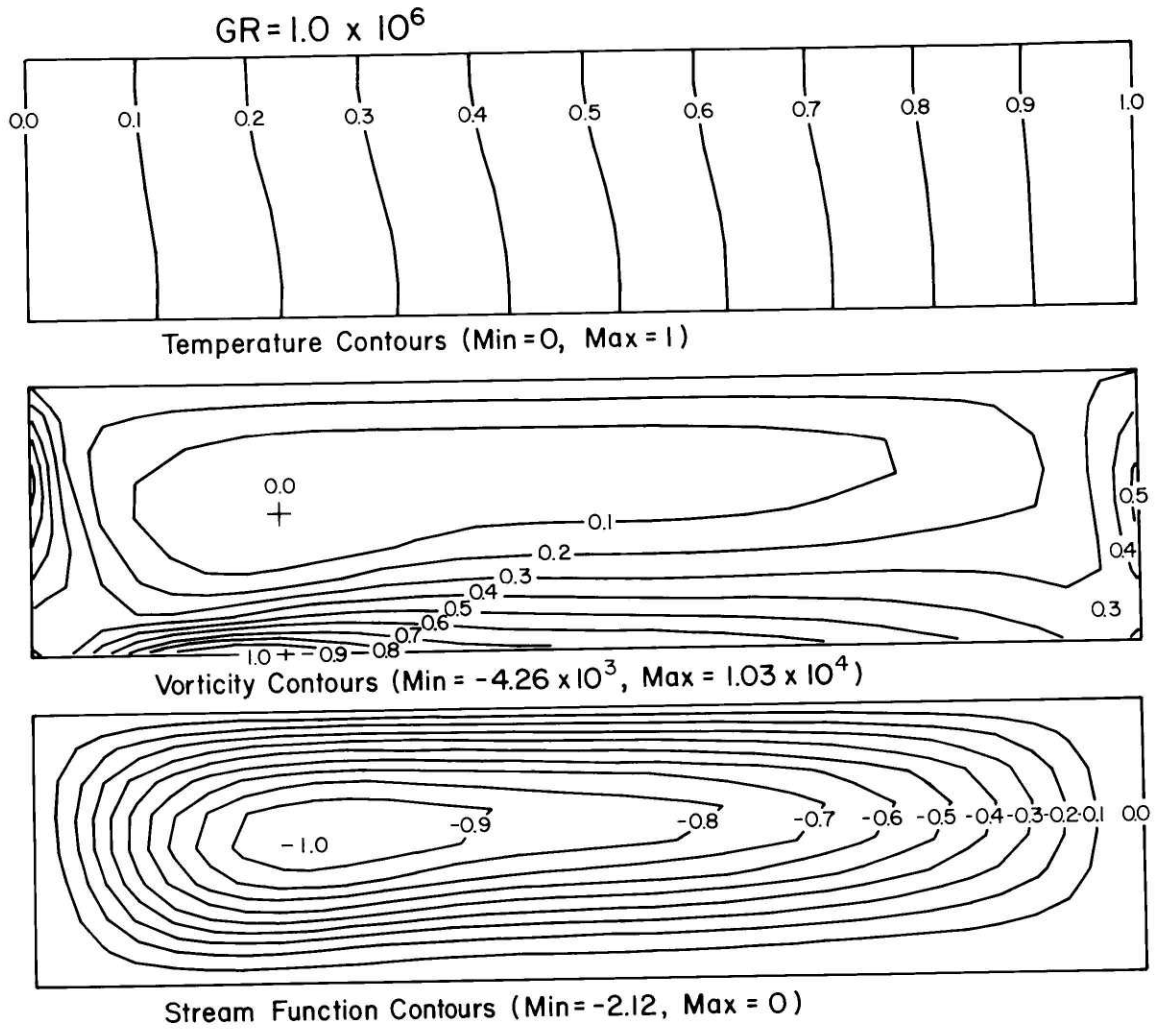


Figure 21. Computed contour plots of dimensionless temperature, vorticity, and stream function for horizontal Bridgman configuration; $Gr = 1 \times 10^6$, $A = 0.25$. Run number 3 in Table 5.

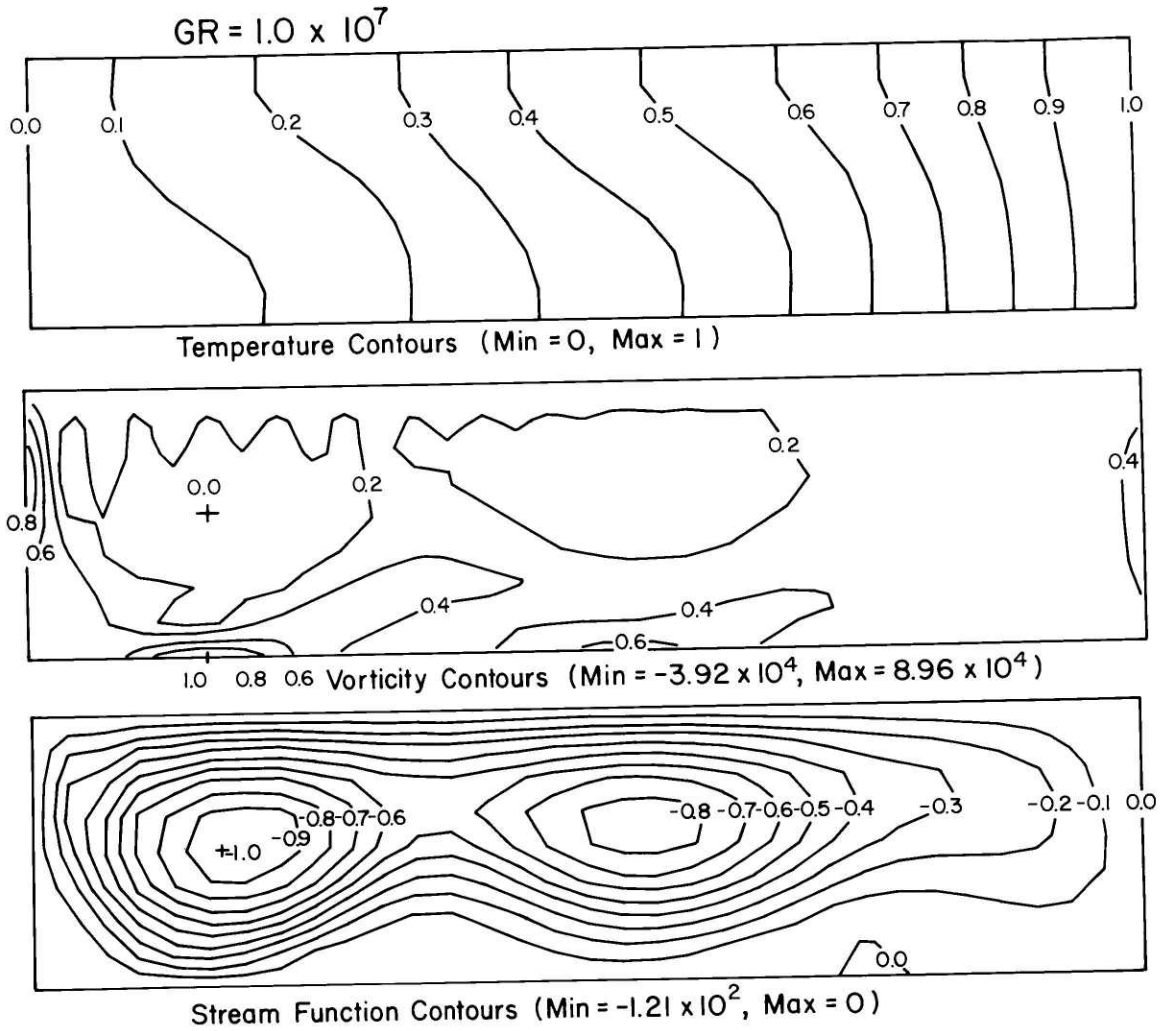


Figure 22. Computed contour plots of dimensionless temperature, vorticity, and stream function for horizontal Bridgman configuration; $Gr = 1 \times 10^7$, $A = 0.25$. Run number 4 in Table 5.

(which is inversely proportional to the stream line spacing) is higher above the center near the melt surface than below. Furthermore, it is evident from the equally spaced and vertical isotherms that conduction heat transfer is dominant at this Grashof number,

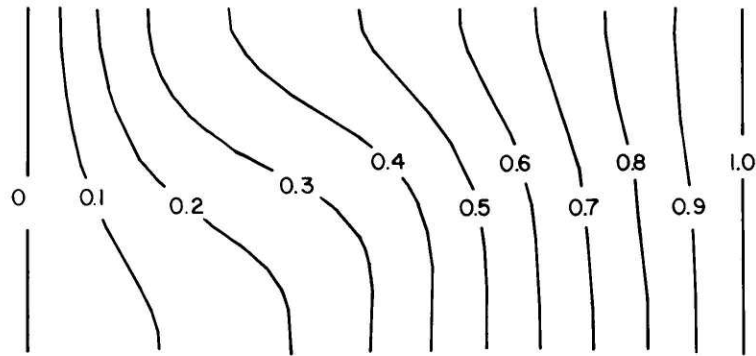
With increasing Grashof number, the vortex strengthens and its center moves towards the cold wall. As this occurs and the amount of convective heat flow increases, the isotherms are curved by the increased flow and are swept towards the more quiescent region of the flow field near the hot wall. Finally, at $Gr = 10^7$ (see Figure 22) a second, but weaker, clockwise vortex forms in the central region of the fluid as two weak reverse vortices develop along the bottom. Due to the lack of smoothness in the vorticity distribution at this higher Grashof number, the computation was continued on a more refined mesh (65x17) as discussed below (see run number 5 in Convective Oscillations).

The sequence of calculations (run numbers 7 to 9) with heat flow across the free surface for the same aspect ratio ($A = 0.25$) indicated similar behavior with increasing Grashof number. Aside from the effect of the surface heat flow on the isotherms near the melt surface, the position of the main vortex center, during flow development, tends to be closer to the cold wall and the circulation about it tends to be slightly lower than the corresponding flow without surface

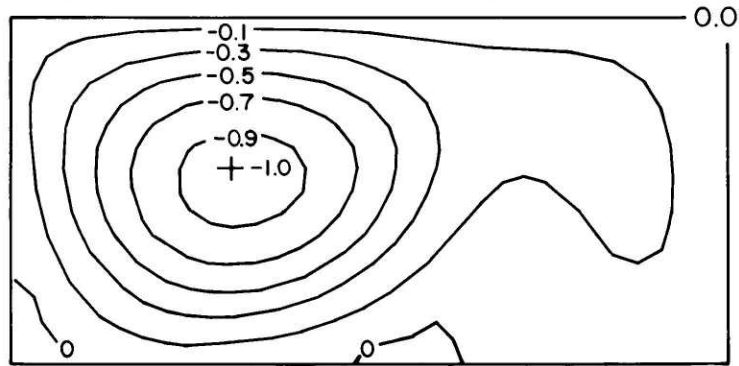
heat flow,

Many of the trends observed with increasing Gr for calculations at the aspect ratio of $A = 0.25$ are carried over to the higher aspect ratios ($A = 0.5$ and 1.0). At $Gr = 10^4$ convective heat transfer is already sufficient to cause bending of the isotherms in an enclosure with aspect ratio $A = 0.5$. The vortex center has moved towards the cold wall and the intensity of the vortex (-2.65) is an order of magnitude larger than that (-0.219) in the cavity of smaller aspect ratio ($A = 0.25$). Furthermore, a secondary clockwise vortex appears in the more quiescent warm fluid and two weak reverse vortices form along the cavity bottom at $Gr = 10^6$ (see Figure 23). At $Gr = 10^4$, a square cavity ($A = 1.0$) shows considerable isotherm bending in response to the increased intensity of the main vortex (-14.3) which is nearly two orders of magnitude higher than that in the cavity of smaller aspect ratio ($A = 0.25$). Apparently, for the larger aspect ratio cavity ($A = 1.0$), the vortex center cannot move toward the cold wall with increasing Gr within the resolution of the 17×17 grid; however, the flow rate is higher near the cold wall than near the hot wall. The solution at $Gr = 10^5$ (see Figure 24) reveals boundary layer separation along the hot and cold walls in the form of the reverse vortices.

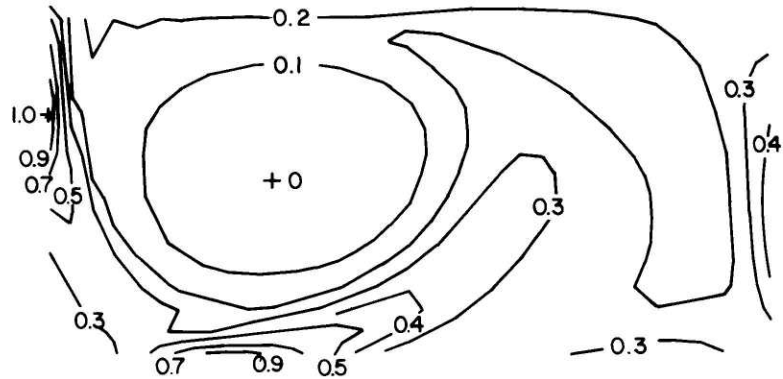
The intensity of the main vortex for the flows discussed in this section is summarized in Figure 25. It can be seen



Temperature Contours (Min=0, Max=1)

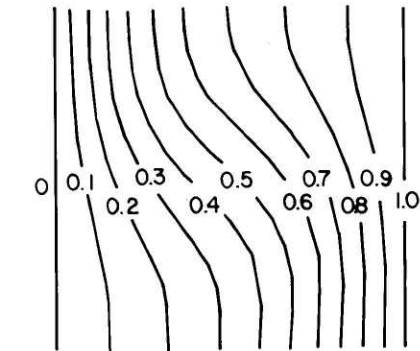


Stream Function Contours (Min = -1.19×10^2 , Max = 3.31×10^{-1})

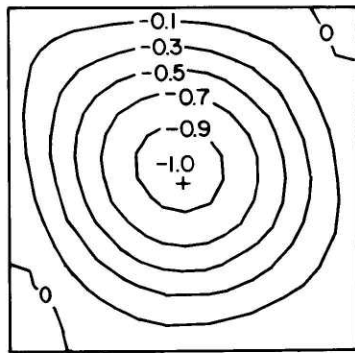


Vorticity Contours (Min = -8.26×10^3 , Max = 2.77×10^4)

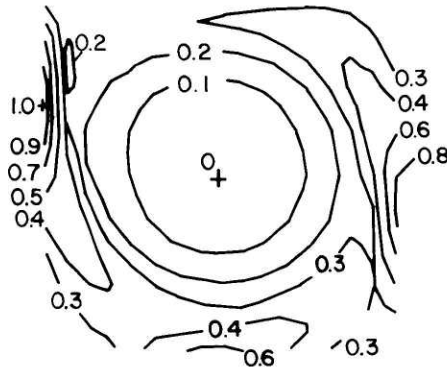
Figure 23. Computed contour plots of dimensionless temperature, stream function, and vorticity for horizontal Bridgman configuration; $Gr = 1 \times 10^6$, $A = 0.5$. Run number 15 in Table 5.



Temperature Contours (Min=0, Max=1)



Stream Function Contours (Min = -1.10×10^2 , Max = 4.37×10^{-1})



Vorticity Contours (Min = -2.82×10^3 , Max = 8.01×10^3)

Figure 24. Computed contour plots of dimensionless temperature, stream function, and vorticity for horizontal Bridgman configuration; $Gr = 1 \times 10^5$, $A = 1.0$, Run number 18 in Table 5.

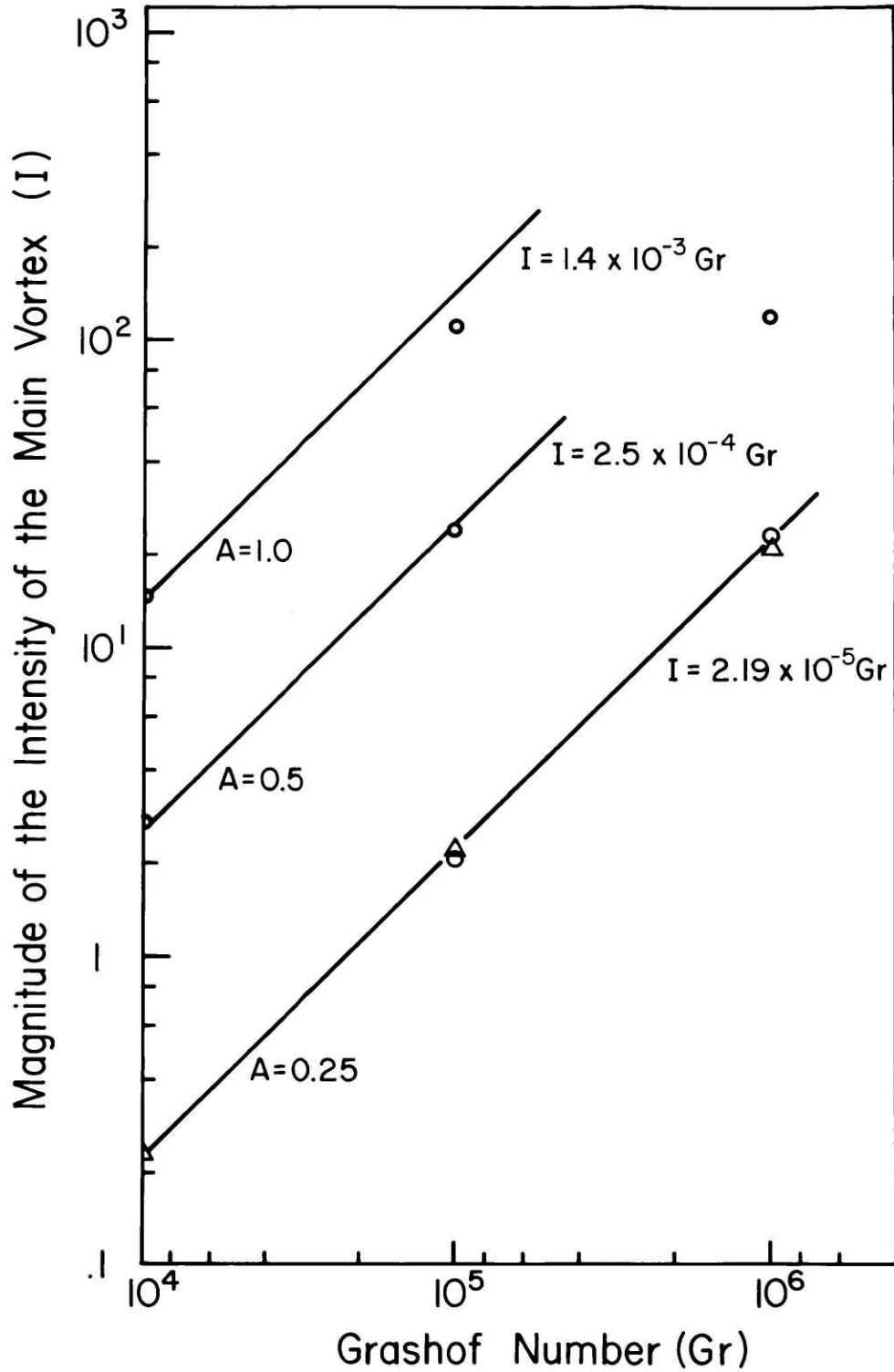


Figure 25. Dependence of main vortex intensity (I) on Grashof number (Gr) for constant aspect ratios (A).

that in the cavity of small aspect ratio ($A = 0.25$) the intensity increases linearly with Grashof number at low Grashof numbers. This behavior is in agreement with the experimental findings of MacAulay³⁵ for thermal convection in molten tin confined in horizontal boats of small aspect ratio. At higher Grashof numbers the dependence becomes sublinear.

2. Dependence of the Flow Intensity on the Aspect Ratio

The numerical results presented in the preceding subsection displayed a strong dependence on aspect ratio. The dependence of the intensity of the main vortex on melt aspect ratio is shown in Figure 26. It can be seen that, for the same Grashof number, the flow intensity decreases with decreasing aspect ratio.

This dependence of flow intensity on aspect ratio can be understood as follows: As discussed in Chapter 3, the viscous shear exerted by the cavity walls on the fluid is proportional to the ratio of the total wetted surface area to the liquid volume. For a fluid with a free upper surface in a rectangular enclosure, the wetted area to volume ratio is $\Gamma = (2/L)(1 + 1/(2A))$. As A decreases (for fixed L), Γ increases, and the viscous shear increases. This increase in viscous shear then results in a decrease of the rate of fluid flow. Thus, other factors being equal, the intensity of the flow is expected to decrease with decreasing aspect ratio.

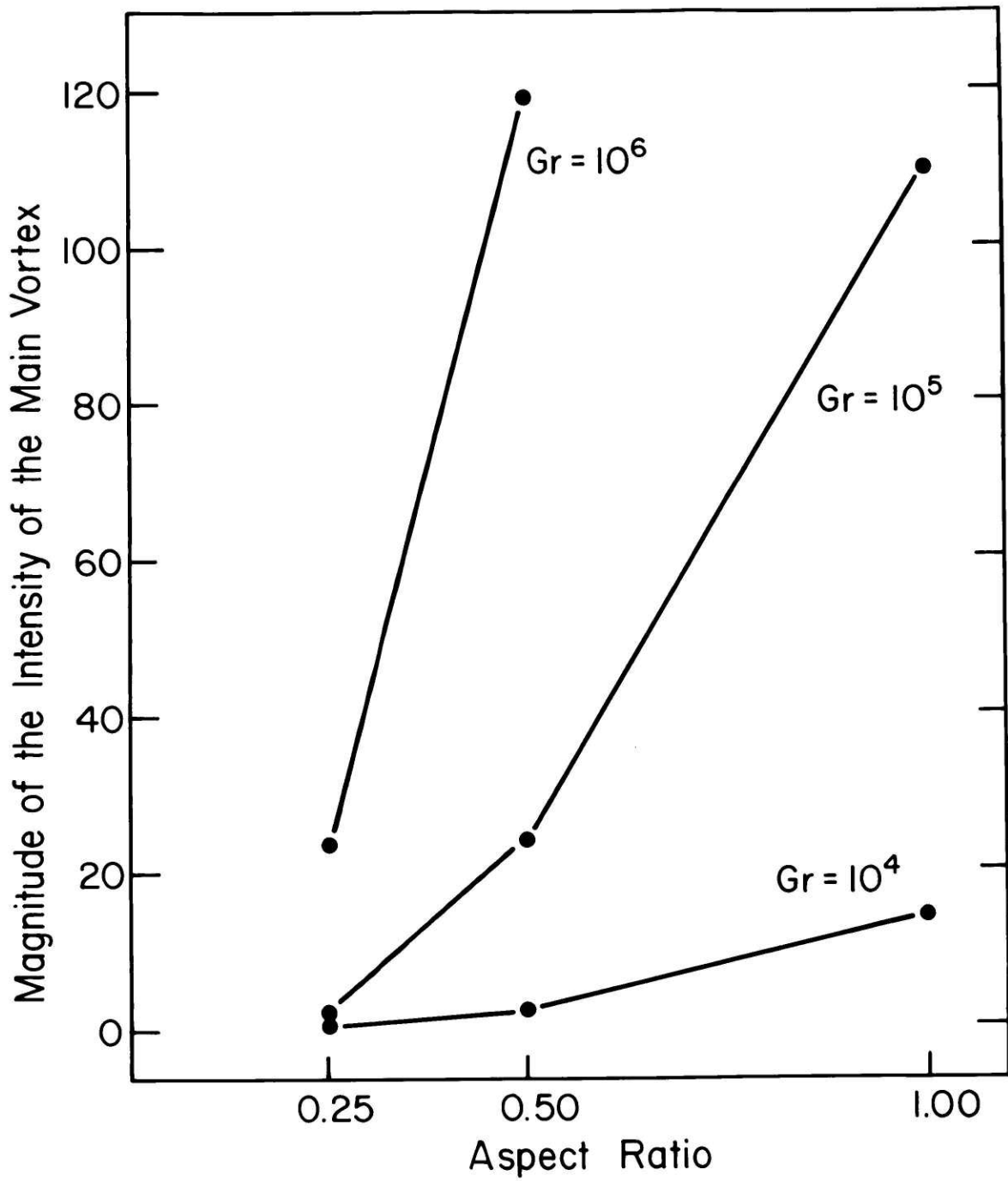


Figure 26. Dependence of main vortex intensity (I) on aspect ratio (A) for constant Grashof numbers (Gr).

3. Convective Oscillations

Several of the numerical solutions obtained during the present study exhibited oscillatory behavior (see Table 5). The onset of convective oscillations was found to coincide with the appearance of a secondary vortex in the warmer regions of the fluid at $Gr = 10^7$ for $A = 0.25$ and $Gr = 10^6$ for $A = 0.5$.

The evolution of the temperature and stream function fields during one oscillation period (0.00254) in a cavity of small aspect ratio (0.25) with an insulating upper surface (run number 5) is shown in Figures 27 and 28. The oscillation consists in the periodic transfer of energy back and forth between the main and secondary vortices as revealed by their flow intensities which grow and decay in tandem (see Table 6) in much the same manner as the oscillation calculated by Fromm¹⁷ for a fluid layer heated from below. During the oscillation the extrema in the intensity of the main vortex lead those of the secondary vortex. Furthermore, the main vortex center undergoes a small counter clockwise circulation as the secondary vortex center undergoes a circulation in the opposite direction.

In response to and coupled with the flow field, the temperature distribution undergoes an oscillation with the same period as revealed by the periodic movement of the isotherms. Thus, a stationary thermocouple positioned at the

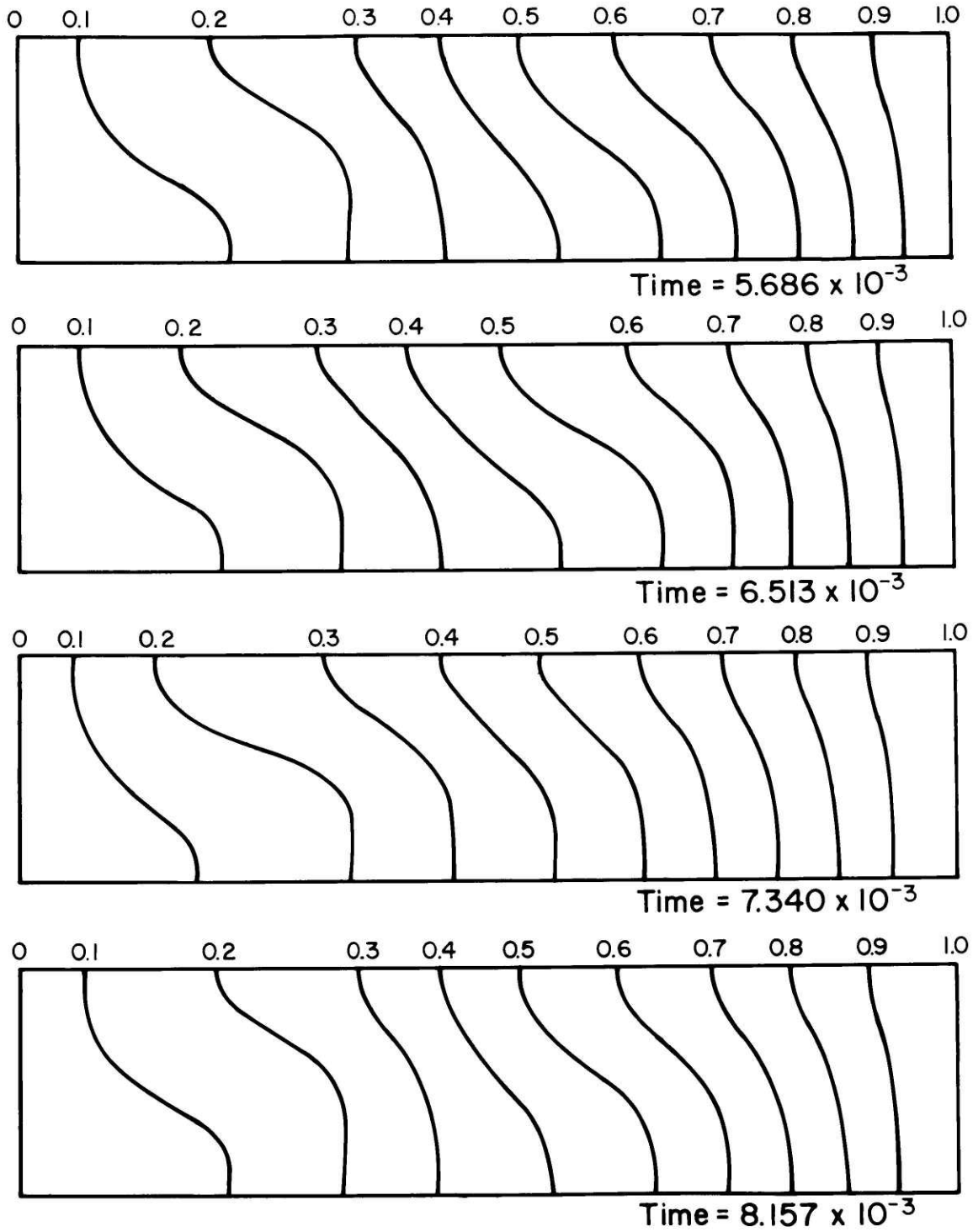
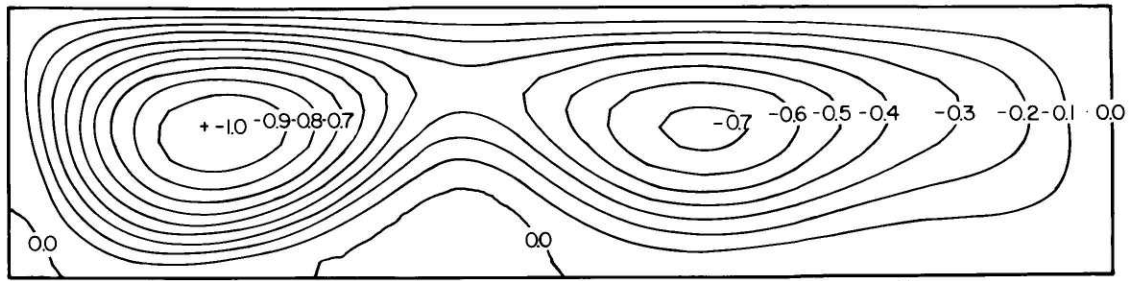
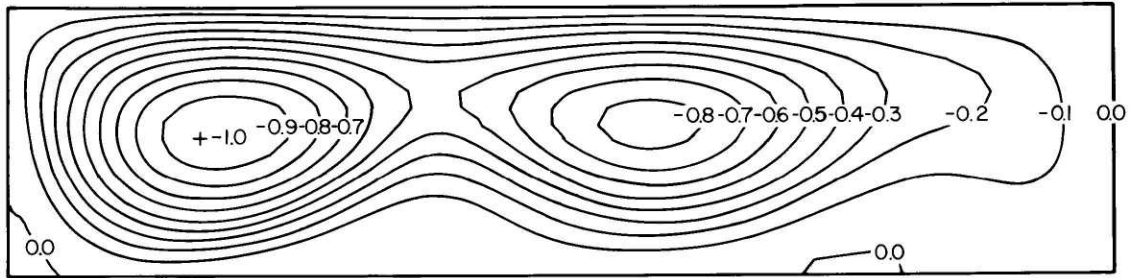


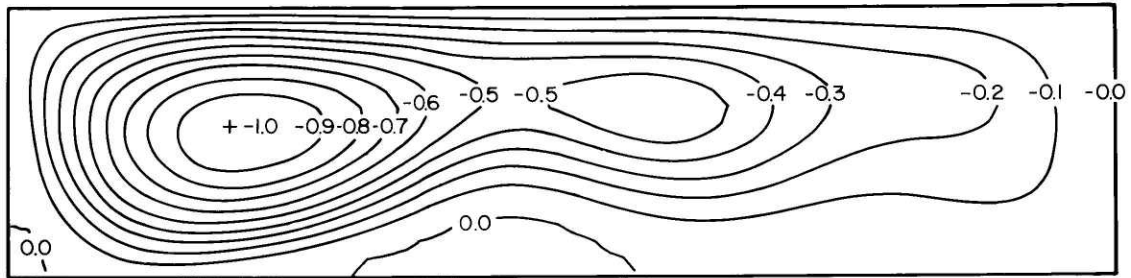
Figure 27. Time evolution of dimensionless temperature field during one convective oscillation; $Gr = 1 \times 10^7$, $A = 0.25$. Run number 5 in Table 5.



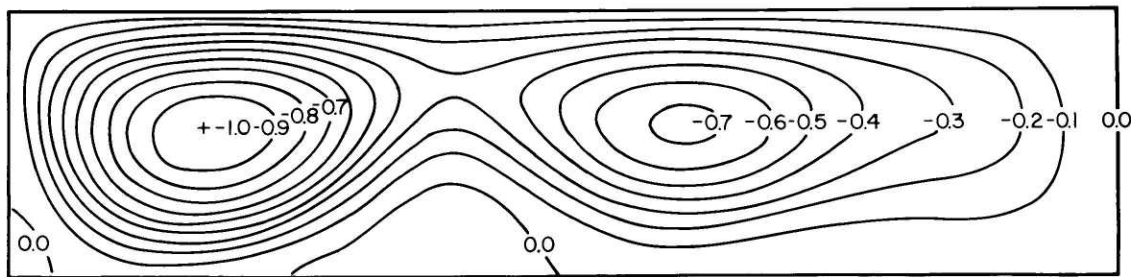
Time = 5.686×10^{-3}



Time = 6.513×10^{-3}



Time = 7.340×10^{-3}



Time = 8.167×10^{-3}

Figure 28. Time evolution of dimensionless stream function field during one convective oscillation; $Gr = 1 \times 10^7$, $A = 0.25$. Run number 5 in Table 5.

cavity center would "see" the 0.4 isotherm move across it, first to the left and then to the right. This thermocouple would record the nearly sinusoidal temperature oscillation shown together with the stream function oscillation in Figure 29.

TABLE 6

Positions and Intensities of the Main and Secondary Vortices During One Convective Oscillation of Computer Run Number 5.

<u>TIME</u>	<u>MAIN VORTEX</u>		<u>SECONDARY VORTEX</u>	
	<u>Position</u>	<u>Intensity</u>	<u>Position</u>	<u>Intensity</u>
0.005686	0.188,0.109	-123.6	0.625,0.109	- 90.3
0.006099	0.188,0.109	-120.1	0.609,0.109	-100.4
0.006513	0.188,0.125	-121.5	0.578,0.109	-102.8
0.006926	0.219,0.125	-127.3	0.578,0.102	- 92.3
0.007340	0.219,0.109	-131.2	0.594,0.094	- 75.6
0.007753	0.203,0.109	-128.9	0.625,0.109	- 75.4
0.008167	0.188,0.109	-123.8	0.609,0.109	- 89.8

Due to the apparent damping of the oscillation amplitude, the above calculation was carried out for a longer time on a less refined (33 x 9) grid (run number 6). The results reveal a damped oscillation of dimensionless period 0.00213 which appears to be asymptotically approaching a constant value somewhat less than 0.008. Additional computations performed for an enclosure of small aspect ratio (0.25) with heat flow across the upper surface showed somewhat longer periods of 0.00215 and 0.02262, respectively, for a coarse (run number 8) and refined (run number 9) grid. One solution for a cavity of

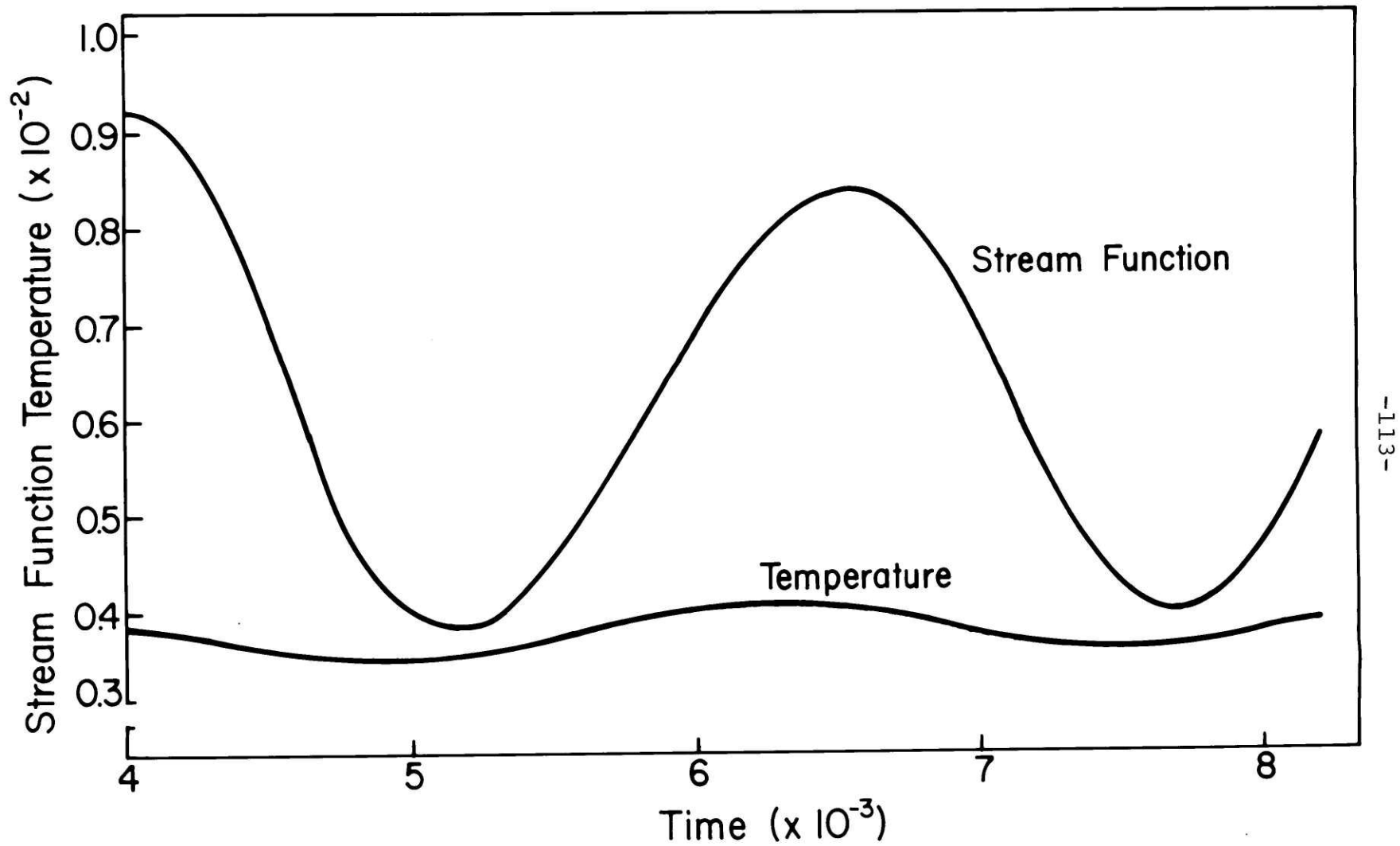


Figure 29. Time evolution of dimensionless temperature and stream function values at center of cavity; $Gr = 1 \times 10^7$, $A = 0.25$. Run number 5 in Table 5.

aspect ratio 0.5 (run number 15) exhibited a period of 0.00708.

It is instructive to compare the numerically predicted oscillation periods with the experimental findings of Hurle et al³³. The pertinent results are listed in Table 7. For comparison with the present numerical results, the critical values of the Rayleigh number ($Ra^H = \alpha g \Delta T H^4 / L \nu \kappa$), as determined by Hurle for the onset of temperature oscillations, were converted to values of the Grashof number ($Gr = Ra / (Pr A^4)$) and were corrected for the difference in the factor ($\alpha g / \kappa \nu$) used by Hurle (320) and that determined from the data in Table 18 (270). The numerical periods have been dimensionalized by the viscous diffusive time (L^2 / ν) and are compiled in Table 8.

TABLE 7

EXPERIMENTAL CONVECTIVE OSCILLATION PERIODS
(From Hurle et al³³)

<u>BOAT LENGTH (CM)</u>	<u>MELT DEPTH (CM)</u>	<u>ASPECT RATIO</u>	<u>RAYLEIGH NUMBER</u>	<u>GRASHOF NUMBER</u>	<u>PERIOD (SEC)</u>
3.0	0.75	0.25	920	1.4×10^7	8.7
2.4	1.2	0.50	7700	7.3×10^6	5.3

TABLE 8

THEORETICAL CONVECTIVE OSCILLATION PERIODS

<u>RUN NUMBER</u>	<u>ASPECT RATIO</u>	<u>GRASHOF NUMBER</u>	<u>DIMENSIONLESS PERIOD (10^{-3})</u>	<u>PERIOD (SEC)</u>
5	0.25	1×10^7	2.45	8.17
6	0.25	1×10^7	2.13	7.10
8	0.25	1×10^7	2.15	7.17
9	0.25	1×10^7	2.62	8.73
15	0.50	1×10^6	7.08	15.01

It can be seen from Tables 7 and 8 that, for the cavity of small aspect ratio (0.25), the agreement between the predicted and experimental period is quite good. In particular, the excellent agreement between the numerical solution with heat flow on the refined grid (run number 9) and the experimental result indicates the importance of surface heat flows. Furthermore, the close agreement between the observed critical Grashof number and that for which the numerical solutions show oscillatory behavior should also be noted. The agreement for the cavity of larger aspect ratio (0.5) is less satisfactory.

C. Numerical Solution of Thermal Convection in the Czochralski Geometry

Only a limited number of computer flow simulations have been carried out for the Czochralski geometry. The dimensionless parameters and boundary conditions employed were based on the preceding thermal characterization study (see Chapter V) and the physical properties of Ge (see Table 17).

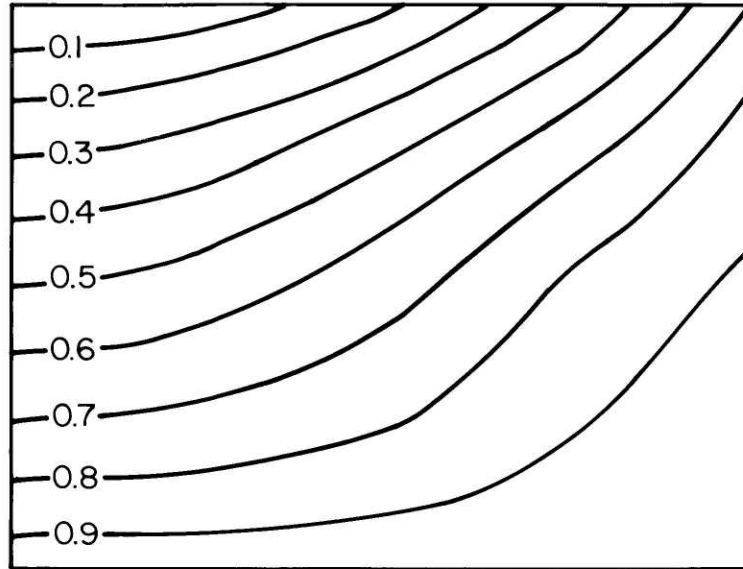
These computations used the melt height (H) which would occur in the absence of meniscus effects (see Comments on Temperature Measurements). The two computer runs to be discussed are summarized in Table 9. In addition to contour plots of the dimensionless temperature (isotherms) and stream function (stream lines) fields, the computational results are presented in dimensional form as radial and vertical temperature profiles, radial profiles of the vertical velocity component, and vertical profiles of the radial velocity component.

The results of computer run number 20 are shown in Figures 30 to 32. The thermal boundary conditions on the crucible wall were based on the temperature measurements shown in Figure 12. In this calculation the radiative heat loss from the melt surface was simulated by specifying a parabolic temperature distribution⁵⁴. The computations indicate that the main counter-clockwise vortex of intensity 102.2 causes the isotherms to bend in the vicinity of its center at (1.2 cm, 0.875 cm) (see Figure 30). The computed vertical temperature profiles (see Figure 31(a)) reveal, furthermore, the existence of an axial temperature gradient which is smaller at the melt surface (7.7°C/cm) and larger near the melt bottom (6.7°C/cm) than indicated by the respective experimental results. The horizontal melt temperature profiles (see Figure 31(b)) are in qualitative agreement with

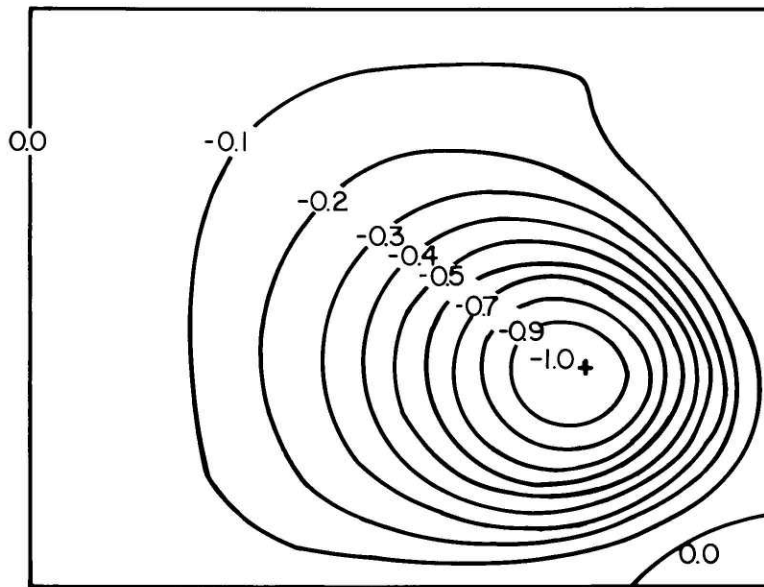
TABLE 9

COMPUTER RUNS FOR THE MODIFIED CZOCHRALSKI CONFIGURATION

<u>RUN NUMBER</u>	<u>ASPECT RATIO</u>	<u>GRASHOF NUMBER</u>	<u>PRANDTL NUMBER</u>	<u>CONVECTION BIOT NUMBER</u>	<u>HEAT FLOW GAS TEMP</u>	<u>RADIATION BIOT NUMBER</u>	<u>WALL TEMP</u>	<u>GRID SIZE</u>
20	0.875	1.23×10^6	6.25×10^{-3}	0	-	0	-	17x17
21	0.813	2.01×10^6	6.67×10^{-3}	0	-	2.40×10^{-2}	80°C	17x17

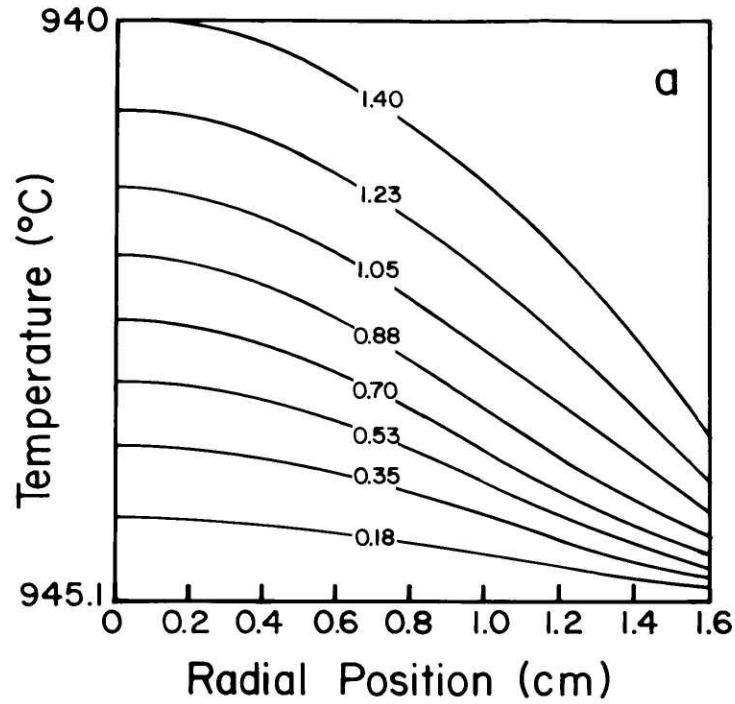


Temperature Contours
(Min = 9.40×10^2 , Max = 9.451×10^2)

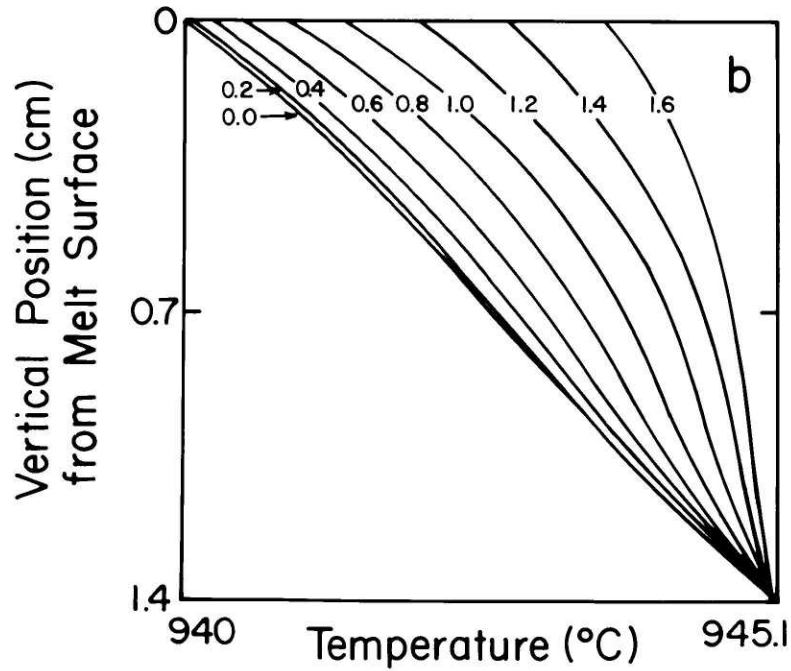


Stream Function Contours
(Min. = -1.608×10^0 , Max. = 1.022×10^2)

Figure 30. Computed contour plots of dimensionless temperature and stream function for Czochralski configuration (run number 20 in Table 9).

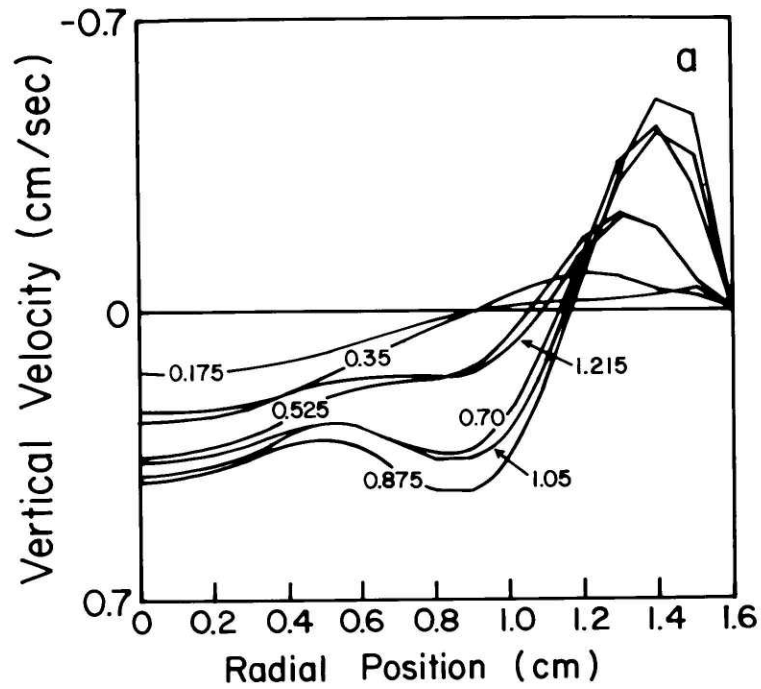


(a) Horizontal temperature profiles at labeled positions (cm) above the crucible bottom.

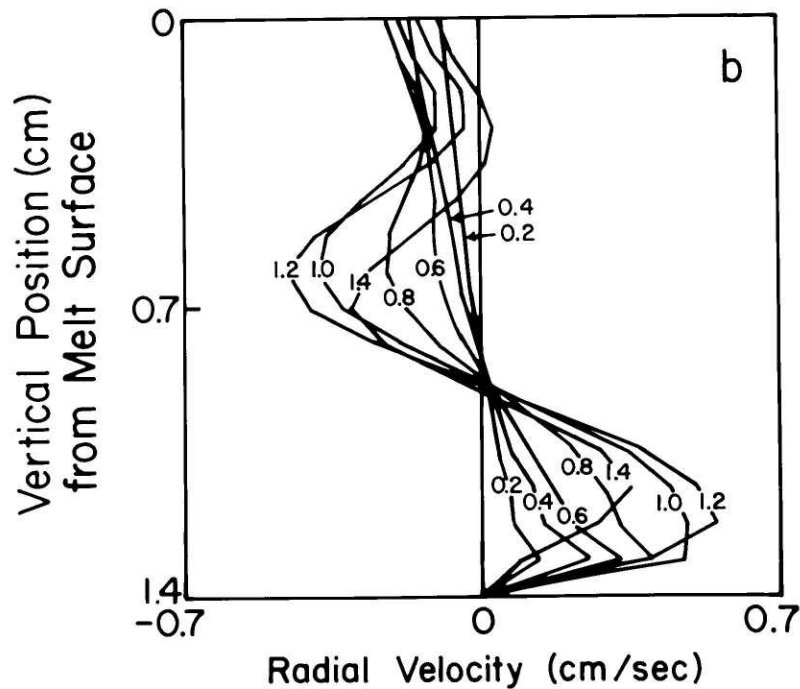


(b) Vertical temperature profiles at labeled radial positions (cm).

Figure 31. Computed temperature profiles for Czochralski configuration (run number 20 in Table 9).



(a) Horizontal profiles of vertical velocity component at labeled vertical positions (cm).



(b) Vertical profiles of radial velocity component at labeled radial positions (cm).

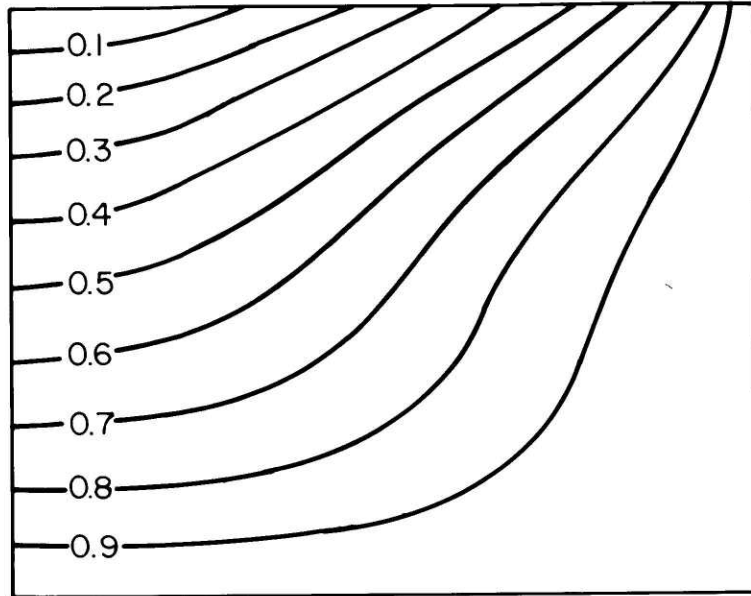
Figure 32. Computed velocity profiles for Czochralski configuration (run number 20 in Table 9).

experiment (see Figure 14(a)) in that the horizontal temperature difference increases with height above the crucible bottom.

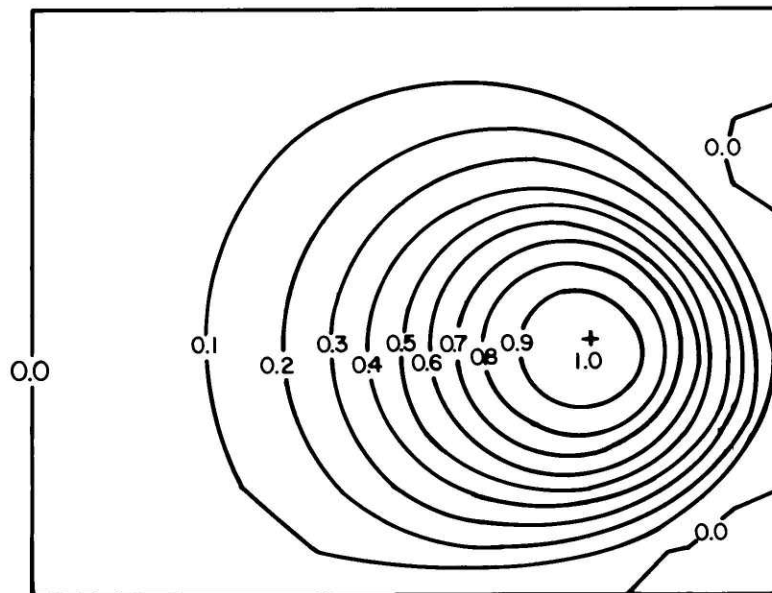
The velocity profiles (see Figure 32) reveal rather high flow rates. The maximum radial velocity component (0.622 cm/sec) occurs in the jet along the crucible bottom, while the maximum vertical component (0.507 cm/sec) occurs in the jet along the crucible wall. The effect of a weak clockwise vortex (see Figure 30) is seen in the flow reversal near the crucible bottom at radial position 1.4 cm.

In order to achieve better computational agreement with the experimental temperature profiles, heat flow across the melt surface was explicitly treated in run number 21. The resulting isotherms, stream lines, temperature profiles, and velocity profiles are shown in Figures 33 to 35. The ideal heat pipe configuration condition (constant crucible wall temperature) was applied and only radiative heat losses were considered.

The flow pattern and temperature distribution (see Figure 33) for this run show many features similar to those found in the preceding run. There exists one main counter-clockwise vortex (of intensity 130.3 at the position (1.2 cm, 0.73 cm)) and two weaker reverse vortices along the crucible side wall. Again the isotherms exhibit bending near the vortex center and they show, furthermore, a similar parabolic

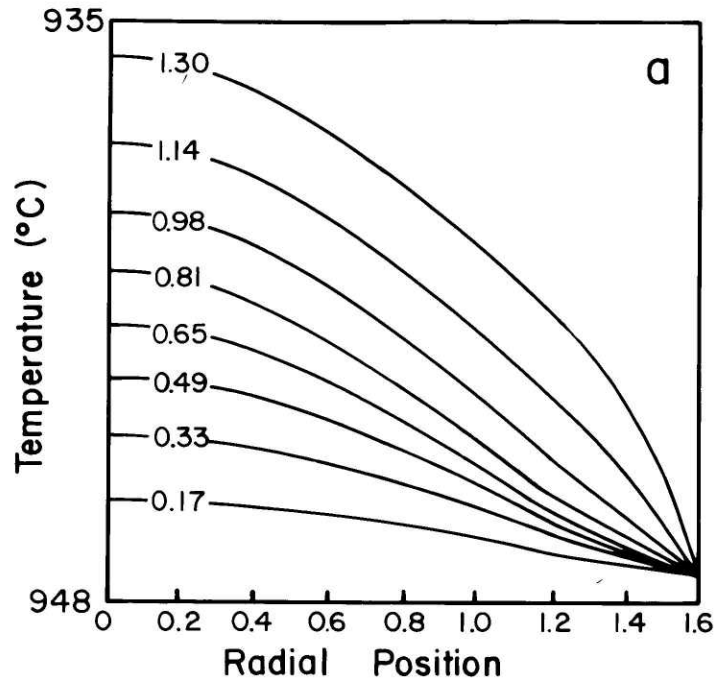


Temperature Contours
(Min. = 9.358×10^2 , Max. = 9.474×10^2)

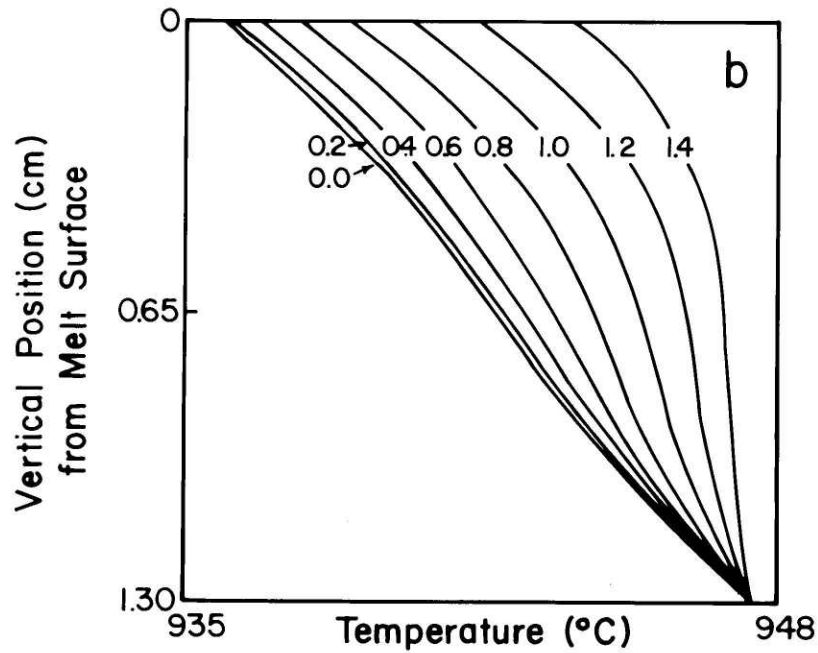


Stream Function Contours
(Min. = -2.563×10^0 , Max. = 1.303×10^2)

Figure 33. Computed contour plots of dimensionless temperature and stream function for Czochralski configuration (run number 21 in Table 9).

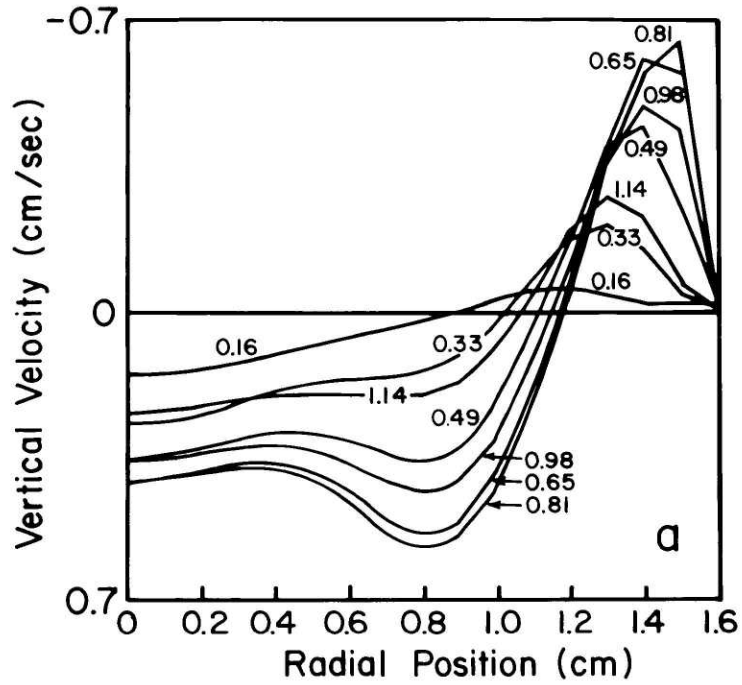


(a) Horizontal temperature profiles at labeled positions (cm) above the crucible bottom.

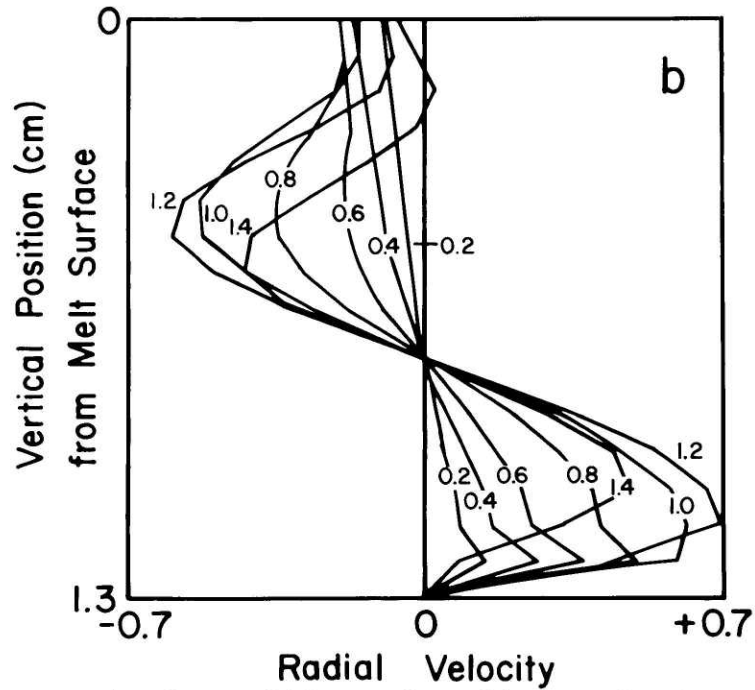


(b) Vertical temperature profiles at labeled radial positions (cm).

Figure 34. Computed temperature profiles for Czochralski configuration (run number 21 in Table 9).



(a) Horizontal profiles of vertical velocity component at labeled vertical positions (cm).



(b) Vertical profiles of radial velocity component at labeled radial positions (cm).

Figure 35. Computed velocity profiles for Czochralski configuration (run number 21 in Table 9).

behavior near the crucible axis at the melt surface. The vertical temperature profiles (see Figure 34 (b)) exhibit a larger axial temperature gradient ($12.48^{\circ}\text{C}/\text{cm}$) near the melt surface, in better agreement with experiment, but the calculated axial gradient ($10.62^{\circ}\text{C}/\text{cm}$) near the crucible bottom is larger. The radial profiles again exhibit an increasing temperature difference as the melt surface is approached.

The corresponding velocity profiles (see Figure 35) show qualitative features similar to those in the previous run. However, at this higher Grashof number, the horizontal velocity maximum ($0.694\text{ cm}/\text{sec}$) in the bottom jet and the vertical velocity maximum ($0.654\text{ cm}/\text{sec}$) in the crucible wall jet are increased.

In summary this chapter has presented the results of a numerical study of thermal convection in the horizontal Bridgman and modified Czochralski configurations. The excellent agreement of the present numerical solutions with previous experimental findings on convective temperature oscillations in the horizontal Bridgman geometry confirms the soundness of the theoretical approach developed to treat thermal convection in growth configurations. The extension of this approach to the Czochralski geometry has been confirmed in principle by a limited number of numerical results. While agreement in detail between the theoretical and experimental temperature profiles has not, as yet, been

achieved, the agreement of computer run number 21 with the experimental results makes it possible to extract useful quantitative information on the form and rate of thermal convective flow in the Ge melt. The lack of detailed agreement can be attributed primarily to the excessive curvature of the Ge melt surface. Furthermore, uncertainties are associated with the precision of the available (required) physical constants of Ge, the assumption of axial symmetry, the neglect of other convection mechanisms, and definition of the boundary conditions.

The implications of these numerical results for segregation in the Czochralski configuration will be discussed in Chapter IX.

CHAPTER VII

BASIC CONSIDERATIONS AND LITERATURE
REVIEW ON FORCED CONVECTION AND SEGREGATION
IN CZOCHRALSKI CRYSTAL GROWTH SYSTEMS

This chapter presents the established theoretical and experimental framework of crystal growth and segregation and reviews the literature pertaining to forced convection and dopant segregation phenomena in Czochralski crystal growth systems. The current state of knowledge on this topic has recently been reviewed by Carruthers and Witt³, who consider fluctuations of growth rate and diffusion boundary layer thickness as the origin of solute striations in melt growth systems; they consider further the phenomena of segregation on faceted interfaces and present the most recent experimental techniques developed for the quantitative study of transient segregation effects.

The study of segregation phenomena in Czochralski growth systems, conducted as part of the present work, is presented in Chapters VII and VIII for reasons discussed in Chapter II. The results of this study are combined with those of the preceding thermal convection analysis in a general discussion of convection and its effects on segregation in the modified Czochralski configuration presented in Chapter IX.

A. Forced Convection

An understanding of forced convective flows generated by differential rotation of bounding surfaces is necessary for analyzing the effects of crystal and crucible rotation (commonly used with Czochralski growth) on the temperature and solute distributions during crystal growth. Cochran's analysis⁵⁵ pictures an infinite rotating disk in a semi-infinite liquid as a centrifugal fan drawing fluid axially toward the disk and spinning it radially outward in a uniform momentum boundary layer whose thickness (δ_m) is of the order of $(\nu/\omega)^{1/2}$, where ω is the angular rotation rate of the disk. Tomlan and Hudson⁵⁶ analyzed the flow near a finite disk rotating rapidly in a crucible with equal radius and showed that although the influence of the crucible walls extended throughout much of the fluid, the momentum boundary layer thickness on the disk increased from center (where $\delta_m = 4.6 (\nu/\omega)^{1/2}$) to the periphery by only 3%. Flow simulation experiments reported by Lehmkuhl and Hudson⁵⁷ were in good agreement with the predictions of Tomlan and Hudson for disks and crucibles of equal radius. However, they found that, when the disk radius was less than about half that of the crucible, a detached shear layer formed at the radius of the disk with fluid spiralling radially outward under the disk and descending to the crucible bottom in the shear layer, while fluid from the crucible wall spiralled radially inward

to the shear layer. They determined further that a finite disk rotating in a confined fluid approximates, to within a few percent, a uniformly accessible surface (constant mass transfer coefficient or, equivalently, constant solute boundary layer thickness).

Carruthers⁵⁸ has simulated thermal and forced convection in the Czochralski geometry using water-glycerine mixtures. In the presence of thermal convection alone, a symmetric toroidal flow pattern was developed with fluid rising along the crucible side wall and descending beneath the solid-liquid interface. Application of slow crystal rotation reduced the intensity of thermal convection in the vicinity of the crystal interface while, at higher rates of crystal rotation, thermal convection was suppressed near the crystal, which behaved as a rotating disk. The effects of thermal convection at low crucible rotation rates were diminished and a non-uniform boundary layer developed adjacent to the crystal interface, while, at higher rotation rates, a Taylor-Proudman cell was formed beneath the crystal. (It consisted of a cylindrical volume beneath the crystal whose boundary formed a detached shear layer separating it from the thermal convection dominated region near the crucible side wall.) Crystal and crucible rotation in the same direction (isorotation) was shown to result only in a modification of flow with crucible rotation alone, while counter rotation stabilized the Taylor-Proudman

cell and isolated it from the outer regions of the crucible. A more detailed simulation study of forced convection by Carruthers and Nassau⁵⁹, while confirming these observations, showed that, with counter rotation, a second Taylor-Proudman cell may form beneath the crystal with the upper cell dominated by crystal rotation and the lower cell dominated by crucible rotation. A series of numerical studies by Kobayashi and Arizumi^{60,61,62} is in good agreement with these observations.

The rotational instabilities which result in a loss of diameter control during Czochralski growth of $\text{Bi}_{20}\text{SiO}_{20}$ crystals were simulated by Whiffin, Bruton, and Brice⁶³. They found that above a critical rotation rate ω_c , the vertical temperature gradient changed drastically and the radial heat flow increased as the Taylor-Proudman cell became unstable and a wave pattern developed on the upper surface of the melt. This behavior was reported to be a disturbance of the baroclinic type, which resembles to some extent the flows computed by Williams⁶⁴ in his numerical study of thermal convection in a rotating annulus.

B. Segregation

1. Segregation Models

The incorporation of solute into a crystal (growing at a rate R) is characterized by the interface distribution coefficient k_i , which is defined as the ratio of the solute concentration being incorporated into the solid phase (C_s)

to the solute concentration in the liquid phase at the (solid-liquid) interface (C_i) : $k_i = C_s/C_i$. It is generally assumed that equilibrium prevails at the interface and k_i is equated with the equilibrium distribution coefficient (k_o) . At the onset of growth, for $k_o < 1$, solute atoms are rejected from the solid at a rate which is faster than the rate at which they can diffuse into the bulk liquid; thus a region of enriched solute concentration, defined as the solute boundary layer of thickness, δ , develops adjacent to the growth interface. Since, under growth conditions, C_i is not experimentally measureable, segregation is characterized by the effective distribution coefficient (k_e) which is defined as the ratio of solute concentration being incorporated into the solid phase (C_s) to the solute concentration in the bulk liquid outside the solute boundary layer (C_1) :

$$k_e = C_s/C_1 \quad . \quad (20)$$

A number of segregation models have been developed which relate k_e to the growth parameters such as k_o , R , and δ . Tiller⁶⁵ analyzed convection-free growth and showed that segregation approaches steady-state ($k_e = 1$) after an initial transient of characteristic length, $D/(R k_o)$, where D is the solute diffusion coefficient in the liquid. The opposite extreme, complete mixing in the melt ($k_e = k_o$), was treated by Pfann⁶⁶. For the intermediate case of partial mixing,

Burton, Prim, and Slitcher⁶⁷ (BPS) determined the steady state effective distribution coefficient to be

$$k_e = k_i / (k_i + (1 - k_i) \exp(-R\delta/D)) \quad . \quad (21)$$

The derivation of the BPS relation was based on a boundary layer solution of the solute conservation equation. This solution was brought into agreement with their exact solution for segregation ahead of a rotating crystal (based on Cochran's analysis⁵⁵) by defining the solute boundary layer thickness (δ) as

$$\delta = AD^{1/3} \nu^{1/6} \omega_s^{-1/2} \quad , \quad (22)$$

where A is a weak function of the rotation rate (ω_s) and has the value 1.6 at low rotation rates.

The effect of a sinusoidal temperature oscillation (applied at the edge of the thermal boundary layer) on segregation has been modeled by Hurle, Jakeman and Pike⁵⁰. They determined the fractional change in k_e to be

$$\frac{\Delta k_e}{k_e} = \frac{k_e^* - k_e}{k_e} = \frac{\omega |\phi \omega C_\omega|}{2R_o C_o} \sin(\epsilon_c - \epsilon_\phi)$$

where k_e^* is the effective distribution coefficient in the presence of fluctuations of frequency ω , $\phi\omega$ and C_ω are the Fourier amplitudes of the interface displacement and

liquid concentration, ϵ_ϕ and ϵ_c are the phase shifts of these with respect to the imposed temperature oscillation, and R_0 and C_0 are the steady-state values of the growth rate and solute concentration in the liquid at the interface. For a crystal on the verge of remelting ($R = \omega\phi_\omega$) Hurle and Jakeman⁶⁸ have shown that, for low frequency ($\omega D/R_0^2 \ll 1$) and low average growth rate ($R_0\delta/D \ll 1$),

$$\frac{\Delta k_e}{k_e} \approx (1 - k_i)R_0\delta/(2D) \quad ;$$

while, for high frequency,

$$\frac{\Delta k_e}{k_e} \approx (1 - k_i)R_0/(2\sqrt{2\omega D}) \quad .$$

It should be noted that, although the analysis of Hurle, Jakeman and Pike⁵⁰ has been found to be in error (see Appendix 2), many of their basic conclusions remain valid.

Several models of non-equilibrium segregation have been suggested^{69,70,71}. Hall⁶⁹ has proposed that, due to the differences in binding energy, the equilibrium concentration in the surface layer of the crystal ($k_s C_i$) differs from that in the interior ($k_o C_i$). At high growth rates, the interior cannot attain equilibrium with the liquid and

$$k_i = k_o + (k_s - k_o)\exp(-R_i/R) \quad ,$$

where R_i is the growth rate at which one atomic layer is

grown in a time interval equal to the solute relaxation time for a single atomic layer. Trainor and Bartlett⁷⁰ have treated nonequilibrium segregation on a faceted interface on which impurity atoms have been absorbed. Their model predicts

$$k_i = k_o \left\{ 1 - \frac{2(1 - k_o \tau_s / \tau_i)}{1 + \left[1 + \frac{4D_i}{v^2} \left(\frac{1}{\tau_i} + \frac{\phi \bar{u}_i n_i}{\sigma_o} \right) \right]^{1/2}} \right\}^{-1},$$

where v is the lateral step velocity; τ_s and τ_i are the solute and solvent dwell times at the interface; D_i , \bar{u}_i , and n_i are the diffusion coefficient, the mean atomic velocity, and the atomic density of the solute; σ_o is the number of sites per unit area on the solid-liquid interface; and ϕ is a constant. Carruthers⁷¹ included the effect of interface acceleration in the expression

$$k_i = k + \frac{\delta^2}{D} \frac{\partial k}{\partial t},$$

where k is Hall's expression for k_i and $\frac{\partial k}{\partial t}$ is its time derivative due to growth rate variations.

2. Segregation Studies

Numerous investigations of segregation during crystal growth from the melt have been reported in the literature. Many early works, though carefully done, suffer from a lack of available experimental techniques with sufficient

sensitivity and resolution. Only recently have such techniques been developed and applied to quantitative segregation analysis⁴.

A classical study of segregation in Ge has been reported by Burton et al.⁷² using a combination of radioactive tracer techniques and resistivity measurements for compositional analysis. By assuming a steady growth rate, identical with the pulling rate, and using the best available values for the physical constants, their experimental data were considered in reasonable agreement with the BPS theory.

Carruthers and Benson⁷³ studied the functional dependence of compositional variations in growth striations on solute concentration in the melt, growth rate, and crystal rotation rate for P doped Si. Their results indicate the existence of non-equilibrium segregation.

Benson⁷⁴ reported a detailed investigation of radial segregation in Si crystals as a function of growth conditions. Applying the insight gained from his flow visualization experiments, Carruthers⁵⁸ attributed variations in radial segregation with solute boundary layer thickness variations caused by the interaction between thermal and forced convective flows.

An extensive series of investigations on microsegregation and interface morphology in semiconductor crystals has been reported by Witt, Gatos, and Coworkers^{4,75-81}. Studies on

dopant segregation in InSb have revealed the existence of six types of impurity striations⁷⁵, established the cause and effect relationship between temperature variations in the melt and non-rotational striations⁷⁶, and developed a theoretical expression relating variations of the microscopic growth rate (R) from its average value (R_o) to the degree of thermal asymmetry (ΔT), the vertical temperature gradient (β), and the seed rotation rate (ω_s)⁷⁷:

$$R = R_o \left(1 - \frac{\omega_s \Delta T}{R_o \beta} \cos \omega_s t \right) . \quad (23)$$

Further, a technique for microscopic growth rate determination employing vibrational rate striations⁷⁸ has been developed and utilized to study the different growth and segregation phenomena operating during facet and off-facet growth⁷⁹. A quantitative approach to the study of microsegregation, combining interface demarcation and spreading resistance measurements, has been developed and applied to segregation in Ga doped Ge for both the facet⁸⁰ and off-facet⁴ regions. Most recently this technique has been applied to the study of rotational striations in Sb doped Si crystals⁸¹ under conditions of pronounced thermal asymmetry⁸².

CHAPTER VIII

SEGREGATION BEHAVIOR IN CZOCHRALSKI
CRYSTAL GROWTH SYSTEMS

The electrical and optical properties of semiconductor materials are sensitive to chemical and structural homogeneity. Of particular importance for device production and performance is the homogeneity of resistivity in these materials which when grown from the melt depends most strongly on the dopant segregation conditions during the liquid-solid phase transformation. Moreover, with the advent of micro-electronics and the increasing tendency towards large scale integrated circuits, compositional control on both the macro and micro scale become increasingly important to device performance as well as device yield.

The most important method for the production of single crystalline semiconductor electronic materials is the Czochralski technique. However, because of the unfavorable dopant segregation characteristics associated with this technique, it is necessary for many device applications to use the material thus obtained as passive substrates and to produce the devices on epitaxially deposited layers of improved compositional homogeneity.

The primary compositional deficiencies in Czochralski grown crystals can be attributed to longitudinal and radial segregation variation on both the macro and micro scales. Longitudinal changes in macrosegregation during growth will

result whenever the diffusion distance (D/R) exceeds the established solute boundary layer thickness (δ) at the interface. Longitudinal microsegregation, on the other hand, can be attributed to temporal variations in either the growth rate (R) or the solute boundary layer thickness (δ). Sources of growth rate variations include: (1) crystal or crucible rotation in the presence of a radially asymmetric temperature distribution in the melt, (2) convective temperature fluctuations in the melt, and (3) faulty crystal pulling mechanisms; the temporal variations in solute boundary layer thickness result from unstable convective flows in the melt. Radial macrosegregation, as yet inadequately understood, is attributed to (1) a radial variation of the solute boundary layer thickness which is sensitive to the flow pattern existing in the melt, (2) the curvature of the crystal-melt interface, and (3) the presence or absence of facets at the growth interface. Radial microsegregation, on the other hand, may result from (1) longitudinal microsegregation in the presence of a curved growth interface and (2) local growth rate or solute boundary layer thickness variations resulting from instabilities of the momentum, thermal, or solute boundary layers.

An analysis indicates that the compositional variations in melt grown materials can be primarily attributed to adverse temperature distributions and associated convective flow patterns existing in crystal growth melts. It was in an

attempt to establish control over these parameters by controlling the temperature distribution at the crucible wall that a heat pipe was introduced coaxially between the crucible and the heater in a Czochralski crystal puller. Through this approach it was expected that improved thermal conditions could be established which would reduce (a) the extent of thermal asymmetry and (b) the intensity of thermal convective instabilities in the melt. Thus crystals grown in this modified Czochralski crystal growth system were expected to exhibit improved radial and longitudinal segregation characteristics.

In this chapter a comparative analysis is presented of the micro and macrosegregation behavior for a conventional and a modified Czochralski crystal growth system.

A. Crystal Growth and Characterization Procedures

This section outlines the growth and characterization procedures used in the present investigation of dopant segregation phenomena in the Czochralski system. (For details of the Czochralski growth system used see Crystal Growth System and Related Equipment in Chapter IV.)

1. Growth Procedures

a. Seed Preparation

The $\langle 111 \rangle$ oriented seed of square cross section (4.5 mm) and 4 to 5 cm in length was prepared in the following manner:

After removing the sharp edges from the "growth" end with 600 grit SiC paper, the seed was degreased with trichloroethylene and acetone and rinsed in distilled, de-ionized water (DDW). Subsequent to drying in a hot air stream, the seed was mounted in the molybdenum seed holder and etched with CP4 (see Charge Preparation in Chapter IV).

b. Seeding and Growth Procedure

Seeding was accomplished as follows: The temperature of the melt was adjusted to seeding temperature (based on previous experiments and temperature measurements). With seed rotation applied, the seed was lowered to about 1 mm above the upper melt surface. After thermal equilibration (about 15 minutes), the seed was inserted into the melt and a small portion was melted back to insure a clean (oxide-free) growth interface. After the temperature was adjusted so that the meniscus was approximately tangential to the seed, the seed was slowly withdrawn from the melt (about 1.3 mm/hr) and the crystal was grown to its desired diameter (typically 1.3 cm) by appropriate power adjustments.

At the final diameter, the pull rate was adjusted to the desired value. Because of a significant thermal inertia of the growth system (introduced into the system by the heat pipe), temperature adjustments were limited to a rate on the order of 0.01 mv (0.25°C) per minute. With this limitation, pull rate changes were made in small steps (typically 1.3 mm/hr).

The growth experiments were conducted for several combinations of seed rotation rate, pull rate, crucible rotation rate, and crucible position.

c. Interface Demarcation

Interface demarcation was employed in all growth experiments (other than those during which temperature fluctuation spectra were recorded). Current pulses (of typical characteristics: amplitude 25 amp/cm², duration 60 msec, and frequency 1 Hz) were applied across the growth interface. Interface demarcation lines were subsequently revealed by interference microscopy after high resolution etching of appropriate samples (see Sample Preparation below).

2. Crystal Characterization and Segregation Analysis

a. Sample Preparation

Crystal segments (see Figure 36) were prepared for analysis as follows: the grown crystals were cut into longitudinal sections (25x15x2 mm) parallel to the <111> growth axis with the large faces being slightly off a (211) orientation. The samples were degreased and etched in CP4 (see Charge Preparation in Chapter IV) for 10 seconds. After drying, the samples were ultrasonically soldered with In-Sn alloy (50/50) onto brass disks (diameter 3.4 cm) to achieve large ohmic back contacts. To avoid contamination during subsequent sample preparation, a thin coating of acid resistant Crystal Clear (polymer) was applied to the sample and

its mount.

After mounting, the samples were lapped successively on an optically flat glass plate with SiC (600 grit), garnet (5 μm), and alumina (3 μm) and polished with Linde A (0.3 μm alumina). The final polish with syton solution (200 ml Syton-HT, 200 ml DDW, 5 ml H_2O_2 , and 2 ml CH_3COOH) achieved a mirror finish. After thoroughly rinsing in distilled water, and while still wet, the samples were immersed for 5 seconds in the differential etchant (1 part H_2O_2 , 1 part HF, 1 part CH_3COOH). Subsequent to rinsing in distilled water, washing in soap and distilled water and thoroughly rinsing in distilled water, the samples were dried in a stream of nitrogen.

b. Microscopic Growth Rate Determination

By employing the interface demarcation technique during crystal growth, the microscopic growth rate, $R(t)$, at the time, t , was determined from the known period (T) of the applied current pulses and the measured position, $X(t)$, of the resulting demarcation lines. The distance measurements on the etched samples (see Sample Preparation above) were made with a filar eyepiece on a Zeiss Ultraphot microscope. The n^{th} demarcation line (see Figure 37) was incorporated into the crystal at the time, $t_n = nT$, and at the position, $X_n = X(t_n)$, when the microscopic growth rate was $R_n = R(t_n)$. The microscopic growth rate was determined by representing the first derivative of position with respect to time by its centered



Figure 36. Polished and etched sample mounted on a brass disk with a large ohmic back contact (see text),

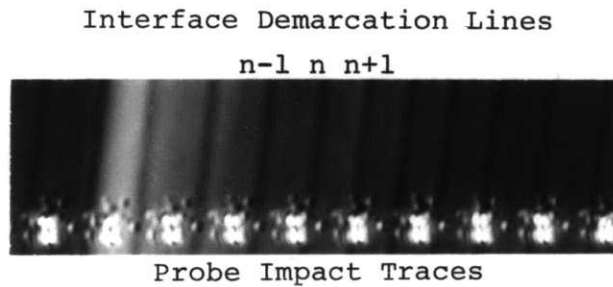


Figure 37. Impact traces of spreading resistance probe (10 μm spacings) and interface demarcation lines on a polished and etched Ge sample.

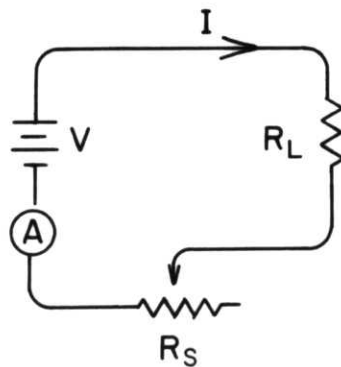


Figure 38. Schematic representation of spreading resistance measurement circuit.

finite difference (see Appendix 3)

$$R_n = (X_{n+1} - X_{n-1})/2T \quad .$$

For microsegregation analysis, the microscopic growth rate had to be known at the position (Y) where the spreading resistance was measured. Generally the probe position will be between two interface demarcation lines (such as $n - 1$ and n). Following Murgai⁸³, a constant acceleration (a_{n-1}) was assumed for positions between demarcation lines, and from kinematics⁸⁴, the growth rate at the probe position was approximated by

$$R = (R_{n-1}^2 + 2a_{n-1}(Y - X_{n-1}))^{1/2} \quad .$$

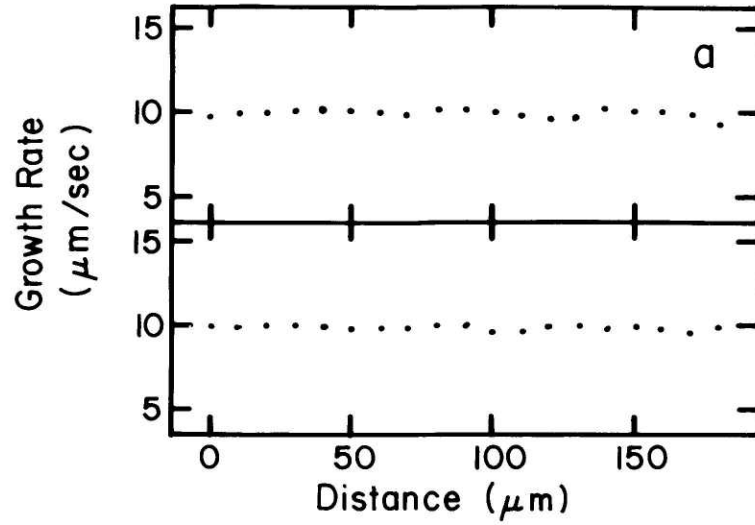
This relation correctly gives $R = R_{n-1}$ when $Y = X_{n-1}$ and, to insure that $R = R_n$ when $Y = X_n$, the acceleration was approximated by

$$a_{n-1} = (R_n^2 - R_{n-1}^2)/2(X_n - X_{n-1}) \quad .$$

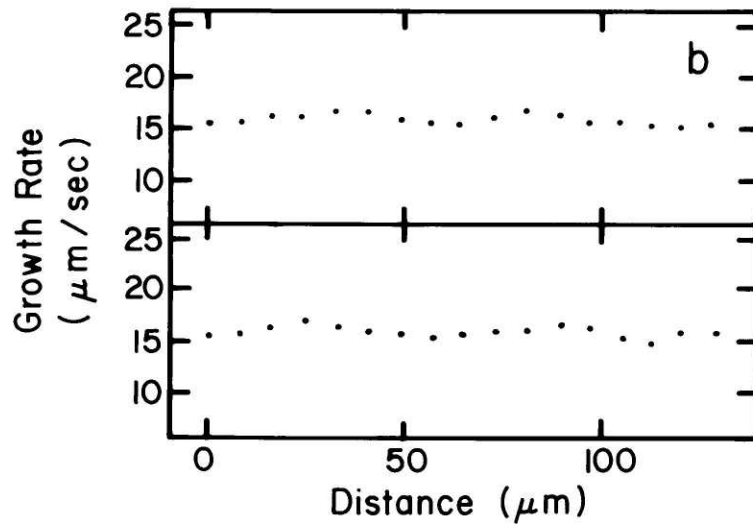
To establish the limitations of the interface demarcation technique for the study of microscopic growth rates, it is important to consider the basic approach taken. Growth interface demarcation by current pulsing results in an instantaneous segregation change across the entire interface. This segregation effect appears on the etched specimen as a

narrow band (groove) which can be detected by interference contrast microscopy. The visibility and the limits of resolution for the spacing between consecutive demarcation lines have been shown to be strongly dependent on the etching procedure and on the optimization of interference contrast through adjustment of the Wollaston prism. Moreover, the accuracy of the determination of the demarcation spacings under the microscope by means of a filar eyepiece is subject to inherent limitations. Thus, the approach taken was tested by (a) determining the maximum measurement accuracy through readings from a calibrated reticule with lines of 0.01 mm spacing and (b) determining measurement reproductivity from a small crystal segment subjected to interface demarcation during growth.

The simulated growth rate profile obtained from the calibrated reticule (see Figure 39(a)) which should yield a constant rate of 10 $\mu\text{m}/\text{sec}$ shows a relative deviation ($\Delta R/R = (R_{\text{max}} - R_{\text{min}})/(R_{\text{max}} + R_{\text{min}})$) of 5% in the upper profile and 2% in the lower profile which can be directly attributed to error in determining the demarcation line positions. While the growth rate data for two successive readings of the same interface demarcation lines in a small segment of a typical crystal grown in the modified puller (see Figure 39(b)) yield the identical average microscopic growth rate and show virtually the same fluctuations, there are distinct



(a) Accuracy test of interface demarcation line position determination. (Readings taken on a reticule with 10 μm spacing; computations used a period of 1 sec.)



(b) Reproducibility test of growth rate determination performed on a selected crystal segment.

Figure 39. Assessment of accuracy and reproducibility of microscopic growth rate determination.

quantitative differences between the two profiles which can be attributed to measurement error. The study indicates that the interface demarcation technique under the presently employed growth conditions (line spacing of about 10 μm) yields growth rate data of at best 5% accuracy.

c. Spreading Resistance Measurement

Spreading resistance measurements were made with an ASR-100 Spreading Resistance Probe in the single point configuration with a constant 10 mv bias applied across the probe and the ohmic back contact. Longitudinal spreading resistance scans (along the direction of growth) were performed with 10 μm spacings, while 50 μm spacings were used for radial scans.

The spreading resistance measurement is basically a measurement of the current (I) flowing in a circuit consisting of a constant voltage source ($v = 10 \text{ mv}$) in series with a variable point contact resistance (R_s) and a constant distributed resistance (R_L) (see Figure 38). The point contact resistance of a lapped Ge surface of moderate resistivity is essentially the spreading resistance with the contribution from the potential barrier being insignificant⁴. The distributed resistance is essentially the resistance of the current leads (0.07 ohms). Thus the total resistance (R) measured by the probe is the sum of the spreading resistance and the lead resistance

$$R = V/I = R_s + R_L \quad .$$

a. Calibration of the Spreading Resistance Probe

The spreading resistance in a material of resistivity, ρ , from a point contact of effective diameter, D , is

$$R_s = \rho/2D \quad .$$

Since the spreading resistance probe does not form an ideal point contact, D is unknown and not well defined (see Figure 37). Thus a calibration procedure must be utilized to convert spreading resistance to resistivity.

Probe calibration in the present study was performed on a Ga doped Ge standard of known resistivity and dopand concentration ($2.97 \times 10^{-3} \Omega\text{-cm}$ and $7.78 \times 10^{18}/\text{cm}^3$, respectively, as determined by Hall measurements in the Vander Pauw configuration⁸²). Spreading resistance scans at 25 μm increments were performed across the standard to determine its average spreading resistance (\bar{R}_s). From this value and the known resistivity, the effective probe diameter was determined by the relation

$$2D = 2.97 \times 10^{-3} / \bar{R}_s \quad .$$

This value was then used to convert spreading resistance to resistivity for the samples analyzed in the present study.

b. Concentration Determination

To be useful for quantitative microsegregation analysis, the spreading resistance values had to be converted to dopant (carrier) concentration values. This was accomplished in the following manner: each spreading resistance value was converted to a resistivity value (see above); the logarithm of resistivity was then converted to the logarithm of concentration by linear interpolation between corresponding known values⁸²; the antilogarithm of this value was the dopant (carrier) concentration value required.

The reproducibility of spreading resistance measurements and their sensitivity to surface treatment are shown in Figure 40. The three profiles shown were taken parallel to one another in a small region of the calibration sample. From top to bottom, these spreading resistance measurements were made as follows: (a) the sample was left unwashed (for more than 24 hours), (b) the sample was washed and dried in nitrogen, the measurement was performed after half an hour delay, and (c) the measurement was performed immediately after the sample was rewashed and dried in nitrogen. For this sequence of treatments the average apparent dopant concentration increases ($6.75 \times 10^{18}/\text{cm}^3$, $7.28 \times 10^{18}/\text{cm}^3$, and $7.79 \times 10^{18}/\text{cm}^3$, respectively), while the measurement scatter and the relative concentration deviation decreases (0.18, 0.11, and 0.07, respectively). In the results reported

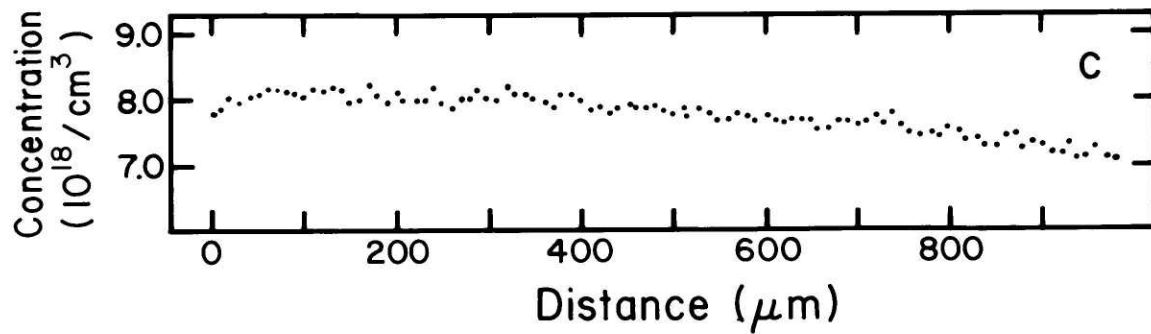
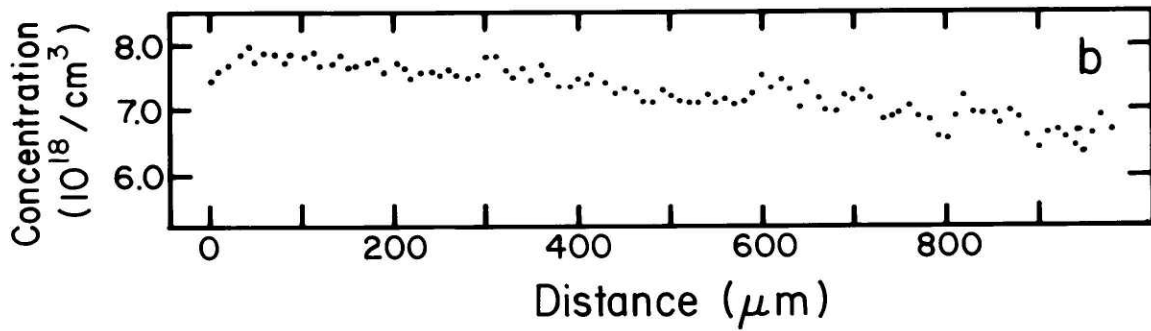
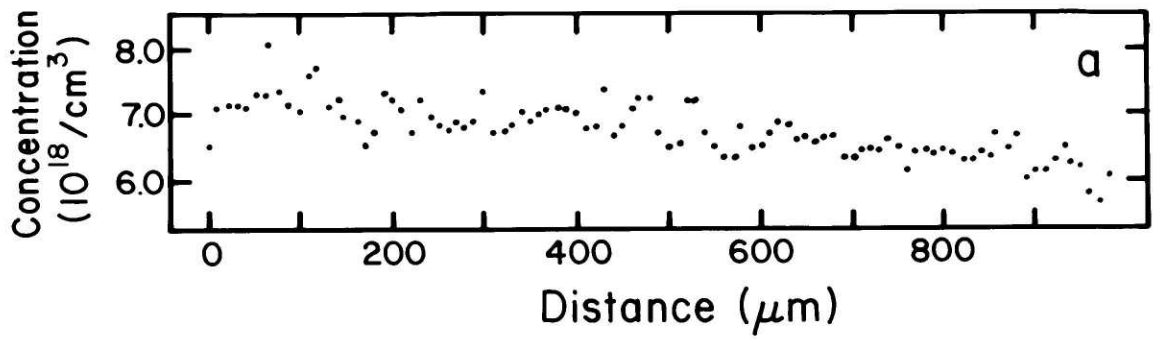


Figure 40. Effect of surface preparation on spreading resistance (Ga concentration) measurements (see text).

below, the problem of this time dependence of the measurement was eliminated and the level of measurement scatter was reduced by the application of a drop of glycerine to the sample surface after cleaning and prior to performing the spreading resistance measurements.

The sensitivity of the spreading resistance probe to concentration variations is limited as follows: The output of the spreading resistance probe is a four digit number proportional to the logarithm of the spreading resistance. A one digit change in the output (for Ge doped with Ga to $1.7 \times 10^{19}/\text{cm}^3$) corresponds to a 0.3% change in the dopant concentration and is thus the minimum change detectable. However, in addition to true concentration changes, such a change in the output signal may also be due to a surface imperfection or electrical noise.

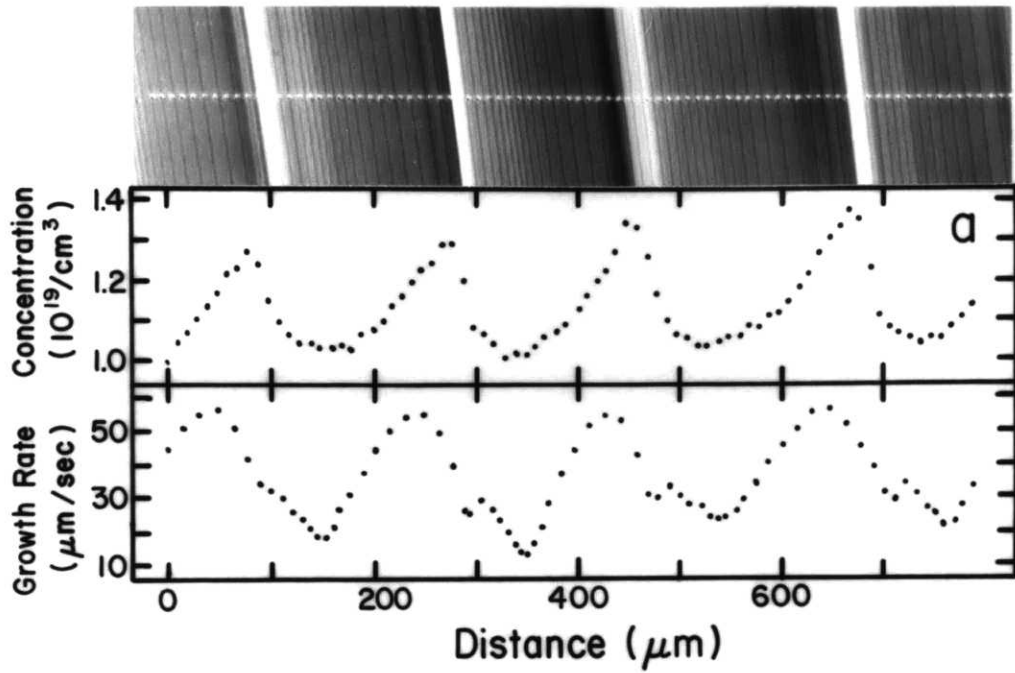
B. Comparative Segregation Analysis

This section presents a comparative segregation analysis of a representative Ga doped Ge crystal grown in a standard Czochralski system and crystals grown under similar conditions in the modified system. Longitudinal and radial segregation behavior both under conditions of crystal and crucible rotation are compared. Additional data on segregation behavior in the absence of rotation are presented for the modified system, although no sample grown under this condition in the standard system was available for comparison. The

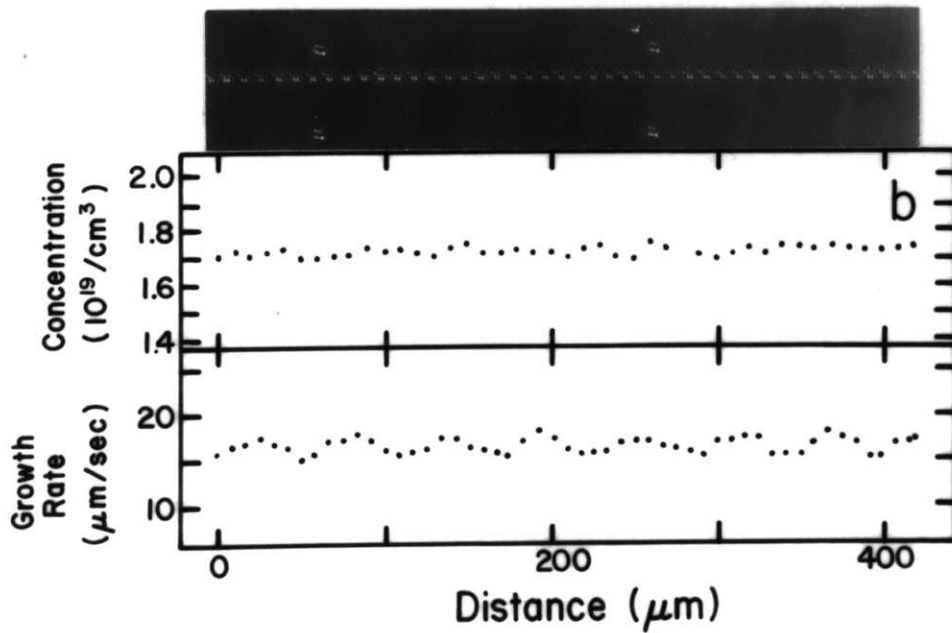
longitudinal data (see Figures 41, 43 and 45 (a)) are presented as composite figures consisting of (1) a photomicrograph of the region of interest showing the impact trace of the spreading resistance probe, the interface demarcation lines, and the contrast due to compositional heterogeneities, (2) a plot of the dopant concentration as determined from the spreading resistance measurements, and (3) a plot of the microscopic growth rate as determined from the interface demarcation lines. These data were obtained in the off-facet regions near the crystal periphery where the thermal asymmetry (ΔT) is a maximum and therefore, by the Morizane relation (Equation 23), the growth rate variations are maximum. The transverse data (see Figures 42, 44 and 45(b)) were obtained by spreading resistance measurements made across the crystal diameters and are presented as plots of dopant concentration as determined from these measurements. The average values and relative deviations of the growth rate and dopant concentration determined from these data are collected in Table 10.

1. Segregation Analysis for Growth With Crystal Rotation

The rather significant improvement of longitudinal microsegregation in crystals grown with seed rotation brought about by the presence of the coaxial heat pipe in the hot zone of the modified Czochralski system is evident in Figure 41. The sample grown in the standard system (6.14 rpm) (see Figure 41 (a)) exhibits large amplitude rotational striations (high contrast in the photomicrograph) with large relative



(a) Standard Czochralski system (6.14 rpm).



(b) Modified Czochralski system (17.1 rpm).

Figure 41. Comparison of longitudinal segregation associated with growth under crystal rotation.

deviations in the growth rate ($\Delta R/R = 0.47$) and in the dopant concentration ($\Delta C/C = 0.16$). By contrast, the crystal grown in the modified system (17.1 rpm) exhibits small amplitude ($\Delta C/C = 0.017$ and $\Delta R/R = 0.09$) rotational striations (low contrast in the photomicrograph). The significant reduction in the intensity of rotational striations for crystals grown in the modified system reflects primarily the increased thermal symmetry in the melt due to the presence of the heat pipe.

These same samples reveal pronounced differences in radial segregation on both the macro and micro scale (see Figure 42). The transverse profiles, obtained from measurements at 50 μm spacings to within 200 μm of the sample edges, provide significant information concerning "coring" associated with facet formation at the respective growth interfaces. The transition from the off-facet to the facet regions is associated with an abrupt drop in dopant concentration. Two important differences in the growth and segregation behavior can be identified. The sample grown in the standard system exhibits a relative segregation change of $\Delta C/C = 0.16$ whereas the corresponding change associated with growth in the modified system is $\Delta C/C = 0.033$. The transverse profiles indicate further a pronounced increase in the extent of growth interface facet formation for the modified growth system, which is indicative of a decreased radial temperature gradient and is consistent with the correspondingly less curved growth interface. The radial microsegregation characteristics for growth

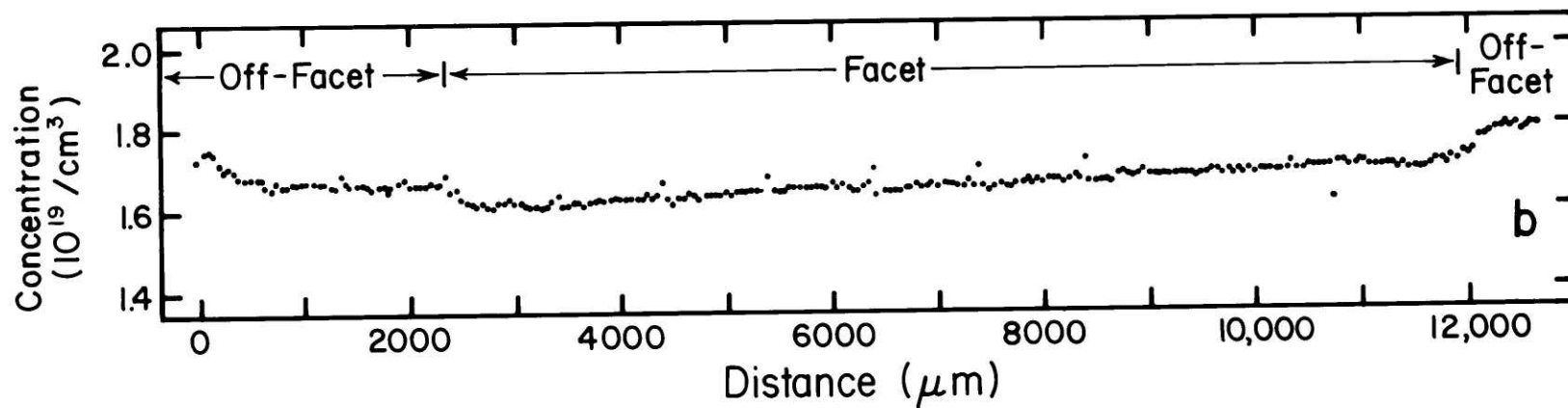
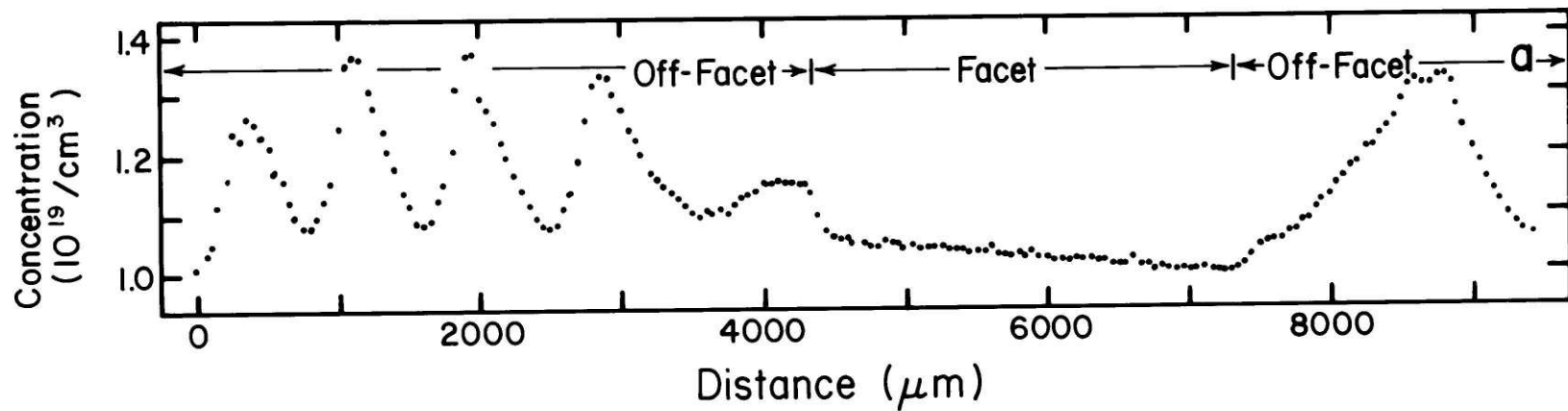


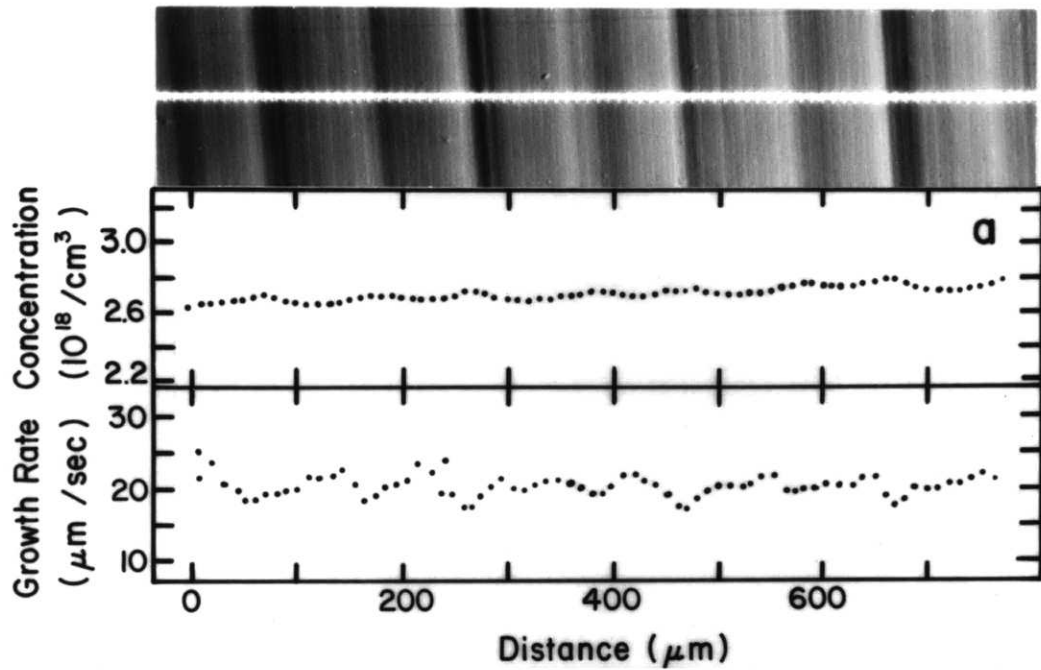
Figure 42. Comparison of radial segregation associated with growth under crystal rotation. (a) Standard Czochralski system (6.14 rpm). (b) Modified Czochralski system (17.1 rpm).

in conventional Czochralski systems must, on the basis of the present results, be attributed to the interaction of (a) the extensive longitudinal microsegregation inhomogeneity and (b) a pronounced curvature of the growth interface.

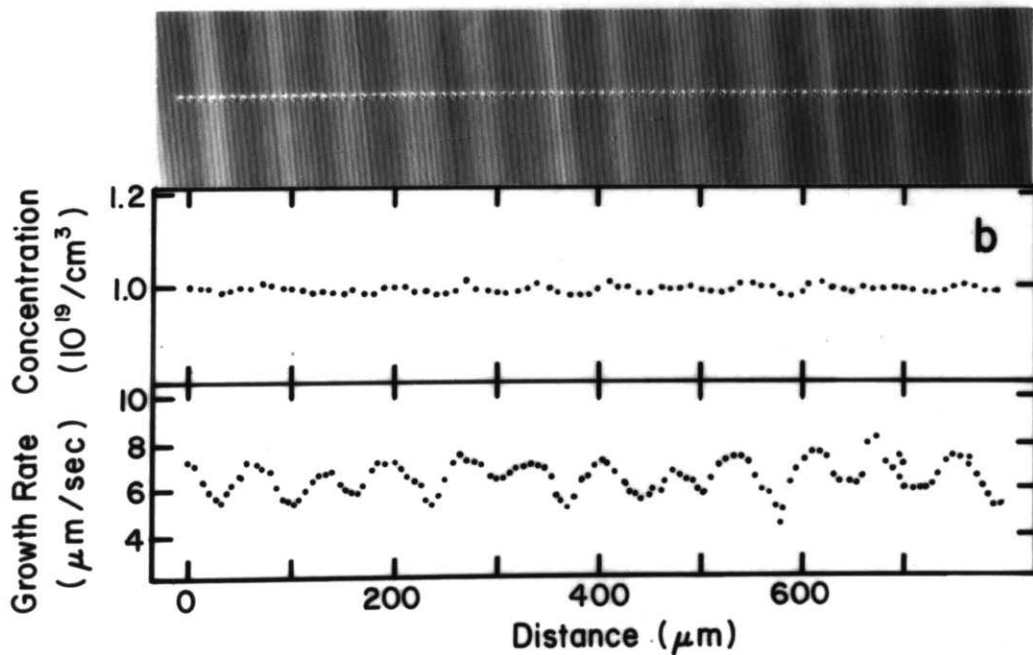
2. Segregation Analysis for Growth With Crucible Rotation

Figure 43 shows that longitudinal microsegregation during growth with crucible rotation is less affected by the heat pipe than growth with seed rotation. The measurements indicate that in both systems crucible rotation leads to small amplitude rotational striations which can be attributed to growth rate variations. For growth in the conventional system (5.78 rpm) $\Delta R/R = 0.15$ and $\Delta C/C = 0.033$, whereas in the modified system (6.0 rpm) $\Delta R/R = 0.29$, and $\Delta C/C = 0.017$.

Thus, while the amplitude of longitudinal microsegregation variations under conditions of crucible rotation is only slightly reduced by the modification of the hot zone, it is evident that the magnitude of such variations is significantly less for crucible rotation than for seed rotation. This pronounced reduction in the amplitude of rotational striations during growth with crucible rotation is attributed to an increase in the thermal symmetry associated with crucible rotation. Thus, it is apparent that the thermal asymmetry of the hot zone in the conventional puller is significantly greater than that in the modified system, since the reduction of the amplitude of rotational



(a) Standard Czochralski system (5.78 rpm).



(b) Modified Czochralski system (6.00 rpm).

Figure 43. Comparison of longitudinal segregation associated with growth under crucible rotation.

striations in changing from crystal to crucible rotation is greater for the conventional than for the modified system.

A comparison of radial segregation behavior of the two samples discussed above is shown in Figure 44. It can be seen that both samples exhibit considerable radial macrosegregation; $\Delta C/C = 0.088$ for the sample grown in the conventional system and $\Delta C/C = 0.041$ for the sample grown in the modified puller. While the crystal grown in the modified puller shows less radial macrosegregation than that grown in the standard puller, it exhibits more pronounced radial microsegregation. The major changes in radial composition in the crystal grown in the modified system occur at the off-facet to facet transitions (at 2000 μm and 6500 μm in Figure 44 (b)) which are not present in the crystal grown in the conventional system. The appearance of a central dopant concentration maximum in both crystals is consistent with an increase in the solute boundary layer thickness at the crystal centers where the forced convective flows (generated by crucible rotation) are expected to exhibit a stagnation point⁵⁹.

3. Segregation in the Modified Growth System Without Rotation

The segregation behavior of crystals grown in the modified Czochralski system without seed or crucible rotation are subject only to the influence of the thermal convective

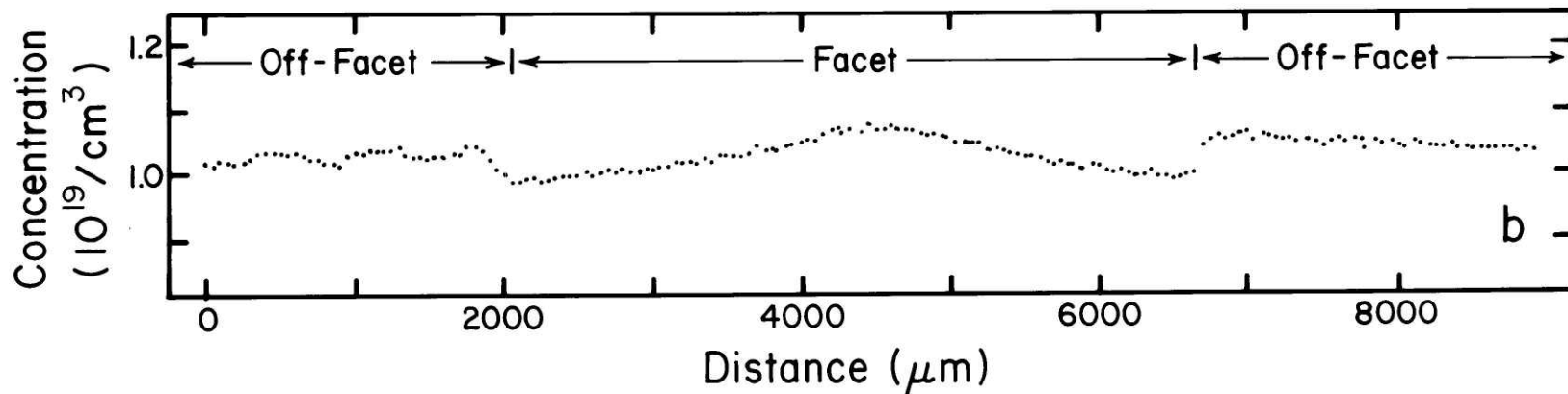
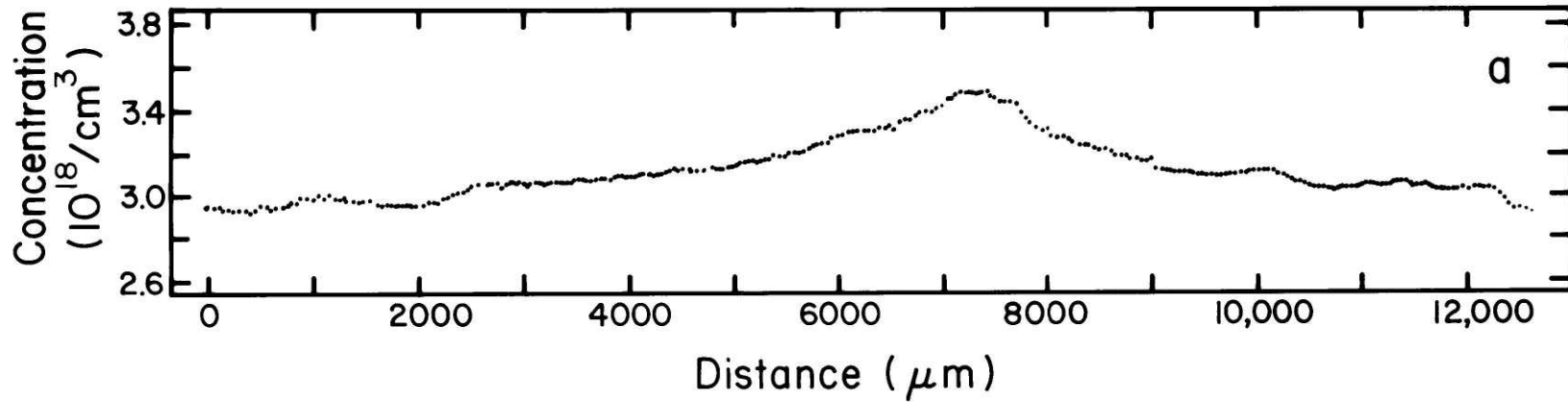


Figure 44. Comparison of radial segregation associated with growth under crucible rotation. (a) Standard Czochralski system (5.78 rpm). (b) Modified Czochralski system (6.00 rpm).

flows within the melt. The longitudinal segregation behavior (see Figure 45 (a)) reveals small random variations of composition ($\Delta C/C = 0.020$) and growth rate ($\Delta R/R = 0.19$) with an average period of 5.8 sec. The source of the observed growth rate variations is most likely the thermal convective instabilities in the melt (the longest dominant period of which was 6.0 sec), however pulling irregularities cannot be ruled out at this time.

The radial segregation behavior in the sample discussed above (see Figure 45 (b)) is quite similar to that found in the modified system under crucible rotation conditions. However, without rotation the concentration profile exhibits a slightly higher relative deviation ($\Delta C/C = 0.048$). The central concentration maximum again suggests a thickening of the solute boundary layer near the crystal center which is consistent with the existence of an axisymmetric toroidal thermal convection roll within the melt, as computed in Chapter VI and observed by Carruthers⁵⁸, with a stagnation point at the center of the growth interface.

In summary, the installation of a coaxial heat pipe within the hot zone of a Czochralski crystal growth system results in a marked improvement of its segregation behavior as shown in Table 10. The amplitude of longitudinal micro-segregation has thus been reduced to a level below two percent of the average concentration for all conditions investigated. Even more significant from the point of view

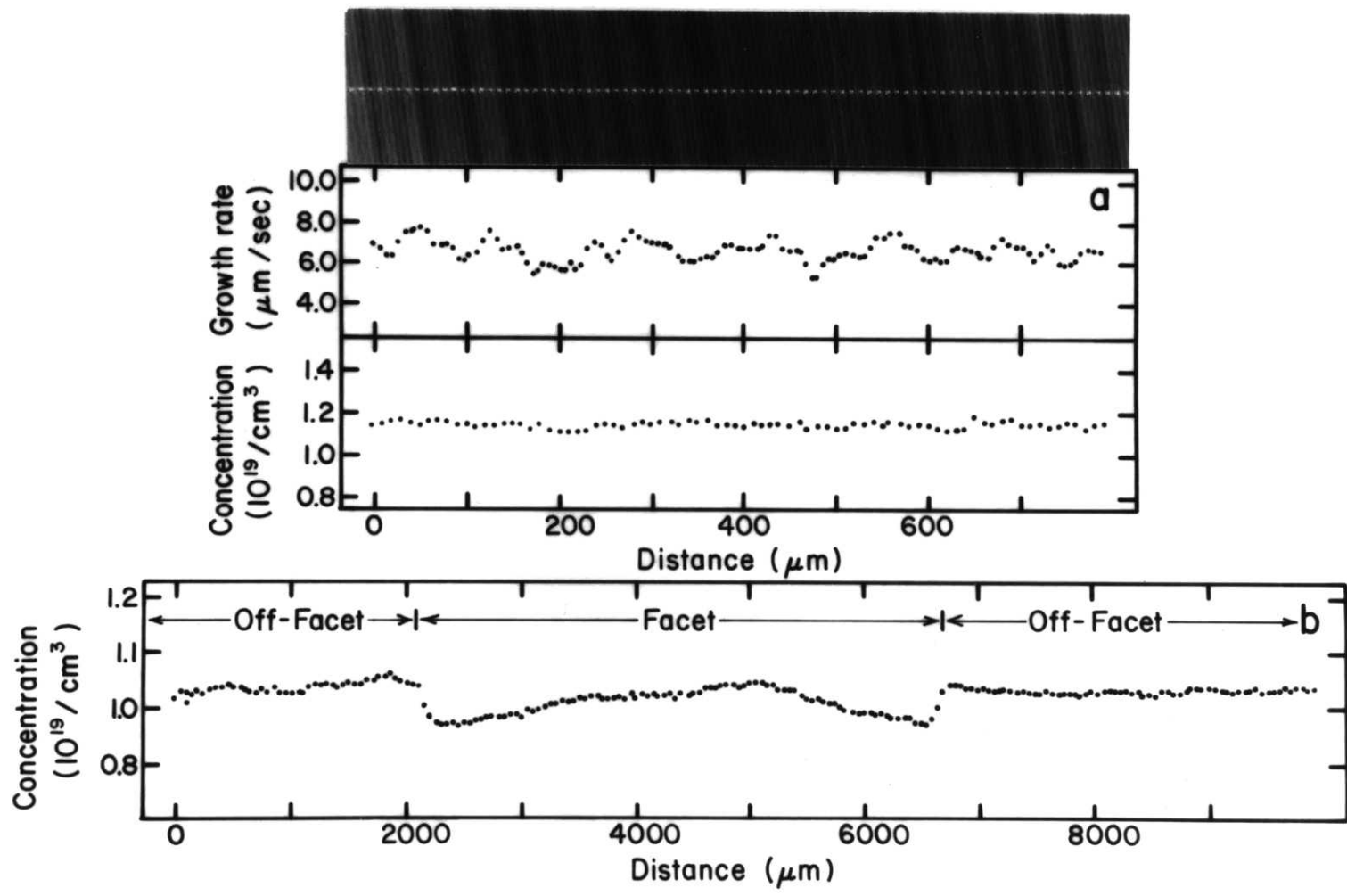


Figure 45. Segregation in modified Czochralski system associated with growth in the absence of rotation. (a) Longitudinal segregation. (b) Radial segregation.

TABLE 10

SUMMARY OF COMPARATIVE SEGREGATION BEHAVIOR

	<u>Longitudinal Segregation</u>				<u>Radial Segregation</u>	
	<u>R</u>	<u>$\Delta R/R$</u>	<u>C</u>	<u>$\Delta C/C$</u>	<u>C</u>	<u>$\Delta C/C$</u>
	(μ/sec)	(%)	($10^{19}/\text{cm}^3$)	(%)	($10^{19}/\text{cm}^3$)	(%)
Crystal Rotation						
Standard System (6.14 rpm)	22.4	0.47	1.14	0.160	1.13	0.160
Modified System (17.1 rpm)	16.8	0.09	1.73	0.017	1.67	0.033
Crucible Rotation						
Standard System (5.78 rpm)	20.7	0.15	0.273	0.033	0.313	0.088
Modified System (6.0 rpm)	6.55	0.29	0.999	0.017	1.03	0.041
No Rotation						
Standard System	--	--	--	--	--	--
Modified System	6.82	0.19	0.975	0.020	1.03	0.048

of semiconductor device applications is the marked reduction in radial segregation to the three percent level under conditions of crystal rotation in the modified thermal environment.

CHAPTER IX

DISCUSSION OF CONVECTION AND
ITS EFFECTS ON SEGREGATION

This chapter presents a discussion and analysis of convection and its effects on dopant segregation during Czochralski crystal growth. The results of the preceding analyses of thermal convection and of growth and segregation in the modified Czochralski system are interrelated and the pertinent cause and effect relationships established. The analysis focuses on the following topics: a determination of the segregation controlling mode of convection by comparing solute boundary layer thicknesses and fluid flow rates, an investigation of the mechanisms of convective temperature fluctuations, and a study of the correlation of growth rate variations with convective instabilities and seed rotation.

A. Solute Boundary Layer Thickness

As previously discussed (see Chapter VII), when the equilibrium distribution coefficient is small ($k_0 < 1$), a layer of increased dopant concentration is established ahead of the crystal-melt interface after the onset of crystal growth. Whenever (as under the present growth conditions) the thickness (δ) of this solute boundary layer is less than the diffusion length (D/R) (where D is the solute diffusion coefficient of the melt and R is the growth rate), the

segregation process at the growth interface is affected by the convective melt flows. Under these conditions, δ may be used as a tool for assessing which mode of convective flow is dominant in controlling the segregation process. The analysis proceeds as follows; (1) A value of δ is determined for each convective mode. (2) If the value of δ for one mode is significantly smaller than those calculated for all other convective modes, then that mode will dominate the mass transfer process at the growth interface.

For the Czochralski growth of low Prandtl number electronic materials, the common melt flows include; thermal convection flows driven by horizontal and vertical temperature (density) gradients and forced convection flows driven by crystal and/or crucible rotation. In low temperature crystal growth systems (Te doped InSb) it has been possible (even at low rotation rates) to establish growth conditions under which forced convection dominates the segregation process at the growth interface, while in high temperature systems (Sb doped Si) under all growth conditions the dominant mode is thermal convection (with the exception of the work reported by Murgai et al.⁸⁶). As yet, the dominant mode of convective flow in moderate temperature systems (Ga doped Ge) has not been unambiguously determined.

In this section values of δ computed by several methods are compared to determine whether thermal convection

or forced convection dominates the segregation process during solidification of Ga doped Ge with crystal rotation (17.1 rpm) in the modified Czochralski system. The values of δ are determined by three experimental estimates which are independent of the convective mode and two theoretical estimates which depend on the dominant mode of convection in the melt.

Assuming the BPS relation (Equation 21) is applicable to segregation during Czochralski pulling and making use of the definition of the effective distribution coefficient (Equation 20), an experimental estimate of the solute boundary layer thickness (δ) may be obtained from the BPS relation in its modified form:

$$\delta = \left(\frac{D}{R}\right) \left\{ \ln \left(\frac{1}{k_0} - 1 \right) - \ln \left(\frac{1}{(C_s/C_1)} \right) \right\} , \quad (24)$$

where C_s is the solute concentration being incorporated into the solid phase and C_1 is the concentration of dopant in the bulk melt outside the solute boundary layer. The use of this approach in earlier studies was associated with a very high degree of uncertainty since no microscopic growth rate data were available prior to the establishment of the growth interface demarcation technique and R had to be identified with the average macroscopic rate of growth. This approximation, while acceptable under the growth conditions presently established in the modified Czochralski configuration, must be considered as unacceptable for conventional

growth systems where during growth with seed rotation in an asymmetric thermal environment, the instantaneous microscopic rate of growth is subjected to continuous variations and may assume average values which are by a factor of up to 10 larger than the average macroscopic growth rate⁷⁸. Moreover, earlier attempts to compute δ were complicated by the necessity of determining C_1 which, in principle, may be obtained through the normal freezing equation

$$C_1 = C_0 (1 - f)^{-(1-k_e)}, \quad (25)$$

where f is the fraction of the melt solidified at the point where C_s and δ are to be determined and C_0 is the original dopant concentration in the melt. Because of excessive radial segregation variations the value of C_1 thus computed (through longitudinal resistivity scans) is, for conventional growth systems, associated with a significant error and the δ value computed is by necessity erroneous. Again the presently modified growth system provides for growth with virtually negligible radial segregation and the application of the normal freezing equation (25) becomes justifiable.

While the modified hot zone configuration (for improved growth conditions) and interface demarcation during growth (for microscopic growth rate determination) make it possible to optimize the indicated approach, computation of the solute boundary layer thickness is still associated with significant

errors. The evaporative loss of Ga during melt down which at present can only be approximately determined, requires adjustment of C_0 on the basis of a wet chemical analysis of the charge remaining after the growth experiment. Moreover, the diffusion constant of Ga has, as yet, not been determined with adequate precision and the presently selected value ($1.9 \times 10^{-4} \text{ cm}^2/\text{sec}$), while taken as the most reliable, cannot be considered as precise. Finally, the generally accepted value of k_0 (0.087) must according to most recent measurements be considered as uncertain and may be in excess of 0.1⁸⁷.

In addition to the procedure outlined above, two other experimental estimates of the solute boundary layer thickness may be obtained as follows: The solute boundary layer thickness may be obtained by assuming that a differential form of the steady state BPS relation (Equation 21) is applicable to the small amplitude compositional and growth rate fluctuations encountered in the modified Czochralski system. The expression thus developed is

$$\delta = (D/R) \left(\frac{1}{1 - k_0} \right) (\Delta C/C) / (\Delta R/R) \quad , \quad (26)$$

which applies (as under the present growth conditions) so long as $R\delta/D \ll 1$. The solute boundary layer thickness may also be obtained through the relationships between the respective thicknesses of the solute (δ), thermal (δ_T) and momentum (δ_m) boundary layers: $\delta = (D/\nu)^{1/3} \delta_m$ when

$\delta < \delta_m$ and $\delta_T = (\kappa/\nu)^{1/2} \delta_m$ when $\delta_T > \delta_m$, where ν is the kinematic viscosity of the melt and κ is its thermal diffusivity. Thus, the solute boundary layer thickness may be estimated from the thermal boundary layer thickness according to the relation

$$\delta = D^{1/3} \nu^{1/2} \kappa^{-1/2} \delta_T \quad . \quad (27)$$

The theoretical solute boundary layer thickness due to forced convection (crystal rotation) may be obtained from the low rotation rate form of the Cochran relation (Equation 22)

$$\delta = 1.6 D^{1/3} \nu^{1/6} \omega^{-1/2} \quad . \quad (28)$$

This relationship was developed by Burton, Prim and Slichter⁶⁷ based on Cochran's analysis⁵⁵. It should be pointed out, however, that Cochran considered the convective flow produced by a rigid, flat disk of infinite lateral extent in a semi-infinite fluid and in the absence of any additional driving forces. Thus, the BPS treatment neglects such effects as fluid confinement in a finite crucible, the finiteness of the crystal radius, the curvature of the growth interface, and the ability of the interface to change morphology in response to convective stimuli. It also neglects the affects of the meniscus column attached to the crystal perimeter and the influence of thermal convective melt flows,

Furthermore, Burton, Prim and Slichter neglected all terms in Cochran's expression for the vertical velocity component larger than second order, which requires that the Schmidt number ($Sc = \nu/D$) be large ($Sc > 64$), whereas for Ga doped Ge the Schmidt number is small ($Sc = 7.4$).

The value of the solute boundary layer thickness due to thermal convection is estimated as follows: The radial velocity (v_r) at the edge of the Cochran momentum boundary layer and the half radius ($R_{1/2}$) position is determined from the numerical solution (see the next section below). By assuming the expression for the momentum boundary layer on a flat plate is valid

$$\delta_m = R_{1/2} / (R_{1/2} v_r / \nu)^{1/2} ,$$

the solute boundary layer thickness can be computed according to the relation

$$\delta = D^{1/2} \nu^{1/6} R_{1/2}^{1/2} v_r^{-1/2} . \quad (29)$$

This estimate the solute boundary layer thickness due to thermal convection is of questionable accuracy since the numerical computations were performed without a crystal contacting the melt and the expression for the momentum boundary layer thickness on a flat plate is not strictly applicable. However, it is believed that this approach should yield a useful order of magnitude estimate for the solute boundary

layer thickness due to thermal convection.

The estimates of the solute boundary layer thickness for the sample grown with crystal rotation (17.1 rpm) in the modified Czochralski system based on the approaches outlined above are collected in Table 11. In the light of the error estimates discussed above and in Appendix 5, all values must be considered as in excellent agreement. Conspicuous in Table 11 is the fact that the boundary layer thickness associated with thermal convection (Equation 29) is virtually the same as that for forced convection (Equation 28) and both are in agreement with two experimental values determined by segregation analysis based on the BPS theory. Only the estimate based on the measured thermal boundary layer thickness differs from these, but still is of an acceptable order of magnitude. Thus for the present growth conditions, both forced convection (due to crystal rotation) and thermal convection (due to density gradients) are important in determining the thickness of the segregation controlling solute boundary layer.

TABLE 11

Computed values of the Solute Boundary Layer Thickness for a Ga Doped Ge Crystal Grown With Seed Rotation (17.1 rpm) in the Modified Czochralski Crystal Growth System

Computation Method	Solute Boundary Layer Thickness (cm)
Equation (24)	0.020
Equation (26)	0.023
Equation (27)	0.013
Equation (28)	0.023
Equation (29)	0.021

This finding explains why the segregation behavior in Ge melt systems is intermediate between that in low melting point systems (InSb) and high melting point systems (Si). Furthermore, it explains the observation that in some published work seed rotation is considered effective in suppressing time-dependent thermal convection effects, while in others this approach is considered as ineffective.

Under the presently discussed conditions thermal convective perturbations in the melt are expected to affect dopant segregation during crystal growth through the response of the solute boundary layer thickness to the melt flow rate variations, and through temperature fluctuation induced growth rate variations. Making use of the modified BPS relation (Equation 24), the concentration and growth rate data

presented in Figure 41, revealed considerable relative deviation in the solute boundary layer thickness ($\Delta\delta/\delta = 0.12$). Further evidence for the existence of solute boundary layer variations in the modified system lies in the poor correlation of growth rate and concentration profiles shown in Figures 41(b), 43(b), and 45(a). It was in the light of these observations that the analysis of Hurle, Jakeman and Pike⁵⁰ was extended to include temporal solute boundary layer variations (see Appendix 2), however, as yet, accurate numerical results for this model have not been achieved.

B. Fluid Flow Rates

In the preceding section, the relative importance of forced and thermal convection in controlling segregation phenomena in the modified Czochralski system was analyzed on the basis of the solute boundary layer thickness. However, the thickness of this region of enriched dopant concentration is a direct consequence of the rate of convective melt flow in the vicinity of crystal-melt interface. Thus additional insight into the relative importance of the various convective modes in determining segregation behavior may be achieved through a direct comparison of the fluid velocities associated with each mode. The mode for which the rate of flow near the growth interface is largest dominates the mass transfer process. In this section the relative importance of forced and thermal convection in controlling segregation in the

modified Czochralski growth system is reanalyzed on the basis of their respective fluid flow rates.

The flow velocities to be compared in the present analysis are the vertical component (v_z) along the rotation axis and the radial component (v_r) at the half radius position ($R_{1/2}$); both components were evaluated at the edge of the Cochran momentum boundary layer ($\delta_m = 3.5 \nu^{1/2} \omega^{-1/2}$), where Cochran's vertical component reaches 80% of its asymptotic value. Along the axis the only non-zero velocity component is the vertical component and the direction of forced convection flow (due to crystal rotation) is opposite to that of thermal convection (due to temperature gradients). At the half radius position fluid flowing under the influence of forced or thermal convection will have travelled equal distances along the growth interface. The edge of the Cochran momentum boundary layer (δ_m) is far enough away from the growth interface to be consistent with the spatial resolution of the numerical solution and to minimize the influence of the free surface boundary condition used in this solution and yet is close enough to the interface to be meaningful in assessing the relative affects of thermal and forced convection on segregation phenomena.

The forced convective flow rates were determined from the Cochran analysis⁵⁵ of flow near an infinite rotating disk in contact with a semi-infinite fluid according to the relations:

$$v_z = (\nu\omega)^{1/2} H$$

$$v_r = R_{1/2} \omega F \quad ,$$

where the dimensionless velocities $H(= 0.800)$ and $F(= 0.038)$ were evaluated at the edge of the Cochran momentum boundary layer. (The limitations on applying the Cochran analysis to the Czochralski system were already discussed in the preceding section.)

The rates of thermal convective flow were determined from the numerical solution of thermal convection in the modified Czochralski system without a seed crystal contacting the melt. The required dimensional components of the flow velocity were computed according to the relations

$$v_z = (\nu/R_c) \left(-\frac{1}{r} \frac{\partial \psi}{\partial r} \right) \quad r = 0 \quad , \quad z = \delta_m/R_c$$

$$v_r = (\nu/R_c) \left(\frac{1}{r} \frac{\partial \psi}{\partial z} \right) \quad r = R_{1/2}/R_c \quad , \quad z = \delta_m/R_c$$

(the term in the first set of parentheses dimensionalizes the dimensionless components computed in the second set of parentheses, R_c is the crucible radius and the dimensionless quantities r , z , and ψ are the radial coordinate, axial coordinate, and stream function, respectively.)

The primary limitation in using the numerical solution

for assessing the flow rate due to thermal convection during crystal growth is its use of a stress free boundary condition over the entire melt surface. The effect of employing the more precise rigid boundary condition at the growth interface is, however, ambiguous. This is so because the presence of a rigid surface will retard the horizontal components of the flow through the action of viscous shear, while the presence of a crystal is expected to increase the radial temperature gradient near the crystal periphery and hence accelerate the radial fluid velocity component. Thus it is likely that the calculated rates of thermal convective flow will be of correct order of magnitude.

The above contention is further supported by the results of two runs of the computer program in two-dimensional rectangular coordinates which were used to simulate thermal convective flow in the Czochralski system. These runs employed the same thermal boundary conditions, however, the first run used a free surface boundary condition, while the second employed a rigid boundary condition at the crystal-melt interface. While the Grashof number employed ($Gr = 3600$) was unrealistically low, both solutions showed the same general flow patterns and the magnitude of the flow rates below the crystal were comparable.

The vertical and radial components of the fluid velocities for thermal and forced convection during crystal growth

with seed rotation (17.1 rpm) in the modified Czochralski system have been computed in accordance with the approach outlined above and are compiled in Table 12.

TABLE 12

Fluid Velocities Due to Thermal and Forced Convection in the Modified Czochralski Crystal Growth System

Mode of Convection	Radial Velocity (cm/sec)	Vertical Velocity (cm/sec)
Thermal Convection	0.266	0.094
Forced Convection	0.026	0.040

It can be seen that the vertical velocity component for thermal convection is double that due to forced convection, while the radial component is an order of magnitude larger for thermal convection. In the light of the limitations of this approach discussed above, these results must be viewed as preliminary and incomplete. However, this comparison does serve to further strengthen the contention that both thermal and forced convective flows affect solute incorporation during Czochralski type crystal growth.

C. Sources of Convective Instabilities

The preceding sections have established the importance of thermal convection in affecting segregation phenomena

during solidification of Ga doped Ge in the modified Czochralski crystal growth system. Furthermore, the existence of solute boundary layer thickness variations and melt temperature fluctuations could be attributed to convective oscillations in the melt. Insight into the mechanisms of convective instability operating within these low Prandtl number melts can be achieved through a comparison of the average periods of the measured temperature fluctuations with the periods predicted by the models of convective temperature oscillations recently reviewed by Carruthers⁷.

1. Models for Convective Temperature Oscillations

The mechanisms of convective instability likely to be operating in crystal growth melts are: (a) convective roll instabilities, (b) thermal boundary layer instabilities, and (c) momentum boundary layer instabilities.

Busse¹⁶ has considered the stability of convective rolls in fluid layers heated from below. Accordingly, instability sets in as a transverse wave oscillation in which the basic roll pattern is shifted perpendicular to its axis in the same manner as a wave propagates along a rope. For a fluid layer of thickness, h , and thermal diffusivity, κ , with free surfaces and infinite lateral extent, the oscillation period of convective rolls with spacing $\sqrt{2}h$ is given by

$$\tau_R = 0.65 (h^2/\kappa) [(Ra - Ra^C)/Ra^C]^{-1/2}$$

where Ra is the Rayleigh number and Ra^C is its critical value. For completely confined fluid layers, this expression should be multiplied by the factor $D/(n\pi h)$ where n is an integer and D is the largest horizontal dimension. In the present work, D is the crucible diameter and n is assumed to be unity so the confinement factor becomes $2/(\pi A)$, where $A = 2h/D$ is the aspect ratio.

A second form of convective roll instability considered by Carruthers⁷ is that of internal gravity wave generation for which the period of oscillation is

$$\tau_G = 2\sqrt{2Dh} (\kappa\nu)^{-1/2} (Ra)^{-1/2} ,$$

where ν is the kinematic viscosity of the fluid.

The instability of the thermal boundary layer in fluids heated from below may take the form of either thermals or plumes. Thermals¹⁵ are generated at the horizontal surfaces when the thermal boundary layer locally becomes gravitationally unstable and emits a "blob" of fluid which reduces the thickness of the thermal boundary layer and momentarily restores it to local stability. Plumes are vertical buoyant jets of fluid which are generated at localized sources of heat and develop instabilities as they rise (a typical example is the instability of a column of smoke rising from a lighted cigarette). The expression developed by Carruthers⁷ for the period of temperature oscillations associated with

thermals is

$$\tau_T = 32 (h^2/\kappa) (Ra)^{-2/3} ,$$

and that for plumes is

$$\tau_P = 77 (h^2/\kappa) (Ra)^{-1} .$$

The periodic release of momentum by a momentum boundary layer adjacent to an isothermal vertical wall has been treated by analogy to the periodic release of thermals by a thermal boundary layer⁷. The period for this boundary layer separation phenomenon is

$$\tau_M = 114 (h^2/\nu) (Gr^*)^{-2/3}$$

where Gr^* is the Grashof number based on the melt height and the horizontal temperature difference ΔT_H between the isothermal vertical wall and the bulk fluid. This mode of instability will set in when the condition $Gr^* > 8 \times 10^5$ is satisfied.

2. Comparison of Theoretical and Experimental Periods

The models presented above have been evaluated for the system presently investigated and the measured and calculated periods have been compiled in Tables 13 and 14. It should be mentioned that these models were developed for idealized situations such as unidirectional heat flow, isothermal walls,

TABLE 13

MEASURED AND COMPUTED PERIODS OF CONVECTIVE
TEMPERATURE OSCILLATIONS

<u>Crucible Position</u>	<u>Profile</u>	$\frac{h}{(\text{cm})}$	$\frac{\Delta T}{(^{\circ}\text{C})}$	Ra	Ra^{C}	Calculated Period (sec)				Measured Period (sec)	
						τ_{R}	τ_{G}	τ_{T}	τ_{P}	τ_{1}	τ_{1}
L	L2	1.6	11.0	1.76×10^4	910	1.18	6.37	0.60	0.05	1.4-1.6	6
	L3	1.6	17.5	2.80×10^4	910	0.99	5.05	0.44	0.03	--	-
M	M1	1.6	15.0	2.40×10^4	910	1.00	5.46	0.48	0.04	0.8-1.9	2.0-2.2
H	H6	1.55	7.0	1.02×10^4	910	1.48	8.11	0.80	0.09	6.6	2.2
	H10	1.6	15.0	2.40×10^4	910	1.00	5.46	0.48	0.04	--	-

TABLE 14

COMPUTED PERIODS FOR MOMENTUM
BOUNDARY LAYER INSTABILITY

<u>Crucible Position</u>	<u>Vertical Thermocouple Position (cm)</u>	<u>ΔT ($^{\circ}C$)</u>	<u>Gr*</u>	<u>τ_M (sec)</u>
H	0.9	6.0	1.44×10^6	16.4
M	0.9	1.2	2.88×10^5	--
-	--	--	8×10^5	24.2

and unbounded fluids. While the exact expressions for the periods of convective oscillations developed for these models are not expected to carry over to the more complex Czochralski geometry, it is anticipated that their orders of magnitude should be maintained.

The vertical temperature differences necessary to compute the Rayleigh numbers were extracted from the axial temperature profiles (presented in Chapter V) as follows. For temperature profiles measured with the S-type thermocouple probe, the surface temperature was estimated by linear extrapolation of the bulk temperature profile to the surface; for temperature profile measurements with an H-type probe, the bottom temperature was determined by linear extrapolation of the bulk temperature profile to the crucible bottom. The temperature differences thus determined are likely to be several degrees too large in the latter case and several degrees too small in the former. The horizontal temperature difference required to compute the Grashof number was determined from the horizontal temperature profiles by a similar procedure.

The value of the critical Rayleigh number ($Ra^C = 910$) employed in the present calculation of the period for convective roll instabilities (τ_R) was estimated in the following manner. From the plot of critical Rayleigh number vs. aspect ratio for confined fluids heated from below, (see Figure 4 in Reference 5) the ratio of the values of the critical

Rayleigh number at aspect ratio (depth over width) of 0,5 to those for corresponding layers of infinite lateral extent were determined for conducting and for insulating horizontal surfaces. The average of these ratios (1.34) was multiplied by the critical Rayleigh number (669) for a heated layer of infinite extent contained between an insulating and free upper surface and a conducting and rigid lower surface (see Table 1) to determine the presently used value of the critical Rayleigh number.

Though some of the measured periods were obtained during crystal growth, all of the calculated periods were determined from measurements made prior to the initiation of growth. During growth the temperature difference is expected to decrease by a small amount, with a larger decrease occurring in the melt height⁴². Both these changes have the effect of reducing the oscillation periods; thus, the calculated periods in Table 13 are considered as overestimates.

A comparison of the calculated and measured periods of convective temperature oscillations listed in Tables 13 and 14 suggests the following conclusions. It is clear that the mechanisms operating in these melts to produce convective temperature fluctuations do not include plume or momentum boundary layer instabilities. The longer period component (τ_2) of the measured temperature fluctuations is bracketed by the two forms of convective roll oscillations, with the period calculated for transverse wave oscillation being

closer to the measured period in most cases. The shorter period component (τ_1) of the measured fluctuations may be attributed either to the generation of thermals or to a higher order ($n > 1$) transverse wave instability.

The data obtained suggest that the convective temperature fluctuations observed in the modified Czochralski system are produced by convective roll oscillations. While the mechanism of thermal boundary layer instability (generation of thermals) may be operating to produce the higher frequency components, it is evident that the other forms of boundary layer instability do not operate in this system.

D. Correlation of Growth Rate Variations With Convective Temperature Fluctuations and Crystal and Crucible Rotation Rate

The microscopic growth rate is a sensitive indicator of the nature of the thermal environment in the vicinity of the solid-liquid interface during crystal growth. Under steady thermal conditions the growth rate will have the constant value required to balance the amount of latent heat liberated at the growth interface with the conductive heat flows to the interface through the thermal boundary layer in the melt and away from the interface into the solid phase. During melt growth the crystal-melt interface generally does not "see" a steady thermal environment but instead is subjected to transient thermal conditions. In response to these transients the microscopic growth rate undergoes the temporal

variations required to maintain a dynamic energy balance at the growth interface.

The growth rate variations generally observed in Czochralski grown crystals fall into two main categories⁷⁵: (1) rotational growth rate variations and (2) non-rotational variations. The rotational growth rate variations result when a crystal is grown with seed or crucible rotation and either the melt temperature distribution is asymmetric or the thermal center of symmetry and the rotational axis do not coincide. The sources of non-rotational variations have been attributed to the presence of convective temperature oscillations in the melt. This section will discuss the relationship of growth rate variations observed in crystals grown from the modified Czochralski system to the crystal or crucible rotation rates applied during growth and the temperature fluctuations measured in the melt.

The correspondence of nonrotational growth rate variations with convective temperature fluctuations is best investigated in samples grown without seed or crucible rotation. In the present study the establishment of a direct one to one correspondence was not possible for the following reasons: (1) The temperature measurements were performed near the bottom of the crucible and (even if the convective knot model of Krishnamurti¹³ were applicable) cannot be expected to exhibit the same fluctuation spectra as the temperature at a point close to the growth interface.

(2) According to the analysis of Hurle, Jakeman, and Pike⁵⁰, further correlation is lost as the temperature fluctuation passes through the thermal boundary layer adjacent to the growth interface where the high frequency components are highly damped. (3) Because of inductive interference associated with current pulsing, temperature fluctuation spectra and growth rate data could not be obtained simultaneously. It would be possible to overcome some of these limitations by positioning a shielded thermocouple probe near the growth interface within the thermal boundary layer. Also Fourier analysis of the temperature fluctuation spectra and growth rate data would allow for a direct comparison of the resulting Fourier components and provide a good test for the theory of Hurle, Jakeman, and Pike⁵⁰.

The growth rate data obtained from the sample grown in the modified Czochralski system without crystal or crucible rotation (see Figure 45(a)) exhibits random non-rotational variations. These variations must be directly related to the time dependent thermal convective melt flow and reflect the random temperature fluctuations in the melt (see Figure 8(b)). The average period of the observed growth rate fluctuations (6.1 sec) is in good agreement with the longest dominant period (5.8 sec) determined from the measured temperature fluctuation spectra. In the light of the limitations discussed above it is apparent that the non-rotational growth rate variations in the modified Czochralski system may be

attributed to the convective temperature fluctuations in the melt.

The correspondence of growth rate variations with crystal or crucible rotation is best achieved through a direct comparison of the observed periods of the growth rate variation and of one revolution. Prior to the establishment of the interface demarcation technique this correspondenece was investigated by comparing the separation between growth striations of etched samples with the distance grown per revolution. In the event that such a correspondence is established under crystal rotation conditions, the extent of thermal asymmetry (ΔT) may be assessed from the relative growth rate variation ($\Delta R/R$) by using a modified form of the Morizane relation (Equation 23):

$$\Delta T = \left(\frac{\Delta R}{R} \right) \frac{R\beta}{\omega_s} \quad , \quad (30)$$

where R is the average growth rate, β is the temperature gradient in the melt at the interface, and ω_s is the angular rotation rate of the crystal.

The periods extracted from growth rate data of samples grown in the modified Czochralski system under conditions of crystal rotation (see Figure 41(b)) and crucible rotation (see Figure 43(b)) have been compiled in Table 15. The agreement between the respective periods indicates a strong correlation between the observed growth variations and

rotation rate. Thus both crystal and crucible rotation during growth in the modified system result in rotational growth rate variations (though less pronounced than those encountered in the standard system). From the data presented in Table 10 and using $\beta = 16^\circ\text{C}/\text{cm}$ (see Table 4), the extent of thermal asymmetry across the rotating crystal is computed by Equation (30) to be $\Delta T = 1.4 \times 10^{-3}^\circ\text{C}$. (A similar computation for the sample grown with crystal rotation in the standard system reveals $\Delta T = 2.6 \times 10^{-2}^\circ\text{C}$ further indicating the marked reduction in thermal asymmetry in the modified system.)

TABLE 15
CORRELATION OF GROWTH RATE
VARIATIONS AND ROTATION RATE

Rotation Type	Rotation Rate (rpm)	Revolution Period (sec)	Growth Rate Variation Period (sec)
Crystal	17.1	3.5	3.4
Crucible	6.0	10.0	10.4

Crystal rotation was initially employed during growth in the Czochralski configuration in an attempt to establish a solute boundary layer of uniform thickness adjacent to the growth interface. Growth under such conditions was expected to eliminate radial segregation (except for facet effects)

and result in crystals with homogeneous dopant distribution. Until now, however, attainment of such dopant homogeneity has been hindered in conventional Czochralski systems by the unavoidable presence of excessive thermal asymmetry which results in large amplitude rotational growth rate variations and corresponding compositional heterogeneities during growth with crystal rotation. Presently, the installation of the coaxial heat pipe in the modified Czochralski system was found to reduce the level of thermal asymmetry so that crystal rotation could now be used to achieve transversd dopant homogeneity without increased periodic longitudinal dopant inhomogeneity.

CHAPTER X

SUMMARY AND CONCLUSIONS

A quantitative approach to the study of thermohydrodynamic and segregation phenomena in semiconductor melt growth systems has been developed and cause and effect relationships between them have been established. This approach required the design and construction of micro-thermocouple probes and manipulators for thermal characterization of the hot zone, the development of two computer programs, for numerical analysis of thermal convection, employing quadratically conservative finite difference schemes for numerical stability at large Grashof number, and the application of an established technique for quantitative segregation analysis. The approach was applied to the Czochralski growth of Ga doped Ge crystals from a hot zone modified by the installation of a coaxial heat pipe. The effect of the heat pipe on convection and segregation was determined through a comparative analysis of the modified and standard Czochralski configurations. The numerical approach was justified by the excellent agreement found between the present computational results and previous experimental findings for thermal convection in the horizontal Bridgman configuration.

The conclusions of the present work may be summarized as follows:

(1) A coaxial heat pipe has been used to control and improve melt convection and segregation associated with

Czochralski crystal growth.

(2) Temperature measurements indicate that the use of a coaxial heat pipe in the hot zone of a Czochralski system results in a significant reduction of thermal asymmetry in the melt.

(3) A number of numerical solutions of thermal convection based on temperature measurements in the modified growth configuration revealed (a) qualitative agreement between computed and measured temperature distributions, (b) a pronounced dependence of the quantitative agreement between computed convection behavior and thermal measurements on precise characterization of established boundary conditions, and (c) the existence of vigorous thermal convective flows in the melt.

(4) Samples grown in the modified system were found to exhibit a pronounced reduction in both longitudinal and transverse segregation inhomogeneities.

(5) The establishment of a virtually symmetric thermal environment associated with the installation of a coaxial heat pipe in the hot zone of a Czochralski system allowed the application of crystal rotation to control the solute boundary layer thickness; thus, during growth, radial dopant uniformity was achieved without the adverse effect of pronounced rotational striations.

(6) A thermal analysis surprisingly revealed that the random temperature fluctuations in the melt assume larger amplitudes with the installation of a coaxial heat pipe;

however, these fluctuations are of higher frequency, and thus, have a decreased adverse effect on growth and segregation.

(7) Low frequency components of temperature fluctuations in the melt could be correlated with convective roll instabilities; the origin of the high frequency components, on the other hand, is somewhat uncertain since they can be explained as due to either convective roll instabilities or due to thermal boundary layer instabilities (thermals).

(8) Various approaches to the determination of the solute boundary layer thickness and the determination of convective melt flow rates gave consistent results which indicated that, for crystal growth with a heat pipe under conventional thermal gradients and seed rotation rates, both forced and thermal convection may simultaneously affect dopant segregation at the crystal-melt interface.

CHAPTER XI

SUGGESTIONS FOR FURTHER WORK

The present work has established a quantitative approach to thermohydrodynamic and segregation phenomena for growth systems involving low Prandtl number melts. The results of its application to growth of Ga doped Ge crystals in a modified Czochralski system was discussed. An analysis of the results suggests the following complementary work be undertaken to establish a quantitative understanding of Czochralski growth necessary for its optimization.

(1) Establishment of growth conditions with a virtually flat free melt surface is required for the experimental boundary conditions to be adequately characterized for computational analysis. A flatter melt surface may be obtained by selecting a crucible material and melt whose contact angle is close to 90° . This could be accomplished either with Ge melts of various dopant compositions and finding an appropriate crucible material or changing both the melt and crucible material (such as Si in a quartz crucible).

(2) In the light of the significant reduction in microsegregation for growth in the modified Czochralski system, more accurate procedures for the determination of interface demarcation line positions and spreading resistance measurements are desirable. In addition, microsegregation could be enhanced by choosing a dopant species with a smaller equilibrium

distribution coefficient (such as Sb in Ge).

(3) In view of its technological importance, a detailed investigation of the origin of radial segregation should be conducted. Solute boundary layer thickness effects can be isolated from facet effects by selecting a nonfaceting growth direction. Furthermore, the angular symmetry of the transverse dopant distribution should be investigated.

(4) Fourier analysis of the temperature and growth rate fluctuation spectra must be undertaken to more accurately establish existing cause and effect relationships and to test theoretical predictions such as those of Hurle, Jakeman, and Pike⁵⁰.

(5) The dependence of convection and segregation phenomena on deviation from coaxial alignment should be established and the heat pipe concept for control of such phenomena should be extended to other materials systems (such as Sb doped Si).

(6) To achieve precise quantitative segregation analyses, the required physical constants must be accurately determined and procedures for determining the melt composition during growth should be established.

(7) The numerical study of convection in the Czochralski configuration, based on experimental boundary conditions, must be extended to include a seed crystal in contact with the melt and should involve the effects of both seed and crucible rotation. Furthermore, the possibility of extending this study to include a numerical treatment of dopant segregation during crystal growth should be investigated.

CHAPTER XI

APPENDICES

A. APPENDIX 1

MATERIALS ANALYSIS AND PROPERTIES

This appendix presents the following information in tabular form: (1) The analyses of the starting materials, Ge and Ga, for major impurities are presented in Table 16. (2) The physical constants of liquid Ge required for computational analysis of thermal convection and segregation in the Czochralski configuration are compiled in Table 17. (3) The physical constants of liquid Ga and silicone oil required for numerical analysis of thermal convection in the horizontal Bridgman configuration are listed in Table 18.

TABLE 16

MATERIALS AND MAJOR IMPURITY ANALYSIS

Material	Impurity	Level (PPM)
Ge ^(a)	Si	< 0.1
	B	< 0.005
	O	< 0.03
Ga ^(b)	Al	< 0.4
	Mg	< 0.04
	Si	< 0.04
	Ca	< 0.06
	Cu	< 0.03

- a. Eagle Picher
- b. Alusuisse

TABLE 17

SELECTED PHYSICAL PROPERTIES OF LIQUID GERMANIUM

Melting point ⁸⁸	$T_m = 937.2^\circ\text{C}$
Density ⁸⁹	$\rho = 5.52 \text{ g cm}^{-3}$
Thermal expansion coefficient ⁸⁹	$\alpha = 1.17 \times 10^{-4} \text{ }^\circ\text{C}^{-1}$
Thermal conductivity ⁹⁰	$k = 0.50 \text{ w cm}^{-2} \text{ }^\circ\text{C}^{-1}$
Specific heat ⁹⁰	$C_p = 2.43 \text{ J cm}^{-3} \text{ }^\circ\text{C}^{-1}$
Emisivity ⁹¹	$\epsilon = 0.53$
Thermal diffusivity ($k/\rho c_p$)	$\kappa = 0.21 \text{ cm}^2 \text{ sec}^{-1}$
Kinematic viscosity ⁹²	$\nu = 1.4 \times 10^{-3} \text{ cm}^2 \text{ sec}^{-1}$
Diffusion coefficient ⁴	$D = 1.9 \times 10^{-4} \text{ cm}^2 \text{ sec}^{-1}$
Equilibrium distribution ⁹³ coefficient of Gallium	$k_o = 0.087$

TABLE 18

SELECTED PHYSICAL PROPERTIES OF LIQUID
GALLIUM AND SILICONE OIL

Liquid Gallium at 100°C

Density ⁹⁴	$\rho = 1.65 \text{ g cm}^{-3}$
Thermal expansion coefficient ⁹⁴	$\alpha = 1.24 \times 10^{-4} \text{ }^{\circ}\text{C}^{-1}$
Viscosity ⁹⁴	$\mu = 1.64 \text{ cp}$
Thermal conductivity ⁹⁵	$k = 0.349 \text{ w cm}^{-1}\text{K}^{-1}$
Thermal diffusivity ⁹⁶	$\kappa = 0.155 \text{ cm}^2 \text{ sec}^{-1}$
Kinematic viscosity (μ/ρ)	$\nu = 2.7 \times 10^{-3} \text{ cm}^2 \text{ sec}^{-1}$

Silicone Oil at 60°C

Thermal conductivity ⁹⁷	$k = 1.36 \times 10^{-3} \text{ w cm}^{-1}\text{ }^{\circ}\text{K}^{-1}$
------------------------------------	--

B. APPENDIX 2

Analysis of Microsegregation Transients Due to
Fluctuations of Fluid Velocity and Temperature

This appendix presents a perturbation analysis of the incorporation of solute at a growth interface in the presence of fluid velocity and temperature fluctuations. The analysis starts with a treatment by Hurle, Jakeman, and Pike⁵⁰ (HJP) based on only temperature fluctuation effects and extends the treatment to include fluid velocity fluctuations acting upon the solute diffusion boundary layer. Some errors in the original HJP analysis were corrected; however, their original conclusions do not appear to be substantially altered. Convective processes in the melt determine not only the overall thickness of the diffusion dominated region but also the boundary conditions required to mathematically describe both the steady and perturbed problems.

The effect of thermohydrodynamic instabilities in the melt is introduced by applying a temperature oscillation, $\theta e^{i\omega t}$, (of amplitude θ and angular frequency ω) at the edge of the thermal boundary layer and allowing for a momentum boundary layer thickness variation, $\delta(0) + \delta e^{i(\omega t + \epsilon)}$, (of amplitude δ which is phase shifted by ϵ from the thermal oscillation). (The boundary layer fluctuation is produced by a fluctuation of fluid velocity associated with the convective instability.) The amplitudes are assumed sufficiently small

that linear perturbation theory may be applied to determine the small deviations from the steady state.

1. The Steady State

The steady state solution to this problem has been presented by HJP for a planar solid-liquid interface advancing with constant velocity v along the z -axis. The distribution of solute and temperature (in a frame moving with the interface) must satisfy the following diffusion equations:

$$\frac{\partial^2 T_s}{\partial z^2} + \frac{v}{\kappa_s} \frac{\partial T_s}{\partial z} = \frac{1}{\kappa_s} \frac{\partial T_s}{\partial t} \quad , \quad z < 0 \quad ; \quad (\text{B1a})$$

$$\frac{\partial^2 T_\ell}{\partial z^2} + \frac{v}{\kappa_\ell} \frac{\partial T_\ell}{\partial z} = \frac{1}{\kappa_\ell} \frac{\partial T_\ell}{\partial t} \quad , \quad z > 0 \quad ; \quad (\text{B1b})$$

$$\frac{\partial^2 C_\ell}{\partial z^2} + \frac{v}{D} \frac{\partial C_\ell}{\partial z} = \frac{1}{D} \frac{\partial C_\ell}{\partial t} \quad , \quad z > 0 \quad ; \quad (\text{B1c})$$

where s and ℓ refer to the solid and liquid, respectively, and T , C , κ , and D are the temperature, solute concentration, thermal diffusivity, and mass diffusion coefficient. Diffusion within the solid can be neglected since the ratio D_s/D_ℓ is small (typically $\sim 10^{-4}$). The following boundary conditions are applied at the solid-liquid interface ($z=0$):

$$m_\ell C_\ell = T_\ell - T^* \quad , \quad (\text{B2a})$$

$$- D_{\ell} \frac{\partial C_{\ell}}{\partial z} = V(C_{\ell} - C_S) \quad , \quad (B2b)$$

$$T_S = T_{\ell} \quad , \quad (B2c)$$

$$\kappa_S \frac{\partial T_S}{\partial z} = \kappa_{\ell} \frac{\partial T_{\ell}}{\partial z} + \zeta V \quad , \quad (B2d)$$

where m_{ℓ} is the liquidus slope (assumed constant); T^* is the melting point of the pure solvent; and $\zeta = L/\rho c_p$ is the ratio of the latent heat to the product (assume equal in both phases) of density and specific heat at constant pressure. In the steady state, the concentration in the solid is equal to the distribution coefficient, k , times that in the liquid. Sufficiently close to the interface ($z \gg -\kappa_S/V$ in the solid and $z \ll \kappa_{\ell}/V$ in the liquid) the steady state solution is

$$T_S = T(0) + \beta_S z \quad , \quad z \leq 0 \quad ; \quad (B3a)$$

$$T_{\ell} = T(0) + \beta_{\ell} z \quad , \quad z \geq 0 \quad ; \quad (B3b)$$

$$C_{\ell} = C(0) [k + (1 - k) \exp(- Vz/D_{\ell})] \quad , \quad z \geq 0 \quad ; \quad (B3c)$$

where $C(0) = (T(0) - T^*)/m_{\ell}$ is the interface concentration in the liquid, $T(0)$ is the interface temperature, and β_S and β_{ℓ} are the respective temperature gradients.

2. The Perturbed State

The presence of thermohydrodynamic instabilities within

the melt will cause the temperature and solute concentration fields to deviate from the steady state distribution presented above. For small deviations, the perturbed distributions can be expanded as

$$T_s = T_s^{(0)} + T_s^{(1)} + \dots \quad , \quad (B4a)$$

$$T_\ell = T_\ell^{(0)} + T_\ell^{(1)} + \dots \quad , \quad (B4b)$$

$$C_\ell = C_\ell^{(0)} + C_\ell^{(1)} + \dots \quad , \quad (B4c)$$

where $T_s^{(0)}$, $T_\ell^{(0)}$, and $C_\ell^{(0)}$ are the previously described steady state fields and $T_s^{(1)}$, $T_\ell^{(1)}$, $C_\ell^{(1)}$ are the first order corrections. In response to the perturbation, the position of the phase boundary is displaced to $z = \phi^{(1)}(t)$ relative to the frame moving with the unperturbed velocity $v^{(0)}$, so that the actual interface velocity is

$$v = v^{(0)} + v^{(1)} = v^{(0)} + d\phi^{(1)}/dt \quad . \quad (B5)$$

The first order corrections can be expressed as Fourier series for which the components of frequency, ω , can be written as

$$T_s^{(1)} = T_s(z)e^{i\omega t} \quad , \quad (B6a)$$

$$T_\ell^{(1)} = T_\ell(z)e^{i\omega t} \quad , \quad (B6b)$$

$$C_\ell^{(1)} = C_\ell(z)e^{i\omega t} \quad , \quad (B6c)$$

$$\phi^{(1)} = \phi e^{i\omega t} \quad . \quad (B6d)$$

The spatially dependent amplitudes of these expressions satisfy the following linear perturbation equations:

$$\frac{\partial^2 T_s}{\partial z^2} + \frac{V^{(0)}}{\kappa_s} \frac{\partial T_s}{\partial z} - \frac{i\omega}{\kappa_s} T_s = -i\omega \frac{\beta_s}{\kappa_s} \phi, \quad z < 0; \quad (B7a)$$

$$\frac{\partial^2 T_\ell}{\partial z^2} + \frac{V^{(0)}}{\kappa_\ell} \frac{\partial T_\ell}{\partial z} - \frac{i\omega}{\kappa_\ell} T_\ell = -i\omega \frac{\beta_\ell}{\kappa_\ell} \phi, \quad z > 0; \quad (B7b)$$

$$\frac{\partial^2 C_\ell}{\partial z^2} + \frac{V^{(0)}}{D_\ell} \frac{\partial C_\ell}{\partial z} - \frac{i\omega}{D_\ell} C_\ell = -\frac{i\omega}{D_\ell} V^{(0)} (1 - k) C(0) \exp\left(-\frac{V^{(0)} z}{D_\ell}\right) \phi, \quad (B7c)$$

$z > 0;$

which are obtained by substituting Equations (B4), (B5), and (B6) into Equation (B1) and neglecting the product of small quantities. The boundary conditions to be satisfied by the perturbation amplitudes at the position of the unperturbed interface ($z = 0$) are

$$m_\ell C_\ell = T_\ell + (m_\ell C(0) (1 - k) V^{(0)} / D_\ell + \beta_\ell) \phi, \quad (B8a)$$

$$-\partial C_\ell / \partial z = C_\ell (1 - k) V^{(0)} / D_\ell + i C(0) (1 - k) \omega \phi / D_\ell, \quad (B8b)$$

$$T_s + \beta_s \phi = T_\ell + \beta_\ell \phi, \quad (B8c)$$

$$\kappa_s \partial T_s / \partial z = \kappa_\ell \partial T_\ell / \partial z + i \zeta \omega \phi, \quad (B8d)$$

which are derived by substituting Equations (B4), (B5), and (B6) into Equation (B2) which apply at $z = \phi^{(1)}$, expanding

about the position of the unperturbed interface, making use of Equation (B3), and linearizing. Since the perturbed concentration at the edge of the perturbed solute boundary layer ($z = \delta_c^{(0)} + \delta_c e^{i\omega t}$) must be equal to the concentration in the bulk of the melt, the amplitude of the perturbed concentration component evaluated at the edge of the unperturbed solute boundary layer ($z = \delta_c^{(0)}$) must satisfy

$$C_\ell = C(0) (1 - k) V^{(0)} \exp(-V^{(0)} \delta_c^{(0)} / D_\ell) \delta_c, \quad (B9)$$

which is determined by expansion about $z = \delta_c^{(0)}$ and linearization. Similarly, the temperature perturbation at the edge of the perturbed thermal boundary layer ($z = \delta_T^{(0)} + \delta_T e^{i\omega t}$) must be equal to the sum of the bulk temperature and the perturbation $\theta e^{i\omega t}$ so that the amplitude of the perturbed temperature component evaluated at the edge of the unperturbed thermal boundary layer ($z = \delta_T^{(0)}$) must satisfy

$$T_\ell = \theta - \beta_\ell \delta_T, \quad (B10)$$

Finally, since the temperature must be bounded in the solid, the amplitude of the temperature perturbation must satisfy

$$T_s \neq \infty, \quad z \rightarrow -\infty. \quad (B11)$$

At the unperturbed interface ($z=0$), the solutions of the perturbation Equations B(7), subject to the above boundary conditions (Equations B(8) to B(11)), are:

$$\phi = \left[p(\theta - \beta_\ell \delta_T) + r\delta_c \right] \left[-2\beta_\ell - \frac{2m_\ell C(0)(1-k)V^{(0)}}{D_\ell} - q + s \right]^{-1} \quad (\text{B12a})$$

$$T_\ell = (\beta_\ell + q)\phi + p(\theta - \beta_\ell \delta_t) \quad , \quad (\text{B12b})$$

$$C_\ell = \left[\frac{\beta_\ell}{m_\ell} + \frac{C(0)(1-k)}{D_\ell} \right] \phi + T_\ell/m_\ell \quad , \quad (\text{B12c})$$

where

$$p = \frac{K_\ell \kappa_\ell \operatorname{cosech}(K_\ell \delta_T^{(0)}) \exp(V^{(0)} \delta_T^{(0)}/2)}{K_s \kappa_s + K_\ell \kappa_\ell \operatorname{coth}(K_\ell \delta_T^{(0)})} \quad , \quad (\text{B13a})$$

$$q = \frac{i\omega\zeta - 2(\beta_\ell - \beta_s)(K_s \kappa_s - V^{(0)}/2)}{K_s \kappa_s + K_\ell \kappa_\ell \operatorname{coth}(K_\ell \delta_T^{(0)})} - \beta_\ell p \quad , \quad (\text{B13b})$$

$$r = \frac{m_\ell C(0)(1-k)V^{(0)}d \operatorname{cosech}(d\delta_c^{(0)}) \exp(-V^{(0)} \delta_c^{(0)}/2D)}{V^{(0)}(2k-1)/2 + Dd \operatorname{coth}(d\delta_c^{(0)})} \quad , \quad (\text{B13c})$$

$$s = \frac{m_\ell C(0)(1-k) \left[kV^{(0)2} + i\omega D \right] / D}{V^{(0)}(2k-1)/2 + Dd \operatorname{coth}(d\delta_c^{(0)})} + r \quad , \quad (\text{B13d})$$

$$K = (V^{(0)2} + 4i\omega\kappa)^{1/2}/2\kappa \quad , \quad (\text{B13e})$$

$$d = (V^{(0)2} + 4i\omega D)^{1/2}/2D \quad . \quad (\text{B13f})$$

The presence of imaginary terms produces a phase shift of the

solution with respect to the temperature perturbation. The same relation is assumed to hold between the deviations in boundary layer thickness as between the steady state values:

$$\delta^{(0)} = Pr^{1/2} \delta_T^{(0)} = S_C^{1/3} \delta_C^{(0)} \quad , \quad (B14a)$$

$$|\delta^{(1)}| = Pr^{1/2} |\delta_T^{(1)}| = S_C^{1/3} |\delta_C^{(1)}| \quad , \quad (B14b)$$

where $Pr = \nu/\kappa_\ell$ is the Prandtl number and $S_C = \nu/D$ is the Schmidt number.

In the absence of boundary layer variations the solution to the perturbed problem presented here in equations (B12) should be identical with that presented in HJP Equations (13). The HJP solution for the deviation in interface position can be expressed as

$$\phi = p\theta / \left[-\beta_\ell - \frac{m_\ell C(0)(1-k)V^{(0)}}{D_\ell} - q + s \right] \quad , \quad (B15)$$

where q and s must be redefined as

$$q = \frac{i\omega\zeta + (\beta_\ell - \beta_s)(K_s\kappa_s + V^{(0)}/2)}{K_s\kappa_s + K_\ell\kappa_\ell \coth(K_\ell\delta_T^{(0)})} \quad , \quad (B16a)$$

$$s = \frac{m_\ell C(0)(1-k) \left[KV^{(0)2} + i\omega D \right]}{V^{(0)}(1-k)/2 + dD \coth(K\delta_C^{(0)})} \quad , \quad (B16b)$$

and p is given by Equation (B12a). Comparison of Equations (B15) and (B12a) shows that the first two terms in the denominator of the HJP expression are incorrect by a factor of two; comparison of Equations (B16a) and (B13b) reveals that the second term in the numerator of the HJP expression for q is missing a factor of two and has two incorrect negative signs and further this expression for q is missing the term $-\beta_\ell p$; and finally comparison of (B16b) and (B13d) indicates that the HJP expression for s is missing the term r . A further error in HJP is their interface boundary condition (B8b) which is

$$D \left[\phi \frac{\partial^2 C_\ell^{(0)}}{\partial z^2} + \frac{\partial C_\ell^{(1)}}{\partial z} - \phi \left(\frac{\partial C_\ell^{(0)}}{\partial z} \right)^2 - \frac{\partial C_\ell^{(0)}}{\partial z} \frac{C_\ell^{(1)} - C_s^{(1)}}{1 - k} \right] = -v^{(1)} C_\ell^{(0)} (1 - k) \quad , \quad (B17)$$

and which by making use of Equations (B3c), (B5), and (B6d) can be written as

$$\begin{aligned} \frac{\partial C_\ell^{(1)}}{\partial z} + C(0) \frac{V^{(0)}}{D} (1 - k) C_\ell^{(1)} &= i\omega C(0) (1 - k) \phi \\ + C(0) \frac{V^{(0)^2}}{D^2} (1 - k) [1 - (1 - k)C(0)] \phi & \end{aligned} \quad (B18)$$

which is not dimensionally correct and further is not in agreement with the corresponding Equation (B8b) developed in

this appendix.

The model presented in this appendix is presently under investigation. Preliminary investigations show general trends which are consistent with the findings of HJP for the case in which boundary layer fluctuations are neglected. As yet, an accurate numerical study of the present model has not been carried out. Thus, although the analytical expressions derived by HJP are seen to be in error, the physical reasoning behind their model is evidently correct.

C. APPENDIX 3
FINITE DIFFERENCE SCHEMES FOR NUMERICAL
INTEGRATION OF THERMAL CONVECTION EQUATIONS

1. Finite Difference Representation of Derivatives

In this section the concept of finite difference representations of derivatives⁹⁸ will be introduced. When formulating a problem in finite differences the region of interest is represented by a network of grid points. Each point represents a small distance, area, or volume depending on whether the region of interest is one, two, or three dimensional. In this section only a one dimensional region will be considered.

In Figure 46 the one dimensional region of interest is a line segment of unit length. This is discretized into $M-2$ interior segments of length ΔX and a segment of length $\Delta X/2$ at either end. Each interior segment has an interior grid point at its center. The boundary grid points are at the boundary end of the respective boundary segments. The positions of the grid points are given by $X_i = (i - 1)\Delta X$ with $X_M = 1 = (M - 1)\Delta X$.

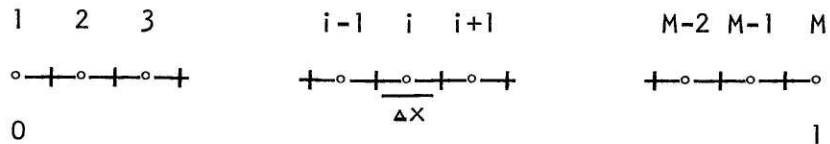


Figure 46. Schematic representation of a one-dimensional finite difference grid.

Consider a field $f(X)$ which takes on a value f_i at the grid point i given by $f_i = f(X_i)$. The values of this field at the neighboring grid points $i + 1$ and $i - 1$ are related to the value of the field and its derivatives at grid point i by the Taylor Series expansions

$$f_{i+1} = f_i + \left. \frac{\partial f}{\partial X} \right|_i \Delta X + \left. \frac{\partial^2 f}{\partial X^2} \right|_i \frac{\Delta X^2}{2} + \left. \frac{\partial^3 f}{\partial X^3} \right|_i \frac{\Delta X^3}{6} + \dots ,$$

$$f_{i-1} = f_i - \left. \frac{\partial f}{\partial X} \right|_i \Delta X + \left. \frac{\partial^2 f}{\partial X^2} \right|_i \frac{\Delta X^2}{2} - \left. \frac{\partial^3 f}{\partial X^3} \right|_i \frac{\Delta X^3}{6} + \dots .$$

These expansions can be used to develop finite difference expressions for the first and second derivatives of the field at the grid point i . Three expressions which can be developed for the first derivative are

$$\text{forward} \quad \left. \frac{\partial f}{\partial X} \right|_i = (f_{i+1} - f_i) / \Delta X + O(\Delta X) ,$$

$$\text{backward} \quad \left. \frac{\partial f}{\partial X} \right|_i = (f_i - f_{i-1}) / \Delta X + O(\Delta X) ,$$

$$\text{centered} \quad \left. \frac{\partial f}{\partial X} \right|_i = (f_{i+1} - f_{i-1}) / 2\Delta X + O(\Delta X^2) ,$$

Three expressions which can be developed for the second derivative are

$$\text{forward} \quad \left. \frac{\partial^2 f}{\partial X^2} \right|_i = (f_{i+2} - 2f_{i+1} + f_i) / \Delta X^2 + O(\Delta X) \quad ,$$

$$\text{backward} \quad \left. \frac{\partial^2 f}{\partial X^2} \right|_i = (f_i - 2f_{i-1} + f_{i-2}) / \Delta X^2 + O(\Delta X) \quad ,$$

$$\text{centered} \quad \left. \frac{\partial^2 f}{\partial X^2} \right|_i = (f_{i+1} - 2f_i + f_{i-1}) / \Delta X^2 + O(\Delta X^2) \quad .$$

The forward and backward difference expressions are only accurate to order ΔX , while the centered difference expressions are accurate to order ΔX^2 .

2. Finite Difference Equations in Two Dimensional Rectangular Coordinates

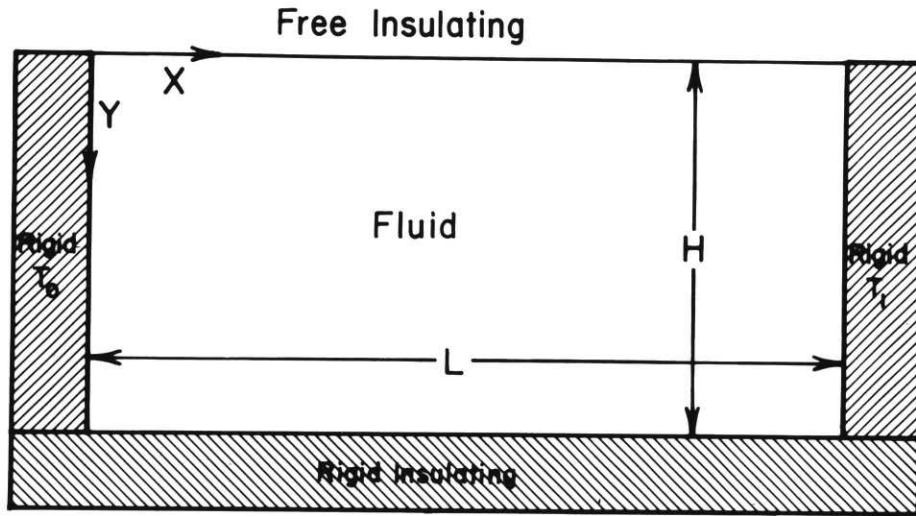
This section will develop the finite difference equations and boundary conditions appropriate for numerical solution of the thermal convection problem in two dimensional rectangular coordinates. By proper choice of boundary conditions these equations can be made to treat a wide variety of important configurations. Some of the possible applications include: the Beñard geometry, horizontal or vertical Bridgman geometry, and a two dimensional simulation of the Czochralski geometry. Here the horizontal Bridgman geometry as investigated by Hurle et al.³³ will be considered.

The geometry treated by Hurle is depicted in Figure 47(a). The fluid fills a rectangular cavity of length L and depth H , across which a constant temperature difference $T_1 - T_0$ is maintained. The side surfaces are rigid and maintained at temperatures T_0 and T_1 , respectively. The bottom surface is rigid and insulating, and the top surface is free and insulating, however, the possibility for heat flow across the upper surface will be included. For this section u and v are the velocity components along the x and y axes, respectively; T, P, ξ , and ψ are respectively, the temperature, reduced pressure, vorticity, and stream function fields; g is the gravitational acceleration; ρ, α, ν , and κ are the fluid density, thermal expansion coefficient, kinematic viscosity and thermal diffusivity, respectively; and the two-dimensional Laplacian ∇^2 is defined by:

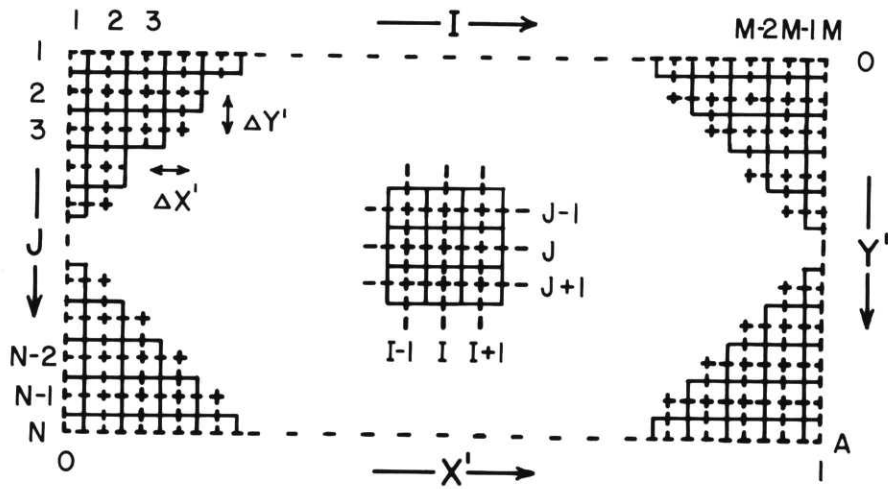
$$\nabla^2 A = \frac{\partial^2 A}{\partial x^2} + \frac{\partial^2 A}{\partial y^2} .$$

a. Development of the Thermal Convection Equations

The equations of mass, momentum, and energy conservation will assume the Boussinesqu approximation¹⁰ which states that the only term in the equations of motion which need include the variation of fluid density with temperature is that involving the body force. Other than this one term the fluid can be treated as an incompressible fluid with constant properties. The equation of mass conservation is



(a)



(b)

Figure 47. Horizontal Bridgman configuration. (a) Schematic representation of horizontal Bridgman geometry with assumed boundary conditions. (b) Schematic representation of finite difference grid used for computation.

$$\frac{\partial u}{\partial x} + \frac{\partial v}{\partial y} = 0 \quad . \quad (C1)$$

The equations of momentum conservation are

$$\frac{\partial u}{\partial t} + \frac{u \partial u}{\partial x} + \frac{v \partial u}{\partial y} = - \frac{1}{\rho} \frac{\partial P}{\partial x} + \nu \nabla^2 u \quad , \quad (C2a)$$

$$\frac{\partial v}{\partial t} + \frac{u \partial v}{\partial x} + \frac{v \partial v}{\partial y} = - \frac{1}{\rho} \frac{\partial P}{\partial y} + \nu \nabla^2 v - \alpha g (T - T_0) \quad . \quad (C2b)$$

The equation of energy conservation is

$$\frac{\partial T}{\partial t} + \frac{u \partial T}{\partial x} + \frac{v \partial T}{\partial y} = \kappa \nabla^2 T \quad . \quad (C3)$$

And the equation of state for the fluid which has been used in developing the y-momentum Equation (C2b) is

$$\rho = \rho_0 (1 - \alpha (T - T_0)) \quad . \quad (C4)$$

The equations of momentum conservation can be put in a more useable form which eliminates the pressure P by defining the Z-component of the vorticity ξ as

$$\xi = \partial v / \partial x - \partial u / \partial y \quad . \quad (C5)$$

With this definition of vorticity the equations of momentum conservation (C2) may be replaced by the equation of vorticity transport which is

$$\frac{\partial \xi}{\partial t} + \frac{u \partial \xi}{\partial x} + \frac{v \partial \xi}{\partial y} = \nu \nabla^2 \xi - \alpha g \frac{\partial}{\partial x} (T - T_0) \quad . \quad (C6)$$

The bouyancy term of this equation, $-\alpha g \frac{\partial}{\partial x} (T - T_0)$, is responsible for the vorticity generation which drives the thermal convective flow²⁴. The equation of mass conservation (C1) can be solved indentically by defining the stream function ψ in terms of which the velocities are

$$u = \frac{\partial \psi}{\partial y} \quad \text{and} \quad v = - \frac{\partial \psi}{\partial x} \quad , \quad (C7)$$

and the definition of vorticity (Equation (C5)) becomes

$$\xi = - \nabla^2 \psi \quad . \quad (C8)$$

The vorticity transport Equation (C6) becomes

$$\frac{\partial \xi}{\partial t} + J(\xi, \psi) = \nu \nabla^2 \xi - \alpha g \frac{\partial}{\partial x} (T - T_0) \quad , \quad (C9)$$

and the energy Equation (C3) becomes

$$\frac{\partial T}{\partial t} + J(T, \psi) = \kappa \nabla^2 T \quad , \quad (C10)$$

where the advective terms have been expressed in terms of a Jacobian J defined as

$$J(\psi , A) = \frac{\partial \psi}{\partial x} \frac{\partial A}{\partial y} - \frac{\partial \psi}{\partial y} \frac{\partial A}{\partial x} \quad . \quad (C11)$$

Thus, there are three basic coupled partial differential equations which describe the stream function, vorticity, and temperature fields.

b. Development of the Boundary Conditions

The boundary conditions appropriate for solution of these equations will be developed next. At all boundary surfaces, the normal fluid velocity must vanish. Thus, for the horizontal boundary surfaces $v = -\partial\psi/\partial x = 0$ and ψ is independent of x . For the vertical boundary surfaces $u = \partial\psi/\partial y = 0$ and ψ is independent of y . Thus ψ is constant on the bounding surfaces and this constant is chosen to be zero. For the rigid boundary surfaces, the no slip boundary condition applies and the tangential fluid velocity vanishes. Thus, for the horizontal rigid surface, $u = \partial\psi/\partial y = 0$, while, for the vertical rigid surfaces, $v = \partial\psi/\partial x = 0$. For the free horizontal boundary surface the tangential stress vanishes¹⁰ and $\tau_{yx} = \frac{\nu}{2} \left(\frac{\partial u}{\partial y} + \frac{\partial v}{\partial x} \right) = 0$ and since $v = 0$ for all x , $\partial v/\partial x = 0$ and thus $\partial u/\partial y = 0$ so that the vorticity $\xi = \partial v/\partial x - \partial u/\partial y = 0$ on the free surface. The boundary conditions on the temperature field are $T = \text{constant}$ on conducting surfaces, $\partial T/\partial y = 0$ on the insulating bottom surface, and $-k\partial T/\partial y = h(T_a - T)$ on the upper surface, where k is the thermal conductivity of the fluid, h is the convective heat transfer coefficient, and T_a is the gas temperature outside of the thermal boundary

layer region.

Thus, the equations will be solved subject to the following boundary conditions:

On the vertical boundaries:

$$\begin{aligned}\psi &= 0, \quad \xi = -\frac{\partial^2 \psi}{\partial X^2} \quad \text{at } X = 0, L \quad \text{for all } y, \\ T &= T_0 \quad \text{at } X = 0 \quad \text{for all } y, \\ T &= T_1 \quad \text{at } X = L \quad \text{for all } y.\end{aligned}\tag{C12}$$

On the lower boundary:

$$\psi = 0, \quad \xi = -\frac{\partial^2 \psi}{\partial y^2}, \quad \frac{\partial T}{\partial y} = 0 \quad \text{at } y = H \quad \text{for all } X.\tag{C13}$$

On the upper boundary:

$$\psi = 0, \quad \xi = 0, \quad -\frac{k\partial T}{\partial y} = h(T_a - T) \quad \text{at } y = 0 \quad \text{for all } X.\tag{C14}$$

c. Non-Dimensionalization of the Equations and Boundary Conditions

To ascertain the parameters which control thermal convection in the horizontal Bridgman geometry, it is convenient to non-dimensionalize the applicable equations and boundary conditions. The non-dimensionalization to be used is L for length, L^2/ν for time, ν/L for velocity, ν/L^2 for vorticity, ψ for stream function, and $T_1 - T_0$ for

temperature. The energy Equation (C10) becomes

$$\partial\theta/\partial t = J(\psi, \theta) + \frac{1}{Pr} \nabla^2 \theta \quad . \quad (C15)$$

The vorticity Equation (C9) becomes

$$\frac{\partial \xi}{\partial t} = J(\psi, \xi) + \nabla^2 \xi - Gr \partial\theta/\partial x \quad . \quad (C16)$$

The stream function Equation (C8) becomes

$$\nabla^2 \psi = - \xi \quad . \quad (C17)$$

The boundary conditions (Equations C12 to C14) become

$$\psi = 0 \quad , \quad \xi = - \partial^2 \psi / \partial x^2 \quad \text{at} \quad x = 0, 1 \quad \text{for all} \quad y \quad ,$$

$$\theta = \theta_0 \quad \text{at} \quad x = 0 \quad \text{for all} \quad y \quad ,$$

$$\theta = \theta_1 \quad \text{at} \quad x = 1 \quad \text{for all} \quad y \quad , \quad (C18)$$

$$\psi = 0 \quad , \quad \xi = 0 \quad , \quad \frac{\partial \theta}{\partial y} = Bi(\theta_a - \theta) \quad \text{at} \quad y = 0 \quad \text{for all} \quad x \quad ,$$

$$\psi = 0 \quad , \quad \xi = - \partial^2 \psi / \partial x^2 \quad , \quad \partial\theta/\partial y = 0 \quad \text{at} \quad y = Asp \quad \text{for all} \quad y \quad .$$

This thermal convection in the horizontal Bridgman geometry is characterized by the four non-dimensional parameters:

(1) the Prandtl number, $Pr = \nu/\kappa$, which characterizes the relative importance of convective and conductive heat flow,

(2) the Grashof number, $Gr = \alpha g(T_1 - T_0)L^3/\nu^2$, which

characterizes the magnitude of the bouyancy term in the vor-
 ticity Equation, (3) the Biot number, $Bi = hL/k$, which
 characterizes the heat flow across the upper surface, and (4)
 the aspect ratio, $Asp = H/L$, which characterizes the shape
 of the region occupied by the fluid.

d. Finite Difference Formulation

Now that the equations and boundary conditions for the
 thermal convection problem have been developed, they will be
 given a finite difference formulation appropriate for numeri-
 cal calculation. The region occupied by the fluid will be
 represented by a rectangular network of M grid points in
 the horizontal direction and N grid points in the vertical
 direction as shown in Figure 47(b). The coordinate axes are
 descretized according to $X_i = (i - 1)\Delta X$ and $y_j = (j - 1)\Delta y$
 where $(M - 1)\Delta X = 1$ and $(N - 1) y = Asp$. The time is
 descretized according to $t_n = n\Delta t$. The temperature, vor-
 ticity, and stream function fields at time t_n are repre-
 sented by $M \times N$ arrays with an element corresponding to
 each grid point and $f_{ij}^n = f(x, y, t_n)$. Each element can
 also be thought of as the average value of the field over a
 grid square and a time step such that

$$f_{ij}^n = \frac{1}{\Delta x \Delta y \Delta t} \int_{X_i - \Delta x/2}^{X_i + \Delta x/2} \int_{y_i - \Delta y/2}^{y_i + \Delta y/2} \int_{t_n - \Delta t/2}^{t_n + \Delta t/2} f(x, y, t) dx dy dt .$$

The explicit finite difference equations are formulated by using a forward difference for the time derivative, special quadratically conservative forms for the Jacobians², and centered differences for all other space derivatives. The energy Equation (C10) becomes

$$\begin{aligned} \frac{\theta_{ij}^{n+1} - \theta_{ij}^n}{\Delta t} = J_{Lij}^n(\psi, \theta) + \frac{\theta_{i+ij}^n - 2\theta_{ij}^n + \theta_{i-ij}^n}{Pr \Delta X^2} \\ + \frac{\theta_{ij+1}^n - 2\theta_{ij}^n + \theta_{ij-1}^n}{Pr \Delta Y^2} \end{aligned} \quad (C19)$$

in the interior,

$$\begin{aligned} \frac{\theta_{il}^{n+1} - \theta_{il}^n}{\Delta t} = J_{Lil}^n(\psi, \theta) + \frac{\theta_{i+1l}^n - 2\theta_{il}^n + \theta_{i-1l}^n}{Pr \Delta X^2} \\ + \frac{2(\theta_{i2}^n - \theta_{il}^n)}{Pr \Delta Y^2} + \frac{2Bi}{Pr \Delta Y} (\theta_a - \theta_{il}^n) \end{aligned} \quad (C20)$$

on the upper surface, and

$$\begin{aligned} \frac{\theta_{iN}^{n+1} - \theta_{iN}^n}{\Delta t} = J_{LiN}^n(\psi, \theta) + \frac{\theta_{i+1N}^n - 2\theta_{iN}^n + \theta_{i-1N}^n}{Pr \Delta X^2} \\ + \frac{2(\theta_{iN-1}^n - \theta_{iN}^n)}{Pr \Delta Y^2} \end{aligned} \quad (C21)$$

on the lower surface. The vorticity Equation (C16) becomes

$$\begin{aligned} \frac{\xi_{ij}^{n+1} - \xi_{ij}^n}{\Delta t} = & J_{Aij}^n(\psi, \xi) + \frac{\xi_{i+1j}^n - 2\xi_{ij}^n + \xi_{i-1j}^n}{\Delta x^2} \\ & + \frac{\xi_{ij+1}^n - 2\xi_{ij}^n + \xi_{ij-1}^n}{\Delta y^2} - Gr \frac{(\theta_{i+1j} - \theta_{i-1j})}{2\Delta x} \end{aligned} \quad (C22)$$

in the interior. The stream function Equation (C17) becomes

$$\frac{\psi_{i+1j} - 2\psi_{ij} + \psi_{i-1j}}{\Delta x^2} + \frac{\psi_{ij+1} - 2\psi_{ij} + \psi_{ij-1}}{\Delta y^2} = -\xi_{ij} \quad (C23)$$

The special Lilly Jacobian⁹⁹ J_{Lij} is

$$J_{Lij}(\psi, \theta) = \frac{1}{8\Delta x \Delta y} \begin{bmatrix} \theta_{i+1j} (\psi_{i+1j-1} - \psi_{i+1j+1} + \psi_{ij-1} - \psi_{ij+1}) \\ +\theta_{i-1j} (\psi_{i-1j+1} - \psi_{i-1j-1} + \psi_{ij+1} - \psi_{ij-1}) \\ +\theta_{ij+1} (\psi_{i+1j+1} - \psi_{i-1j+1} + \psi_{i+1j} - \psi_{i-1j}) \\ +\theta_{ij-1} (\psi_{i-1j-1} - \psi_{i+1j-1} + \psi_{i-1j} - \psi_{i+1j}) \end{bmatrix} \quad (C24)$$

and J_{Lil} is

$$J_{Lil}(\psi, \theta) = \frac{1}{4\Delta x \Delta y} \begin{bmatrix} -\theta_{i+11} (\psi_{i+12} + \psi_{i2}) \\ +\theta_{i-11} (\psi_{i-12} + \psi_{i2}) \\ +\theta_{i2} (\psi_{i+12} - \psi_{i-12}) \end{bmatrix} \quad (C25)$$

The special Arakawa² Jacobian J_{Aij} is

$$J_{Aij}(\psi, \xi) = \frac{1}{12\Delta X \Delta Y} \left[\begin{aligned} &\xi_{i+1j+1} (\psi_{i+1j} - \psi_{ij+1}) + \xi_{i+1j-1} (\psi_{ij-1} - \psi_{i+1j}) \\ &+ \xi_{i-1j+1} (\psi_{ij+1} - \psi_{i-1j}) + \xi_{i-1j-1} (\psi_{i-1j} - \psi_{ij-1}) \\ &+ \xi_{i+1j} (\psi_{i+1j-1} - \psi_{i+1j+1} + \psi_{ij-1} - \psi_{ij+1}) \\ &+ \xi_{i-1j} (\psi_{i-1j+1} - \psi_{i-1j-1} + \psi_{ij+1} - \psi_{ij-1}) \\ &+ \xi_{ij+1} (\psi_{i+1j+1} - \psi_{i-1j+1} + \psi_{i+1j} - \psi_{i-1j}) \\ &+ \xi_{ij-1} (\psi_{i-1j-1} - \psi_{i+1j-1} + \psi_{i-1j} - \psi_{i+1j}) \end{aligned} \right] \quad (C26)$$

The special finite difference forms of the advection Jacobians were selected for their conservation properties. The Jacobian J_{Lij} has the desirable feature of conserving the temperature and its square within the grid. The Jacobian J_{Aij} conserves vorticity, square vorticity, and kinetic energy within the finite difference grid. The lack of spurious sources or sinks of these quantities is expected to result in an accurate finite difference scheme which is numerically stable at high Grashof numbers.

The finite difference forms of the boundary conditions (C18) are

$$\begin{aligned} \theta_{ij}^n = 0, \quad \psi_{ij}^n = 0, \quad \xi_{ij}^n = \frac{-2\psi_{2j}^n}{\Delta X^2} \quad \text{at } i = 1 \quad \text{for all } j, \\ \theta_{Mj}^n = 1, \quad \psi_{Mj}^n = 0, \quad \xi_{Mj}^n = \frac{-2\psi_{M-1j}^n}{\Delta X^2} \quad \text{at } i = M \quad \text{for all } j, \end{aligned} \quad (C27)$$

$$\psi_{i1}^n = 0, \quad \xi_{i1}^n = 0 \quad \text{at } j = 1 \quad \text{for all } i,$$

$$\psi_{iN}^n = 0, \quad \xi_{iN}^n = \frac{-2\psi_{iN-1}^n}{\Delta Y^2} \quad \text{at } j = N \quad \text{for all } i.$$

The no slip boundary conditions are included in the problem through the expressions used for calculating the boundary vorticity. The boundary conditions for the temperature field at the upper and lower surfaces are included in the finite difference energy equations to be applied at these surfaces.

e. Requirements for Numerical Stability

Next the requirements for computational stability of the finite difference scheme ¹⁰⁰ will be discussed. There are two basic requirements for computational stability. One is required for stability of the diffusive terms and one is required for stability of the advection terms.

Since the finite difference scheme chosen for solution of the thermal convection problem in the horizontal Bridgman geometry represents the time derivatives with forward differences and evaluates all other terms at the current time step, it is of the explicit type. It is well known that care must be used in choosing the size of the time increment to insure

computational stability of an explicit finite difference scheme. The equations for temperature and vorticity fields can be written as

$$\begin{aligned} \theta_{ij}^{n+1} = & a_1 \theta_{i+1j}^n + a_2 \theta_{i-1j}^n + a_3 \theta_{ij}^n + a_4 \theta_{ij+1}^n \\ & + a_5 \theta_{ij-1}^n + \Delta t J_{Lij}^n(\psi, \theta) \end{aligned} \quad (C28)$$

$$\begin{aligned} \xi_{ij}^{n+1} = & b_1 \xi_{i+1j}^n + b_2 \xi_{i-1j}^n + b_3 \xi_{ij}^n + b_4 \xi_{ij+1}^n \\ & + b_5 \xi_{ij-1}^n + \Delta t J_{Aij}^n(\psi, \xi) - \frac{\Delta t}{2\Delta X} (\theta_{i+1j}^{n+1} - \theta_{i-1j}^{n+1}) \end{aligned} \quad .$$

In order to insure computational stability all the a's and b's must be positive. This requirement reduces to one only on a_3 and b_3 since all the other a's and b's are always positive. In the interior

$$\begin{aligned} a_3 = 1 - \Delta t \left(\frac{2}{Pr\Delta X^2} + \frac{2}{Pr\Delta Y^2} \right) > 0 \quad , \\ b_3 = 1 - \Delta t \left(\frac{2}{\Delta X^2} + \frac{2}{\Delta Y^2} \right) > 0 \quad , \end{aligned} \quad (C29)$$

and on the upper surface

$$a_3 = 1 - \Delta t \left(\frac{2}{Pr\Delta X^2} + \frac{2}{Pr\Delta Y^2} + \frac{2Bi}{Pr\Delta Y} \right) > 0 \quad . \quad (C30)$$

For low Prandtl number fluids the most stringent requirement on the size of the time step is that for the temperature field

on the upper surface

$$\Delta t < 1 / \left(\frac{2}{Pr\Delta X^2} + \frac{2}{Pr\Delta y^2} + \frac{2Bi}{Pr\Delta y} \right) . \quad (C31)$$

The requirement for computational stability of the advection terms is essentially that during one time step each fluid particle moves less than one grid spacing. This can be expressed as

$$\Delta t < \text{Min} \left(\frac{\Delta x}{u} , \frac{\Delta y}{v} \right) . \quad (C32)$$

That is Δt must be less than which ever is smaller between the horizontal spacing divided by the maximum horizontal velocity and the vertical spacing divided by the maximum vertical velocity.

f. Solution of Poisson's Equation

The stream function is computed by using a subroutine XYPOIS developed by O'Buneman¹⁰⁷ for solving Poisson's equation in two dimensional Cartesian coordinates. This subroutine produces a solution which is exact within the framework of the finite difference technique.

g. Computational Strategy

The computation proceeds as flow charted in Figure 48. The computation is begun by specifying the dimensionless parameters Gr , Pr , Asp , Bi , and θ_a , the grid size $M \times N$

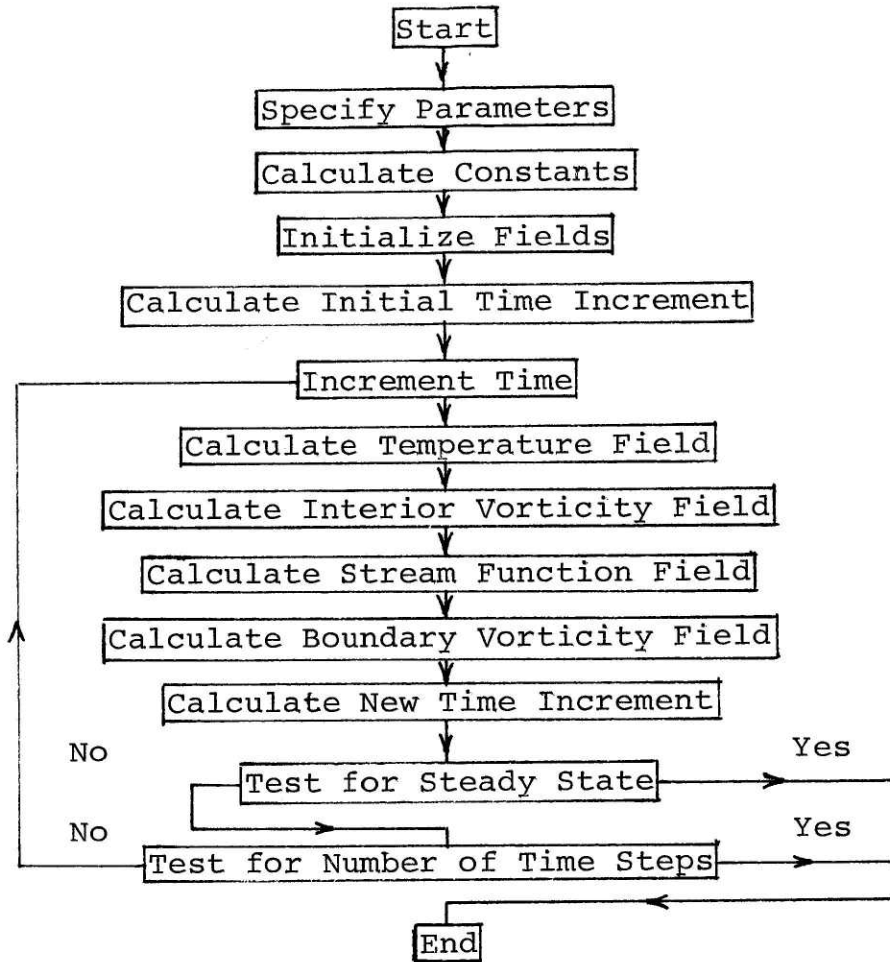


Figure 48. Flow Chart of Numerical Solution of Thermal Convection in the Horizontal Bridgman Configuration

and a number of control parameters. From these a number of constants are calculated, after which, the temperature, vorticity, and stream function fields are initialized and an initial time increment is determined. The computational loop consists of the following steps:

(1) The time is incremented. (2) The new temperature field is calculated. (3) The new interior vorticity field is calculated. (4) The new stream function field is calculated. (5) The new boundary vorticity is calculated. (6) A new time increment is determined and the process is repeated until either a specified number of time steps are executed or steady state is achieved. Analysis of early results indicated an adequate test for convergence was

$$\left| \frac{1}{\psi_{cc}} \frac{\partial \psi_{cc}}{\partial t} \right| = \left| \frac{\psi_{cc}^{n+1} - \psi_{cc}^n}{\psi_{cc}^n \Delta t} \right| < .00001 \quad (C33)$$

where ψ_{cc} is the value of the stream function at the center of the grid.

3. Finite Difference Equations in Axisymmetric Cylindrical Coordinates

This section will develop the finite difference equations and boundary conditions appropriate for numerical solution of the thermal convection problem in axisymmetric cylindrical coordinates. By proper choice of boundary conditions, these equations can be made to treat a wide variety of important

configurations. Several of the possible applications include: the Bénard geometry, horizontal and vertical Bridgman geometry, and the Czochralski geometry. Here the Czochralski geometry will be considered.

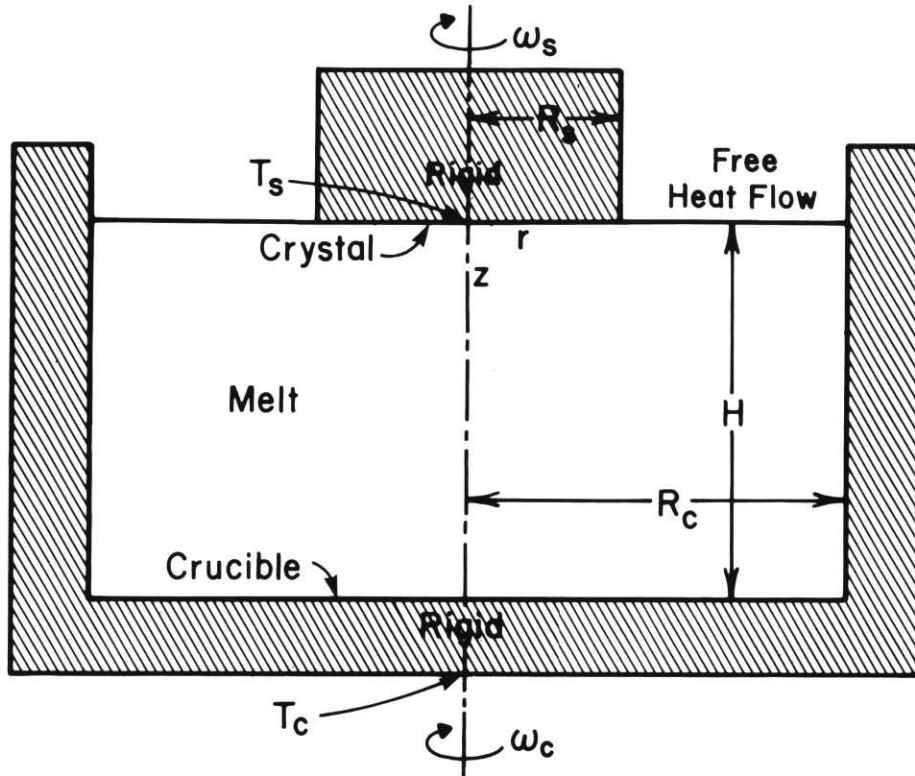
The geometry appropriate for treating thermal convection in the Czochralski crystal growth configuration is illustrated in Figure 49(a). The fluid fills a cylindrical crucible of radius R_c and depth H . A cylindrical crystal of radius R_s is coaxial with the crucible and in contact with the upper surface of the fluid. The crucible wall and the crystal interface are rigid and maintained at temperatures T_c and T_s , respectively. The upper surface between the crystal and the crucible wall is free and allows heat flow with the surroundings. The crystal may be rotated at a rate ω_s and the crucible may be rotated at a rate ω_c .

a. Development of the Thermal Convection Equations

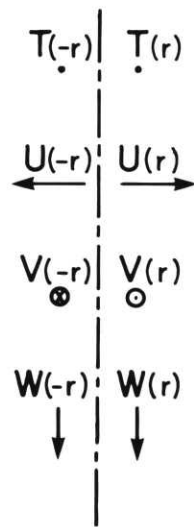
The equations of mass, momentum and energy conservation will assume the Bousinesqu approximation and will be developed for axially symmetric cylindrical coordinates¹⁰². The equation of mass conservation is

$$\frac{1}{r} \frac{\partial}{\partial r} (ru) + \frac{\partial w}{\partial z} = 0 \quad . \quad (C34)$$

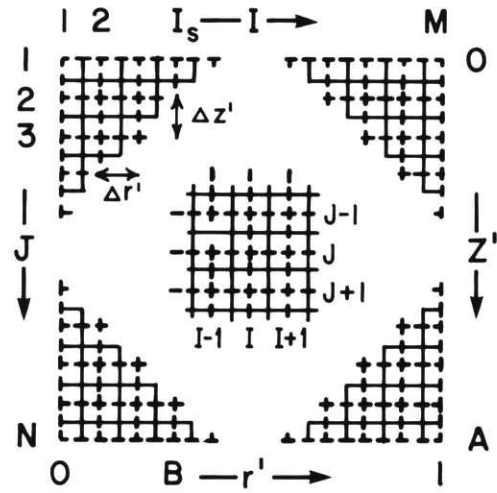
The equations of momentum conservation are



(a) Schematic representation of Czochralski geometry with assumed boundary conditions.



(b) Visualization of axial boundary conditions.



(c) Schematic representation of finite difference grid used for computation.

Figure 49. Czochralski configuration.

$$\frac{\partial u}{\partial t} + \frac{u \partial u}{\partial r} + \frac{w \partial u}{\partial z} - \frac{v^2}{r} = - \frac{1}{\rho} \frac{\partial P}{\partial r} + \nu D^2 u \quad , \quad (C35a)$$

$$\frac{\partial v}{\partial t} + \frac{u \partial v}{\partial r} + \frac{w \partial v}{\partial z} + \frac{v u}{r} = + \nu D^2 v \quad , \quad (C35b)$$

$$\frac{\partial w}{\partial t} + \frac{u \partial w}{\partial r} + \frac{w \partial w}{\partial z} = - \frac{1}{\rho} \frac{\partial P}{\partial z} + \nu \nabla^2 w - g \alpha (T - T_0) \quad . (C35c)$$

The equation of energy conservation is

$$\frac{\partial T}{\partial t} + \frac{u \partial T}{\partial r} + \frac{w \partial T}{\partial z} = \kappa \nabla^2 T \quad (C36)$$

and the equation of state for the fluid which was used in developing the z-momentum Equation (C35c) is

$$\rho = \rho_0 (1 - \alpha (T - T_0)) \quad .$$

In the above equations u , v , and w are respectively the radial, azimuthal, and vertical velocity components and the operators ∇^2 and D^2 are defined by

$$\nabla^2 A = \frac{1}{r} \frac{\partial}{\partial r} \left(\frac{r \partial A}{\partial r} \right) + \frac{\partial^2 A}{\partial z^2} \quad ,$$

$$D^2 A = \frac{\partial}{\partial r} \left(\frac{1}{r} \frac{\partial}{\partial r} (rA) \right) + \frac{\partial^2 A}{\partial z^2} \quad .$$

The equations of momentum conservation (C35) can be modified to eliminate the pressure by defining the zonal vorticity component η by

$$\eta = \frac{\partial u}{\partial z} - \frac{\partial w}{\partial r} \quad . \quad (C37)$$

With this definition of vorticity the r-momentum and z-momentum Equations (C35a and C35c) are replaced by the equation of vorticity transport

$$\frac{\partial \eta}{\partial t} + \frac{u \partial \eta}{\partial r} + \frac{w \partial \eta}{\partial z} - \frac{u \eta}{r} - \frac{1}{r} \frac{\partial v^2}{\partial z} = g \alpha \frac{\partial T}{\partial r} + \nu D^2 \eta \quad . \quad (C38)$$

The equation of mass conservation (C34) can be solved identically by introducing the Stokes stream function ψ in terms of which the radial and axial velocities become

$$u = - \frac{1}{r} \frac{\partial \psi}{\partial z} \quad \text{and} \quad w = \frac{1}{r} \frac{\partial \psi}{\partial r} \quad , \quad (C39)$$

and the definition of vorticity (Equation C37) becomes

$$\eta = - \frac{\partial}{\partial r} \left(\frac{1}{r} \frac{\partial \psi}{\partial r} \right) - \frac{1}{r} \frac{\partial^2 \psi}{\partial z^2} \quad . \quad (C40)$$

The vorticity transport Equation (C38) becomes

$$\frac{\partial \eta}{\partial t} + J(\psi, \eta) - \frac{1}{r} \frac{\partial v^2}{\partial z} = g \alpha \frac{\partial T}{\partial r} + \nu D^2 \eta \quad . \quad (C41)$$

The zonal momentum Equation (C35c) becomes

$$\frac{\partial v}{\partial t} + \frac{1}{r} J(\psi, v) - \frac{v}{r^2} \frac{\partial \psi}{\partial z} = \nu D^2 v \quad . \quad (C42)$$

The energy transport Equation (C36) becomes

$$\frac{\partial T}{\partial t} + \frac{1}{r} J(\psi, T) = \kappa \nabla^2 T \quad . \quad (C43)$$

The advection terms have been expressed in terms of a Jacobian defined as

$$J(\psi, A) = \frac{\partial \psi}{\partial r} \frac{\partial A}{\partial z} - \frac{\partial \psi}{\partial z} \frac{\partial A}{\partial r} \quad . \quad (C44)$$

Thus, in the stream function-vorticity formulation, thermal convection in the axially symmetric Czochralski geometry is described by four coupled partial differential equations which together with the boundary conditions determine the stream function, vorticity, zonal velocity, and temperature fields.

b. Development of the Boundary Conditions

The boundary conditions appropriate for solution of these equations will be developed next. At all boundary surfaces the normal velocity must vanish. Thus, for $z = 0$ and $z = H$, $w = 0$ and, thus, $\psi = 0$ and $\partial w / \partial r = 0$, so that, $\eta = \partial u / \partial z = -\frac{1}{r} \frac{\partial^2 \psi}{\partial z^2}$. For $r = R_c$, $u = 0$ and, thus, $\psi = 0$ and $\partial u / \partial z = 0$, so that, $\eta = -\partial w / \partial r = -\frac{\partial}{\partial r} \left(\frac{1}{r} \frac{\partial \psi}{\partial r} \right)$.

At the free surface, $z = 0$ and $R_s < r < R_c$, the two components of the shear stress vanish. Thus,

$$\tau_{zr} = \frac{\nu}{2} \left(\frac{\partial u}{\partial z} + \frac{\partial w}{\partial r} \right) = 0 \quad , \quad (C45)$$

$$\tau_{z\theta} = \frac{v}{2} \left(\frac{\partial v}{\partial z} + \frac{1}{r} \frac{\partial w}{\partial \theta} \right) = 0 \quad , \quad \text{(C45-cont'd)}$$

and since $\partial w/\partial r = 0$ and $\partial w/\partial \theta = 0$, it follows that $\partial u/\partial z = 0$ and $\partial v/\partial z = 0$. Also, since $\partial w/\partial r = 0$ and $\partial u/\partial z = 0$, then $\eta = 0$.

At the rigid surfaces the no slip boundary condition must hold. Thus, for $z = 0$ and $0 < r < R_s$, $v = r\omega_s$ and $u = 0$, so that $\psi/\partial z = 0$. For $z = H$, $v = r\omega_c$ and $u = 0$, so that $\partial\psi/\partial z = 0$ and, for $r = R_c$, it follows that $v = R_c\omega_c$ and $w = 0$, so that $\partial\psi/\partial r = 0$.

There are three types of thermal boundary conditions which may be considered. At a "conducting" surface the temperature is specified and fixed. For surfaces which allow heat flow Q , the temperature field must satisfy $\frac{\partial T}{\partial z} = -Q/k$. For insulating surfaces, there is no heat flow $Q = 0$ and the temperature field must satisfy $\frac{\partial T}{\partial z} = 0$. Two types of heat flow at the boundary surface will be considered, radiative heat transfer to the chamber walls at temperature T_ω

$$Q_r = \epsilon\sigma(T^4 - T_\omega^4) \quad \text{(C46)}$$

and convective heat transfer through the thermal boundary layer to the ambient gas at temperature T_a

$$Q_c = h(T - T_a) \quad , \quad \text{(C47)}$$

The conditions to be imposed at the axis of symmetry will be considered next. Consideration of axial symmetry (see Figure 49(b)) leads to the following conditions: $T(r) = T(-r)$ so that $\partial T / \partial R = 0$. $u(r) = -u(-r)$ so that $u = 0$; $v(r) = -v(-r)$ so that $v = 0$, and $w(r) = w(-r)$ so that $\partial w / \partial r = 0$. Thus on the axis of symmetry, $u = v = 0$ and $\partial T / \partial z = \partial w / \partial r = 0$. From these it follows that $\eta = \frac{\partial u}{\partial z} - \frac{\partial w}{\partial r} = 0$ and $\psi = 0$.

c. Non-Dimensionalization of the Equations and Boundary Conditions

The parameters which control convection in the Czochralski configuration can be revealed by non-dimensionalizing the applicable equations and boundary conditions. The non-dimensionalization to be used is R_c for length, R_c/v for velocity, R_c^2/v for vorticity, vR_c for stream function, and $T_c - T_s$ for temperature, where T_c is the hottest and T_s is the coldest temperature on the fluid boundary.

The energy Equation (C43) becomes

$$\frac{\partial T}{\partial t} + \frac{1}{r} J(\psi, T) = \frac{1}{Pr} \nabla^2 T \quad . \quad (C48)$$

The zonal momentum Equation (C42) becomes

$$\frac{\partial v}{\partial t} + \frac{1}{r} J(\psi, v) - \frac{v}{r^2} \frac{\partial \psi}{\partial z} = D^2 v \quad . \quad (C49)$$

The vorticity transport Equation (C41) becomes

$$\frac{\partial \eta}{\partial t} + J(\psi, \frac{\eta}{r}) - \frac{1}{r} \frac{\partial v^2}{\partial z} = Gr \frac{\partial T}{\partial r} + D^2 \eta \quad . \quad (C50)$$

The stream function Equation (C40) becomes

$$\frac{\partial}{\partial r} \left(\frac{1}{r} \frac{\partial \psi}{\partial r} \right) + \frac{1}{r} \frac{\partial^2 \psi}{\partial z^2} = - \eta \quad . \quad (C51)$$

The boundary conditions become

$$\psi = 0 \quad , \quad \eta = 0 \quad , \quad \frac{\partial T}{\partial r} = 0 \quad , \quad v = 0 \quad \text{for } r = 0 \quad , \quad 0 \leq z \leq A \quad ,$$

$$\psi = 0 \quad , \quad \eta = - \frac{\partial}{\partial r} \left(\frac{1}{r} \frac{\partial \psi}{\partial r} \right) \quad , \quad T = T_c \quad , \quad v = R_{ec} \quad \text{for } r = 1 \quad ,$$

$$0 \leq z \leq A \quad ,$$

$$\psi = 0 \quad , \quad \eta = - \frac{1}{r} \frac{\partial^2 \psi}{\partial z^2} \quad , \quad T = T_s \quad , \quad v = R_{es} r \quad \text{for } z = 0 \quad ,$$

$$0 \leq r \leq B \quad ,$$

$$\psi = 0 \quad , \quad \eta = 0 \quad , \quad \frac{\partial T}{\partial z} = Bic(T - T_a) + Bir[(T + T')^4 - (T + T')^4]$$

$$\text{for } z = 0 \quad , \quad B \leq r \leq 1 \quad ,$$

$$\psi = 0 \quad , \quad \eta = - \frac{1}{r} \frac{\partial^2 \psi}{\partial z^2} \quad , \quad T = T_c \quad , \quad v = R_{ec} r \quad \text{for } z = A \quad ,$$

$$0 \leq r \leq 1 \quad .$$

Thus, thermal convection in the Czochralski configuration is characterized by nine non-dimensional parameters:

(1) the Prandtl number, $Pr = \nu/\kappa$, (2) the Grashof number,

$Gr = \alpha g(T_C - T_S)R_C^3/\nu^2$, (3) the aspect ratio, $A = H/R_C$,
 (4) the radius ratio, $B = R_S/R_C$, (5) the convection Biot
 number, $Bic = hR_C/k$, (6) the radiation Biot number,
 $Bir = \epsilon\sigma(T_C - T_S)^3R_C/k$, (7) the temperature ratio,
 $T' = T_S/(T_C - T_S)$, (8) the seed rotational Reynolds number,
 $R_{es} = \omega_S R_C^2/\nu$, and (9) the crucible rotational Reynolds
 number, $R_{ec} = \omega_C R_C^2/\nu$.

d. Finite Difference Formulation

The above equations and boundary conditions will be formulated by finite differences. The region occupied by the fluid is represented by a rectangular network with M grid points in the horizontal direction and N grid points in the vertical direction as shown in Figure 49(c). The coordinate axes are discretized according to $r_I = (I - 1)\Delta r$ and $z_J = (J - 1)\Delta z$ where $(M - 1)\Delta r = 1$ and $(N - 1)\Delta z = A$. The crystal edge is at $I = I_S$. Time is discretized according to $t_n = n\Delta t$. The temperature, zonal velocity, vorticity, and stream function fields at time t_n are represented by M by N arrays with an element corresponding to each grid point and $f_{IJ}^n = f(r_I, z_J, t_n)$. Each element can be envisioned as the average value of the field over a grid square and time step:

$$f_{IJ}^n = \frac{1}{r_I \Delta r \Delta z \Delta t} \int_{r_I - \frac{\Delta r}{2}}^{r_I + \frac{\Delta r}{2}} \int_{z_J - \frac{\Delta z}{2}}^{z_J + \frac{\Delta z}{2}} \int_{t_n - \frac{\Delta t}{2}}^{t_n + \frac{\Delta t}{2}} f(r, z, t) r dr dz dt.$$

The finite difference equations are formulated in a manner similar to that employed by Williams¹⁰² for thermal convection in a rotating annulus. The explicit finite difference scheme incorporates centered time differences, special quadratically conservative difference forms for the Jacobians, and centered space differences for all other terms. For reasons of numerical stability the diffusive terms are evaluated with values at the preceding time step. The energy Equation (C48) becomes

$$\begin{aligned} \frac{T_{IJ}^{n+1} - T_{IJ}^{n-1}}{2\Delta t} = & \frac{1}{\Delta r(I-1)} J_{LIJ}(\psi^n, T^n) + \frac{1}{Pr\Delta r^2} \left[\frac{I-3/2}{I-1} T_{I-1J}^{n-1} \right. \\ & \left. - 2T_{IJ}^{n-1} + \frac{I-1/2}{I-1} T_{I+1J}^{n-1} \right] + \frac{1}{Pr\Delta z^2} \left[T_{IJ-1}^{n-1} \right. \\ & \left. - 2T_{IJ}^{n-1} + T_{IJ+1}^{n-1} \right] \end{aligned} \quad (C53)$$

in the interior of the grid,

$$\begin{aligned} \frac{T_{1J}^{n+1} - T_{1J}^{n-1}}{2\Delta t} = & \frac{1}{\Delta r^2 \Delta z} T_{2J}^n (\psi_{2J+1}^n - \psi_{2J-1}^n) + T_{1J-1}^n (\psi_{2J-1}^n + \psi_{2J}^n) \\ & - T_{1J+1}^n (\psi_{2J}^n + \psi_{2J+1}^n) \\ & + \frac{4}{Pr\Delta r^2} \left[T_{2J}^{n-1} - T_{1J}^{n-1} \right] + \frac{1}{Pr\Delta z^2} \left[T_{1J-1}^{n-1} - 2T_{1J}^{n-1} \right. \\ & \left. + T_{1J+1}^{n-1} \right] \end{aligned} \quad (C54)$$

$$\begin{aligned}
 \frac{v_{IJ}^{n+1} - v_{IJ}^{n-1}}{2\Delta t} &= \frac{1}{\Delta r(I-1)} J_{LIJ}(\psi^n, v^n) \\
 &+ \frac{v_{IJ}^n}{2\Delta r^2 \Delta z (I-1)^2} (\psi_{IJ+1}^n - \psi_{IJ-1}^n) \\
 &+ \frac{1}{\Delta r^2} \left[\frac{I-2}{I-3/2} v_{I-1J}^{n-1} - \frac{2(I-1)^2}{(I-1/2)(I-3/2)} v_{IJ}^{n-1} \right. \\
 &\left. + \frac{I}{I-1/2} v_{I+1J}^{n-1} \right] + \frac{1}{\Delta z^2} \left[v_{IJ-1}^{n-1} - 2v_{IJ}^{n-1} + v_{IJ+1}^{n-1} \right],
 \end{aligned} \tag{C57}$$

in the interior and

$$\begin{aligned}
 \frac{v_{I1}^{n+1} - v_{I1}^{n-1}}{2\Delta t} &= \frac{1}{4\Delta r^2 \Delta z} \frac{1}{I-1} \left[v_{I2}^n (\psi_{I-12}^n - \psi_{I+12}^n) \right. \\
 &\left. - v_{I-11}^n (\psi_{I-12}^n + \psi_{I2}^n) + v_{I+1}^n (\psi_{I2}^n + \psi_{I+12}^n) \right] \\
 &+ \frac{v_{I1}^n}{\Delta r^2 \Delta z (I-1)^2} \psi_{I2}^n \\
 &+ \frac{1}{\Delta r^2} \left[\frac{I-2}{I-3/2} v_{I-11}^{n-1} - \frac{2(I-1)^2}{(I-1/2)(I-3/2)} v_{I1}^{n-1} \right. \\
 &\left. + \frac{I}{I-1/2} v_{I+11}^{n-1} \right] + \frac{2}{\Delta z^2} \left[v_{I2}^{n-1} - v_{I1}^{n-1} \right],
 \end{aligned} \tag{C58}$$

at the upper free surface. The vorticity transport Equation (C50) becomes

$$\begin{aligned}
 \frac{\eta_{IJ}^{n+1} - \eta_{IJ}^{n-1}}{2\Delta T} &= J_{A_{IJ}}(\psi^n, \eta^n) + \frac{v_{IJ}^{n+1}}{\Delta r \Delta z (I-1)} (v_{IJ+1}^{n+1} - v_{IJ-1}^{n+1}) \\
 &\quad + \frac{Gr}{2\Delta r} (T_{I+1J}^{n+1} - T_{I-1J}^{n+1}) \\
 &\quad + \frac{1}{\Delta r^2} \left[\frac{I-2}{I-3/2} \eta_{I-1J}^{n-1} - \frac{2(I-1)^2}{(I-3/2)(I-1/2)} \eta_{IJ}^{n-1} \right. \\
 &\quad \left. + \frac{I}{I-1/2} \eta_{I+1J}^{n-1} \right] + \frac{1}{\Delta z^2} \left[\eta_{IJ+1}^{n-1} - 2\eta_{IJ}^{n-1} + \eta_{IJ-1}^{n-1} \right] .
 \end{aligned} \tag{C59}$$

The stream function Equation (C51) becomes

$$\begin{aligned}
 \frac{1}{\Delta r^3} \left[\frac{1}{I-3/2} \psi_{I-1J}^{n+1} - \frac{2(I-1)}{(I-3/2)(I-1/2)} \psi_{IJ}^{n+1} + \frac{1}{I-1/2} \psi_{I+1J}^{n+1} \right] \\
 + \frac{1}{\Delta r \Delta z^2 (I-1)} \left[\psi_{IJ-1}^{n+1} - 2\psi_{IJ}^{n+1} + \psi_{IJ+1}^{n+1} \right] = -\eta_{IJ}^{n+1} .
 \end{aligned} \tag{C60}$$

The special Jacobian $J_{L_{IJ}}$ for the temperature and zonal momentum equation is

$$J_{LIJ}(\psi, T) = \frac{1}{8\Delta x \Delta z} \left[\begin{array}{l} T_{I+1J}(\psi_{I+1 J+1} - \psi_{I+1 J-1} + \psi_{IJ+1} - \psi_{IJ-1}) \\ + T_{I-1J}(\psi_{I-1 J-1} - \psi_{I-1 J+1} + \psi_{IJ-1} - \psi_{IJ+1}) \\ + T_{IJ+1}(\psi_{I-1 J+1} - \psi_{I+1 J+1} + \psi_{I-1J} - \psi_{I+1J}) \\ + T_{IJ-1}(\psi_{I+1 J-1} - \psi_{I-1 J-1} + \psi_{I+1J} - \psi_{I-1J}) \end{array} \right] \quad (C61)$$

and the special Jacobian J_{AIJ} for the vorticity transport equation is

$$J_{AIJ}(\psi, \eta) = \frac{1}{12\Delta r^2 \Delta z} \left[\begin{array}{l} \left[\eta_{I+1 J+1}(\psi_{IJ+1} - \psi_{I+1J}) + \eta_{I+1J-1}(\psi_{I+1J} - \psi_{IJ-1}) \right. \\ \left. + \eta_{I+1J}(\psi_{I+1 J+1} - \psi_{I+1 J-1} + \psi_{IJ+1} - \psi_{IJ-1}) \right] / I \\ + \left[\eta_{IJ+1}(\psi_{I-1 J-1} - \psi_{I+1 J+1} - \psi_{I-1J} - \psi_{I+1J}) \right. \\ \left. + \eta_{IJ-1}(\psi_{I+1 J-1} - \psi_{I-1 J-1} + \psi_{I+1J} - \psi_{I-1J}) \right] \\ + \left[\eta_{I-1 J+1}(\psi_{I-1J} - \psi_{IJ+1}) + \psi_{I-1J-1}(\psi_{IJ-1} \right. \\ \left. - \psi_{I-1J}) \right] / (I-1) \\ + \eta_{I-1J}(\psi_{I-1 J-1} - \psi_{I-1 J+1} + \psi_{IJ-1} - \psi_{IJ+1}) \\ \left. \right] / (I-2) \quad (C62)$$

in the interior and

$$J_{A2J}(\psi, \eta) = \frac{1}{12\Delta r^2 \Delta z} \left[\begin{aligned} & \left[\eta_{3J+1} (\psi_{2J+1} - \psi_{3J}) + \eta_{3J-1} (\psi_{3J} - \psi_{2J-1}) \right. \\ & \quad \left. + \eta_{3J} (\psi_{3J+1} - \psi_{3J-1} + \psi_{2J+1} - \psi_{2J-1}) \right] / 2 \\ & + \left[\eta_{2J-1} (\psi_{3J-1} + \psi_{2J-1} + \psi_{3J}) \right. \\ & \quad - \eta_{2J+1} (\psi_{3J+1} + \psi_{2J+1} + \psi_{3J}) \\ & \quad \left. + \eta_{2J} (\psi_{2J-1} - \psi_{2J+1}) \right] \end{aligned} \right] \quad (C63)$$

at one grid point from the symmetry axis. The Lilly Jacobian⁹⁹ J_{LIJ} has the desirable feature of conserving temperature and its square within the grid. The Arakawa Jacobian² J_{AIJ} conserves vorticity, square vorticity and kinetic energy within the grid. As a result, these special Jacobians do not produce any spurious sources of energy or vorticity within the grid which results in a stable and accurate difference scheme.

In terms of finite differences the boundary conditions (Equations C52) are

$$\psi_{1J} = 0 , \quad \eta_{1J} = 0 , \quad v_{1J} = 0 \quad \text{at } I = 1 \quad \text{for all } J ,$$

$$T_{MJ} = T_{CJ} , \quad \psi_{MJ} = 0 , \quad \eta_{MJ} = - \frac{8(M-1)^4}{4(M-1)^2 - 1} \psi_{M-1J} ,$$

$$v_{MJ} = R_{ec} \quad \text{at } I = M \quad \text{for all } J , \quad (C64)$$

$$T_{I1} = T_s , \quad \psi_{I1} = 0 , \quad \eta_{I1} = - \frac{2}{\Delta r \Delta z^2 (I-1)} \psi_{I2} ,$$

$$v_{IJ} = \Delta r (I-1) R_{es} \quad \text{at } J = 1 \quad \text{for } I \leq I_s ,$$

$$\psi_{I1} = 0 , \quad \eta_{I1} = 0 \quad \text{at } J = 1 \quad \text{for } I > I_s ,$$

$$T_{IN} = T_{CI} , \quad \psi_{IN} = 0 , \quad \eta_{IN} = \frac{-2}{\Delta r \Delta z^2 (I-1)} \psi_{IN-1} ,$$

$$v_{IN} = \Delta r (I-1) R_{ec} \quad \text{at } J = N \quad \text{for all } I .$$

The no slip boundary condition at the rigid surfaces is included in this scheme through the boundary vorticity expressions. The boundary conditions for the temperature and zonal velocity fields at the free surface have been included in the finite difference formulation of the energy and the zonal momentum equations.

e. Requirements for Numerical Stability

Incorporation of a centered difference for the time derivative and evaluation of all other terms at the current and previous time step makes the scheme developed above of the explicit type. To avoid time splitting instability, solutions from adjacent time steps were periodically averaged¹⁰². It is well known that, to insure computational stability of an explicit finite difference scheme, the time increment must be chosen to be sufficiently small. The vorticity, zonal momentum, and energy equations may be written in the form.

$$\begin{aligned} \eta_{IJ}^{n+1} = & A_1 \eta_{I+1J}^{n-1} + A_2 \eta_{I-1J}^{n-1} + A_3 \eta_{IJ}^{n-1} + A_n \eta_{IJ+1}^{n-1} + A_5 \eta_{IJ-1}^{n-1} \\ & + 2\Delta t J_{AIJ}(\psi^n, \eta^n) + \frac{\Delta t}{\Delta r} Gr(T_{I+1J}^n - T_{I-1J}^n) \quad , \end{aligned} \quad (C65)$$

$$\begin{aligned} V_{IJ}^{n+1} = & A_1 V_{I+1J}^{n-1} + A_2 V_{I-1J}^{n-1} + A_3^1 V_{IJ}^{n-1} + A_4 V_{IJ+1}^{n-1} + A_5 V_{IJ-1}^{n-1} \\ & + \Delta \tau J_{LIJ}(\psi^n, V^n) \quad , \end{aligned} \quad (C66)$$

$$\begin{aligned} T_{IJ}^{n+1} = & B_1 T_{I+1J}^{n-1} + B_2 T_{I-1J}^{n-1} + B_3 T_{IJ}^{n-1} + B_4 T_{IJ+1}^{n-1} + B_5 T_{IJ-1}^{n-1} \\ & + \Delta \tau J_{Lij}^n(\psi, T) \quad . \end{aligned} \quad (C67)$$

In order to insure computational stability, all the A's and B's must be positive. This requirement reduces to a requirement that A_3 , A'_3 , and B_3 be positive, since all the other coefficients are always positive. In the interior

$$\begin{aligned}
 A_3 &= 1 - \Delta t \left[\frac{1}{\Delta r^2} \frac{2(I-1)^2}{(I-3/2)(I-1/2)} + \frac{2}{\Delta z^2} \right] > 0 \\
 A'_3 &= 1 - \Delta t \left[\frac{1}{\Delta r^2} \frac{2(I-1)^2}{(I-3/2)(I-1/2)} + \frac{2}{\Delta z^2} \right. \\
 &\quad \left. + \frac{1}{\Delta r^2 \Delta z (I-1)^2} \left(\psi_{IJ-1}^n - \psi_{IJ+1}^n \right) \right] > 0, \tag{C68} \\
 B_3 &= 1 - \Delta t \left[\frac{2}{Pr \Delta r^2} + \frac{2}{Pr \Delta z^2} \right] > 0.
 \end{aligned}$$

On the free surface

$$\begin{aligned}
 A'_3 &= 1 - \Delta t \left[\frac{1}{\Delta r^2} \frac{2(I-1)^2}{(I-3/2)(I-1/2)} + \frac{2}{\Delta z^2} \right. \\
 &\quad \left. - \frac{2}{\Delta r^2 \Delta z (I-1)^2} \psi_{I2}^n \right] > 0, \\
 B_3 &= 1 - \Delta t \left[\frac{2}{Pr \Delta r^2} + \frac{2}{Pr \Delta z^2} + \frac{2B_{ic}}{Pr \Delta z} + \frac{2B_{ir}}{Pr \Delta z} \right]. \tag{C69}
 \end{aligned}$$

On the axis

$$B_3 = 1 - \Delta t \left[\frac{4}{Pr\Delta r^2} + \frac{2}{Pr\Delta z^2} \right] > 0 \quad (C70)$$

and on the axis at the upper surface in the absence of a crystal

$$B_3 = 1 - \Delta t \left[\frac{4}{Pr\Delta r^2} + \frac{2}{Pr\Delta z^2} + \frac{ic}{Pr\Delta z} + \frac{ir}{Pr\Delta z} \right] \quad (C71)$$

For low Prandtl number fluids the most stringent requirement is that on the coefficient B_3 . For the case of germanium in argon both B_{ic} and B_{ir} are small so that the requirement becomes

$$\Delta t < 1 / \left(\frac{4}{Pr\Delta r^2} + \frac{2}{Pr\Delta z^2} \right) \quad (C72)$$

when a crystal is present and

$$\Delta t < 1 / \left(\frac{4}{Pr\Delta r^2} + \frac{2}{Pr\Delta z^2} + \frac{2B_{ic}}{Pr\Delta z} + \frac{2B_{ir}}{Pr\Delta z} \right) \quad (C73)$$

when no crystal is present. The requirement for computational stability of the advection terms can be expressed as

$$\Delta t < \text{Min} \left(\frac{\Delta r}{u}, \frac{\Delta z}{w} \right) \quad (C74)$$

That is Δt must be less than whichever is smaller between

the radial spacing divided by the maximum radial velocity and the vertical spacing divided by the maximum vertical velocity.

f. Solution of Stream Function Equation

The stream function is solved by using a trigonometric interpolation method used by Williams¹⁰². The stream function and vorticity are expanded in the trigonometric series:

$$\psi_{ij}^n = \sum_{k=1}^{N-2} A_{ik} \sin \left[\frac{\pi k}{N-1} (j-1) \right] ,$$

$$\eta_{ij}^n = \sum_{k=1}^{N-2} B_{ik} \sin \left[\frac{\pi k}{N-1} (j-1) \right] .$$

(C75)

Upon substituting these expressions, the stream function equation becomes

$$- a_i A_{i+1k} + b_{ik} A_{ik} - c_i A_{i-1k} = B_{ik} ,$$

(C76)

where

$$a_i = 1/(\Delta r)^2 \left(r + \frac{\Delta r}{2} \right) ,$$

$$c_i = 1/(\Delta r)^2 \left(r - \frac{\Delta r}{2} \right) ,$$

$$b_{ik} = a_i + c_i + \frac{2}{r(\Delta z)^2} \left(1 - \cos \frac{\pi k}{N-1} \right) .$$

(C77)

This equation is solved for the coefficients A_{i+1k} using Richtmyer's iteration method¹⁰³ which involves determining E_{ik} and F_{ik} so that

$$A_{ik} = E_{ik}A_{i+1k} + F_{ik} \quad . \quad (C78)$$

Upon substituting this expression in the above Equation E_{ik} and F_{ik} satisfy the recursion relations:

$$E_{ik} = a_i / (b_{ik} - c_i E_{i-1k}) \quad (C79)$$

$$F_{ik} = (b_{ik} + c_i F_{i-1k}) / (b_{ik} - c_i E_{i-1k}) \quad .$$

The condition that the stream function vanishes on the axis provides the starting values $E_{ik} = 0$ and $F_{ik} = 0$. The condition that the stream function vanishes at the wall provides that $A_{M-1k} = F_{M-1k}$.

The procedure used in calculating the stream function is as follows: (1) The B's are found by analyzing the vorticity field:

$$B_{ik} = \frac{2}{N} \sum_{j=1}^N \eta_{ij}^n \sin \left[\frac{\pi k}{N-1} (j-1) \right] \quad . \quad (C80)$$

(2) The E's and F's are found in increasing order by using the recursion relations together with the starting values, (3) The A's are found in decreasing order starting

with A_{M-1k} . (4) The stream function is found by evaluating the trigonometric series (Equation C75).

g. Computational Strategy

The computation proceeds according to the flow chart in Figure 50. The computation begins by specifying the dimensionless parameters, the grid size, and the control parameters. These are used to compute the numerical constants, after which, the temperature, zonal velocity, vorticity, and stream function fields are initialized and an initial time increment is determined. The computational loop consists of the following steps: (1) The time is incremented. (2) The new temperature field is calculated. (3) The new zonal velocity field is calculated. (4) The new interior vorticity field is calculated. (5) The new stream function field is calculated. (6) The new boundary vorticity field is calculated. (7) A new time increment is calculated and the process is repeated until either a specified number of time steps are executed or steady state is reached. The test for convergence to steady state is

$$\left| \frac{\psi_{cc}^{n+1} - \psi_{cc}^n}{\psi_{cc}^{n+1} \Delta t} \right| < .00001 \quad ,$$

where ψ_{cc} is the value of the stream function field at the center of the grid.

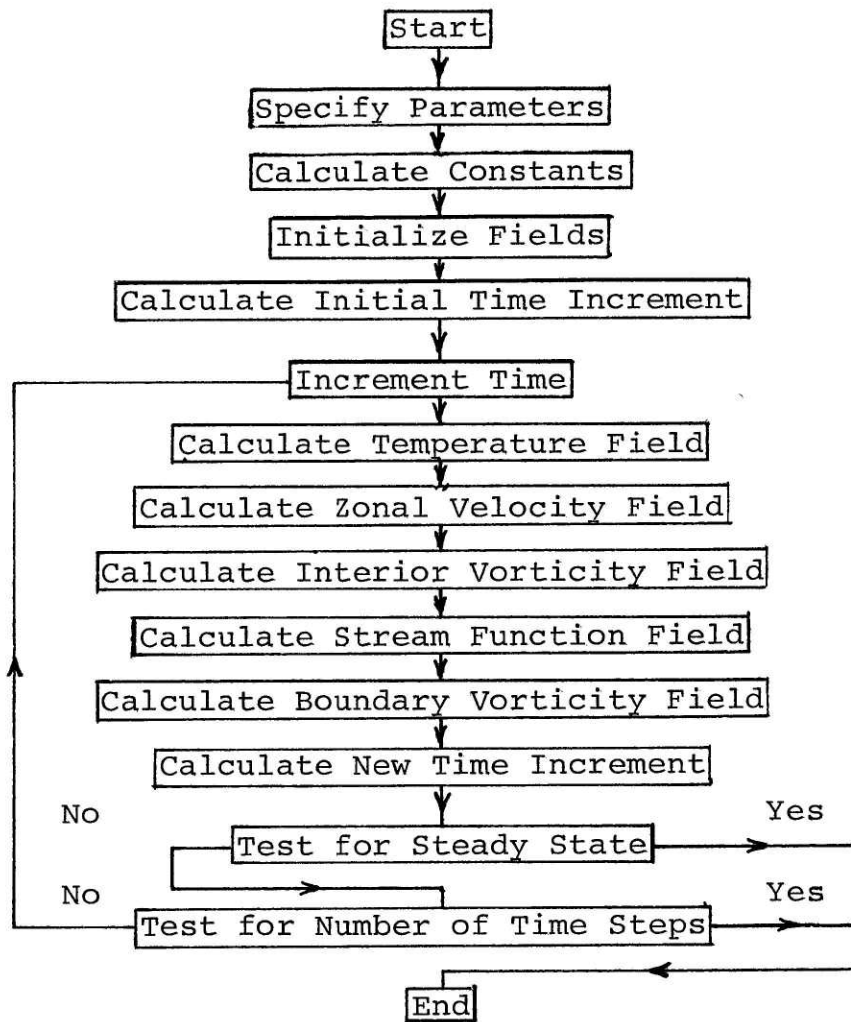


Figure 50. Flow Chart of Numerical Solution of Thermal Convection in the Czochralski Configuration

D. APPENDIX 4

COMPUTER PROGRAMS

1. Computer Program for Computation of Thermal Convection in the Horizontal Bridgman Configuration

COMMON M,M1,M2,N,N1,N2,JU,S,KMAX,KDEL,LMAX	MAIN0001
DIMENSION THETA(33,9),OMEGA(33,9),CALC(33,9),PSI(33,9),	MAIN0002
1 Q(295),P(32),TWCOS(8),RECIP(16),XVEL(33,9),YVEL(33,9)	MAIN0003
EQUIVALENCE (Q(1),PSI(2,1)),(XVEL(1,1),CALC(1,1))	MAIN0004
C SPECIFY THE PARAMETERS FOR THE CALCULATION.	MAIN0005
C INITIALIZE TO ZERO THE STREAM FUNCTION FIELD, PSI; THE VORTICITY FIELD,	MAIN0006
C OMEGA; THE CALCULATIONAL AND X VELOCITY FIELD, CALC; AND THE Y VELOCITY	MAIN0007
C FIELD, YVEL.	MAIN0008
CALL ERASE(PSI,297,OMEGA,297,CALC,297,YVEL,297)	MAIN0009
GR = 1000000.	MAIN0010
PR = .0171	MAIN0011
ASP = .25	MAIN0012
BI = 0.	MAIN0013
THETA0 = 0.	MAIN0014
C SPECIFY THE FINITE DIFFERECCE GRID.	MAIN0015
M=33	MAIN0016
N=9	MAIN0017
C DETERMINE FREQUENTLY USED INTEGERS.	MAIN0018
M1=M-1	MAIN0019
M2=M-2	MAIN0020
N1=N-1	MAIN0021
N2=N-2	MAIN0022
JU=M*N2	MAIN0023
IC=(M+1)/2	MAIN0024
JC=(N+1)/2	MAIN0025
IE=3	MAIN0026
JE=N-IE+1	MAIN0027
C SPECIFY THE CONTROL INTEGERS.	MAIN0028
JWRITE=1	MAIN0029
JPRINT=200	MAIN0030
JPUNCH=1000	MAIN0031
IWRITE=JWRITE	MAIN0032
IPRINT=JPRINT	MAIN0033
IPUNCH=JPUNCH	MAIN0034
ISTOP=0	MAIN0035
ICHECK=1000	MAIN0036

C	INITIALIZE TO ZERO THE TIME AND THE COUNTER, ICOUNT.	MAIN0037
	TIME=0.	MAIN0038
	ICOUNT=0	MAIN0039
C	DETERMINE THE CONTROL INTEGERS KMAX AND KDEL FOR SUBROUTINE EPUNCH AND	MAIN0040
C	SUBROUTINE EREAD.	MAIN0041
	KDEL=M	MAIN0042
	KMAX=0	MAIN0043
	5 KDEL=KDEL-6	MAIN0044
	KMAX=KMAX+1	MAIN0045
	IF(KDEL .GT. 6) GO TO 5	MAIN0046
	IF(KDEL .EQ. 3) KDEL = 2	MAIN0047
	IF(KDEL .EQ. 5) KDEL = 3	MAIN0048
C	DETERMINE THE CONTROL INTEGER LMAX FOR SUBROUTINE EPRINT.	MAIN0049
	LDEL=M1	MAIN0050
	LMAX=0	MAIN0051
	10 LDEL=LDEL-8	MAIN0052
	LMAX=LMAX+1	MAIN0053
	IF(LDEL .GT. 0) GO TO 10	MAIN0054
C	INITIALIZE THE TEMPERATURE FIELD, THETA.	MAIN0055
	AT = 0.	MAIN0056
	DT = 1./FLOAT(M1)	MAIN0057
	DO 15 I=2,M1	MAIN0058
	AT = AT + DT	MAIN0059
	DO 15 J=1,N	MAIN0060
	15 THETA(I,J) = AT	MAIN0061
	DO 20 J=1,N	MAIN0062
	THETA(1,J) = 0.	MAIN0063
	20 THETA(M,J) = 1.	MAIN0064
C	INITIALIZE TO ZERO THE VARIABLES FOR DETERMINING CONVERGECE, OLDT AND OLDP.	MAIN0065
	OLDP=0.	MAIN0066
	OLDT=0.	MAIN0067
C	DETERMINE THE ARRAY TWOCOS FOR SUBROUTINE XYPOIS.	MAIN0068
	LO=N1/2	MAIN0069
	TWOCOS(LO) = 0.	MAIN0070
	40 L=LO/2	MAIN0071
	TWOCOS(L) = SQRT(2. + TWOCOS(LO))	MAIN0072

	LO=L	MAIN0073
50	TWOCOS(N1-L) = -TWOCOS(L)	MAIN0074
	L=L+2*LO	MAIN0075
	IF((2*L/N1)*(2*LO-3)) 70,60,40	MAIN0076
60	TWOCOS(L)=(TWOCOS(L+LO) + TWOCOS(L-LO))/TWOCOS(LO)	MAIN0077
	GO TO 50	MAIN0078
C	DETERMINE THE CONSTANTS APPEARING IN THE FINITE DIFFERENCE EQUATIONS.	MAIN0079
70	A7=FLOAT(M1*M1)	MAIN0080
	A8=FLOAT(N1*N1)/(ASP*ASP)	MAIN0081
	A13=2.*A7	MAIN0082
	A14=2.*A8	MAIN0083
	A9=A13+A14	MAIN0084
	A1=A7/PR	MAIN0085
	A2=A8/PR	MAIN0086
	A3=A9/PR	MAIN0087
	A5=A14/PR	MAIN0088
	L=M1*N1	MAIN0089
	A4=FLOAT(L/8)/ASP	MAIN0090
	A6=FLOAT(L/4)/ASP	MAIN0091
	A10=A6/3.	MAIN0092
	A11=GR*FLOAT(M1/2)	MAIN0093
	A12=1./FLOAT(2*M1*M1)	MAIN0094
	A15 = FLOAT(N1/2)/ASP	MAIN0095
	A16 = FLOAT(M1/2)	MAIN0096
	A17 = 2.*BI*FLOAT(N1)/ASP/PR	MAIN0097
	AKE = FLOAT(L/2)/ASP	MAIN0098
	AT=1.6*ASP/FLOAT(L)	MAIN0099
	BBIG=FLOAT(M1)*ASP/FLOAT(N1)	MAIN0100
	S = BBIG*BBIG	MAIN0101
	BBIG=2.*(BBIG+1./BBIG)/PR	MAIN0102
	BIG=2.*BBIG	MAIN0103
C	THIS READ STATEMENT READS THE INTEGER I.	MAIN0104
	READ(5,75) I	MAIN0105
75	FORMAT(1X,I1)	MAIN0106
	WRITE(6,75) I	MAIN0107
C	IF I=0, THEN THE CALULATION PROCEEDS TO STATEMENT NUMBER 80. IF NOT, THEN	MAIN0108

C	A PREVIOUSLY TERMINATED CALCULATION IS TO BE CONTINUED AND THE VALUES OF TIME	MAIN0109
C	AND BIG ARE TO BE READ BY THE READ STATEMENT AND THE FIELDS THETA, PSI, AND	MAIN0110
C	OMEGA ARE TO BE READ IN BY SUBROUTINE EREAD.	MAIN0111
	IF(I .EQ. 0) GO TO 80	MAIN0112
	READ(5,360) TIME,BIG	MAIN0113
	CALL EREAD(THETA)	MAIN0114
	CALL EREAD(PHI)	MAIN0115
	CALL EREAD(OMEGA)	MAIN0116
C	THIS WRITE STATEMENT PROVIDES LABELING ON THE PRINTED OUTPUT AND IS THE	MAIN0117
C	STATEMENT BEGINNING A NEW TIME STEP AFTER SUBROUTINE EPRINT OR SUBROUTINE	MAIN0118
C	EPUNCH ARE USED.	MAIN0119
	80 WRITE(6,90) IC,JC,IC,JC,IC,IE,IE,IE,IE,JC,IE,JE	MAIN0120
	90 FORMAT(5X,'TIME',9X,'KE',8X,'OLDP',4X,'PSI(',I2,',',I2,')',	MAIN0121
	1 6X,'OLDT',2X,5(' THETA(',I2,',',I2,')'))	MAIN0122
C	EACH NEW TIME STEP BEGINS AT THIS STATEMENT EXCEPT WHEN SUBROUTINE EPRINT	MAIN0123
C	OR SUBROUTINE EPUNCH ARE USED. THE NEW TIME INCREMENT DT IS CALCULATED AND	MAIN0124
C	THE TIME IS INCREMENTED.	MAIN0125
	95 DT=AT/BIG	MAIN0126
	TIME=TIME+DT	MAIN0127
C	THIS DO LOOP DETERMINES THE CALCULATIONAL FIELD, CALC, FOR THE TEMPERATURE	MAIN0128
C	FIELD, THETA.	MAIN0129
	DO 105 I=2,M1	MAIN0130
C	THIS INNER DO LOOP DETERMINES CALC ON THE INTERIOR OF THE GRID.	MAIN0131
	DO 100 J=2,N1	MAIN0132
	100 CALC(I,J) = A1*(THETA(I+1,J) + THETA(I-1,J))	MAIN0133
	1 + A2*(THETA(I,J+1) + THETA(I,J-1))	MAIN0134
	2 - A3*THETA(I,J) + A4*	MAIN0135
	3 (THETA(I+1,J)*(PSI(I+1,J-1)-PSI(I+1,J+1)+PSI(I,J-1)-PSI(I,J+1))	MAIN0136
	4 +THETA(I-1,J)*(PSI(I-1,J+1)-PSI(I-1,J-1)+PSI(I,J+1)-PSI(I,J-1))	MAIN0137
	5 +THETA(I,J+1)*(PSI(I+1,J+1)-PSI(I-1,J+1)+PSI(I+1,J)-PSI(I-1,J))	MAIN0138
	6 +THETA(I,J-1)*(PSI(I-1,J-1)-PSI(I+1,J-1)+PSI(I-1,J)-PSI(I+1,J)))	MAIN0139
C	THIS STATEMENT DETERMINES CALC ON THE UPPER BOUNDARY OF THE GRID.	MAIN0140
	CALC(I,1) = A1*(THETA(I+1,1) + THETA(I-1,1))	MAIN0141
	1 + A5*THETA(I,2) - A3*THETA(I,1)	MAIN0142
	2 + A7*(THETA0-THETA(I,1))	MAIN0143
C	THIS STATEMENT DETERMINES CALC ON THE LOWER BOUNDARY OF THE GRID.	MAIN0144

105	CALC(I,N) = A1*(THETA(I+1,N) + THETA(I-1,N))	MAIN0145
1	+ A5*THETA(I,N1) - A3*THETA(I,N)	MAIN0146
C	THESE TWO DO LOOPS CALCULATE THE NEW TEMPERATURE FIELD.	MAIN0147
	DO 110 J=1,N	MAIN0148
	DO 110 I=2,M1	MAIN0149
110	THETA(I,J) = THETA(I,J) + DT*CALC(I,J)	MAIN0150
C	THESE TWO DO LOOPS DETERMINE THE CALCULATIONAL FIELD, CALC, FOR THE INTERIOR	MAIN0151
C	VORTICITY FIELD, OMEGA.	MAIN0152
	DO 200 J=2,N1	MAIN0153
	DO 200 I=2,M1	MAIN0154
200	CALC(I,J) = A7*(OMEGA(I+1,J) + OMEGA(I-1,J))	MAIN0155
1	+ A8*(OMEGA(I,J+1) + OMEGA(I,J-1))	MAIN0156
2	- A9*OMEGA(I,J) + A10*	MAIN0157
3	(OMEGA(I+1,J)*(PSI(I+1,J-1)-PSI(I+1,J+1)+PSI(I,J-1)-PSI(I,J+1))	MAIN0158
4	+OMEGA(I-1,J)*(PSI(I-1,J+1)-PSI(I-1,J-1)+PSI(I,J+1)-PSI(I,J-1))	MAIN0159
5	+OMEGA(I,J+1)*(PSI(I+1,J+1)-PSI(I-1,J+1)+PSI(I+1,J)-PSI(I-1,J))	MAIN0160
6	+OMEGA(I,J-1)*(PSI(I-1,J-1)-PSI(I+1,J-1)+PSI(I-1,J)-PSI(I+1,J))	MAIN0161
7	+ OMEGA(I+1,J+1)*(PSI(I+1,J) - PSI(I,J+1))	MAIN0162
8	+ OMEGA(I+1,J-1)*(PSI(I,J-1) - PSI(I+1,J))	MAIN0163
9	+ OMEGA(I-1,J+1)*(PSI(I,J+1) - PSI(I-1,J))	MAIN0164
A	+ OMEGA(I-1,J-1)*(PSI(I-1,J) - PSI(I,J-1))	MAIN0165
B	- A11*(THETA(I+1,J) - THETA(I-1,J))	MAIN0166
C	THESE TWO DO LOOPS CALCULATE THE NEW INTERIOR VORTICITY FIELD.	MAIN0167
	DO 210 J=2,N1	MAIN0168
	DO 210 I=2,M1	MAIN0169
210	OMEGA(I,J) = OMEGA(I,J) + DT*CALC(I,J)	MAIN0170
	L=0	MAIN0171
C	THIS DO LOOP PREPARES THE INTERIOR VORTICITY FOR INPUT TO SUBROUTINE XYPOIS	MAIN0172
C	WHICH SOLVES POISSON'S EQUATION FOR DETERMINING THE STREAM FUNCTION, PSI.	MAIN0173
	DO 300 J=2,N1	MAIN0174
	L=L+M	MAIN0175
	K=L	MAIN0176
	DO 300 I=2,M1	MAIN0177
	K=K+1	MAIN0178
300	Q(K) = A12*OMEGA(I,J)	MAIN0179
C	SUBROUTINE XYPOIS RETURNS THE STREAM FUNCTION, PSI, IN THE FIELD Q.	MAIN0180

CALL XYPOIS(Q,P,TWOCOS,RECIP)	MAIN0181
C THE NEXT TWO DO LOOPS DETERMINE THE NEW VORTICICITY ON THE GRID BOUNDARY.	MAIN0182
DO 310 J=2,N1	MAIN0183
C THIS STATEMENT CALCULATES THE NEW VORTICITY ON THE LEFT BOUNDARY.	MAIN0184
OMEGA(1,J) = -A13*PSI(2,J)	MAIN0185
C THIS STATEMENT CALCULATES THE NEW VORTICITY ON THE RIGHT BOUNDARY.	MAIN0186
310 OMEGA(M,J) = -A13*PSI(M1,J)	MAIN0187
DO 315 I=2,M1	MAIN0188
C THIS STATEMENT CALCULATES THE NEW VORTICITY ON THE LOWER BOUNDARY.	MAIN0189
315 OMEGA(I,N) = -A14*PSI(I,N1)	MAIN0190
C DETERMINE THE PARAMETER BIG. IF BIG = 2*BBIG, THEN THE MAXIMUM TIME STEP IS	MAIN0191
C BASED ON A DIFFUSIVE REQUIRMENT. IF BIG = MAXIMUM DIFFERENCE OF PSI, THEN	MAIN0192
C THE MAXIMUM TIME STEP IS BASED ON THE NONLINEAR REQUIREMENT.	MAIN0193
BIG = BBIG	MAIN0194
BIG = 2.*BIG	MAIN0195
DO 325 J=2,N1	MAIN0196
DO 325 I=2,M1	MAIN0197
DIFFI = ABS(PSI(I+1,J) - PSI(I-1,J))	MAIN0198
DIFFJ = ABS(PSI(I,J+1) - PSI(I,J-1))	MAIN0199
IF(DIFFJ .GT. BIG) BIG = DIFFJ	MAIN0200
IF(DIFFI .GT. BIG) BIG = DIFFI	MAIN0201
325 CONTINUE	MAIN0202
C INCREMENT THE COUNTER.	MAIN0203
ICOUNT = ICOUNT + 1	MAIN0204
C TEST FOR CONVERGENCE OF THE CALCULATION.	MAIN0205
TEST = THETA(IC,JC)	MAIN0206
OLDT = (TEST - OLDT)/TEST/DT	MAIN0207
PEST = PSI(IC,JC)	MAIN0208
IF(PEST .EQ. 0.) GO TO 330	MAIN0209
OLDP = (PEST - OLDP)/PEST/DT	MAIN0210
IF(ABS(OLDT) .GT. 1. .OR. ABS(OLDP) .GT. 1.) GO TO 330	MAIN0211
IF(ISTOP .EQ. 1) GO TO 330	MAIN0212
ISTOP = 1	MAIN0213
IPUNCH = IPRINT + JPRINT	MAIN0214
C COMPARE THE COUNTER WITH IWRITE TO DETERMINE IF OUTPUT IS REQUIRED.	MAIN0215
330 IF(ICOUNT .LT. IWRITE) GO TO 345	MAIN0216

IWRITE = IWRITE + JWRITE	MAIN0217
KE = 0.	MAIN0218
C THESE TWO DO LOOPS DETERMINE THE KINETIC ENERGY OF THE FLUID.	MAIN0219
DO 335 J=2,N1	MAIN0220
DO 335 I=2,M1	MAIN0221
335 KE = KE + PSI(I,J)*OMEGA(I,J)	MAIN0222
KE = AKE*KE	MAIN0223
C THIS WRITE STATEMENT PRINTS INFORMATION ON THE CALCULATION.	MAIN0224
WRITE(6,340) TIME,KE,OLDP,PSI(IC,JC),OLDT,THETA(IC,JC),	MAIN0225
1 THETA(IC,IE),THETA(IE,IE),THETA(IE,JC),THETA(IE,JE)	MAIN0226
340 FORMAT(1X,E12.6,E11.4,1X,E9.2,1X,E13.6,1X,E9.2,5E13.6)	MAIN0227
C UP DATE THE PARAMETERS FOR DETERMINING CONVERGENCE.	MAIN0228
345 OLDT = TEST	MAIN0229
OLDP = PEST	MAIN0230
C COMPARE THE COUNTER WITH IPRINT TO DETERMINE IF THE FIELDS THETA, PSI, AND	MAIN0231
C OMEGA SHOULD BE PRINTED BY SUBROUTINE EPRINT.	MAIN0232
IF(ICOUNT .LT. IPRINT) GO TO 95	MAIN0233
IPRINT = IPRINT + JPRINT	MAIN0234
WRITE(6,346)	MAIN0235
346 FORMAT(//1X,"THETA"//)	MAIN0236
CALL EPRINT(THETA)	MAIN0237
WRITE(6,347)	MAIN0238
347 FORMAT(//1X,"PSI"//)	MAIN0239
CALL EPRINT(PSI)	MAIN0240
WRITE(6,348)	MAIN0241
348 FORMAT(//1X,"OMEGA"//)	MAIN0242
CALL EPRINT(OMEGA)	MAIN0243
C COMPARE THE COUNTER WITH IPUNCH TO DETERMINE IF THE FIELDS THETA, PSI,	MAIN0244
C OMEGA, XVEL, AND YVEL SHOULD BE PUNCHED ON CARDS BY SUBROUTINE EPUNCH.	MAIN0245
IF(ICOUNT .LT. IPUNCH) GO TO 80	MAIN0246
IPUNCH = IPUNCH + JPUNCH	MAIN0247
C THESE TWO DO LOOPS DETERMINE THE VELOCITY FIELDS, XVEL AND YVEL.	MAIN0248
DO 355 I=2,M1	MAIN0249
DO 350 J=2,N1	MAIN0250
XVEL(I,J) = A14*(PSI(I,J+1) - PSI(I,J-1))	MAIN0251
350 YVEL(I,J) = A15*(PSI(I-1,J) - PSI(I+1,J))	MAIN0252

XVEL(I,1) =2.*A14*PSI(I,2)	MAIN0253
355 XVEL(I,N) = 0.	MAIN0254
C THIS WRITE STATEMENT PUNCHES ON CARDS THE TIME AND ITS INCREMENT PARAMETER,	MAIN0255
C BIG, THE PARAMETERS FOR THE CALCULATION, AND THE GRID PARAMETERS.	MAIN0256
WRITE(7,360) TIME,BIG,ASP,GR,PR,HEAT,THETA0,M,N	MAIN0257
360 FORMAT(1X,2E13.6,4E10.3,F7.3,2I3)	MAIN0258
C THE FIELDS ARE NOW PUNCHED ON CARDS BY EPUNCH.	MAIN0259
CALL EPUNCH(THETA)	MAIN0260
CALL EPUNCH(OMEGA)	MAIN0261
CALL EPUNCH(PSI)	MAIN0262
CALL EPUNCH(XVEL)	MAIN0263
CALL EPUNCH(YVEL)	MAIN0264
C IF ISTOP=1, THEN THE CALCULATION HAS CONVERGED AND THE CALCULATION STOPS.	MAIN0265
IF(ISTOP .EQ. 1) GO TO 400	MAIN0266
C IF THE COUNTER IS GREATER THAN OR EQUAL TO ICHECK, THEN THE MAXIMUM ALLOWED	MAIN0267
C NUMBER OF TIME STEPS HAS BEEN REACHED AND THE CALCULATION STOPS.	MAIN0268
IF(ICOUNT .GE. ICHECK) GO TO 420	MAIN0269
GO TO 80	MAIN0270
400 WRITE(6,410)	MAIN0271
410 FORMAT(////////// ' ISTOP IS ONE')	MAIN0272
CALL EXIT	MAIN0273
420 WRITE(6,430)	MAIN0274
430 FORMAT(////////// ' ICHECK HAS BEEN EXCEEDED')	MAIN0275
CALL EXIT	MAIN0276
END	MAIN0277

```

SUBROUTINE XYPOIS(Q,P,TWOCOS,RECIP)
COMM O M,M1,IU,N,N1,N2,JU,S,KMAX,KDEL,LMAX
DIMENSION Q(295),P(32),TWOCOS(8),RECIP(16)
LO = N1/2
P(M1) = 0.
ID = 1
MODE = 2
15 LI = 2*LO
  IPHASE = 2*MODE - LI/N1
  JD = M*N1/LI
  JH = M*(N1/(2*LI))
  JT = JD + JH
  JI = 2*JD
  JO = JD*MODE
  DO 11 J=JO,JU,JI
    J1 = J + 1
    JIU = J + IU
    GO TO (20, 24, 26, 28), IPHASE
28 DO 29 I=J1,JIU
  PI = Q(I) - Q(I-JT) - Q(I+JT)
  Q(I) = Q(I) - Q(I-JH) - Q(I+JH) + Q(I+JD) + Q(I-JD)
29 P(I-J) = PI + Q(I)
  GO TO 10
26 DO 27 I=J1,JIU
  P(I-J) = 2.*Q(I)
27 Q(I) = Q(I+JD) + Q(I-JD)
  GO TO 10
24 DO 25 I=J1,JIU
  P(I-J) = 2.*Q(I) + Q(I+JD) + Q(I-JD)
25 Q(I) = Q(I) - Q(I+JH) - Q(I-JH)
  GO TO 10
20 DO 23 I=J1,JIU
  P(I-J) = 2.*Q(I) + Q(I+JD) + Q(I-JD)
23 Q(I) = 0.
10 DO 22 L=LO,N1,LI
  A = 2. + S*(2. - TWOCOS(L))

```

```

POIS0001
POIS0002
POIS0003
POIS0004
POIS0005
POIS0006
POIS0007
POIS0008
POIS0009
POIS0010
POIS0011
POIS0012
POIS0013
POIS0014
POIS0015
POIS0016
POIS0017
POIS0018
POIS0019
POIS0020
POIS0021
POIS0022
POIS0023
POIS0024
POIS0025
POIS0026
POIS0027
POIS0028
POIS0029
POIS0030
POIS0031
POIS0032
POIS0033
POIS0034
POIS0035
POIS0036

```

```

19  RECIP(ID) = 1./A
    II = 2*ID
    DO 21 I=II,IU,II
21  P(I) = P(I)*A + P(I+ID) + P(I-ID)
    A = A*A - 2.
    ID = II
    IF ((A .LT. 1.E8) .AND. (ID .LT. M1/2)) GO TO 19
    A = S/A
    DO 18 I=II,IU,II
18  P(I) = P(I)*A
16  ID = II/2
    A = RECIP(ID)
    P(ID) = (S*P(ID) + P(II))*A
    IO = ID + II
    DO 17 I=IO,IU,II
17  P(I) = (S*P(I) + P(I+ID) + P(I-ID))*A
    II = ID
    IF (ID .GT. 1) GO TO 16
22  CONTINUE
    DO 11 I =J1,JIU
11  Q(I) = Q(I) + P(I-J)
    GO TO (14, 13, 12, 12), IPHASE
12  LO = LO/2
    IF (LO .EQ. 1) MODE = 1
    GO TO 15
13  LO = 2*LO
    IF (LO .LT. N1) GO TO 15
14  RETURN
    END

```

```

POIS0037
POIS0038
POIS0039
POIS0040
POIS0041
POIS0042
POIS0043
POIS0044
POIS0045
POIS0046
POIS0047
POIS0048
POIS0049
POIS0050
POIS0051
POIS0052
POIS0053
POIS0054
POIS0055
POIS0056
POIS0057
POIS0058
POIS0059
POIS0060
POIS0061
POIS0062
POIS0063
POIS0064
POIS0065

```


	SUBROUTINE EPRINT(FUN)	PRNT0001
C	SUBROUTINE EPRINT OUTPUTS A FIELD FUN (THETA, PSI, OR, OMEGA) ON	PRNT0002
C	THE PRINTER. LMAX CONTROLS THE OUTPUT OF THE FIELD WHICH CONSISTS OF LMAX	PRNT0003
C	BLOCKS. EACH BLOCK CONSISTS OF N LINES WITH 9 ELEMENTS PER LINE. THE FIRST	PRNT0004
C	COLUMN OF ONE BLOCK IS IDENTICAL TO THE LAST COLUMN OF THE PRECEEDING BLOCK.	PRNT0005
	COMMON M,M1,M2,N,N1,N2,JU,S,KMAX,KDEL,LMAX	PRNT0006
	DIMENSION FUN(33,9)	PRNT0007
	I2 = 1	PRNT0008
	DO 15 L=1,LMAX	PRNT0009
	I1=I2	PRNT0010
	I2=I2+8	PRNT0011
	WRITE(6,10)((FUN(I,J),I=I1,I2),J=1,N)	PRNT0012
10	FORMAT(4X,9E14.6)	PRNT0013
15	WRITE(6,20)	PRNT0014
20	FORMAT(//)	PRNT0015
	RETURN	PRNT0016
	END	PRNT0017

	SUBROUTINE EREAD (FUN)	READ0001
C	SUBROUTINE EREAD INPUTS A FIELD FUN FROM CARDS. THIS FIELD CAN BE THETA,	READ0002
C	PSI, OR OMEGA. KMAX AND KDEL CONTROL THE INPUT OF THE FIELD WHICH CONSISTS	READ0003
C	OF KMAX BLOCKS OF SIZE 6 BY N ELEMENTS AND 1 BLOCK OF SIZE 1 BY N, 3 BY N,	READ0004
C	OR 5 BY N ELEMENTS. EACH OF THE KMAX BLOCKS CONSISTS OF N CARDS WITH 6	READ0005
C	ELEMENTS PER CARD. THE REMAINING BLOCK CONSISTS OF L CARDS WITH 6 ELEMENTS	READ0006
C	PER CARD AND 1 CARD WITH N-6*L ELEMENTS WHEN KDEL=1, N CARDS WITH 3 ELEMENTS	READ0007
C	PER CARD WHEN KDEL=2, AND N CARDS WITH 5 ELEMENTS PER CARD WHEN KDEL=3.	READ0008
	COMMON M,M1,M2,N,N1,N2,JU,S,KMAX,KDEL,LMAX	READ0009
	DIMENSION FUN(33,9)	READ0010
	IMAX = 0	READ0011
C	THIS DO LOOP READS KMAX*N CARDS WITH 6 ELEMENTS PER CARD.	READ0012
	DO 1 K=1,KMAX	READ0013
	IMIN = IMAX + 1	READ0014
	IMAX = IMAX + 6	READ0015
	1 READ (5,2)((FUN(I,J),I=IMIN,IMAX),J=1,N)	READ0016
	2 FORMAT(1X,6E13.6)	READ0017
	IMIN = IMAX + 1	READ0018
	GO TO (3,5,7),KDEL	READ0019
C	IF KDEL=1, THIS READ STATEMENT READS L CARDS WITH 6 ELEMENTS PER CARD AND	READ0020
C	1 CARD WITH N-6*L ELEMENTS.	READ0021
	3 READ (5,4) (FUN(M,J),J=1,N)	READ0022
	4 FORMAT(1X,6E13.6)	READ0023
	RETURN	READ0024
C	IF KDEL=2, THIS READ STATEMENT READS N CARDS WITH 3 ELEMENTS PER CARD.	READ0025
	5 READ (5,6)((FUN(I,J),I=IMIN,M),J=1,N)	READ0026
	6 FORMAT(1X,3E13.6)	READ0027
	RETURN	READ0028
C	IF KDEL=3, THIS READ STATEMENT READS N CARDS WITH 5 ELEMENTS PER CARD.	READ0029
	7 READ (5,8)((FUN(I,J),I=IMIN,M),J=1,N)	READ0030
	8 FORMAT(1X,5E13.6)	READ0031
	RETURN	READ0032
	END	READ0033

	SUBROUTINE EPUNCH(FUN)	PNCH0001
C	SUBROUTINE EPUNCH OUTPUTS A FIELD FUN ON CARDS. THIS FIELD CAN BE THETA,	PNCH0002
C	PSI, OR OMEGA. KMAX AND KDEL CONTROL THE OUTPUT OF THE FIELD WHICH CONSISTS	PNCH0003
C	OF KMAX BLOCKS OF SIZE 6 BY N ELEMENTS AND 1 BLOCK OF SIZE 1 BY N, 3 BY N,	PNCH0004
C	OR 5 BY N ELEMENTS. EACH OF THE KMAX BLOCKS CONSISTS OF N CARDS WITH 6	PNCH0005
C	ELEMENTS PER CARD. THE REMAINING BLOCK CONSISTS OF L CARDS WITH 6 ELEMENTS	PNCH0006
C	PER CARD AND 1 CARD WITH N-6*L ELEMENTS WHEN KDEL=1, N CARDS WITH 3 ELEMENTS	PNCH0007
C	PER CARD WHEN KDEL=2, AND N CARDS WITH 5 ELEMENTS PER CARD WHEN KDEL=3.	PNCH0008
	COMMON M,M1,M2,N,N1,N2,JU,S,KMAX,KDEL,LMAX	PNCH0009
	DIMENSION FUN(33,9)	PNCH0010
	IMAX = 0	PNCH0011
C	THIS DO LOOP PUNCHS KMAX*N CARDS WITH 6 ELEMENTS PER CARD.	PNCH0012
	DO 1 K=1,KMAX	PNCH0013
	IMIN = IMAX + 1	PNCH0014
	IMAX = IMAX + 6	PNCH0015
	1 WRITE(7,2)((FUN(I,J),I=IMIN,IMAX),J=1,N)	PNCH0016
	2 FORMAT(1X,6E13.6)	PNCH0017
	IMIN = IMAX + 1	PNCH0018
	GO TO (3,5,7),KDEL	PNCH0019
C	IF KDEL=1, THIS WRITE STATEMENT PUNCHS L CARDS WITH 6 ELEMENTS PER CARD AND	PNCH0020
C	1 CARD WITH N-6*L ELEMENTS.	PNCH0021
	3 WRITE(7,4) (FUN(M,J),J=1,N)	PNCH0022
	4 FORMAT(1X,6E13.6)	PNCH0023
	RETURN	PNCH0024
C	IF KDEL=2, THIS WRITE STATEMENT PUNCHS N CARDS WITH 3 ELEMENTS PER CARD.	PNCH0025
	5 WRITE(7,6)((FUN(I,J),I=IMIN,M),J=1,N)	PNCH0026
	6 FORMAT(1X,3E13.6)	PNCH0027
	RETURN	PNCH0028
C	IF KDEL=3, THIS WRITE STATEMENT PUNCHS N CARDS WITH 5 ELEMENTS PER CARD.	PNCH0029
	7 WRITE(7,8)((FUN(I,J),I=IMIN,M),J=1,N)	PNCH0030
	8 FORMAT(1X,5E13.6)	PNCH0031
	RETURN	PNCH0032
	END	PNCH0033

2. Computer Program for Computation of Thermal Convection in the Czochralski Configuration

```

COMMON I,K,L,IK,FSIN,FCOS,N,JN,JM,JM1,N2,M,KMAX,KDEL,ACOS
DIMENSION TA(17),T(17,17),U(17,17),V(17,17),S(17,17),CALC(17,17)
1      ,TO(17,17),UO(17,17),VO(17,17)
1      ,GSIN(7),FSIN(4,15),FCOS(4, 8),G(15)
1      ,AA(15),BB(15),CC(15),D(15),E(15),F(15),SUM(15)
DATA TR/50./,TA(1),TA(17)/840.,848.4/,
1      T(1,1),T(1,17)/939.,947.4/,T(17,1),T(17,17)/947.4,947.4/
TIME = 0.
PR = .00667
C TEMPERATURES ARE NOT NON DIMENSIONALIZED
C GR=GR/(TH-TC)
GR = 2.39616E+05
ASP = .8125
BI = 0.
BIR = 9.61615E-12
REC = 0.
RES = 4021.24
TB = 0.
M=17
N=17
IXTL = 5
JPRINT = 1
JPUNCH = 100
ICHECK = 100
JVRG = 20
K1 = 2
K2 = M + 1 - K1
K3 = N + 1 - K1
INDEX = 0
IXTL1 = IXTL + 1
M1 = M-1
M2 = M-2
N1 = N-1
N2 = N-2
JM = N1/4
JM1 = JM-1

```

```

MAIN0001
MAIN0002
MAIN0003
MAIN0004
MAIN0005
MAIN0006
MAIN0007
MAIN0008
MAIN0009
MAIN0010
MAIN0011
MAIN0012
MAIN0013
MAIN0014
MAIN0015
MAIN0016
MAIN0017
MAIN0018
MAIN0019
MAIN0020
MAIN0021
MAIN0022
MAIN0023
MAIN0024
MAIN0025
MAIN0026
MAIN0027
MAIN0028
MAIN0029
MAIN0030
MAIN0031
MAIN0032
MAIN0033
MAIN0034
MAIN0035
MAIN0036

```

```

JN1 = N1/2
JN = JN1 + 1
JN2 = JN1 - 1
IC = M1/2 + 1
JC = N1/2 + 1
IPUNCH = JPUNCH
IPRINT = JPRINT
      IVRG = JVRG
KDEL = M
KMAX = 0
1 KDEL = KDEL - 6
  KMAX = KMAX + 1
  IF(KDEL .GT. 6) GO TO 1
  IF(KDEL .EQ. 3) KDEL = 2
  IF(KDEL .EQ. 5) KDEL = 3
  X = M1
  Y = N1
C  TEMPRATURES ARE NOT NON DIMENSIONALIZED
  A1 = TA(1)
  B1 = TA(M) - A1
  B2 = T(M,1)
  A3 = T(1,N)
  B3 = T(M,N) - A3
  A = 1./X
  B = A
  DO 5 I=2,M1
    C = B*B
    TA(I) = A1 + B1*C
    T(I,1) = B2*C
    T(I,N) = A3 + B3*C
5  B = B + A
  DO 10 I=1,M
    A = T(I,1)
    B = (T(I,N)-A)/Y
  DO 10 J=2,N1
    A = A + B

```

```

MAIN0037
MAIN0038
MAIN0039
MAIN0040
MAIN0041
MAIN0042
MAIN0043
MAIN0044
MAIN0045
MAIN0046
MAIN0047
MAIN0048
MAIN0049
MAIN0050
MAIN0051
MAIN0052
MAIN0053
MAIN0054
MAIN0055
MAIN0056
MAIN0057
MAIN0058
MAIN0059
MAIN0060
MAIN0061
MAIN0062
MAIN0063
MAIN0064
MAIN0065
MAIN0066
MAIN0067
MAIN0068
MAIN0069
MAIN0070
MAIN0071
MAIN0072

```

```

10 T(I,J) = A
   TB = TA(1)
   TR4 = (TR+273.)*4.
   CALL ERASE(S,289,V,289,U,289)
   CALL EREAD(T)
   CALL EREAD(S)
   CALL EREAD(V)
   X = M1
   Y = N1/ASP
   A1 = RES*X
   B1 = REC*X
   A2 = 0.
   B2 = 0.
   DO 15 I=2,M1
     A2 = A2 + A1
     B2 = B2 + B1
     IF(I .LE. IXTL) U(I,1) = A2
15  U(I,N) = B2
     DO 20 J=1,N
20  U(M,J) = REC
     DO 21 I=1,IXTL
21  T(I,1) = 937.
     DO 25 J=1,N
     DO 25 I=1,M
     TO(I,J) = T(I,J)
     UO(I,J) = U(I,J)
25  VO(I,J) = V(I,J)
     WRITE(6,850)(TA(I),I=1,9)
     WRITE(6,850)(TA(I),I=9,17)
     WRITE(6,850)((T(I,J),I=1,9),J=1,17)
     WRITE(6,850)((T(I,J),I=9,17),J=1,17)
     A10 = X*X
     A9 = Y*Y
     A18 = X*Y/2.
     A5 = A10*Y
     A1 = A5/8.

```

```

MAIN0073
MAIN0074
MAIN0075
MAIN0076
MAIN0077
MAIN0078
MAIN0079
MAIN0080
MAIN0081
MAIN0082
MAIN0083
MAIN0084
MAIN0085
MAIN0086
MAIN0087
MAIN0088
MAIN0089
MAIN0090
MAIN0091
MAIN0092
MAIN0093
MAIN0094
MAIN0095
MAIN0096
MAIN0097
MAIN0098
MAIN0099
MAIN0100
MAIN0101
MAIN0102
MAIN0103
MAIN0104
MAIN0105
MAIN0106
MAIN0107
MAIN0108

```

```

A12 = A5/4.
A14 = 2.*A5
A16 = A5/12.
  A20 = A16/2.
A2 = A9/PR
A3 = A10/PR
A4 = -2.*(A2+A3)
A6 = 4.*A3
A7 = 2.*A2
A15 = -A6-A7
A8 = 2.*BI*Y/PR
A8R = 2.*BIR*Y/PR
A11 = 2.*A9
A13 = -2.*A9
A19 = GR*X/8.
A21 = A13*X
A22 = -8.*A10*A10/(4.*A10-1.)
A23 = -2.*A10
A24 = A13/A20
A25 = A23/A20
A26 = -2.*A25/A5
  A27 = 4.*A10/3.
  A28 = -2.*A27+A13
DT1 = .5/(A8+A8R-A15)
DT = X*(.5*ASP/GR)**.5
IF( DT .LT. DT1) DT1=DT
BIGG = 1./(A14*DT1)
AT = 1.8/A5
BIG = 4.*BIGG
WRITE (6,30) A1,A2,A3,A4,A5,A6,A7,A8,A9,A10,A11,A12,A13,A14,A15,
1      A16,A17,A18,A19,A20,A21,A22,A23,A24,A25,A26,AT,BIGG
2      ,A8R,TR
30 FORMAT(/7(6X,E13.6)/)
CALC(1,1) = 0.
OLDT = T(IC,JC)
OLDS = S(IC,JC)

```

```

MAIN0109
MAIN0110
MAIN0111
MAIN0112
MAIN0113
MAIN0114
MAIN0115
MAIN0116
MAIN0117
MAIN0118
MAIN0119
MAIN0120
MAIN0121
MAIN0122
MAIN0123
MAIN0124
MAIN0125
MAIN0126
MAIN0127
MAIN0128
MAIN0129
MAIN0130
MAIN0131
MAIN0132
MAIN0133
MAIN0134
MAIN0135
MAIN0136
MAIN0137
MAIN0138
MAIN0139
MAIN0140
MAIN0141
MAIN0142
MAIN0143
MAIN0144

```



```

G(N1/2) = 0.
LO = N1/2
35 L = LO/2
G(L) = SQRT(2.+G(LO))
LO = L
36 G(N1-L) = -G(L)
L = L + 2*LO
IF((2*L/N1)*(2*LC-3)) 38,37,35
37 G(L) = (G(L+LO) + G(L-LO))/G(LO)
GO TO 36
38 ACOS = 1.
DO 39 K=1,JN2
39 GSIN(K) = G(JN1-K)/2.
DO 49 I=1,JM
LO = 0
DO 49 J=1,N2
L1 = (J+1)/2
SIGN=1.
K=I*J
41 IF(K-N1) 43,47,42
42 K=K-N1
SIGN=-SIGN
GO TO 41
43 SIGNN=SIGN
L = JN1 - K
IF(L) 45,48,46
45 L=-L
SIGNN=-SIGNN
K=N1-K
46 FSIN(I,J)=SIGN*GSIN(K)
IF(L1 .EQ. LO+1) FCOS(I,L1) = SIGNN*GSIN(L)
GO TO 49
47 FSIN(I,J)=0.
IF(L1 .EQ. LO+1) FCOS(I,L1) = -SIGN*ACOS
GO TO 49
48 FSIN(I,J)=SIGN*ACOS

```

```

MAIN0145
MAIN0146
MAIN0147
MAIN0148
MAIN0149
MAIN0150
MAIN0151
MAIN0152
MAIN0153
MAIN0154
MAIN0155
MAIN0156
MAIN0157
MAIN0158
MAIN0159
MAIN0160
MAIN0161
MAIN0162
MAIN0163
MAIN0164
MAIN0165
MAIN0166
MAIN0167
MAIN0168
MAIN0169
MAIN0170
MAIN0171
MAIN0172
MAIN0173
MAIN0174
MAIN0175
MAIN0176
MAIN0177
MAIN0178
MAIN0179
MAIN0180

```

```

IF(L1 .EQ. LO+1) FCOS(I,L1) = 0.
49 LO = L1
DO 50 J=1,N2
50 G(J) = 2. - G(J)
IK = 0
DO 55 K=1,N2
L = (K+1)/2
IK = IK + 1
IF(IK .EQ. 3) IK = 1
GO TO (51,53),IK
51 SUM(K) = 2.*FSIN(JM,K)*FSIN(JM,K) + ACOS*ACOS
DO 52 J=1,JM1
52 SUM(K) = SUM(K) + 2.*FSIN(J,K)*FSIN(J,K) + 2.*FCOS(J,L)*FCOS(J,L)
GO TO 55
53 SUM(K) = 2.*FSIN(JM,K)*FSIN(JM,K)
DO 54 J=1,JM1
54 SUM(K) = SUM(K) + 4.*FSIN(J,K)*FSIN(J,K)
55 CONTINUE
A = X*A10
B = A9/A10
DO 60 I=1,M2
C = I+.5
AA(I) = B*C/(C-.5)
BB(I) = C/(C-1.)
60 CC(I) = C/A
WRITE(6,85) IC,JC,IC,JC,IC,JC,IC,JC,K2,K1,K1,K1,K1,K3,K2,K3
85 FORMAT(///4X,'TIME',6X,'OLDT',5X,'OLDS',5X,'T(',I2,',',I2,')',5X,
1 'S(',I2,',',I2,')',5X,'U(',I2,',',I2,')',5X,'V(',I2,',',I2,')',
2 4(5X,'T(',I2,',',I2,')'))
90 DT = AT/BIG
TWO DT = 2.*DT
TIME = TIME + DT
DO 110 I=2,M1
B3 = I-1
B1 = A3*(B3+.5)/B3
B2 = A3*(B3-.5)/B3

```

```

MAIN0181
MAIN0182
MAIN0183
MAIN0184
MAIN0185
MAIN0186
MAIN0187
MAIN0188
MAIN0189
MAIN0190
MAIN0191
MAIN0192
MAIN0193
MAIN0194
MAIN0195
MAIN0196
MAIN0197
MAIN0198
MAIN0199
MAIN0200
MAIN0201
MAIN0202
MAIN0203
MAIN0204
MAIN0205
MAIN0206
MAIN0207
MAIN0208
MAIN0209
MAIN0210
MAIN0211
MAIN0212
MAIN0213
MAIN0214
MAIN0215
MAIN0216

```

B3 = A1/B3	MAIN0217
DO 100 J=2,N1	MAIN0218
100 CALC(I,J)=A2*(TO(I,J+1)+TO(I,J-1))+B1*TO(I+1,J)+B2*TO(I-1,J)	MAIN0219
1 +A4*TO(I,J)	MAIN0220
1 +B3*(T(I,J-1)*(S(I+1,J)+S(I+1,J-1)-S(I-1,J)-S(I-1,J-1))	MAIN0221
2 -T(I,J+1)*(S(I+1,J+1)+S(I+1,J)-S(I-1,J+1)-S(I-1,J))	MAIN0222
3 +T(I+1,J)*(S(I+1,J+1)+S(I,J+1)-S(I+1,J-1)-S(I,J-1))	MAIN0223
4 -T(I-1,J)*(S(I,J+1)+S(I-1,J+1)-S(I,J-1)-S(I-1,J-1)))	MAIN0224
IF(IXTL .NE. 0) GO TO 125	MAIN0225
CALC(1,1)=A14*S(2,2)*(T(2,1)-T(1,2))+A6*TO(2,1)+A7*TO(1,2)	MAIN0226
1 +A15*TO(1,1)+A8R*(TR4-(TC(1,1)+273.))**4.)+A8*(TA(1)-TO(1,1))	MAIN0227
125 IF(IXTL1 .GT. M1) GO TO 110	MAIN0228
CALC(I,1)=A7*TO(I,2)+B1*TO(I+1,1)+B2*TO(I-1,1)+A4*TO(I,1)	MAIN0229
1 +2.*B3*(T(I+1,1)*(S(I+1,2)+S(I,2)) - T(I-1,1)*(S(I-1,2)+S(I,2)))	MAIN0230
2 -T(I,2)*(S(I+1,2)-S(I-1,2))) + A8*(TA(I)-TO(I,1))	MAIN0231
3 + A8R*(TR4-(TC(I,1)+273.))**4.)	MAIN0232
110 CONTINUE	MAIN0233
DO 120 J=2,N1	MAIN0234
120 CALC(1,J)=A2*(TO(1,J+1)+TO(1,J-1)-2.*TO(1,J))+A6*(TO(2,J)-TO(1,J))	MAIN0235
1 +A5*(T(1,J-1)*(S(2,J)+S(2,J-1))-T(1,J+1)*(S(2,J+1)+S(2,J)))	MAIN0236
2 +T(2,J)*(S(2,J+1)-S(2,J-1)))	MAIN0237
DO 160 J=1,N1	MAIN0238
DO 150 I=1,M1	MAIN0239
IF(J .EQ. 1 .AND. I .LT. IXTL1) GO TO 160	MAIN0240
SAVE = TO(I,J)	MAIN0241
TO(I,J) = T(I,J)	MAIN0242
150 T(I,J) = SAVE + TWODT*CALC(I,J)	MAIN0243
160 CONTINUE	MAIN0244
DO 210 I=2,M1	MAIN0245
B4 = I-1	MAIN0246
B1 = A1/B4	MAIN0247
B2 = A10*(B4+1.)/(B4+.5)	MAIN0248
B3 = A10*(B4-1.)/(B4-.5)	MAIN0249
B4 = B4*B4	MAIN0250
B6 = A5/B4	MAIN0251
B4 = A13 + A23*B4/(B4-.25)	MAIN0252

DO 200 J=2,N1	MAIN0253
200 CALC(I,J)=B1*(U(I,J-1)*(S(I+1,J)+S(I+1,J-1)-S(I-1,J)-S(I-1,J-1))	MAIN0254
1 -U(I,J+1)*(S(I+1,J+1)+S(I+1,J)-S(I-1,J+1)-S(I-1,J))	MAIN0255
2 +U(I+1,J)*(S(I+1,J+1)+S(I,J+1)-S(I+1,J-1)-S(I,J-1))	MAIN0256
3 -U(I-1,J)*(S(I,J+1)+S(I-1,J+1)-S(I,J-1)-S(I-1,J-1))	MAIN0257
4 +A9*(UO(I,J+1)+UO(I,J-1))+B2*UO(I+1,J)+B3*UO(I-1,J)+B4*UO(I,J)	MAIN0258
5 +B6*U(I,J) *(S(I,J+1)-S(I,J-1))	MAIN0259
IF(I .LT. IXTL1) GO TO 210	MAIN0260
CALC(I,1) =	MAIN0261
1 2.*B1*(U(I+1,1)*(S(I+1,2)+S(I,2))	MAIN0262
2 -U(I-1,1)*(S(I-1,2)+S(I,2))	MAIN0263
3 +U(I,2)*(S(I-1,2)-S(I+1,2))	MAIN0264
4 +A11*UO(I,2)+B2*UO(I+1,1)+B3*UO(I-1,1)+B4*UO(I,1)	MAIN0265
5 +2.*B6*U(I,1)*S(I,2)	MAIN0266
210 CONTINUE	MAIN0267
DO 260 J=1,N1	MAIN0268
DO 250 I=2,M1	MAIN0269
IF(J .EQ. 1 .AND. I .LT. IXTL1) GO TO 260	MAIN0270
SAVE = UO(I,J)	MAIN0271
UO(I,J) = U(I,J)	MAIN0272
250 U(I,J) = SAVE + TWODT*CALC(I,J)	MAIN0273
DO 300 I=3,M1	MAIN0274
B6 = I-1	MAIN0275
B1 = A16/(B6+1.)	MAIN0276
B2 = A16/B6	MAIN0277
B3 = A16/(B6-1.)	MAIN0278
B4 = A10*(B6+1.)/(B6+.5)	MAIN0279
B5 = A10*(B6-1.)/(B6-.5)	MAIN0280
B7 = A18/B6	MAIN0281
B6 = B6*B6	MAIN0282
B6 = A13 + A23*B6/(B6-.25)	MAIN0283
DO 300 J=2,N1	MAIN0284
300 CALC(I,J)=B1*(V(I+1,J+1)*(S(I,J+1)-S(I+1,J))	MAIN0285
1 +V(I+1,J-1)*(S(I+1,J)-S(I,J-1))	MAIN0286
2 +V(I+1,J)*(S(I+1,J+1)-S(I+1,J-1)+S(I,J+1)-S(I,J-1))	MAIN0287
3 +B2*(V(I,J+1)*(S(I-1,J+1)-S(I+1,J+1)+S(I-1,J)-S(I+1,J))	MAIN0288

4	+V(I,J-1)*(S(I+1,J-1)-S(I-1,J-1)+S(I+1,J)-S(I-1,J))	MAIN0289
5	+B3*(V(I-1,J)*(S(I-1,J-1)-S(I-1,J+1)+S(I,J-1)-S(I,J+1))	MAIN0290
6	+V(I-1,J+1)*(S(I-1,J)-S(I,J+1))	MAIN0291
7	+V(I-1,J-1)*(S(I,J-1)-S(I-1,J))	MAIN0292
8	+A9*(VO(I,J+1)+VO(I,J-1))+B4*VO(I+1,J)+B5*VO(I-1,J)+B6*VO(I,J)	MAIN0293
9	+A19*(T(I+1,J+1)-T(I-1,J+1)+2.*(T(I+1,J)-T(I-1,J))	MAIN0294
9	+T(I+1,J-1)-T(I-1,J-1))	MAIN0295
9	+B7*(U(I,J+1)+U(I,J-1))*(U(I,J+1)-U(I,J-1))	MAIN0296
	DO 310 J=2,N1	MAIN0297
310	CALC(2,J)=A16*(V(2,J)*(S(2,J-1)-S(2,J+1))	MAIN0298
1	-V(2,J+1)*(S(3,J+1)+S(2,J+1)+S(3,J))	MAIN0299
2	+V(2,J-1)*(S(3,J-1)+S(2,J-1)+S(3,J))	MAIN0300
3	+A20*(V(3,J)*(S(3,J+1)-S(3,J-1)+S(2,J+1)-S(2,J-1))	MAIN0301
4	+V(3,J+1)*(S(2,J+1)-S(3,J))	MAIN0302
5	+V(3,J-1)*(S(3,J)-S(2,J-1))	MAIN0303
6	+A9*(VO(2,J+1)+VO(2,J-1))+A27*VO(3,J)+A28*VO(2,J)	MAIN0304
7	+A18*(U(2,J+1)+U(2,J-1))*(U(2,J+1)-U(2,J-1))	MAIN0305
8	+A19*(T(3,J+1)-T(1,J+1)+2.*(T(3,J)-T(1,J))+T(3,J-1)-T(1,J-1))	MAIN0306
	DO 350 J=2,N1	MAIN0307
	DO 350 I=2,M1	MAIN0308
	SAVE = VO(I,J)	MAIN0309
	VO(I,J) = V(I,J)	MAIN0310
350	V(I,J) = SAVE + TWODT*CALC(I,J)	MAIN0311
	IK = 0	MAIN0312
	DO 420 K=1,N2	MAIN0313
	L = (K+1)/2	MAIN0314
	IK = IK+1	MAIN0315
	IF(IK .EQ. 5) IK=1	MAIN0316
	DO 400 I=1,M2	MAIN0317
400	D(I) = TRANFG(V)	MAIN0318
	G1 = G(K)	MAIN0319
	E(1) = 1./(1.+G1*AA(1)+BB(1))	MAIN0320
	F(1) = CC(1)*D(1)*E(1)	MAIN0321
	DO 410 I=2,M2	MAIN0322
	E(I) = 1./(1. + G1*AA(I) + BB(I)*(1.-E(I-1)))	MAIN0323
410	F(I) = (CC(I)*D(I) + BB(I)*F(I-1))*E(I)	MAIN0324

```

      CALC(M1,K+1) = F(M2)
      DO 420 I=2,M2
      J = M1-I
420  CALC(J+1,K+1) = E(J)*CALC(J+2,K+1) + F(J)
      IK = 0
      DO 430 K=1,N2
      SUM1 = SUM(K)
      L = (K+1)/2
      IK = IK+1
      IF(IK .EQ. 5) IK=1
      DO 430 I=1,M2
430  S(I+1,K+1) = TRANFG(CALC)/SUM1
      IF(IXTL .LT. 2) GO TO 445
      DO 440 I=2,IXTL
440  V(I,1) = A21*S(I,2)/FLOAT(I-1)
445  DO 450 I=2,M1
450  V(I,N) = A21*S(I,N1)/FLOAT(I-1)
      DO 460 J=2,N1
460  V(M,J) = A22*S(M1,J)
      BIG = BIGG
      DO 470 J=2,N1
470  IF(ABS(S(2,J)) .GT. BIG ) BIG=ABS(S(2,4))
      BIG = 2.*BIG
      IF(IXTL1 .GT. M1 ) GO TO 485
      DO 480 I=IXTL1,M1
480  IF( ABS(S(2,J))/FLOAT(I-1) .GT. BIG ) BIG=ABS(S(2,J))/FLOAT(I-1)
485  BIG = 2.*BIG
      SMAX = 0.
      DO 490 I=2,M1
      B1=FLOAT(I-1)
      DO 490 J=2,N1
      IF(ABS(S(I,J)) .LE. SMAX) GO TO 489
      IC=I
      JC=J
      SMAX = ABS(S(I,J))
489  IF(ABS(S(I+1,J))-S(I-1,J))/B1.GT.BIG) BIG=ABS(S(I+1,J)-S(I-1,J))/B1

```

```

MAIN0325
MAIN0326
MAIN0327
MAIN0328
MAIN0329
MAIN0330
MAIN0331
MAIN0332
MAIN0333
MAIN0334
MAIN0335
MAIN0336
MAIN0337
MAIN0338
MAIN0339
MAIN0340
MAIN0341
MAIN0342
MAIN0343
MAIN0344
MAIN0345
MAIN0346
MAIN0347
MAIN0348
MAIN0349
MAIN0350
MAIN0351
MAIN0352
MAIN0353
MAIN0354
MAIN0355
MAIN0356
MAIN0357
MAIN0358
MAIN0359
MAIN0360

```

490	IF(ABS(S(I,J+1)-S(I,J-1))/B1.GT.BIG) BIG=ABS(S(I,J+1)-S(I,J-1))/B1	MAIN0361
	INDEX = INDEX + 1	MAIN0362
	TEST = T(IC,JC)	MAIN0363
	OLDT = (TEST - OLDT)/TEST/DT	MAIN0364
	SEST = S(IC,JC)	MAIN0365
	OLDS = (SEST - OLDS)/SEST/DT	MAIN0366
500	IF(INDEX .LT. IPRINT) GO TO 530	MAIN0367
	WRITE(6,510) TIME,OLDT,OLDS,TEST,SEST,IC,JC ,V(IC,JC),	MAIN0368
	1 T(K2,K1),T(K1,K1),T(K1,K3),T(K2,K3)	MAIN0369
510	FORMAT(1X,F10.9,2E9.2,2E13.5,I4,3X,I4,5E13.5)	MAIN0370
	IPRINT = IPRINT + JPRINT	MAIN0371
	IF(INDEX .LT. IPUNCH) GO TO 530	MAIN0372
	WRITE(6,850)((T(I,J),I=1,9),J=1,17)	MAIN0373
	WRITE(6,850)((T(I,J),I=9,17),J=1,17)	MAIN0374
	WRITE(6,850)((S(I,J),I=1,9),J=1,17)	MAIN0375
	WRITE(6,850)((S(I,J),I=9,17),J=1,17)	MAIN0376
	WRITE(6,850)((U(I,J),I=1,9),J=1,17)	MAIN0377
	WRITE(6,850)((U(I,J),I=9,17),J=1,17)	MAIN0378
	WRITE(6,850)((V(I,J),I=1,9),J=1,17)	MAIN0379
	WRITE(6,850)((V(I,J),I=9,17),J=1,17)	MAIN0380
850	FORMAT(///(4X,9E14.6))	MAIN0381
	WRITE(6,85) IC,JC,IC,JC,IC,JC,IC,JC,K2,K1,K1,K1,K1,K3,K2,K3	MAIN0382
	IPUNCH = IPUNCH + JPUNCH	MAIN0383
	IF(INDEX .GE. ICHECK) GO TO 920	MAIN0384
	IF(ISTOP .EQ. 1) GO TO 900	MAIN0385
530	OLDS = SEST	MAIN0386
	OLDT = TEST	MAIN0387
	IF (INDEX .LT. IVRG) GO TO 90	MAIN0388
	IVRG = IRVG + JVRG	MAIN0389
	DO 540 I=1,M	MAIN0390
	DO 540 J=1,N	MAIN0391
	AVRG = (T(I,J) + TO(I,J))/2.	MAIN0392
	T(I,J) = AVRG	MAIN0393
	TO(I,J) = AVRG	MAIN0394
	AVRG = (V(I,J) + VO(I,J))/2.	MAIN0395
	V(I,J) = AVRG	MAIN0396

540	VO(I,J) = AVRG	MAIN0397
	GO TO 90	MAIN0398
900	WRITE(6,910)	MAIN0399
910	FORMAT(////' STEADY STATE HAS BEEN REACHED')	MAIN0400
	WRITE(7,520) TIME,BIG,GR,PR,ASP,BI	MAIN0401
520	FORMAT(1X,6E13.6)	MAIN0402
	WRITE(7,525) TB,RES,REC,M,N,IXTL	MAIN0403
525	FORMAT(1X,3E13.6,3I5)	MAIN0404
	CALL EPUNCH(T)	MAIN0405
	CALL EPUNCH(S)	MAIN0406
	CALL EPUNCH(U)	MAIN0407
	CALL EPUNCH(V)	MAIN0408
	CALL EXIT	MAIN0409
920	WRITE(6,930)	MAIN0410
930	FORMAT(////' ICHECK HAS BEEN EXCEEDED')	MAIN0411
	WRITE(7,520) TIME,BIG,GR,PR,ASP,BI	MAIN0412
	WRITE(7,525) TB,RES,REC,M,N,IXTL	MAIN0413
	CALL EPUNCH(T)	MAIN0414
	CALL EPUNCH(S)	MAIN0415
	CALL EPUNCH(U)	MAIN0416
	CALL EPUNCH(V)	MAIN0417
	CALL EXIT	MAIN0418
940	WRITE(6,950)	MAIN0419
950	FORMAT(////' TEMPERATURE IS NEGATIVE')	MAIN0420
	CALL EXIT	MAIN0421
	END	MAIN0422


```

FUNCTION TRANFG(FUN)
COMMON I,K,L,IK,FSIN,FCOS,N,JN,JM,JM1,N2,M,KMAX,KDEL,ACOS
DIMENSION FUN(17,17),FSIN(4,15),FCOS(4,8)
GO TO (10,20,30,40),IK
10 TRANFG = (FUN(I+1,JM+1)+FUN(I+1,N-JM))*FSIN(JM,K)+ACOS*FUN(I+1,JN)
DO 15 J=1,JM1
15 TRANFG = TRANFG + (FUN(I+1,J+1)+FUN(I+1,N-J))*FSIN(J,K)
1 + (FUN(I+1,JN-J)+FUN(I+1,JN+J))*FCOS(J,L)
RETURN
20 TRANFG = (FUN(I+1,JM+1)-FUN(I+1,N-JM))*FSIN(JM,K)
DO 25 J=1,JM1
25 TRANFG = TRANFG + (FUN(I+1,J+1)+FUN(I+1,JN-J)
1 -FUN(I+1,JN+J)-FUN(I+1,N-J))*FSIN(J,K)
RETURN
30 TRANFG = (FUN(I+1,JM+1)+FUN(I+1,N-JM))*FSIN(JM,K)-ACOS*FUN(I+1,JN)
DO 35 J=1,JM1
35 TRANFG = TRANFG + (FUN(I+1,J+1)+FUN(I+1,N-J))*FSIN(J,K)
1 - (FUN(I+1,JN-J)+FUN(I+1,JN+J))*FCOS(J,L)
RETURN
40 TRANFG = 0.
DO 45 J=1,JM1
45 TRANFG = TRANFG + (FUN(I+1,J+1)-FUN(I+1,JN-J)
1 +FUN(I+1,JN+J)-FUN(I+1,N-J))*FSIN(J,K)
RETURN
END

```

```

TRAN0001
TRAN0002
TRAN0003
TRAN0004
TRAN0005
TRAN0006
TRAN0007
TRAN0008
TRAN0009
TRAN0010
TRAN0011
TRAN0012
TRAN0013
TRAN0014
TRAN0015
TRAN0016
TRAN0017
TRAN0018
TRAN0019
TRAN0020
TRAN0021
TRAN0022
TRAN0023
TRAN0024
TRAN0025

```

```

SUBROUTINE EPUNCH(FUN)
COMMON I,K,L,IK,FSIN,FCOS,N,JN,JM,JM1,N2,M,KMAX,KDEL,ACOS
DIMENSION FUN(17,17),FSIN(4,15),FCOS(4,8)
IMAX = 0
DO 1 K=1,KMAX
IMIN = IMAX + 1
IMAX = IMAX + 6
1 WRITE(7,2)((FUN(I,J),I=IMIN,IMAX),J=1,N)
2 FORMAT(1X,6E13.6)
IMIN = IMAX + 1
GO TO (3,5,7),KDEL
3 WRITE(7,4) (FUN(M,J),J=1,N)
4 FORMAT(1X,6E13.6)
RETURN
5 WRITE(7,6)((FUN(I,J),I=IMIN,M),J=1,N)
6 FORMAT(1X,3E13.6)
RETURN
7 WRITE(7,8)((FUN(I,J),I=IMIN,M),J=1,N)
8 FORMAT(1X,5E13.6)
RETURN
END

```

```

PNCH0001
PNCH0002
PNCH0003
PNCH0004
PNCH0005
PNCH0006
PNCH0007
PNCH0008
PNCH0009
PNCH0010
PNCH0011
PNCH0012
PNCH0013
PNCH0014
PNCH0015
PNCH0016
PNCH0017
PNCH0018
PNCH0019
PNCH0020
PNCH0021

```

```

SUBROUTINE EREAD(FUN)
COMMON I,K,L,IK,FSIN,FCOS,N,JN,JM,JM1,N2,M,KMAX,KDEL,ACOS
DIMENSION FUN(17,17),FSIN(4,15),FCOS(4,8)
IMAX = 0
DO 1 K=1,KMAX
IMIN = IMAX + 1
IMAX = IMAX + 6
1 READ(5,2)((FUN(I,J),I=IMIN,IMAX),J=1,N)
2 FORMAT(1X,6E13.6)
IMIN = IMAX + 1
GO TO (3,5,7),KDEL
3 READ(5,4) (FUN(M,J),J=1,N)
4 FORMAT(1X,6E13.6)
RETURN
5 READ(5,6)((FUN(I,J),I=IMIN,M),J=1,N)
6 FORMAT(1X,3E13.6)
RETURN
7 READ(5,8)((FUN(I,J),I=IMIN,M),J=1,N)
8 FORMAT(1X,5E13.6)
RETURN
END

```

```

READ0001
READ0002
READ0003
READ0004
READ0005
READ0006
READ0007
READ0008
READ0009
READ0010
READ0011
READ0012
READ0013
READ0014
READ0015
READ0016
READ0017
READ0018
READ0019
READ0020
READ0021

```

E. APPENDIX 5

ERROR ESTIMATES OF SOLUTE BOUNDARY
LAYER THICKNESS CALCULATIONS

The various methods used in Chapter IX for computing values of the solute boundary layer thickness can be shown to have the following expression for their relative errors:

(1) From the BPS relation (Equation (24))

$$\frac{\Delta\delta_1}{\delta_1} = \frac{\Delta D}{D} - \frac{\Delta R}{R} + 6.29 \left(\frac{\Delta c_s}{c_s} - \frac{\Delta c_l}{c_l} \right) - 6.19 \frac{\Delta k_o}{k_o} .$$

(2) From the relative deviation ratio relation (Equation (26))

$$\frac{\Delta\delta_2}{\delta_2} = \frac{\Delta D}{D} + 0.09 \frac{\Delta k_o}{k_o} + \frac{\Delta(\Delta c/c)}{(\Delta c/c)} - \frac{\Delta(\Delta R/R)}{(\Delta R/R)} .$$

(3) From the thermal boundary layer thickness relation (Equation (27))

$$\frac{\Delta\delta_3}{\delta_3} = \frac{\Delta D}{3D} + \frac{\Delta v}{bv} - \frac{\Delta \kappa}{2\kappa} + \frac{\Delta\delta_T}{\delta_T} .$$

(4) From the Cochran relation (Equation (28))

$$\frac{\Delta\delta_4}{\delta_4} = \frac{\Delta D}{3D} + \frac{\Delta v}{bv} - \frac{\Delta \omega}{2\omega} .$$

In deriving these expressions the following values of the required parameters were used: $k_o = 0.087$, $D = 1.9 \times 10^{-4} \text{ cm}^2/\text{sec}$, $R = 16.8 \text{ cm/sec}$, $c_s = 1.73 \times 10^{19}/\text{cm}^3$, $k_e = 0.101$, and $c_l = 1.71 \times 10^{20}/\text{cm}^3$.

Recent work has suggested that k_o may be as large as 0.11⁸⁷ so its relative error is estimated to be $\Delta k_o/k_o = 30\%$. Other estimates of the relative errors in the required parameters are the following: $\Delta D/D < 50\%$, $\Delta R/R < 5\%$, $\Delta c_s/c_s < 1\%$, $\Delta C_L/C_L < 50\%$, $\Delta v/v < 30\%$, $\Delta \omega/\omega < 1\%$, $\Delta \kappa/\kappa < 50\%$, and $\Delta \delta_T/\delta_T < 20\%$. Using these values in the relations derived above results in the following error estimates: $\Delta \delta_1/\delta_1 < 300\%$, $\Delta \delta_2/\delta_2 < 50\%$, $\Delta \delta_3/\delta_3 < 20\%$, and $\Delta \delta_4/\delta_4 < 20\%$. The primary sources of the large error in δ_1 are the determination of the bulk liquid concentration C_ℓ and the precision of the equilibrium distribution coefficient k_o .

BIOGRAPHICAL NOTE

The author was born on February 23, 1948 in Waltham, Massachusetts to Edward and Ethel Martin. He lived in Watertown, Massachusetts for two years prior to moving to Lexington, Massachusetts, where he was raised and attended elementary and secondary school. He graduated from Lexington High School in 1966.

He entered Boston College in September 1966, majoring in Physics. As an undergraduate, he assisted in the analysis of nuclear cross section data, was a corrector for an advanced calculus course, and participated on the varsity golf team. His senior project, concerning the effects of radiation damage on the electrical and optical properties of CDS, resulted in a paper presented in conjunction with several others at the Second Conference on the Educational Uses of Small Accelerators at Oakridge, Tennessee. He was awarded a Bachelor of Science degree in Physics in June, 1970.

While in attendance at Boston College, he enlisted in the Massachusetts Army National Guard; upon graduation, he attended BCT and AIT at Fort Knox, Kentucky, and later, after being commissioned a second lieutenant served as an armored cavalry platoon leader.

He entered the graduate school at Massachusetts Institute of Technology in the Department of Metallurgy and Materials Science (now the Department of Materials Science and Engineering) in February 1971, becoming a member of the Electronic

Materials Group. He completed the general examination for the doctoral program in the field of physics of solids (now included in the field of materials science). He served as a member on the Metallurgy Graduate Student Committee and competed with the metallurgy intramural football team. While in attendance at MIT, he and Norine Kofron were married and blessed with their son, Edward P. Martin III.

REFERENCES

1. J. Steininger and T. B. Reed, J. Cryst. Growth, 13/14, (1972), 106.
2. A. Arakawa, J. Comp. Phys., 1, (1966), 119.
3. J. R. Carruthers and A. F. Witt, 2nd International Spring School on Crystal Growth, Lecture Notes, Japan, 1974.
4. A. F. Witt, M. Lichtensteiger, and H. C. Gatos, J. Electrochem. Soc., 120, (1973), 1119.
5. J. R. Carruthers, in: Preparation and Properties of Solid State Materials, Vol. 2, Ed. W. R. Wilcox (Dehker, New York, 1975).
6. E. Jakeman and D. T. J. Hurle, Rev. of Phys. of Tech., 3, (1972), 3.
7. J. R. Carruthers, J. Cryst. Growth, 32, (1976), 13.
8. H. Bénard, Rev. Gen. Sci. Pures Appl., 11, (1900), 1261, 1309.
9. Lord Rayleigh, Phil. Mag., 32, (1916), 529.
10. S. Chandrasekhar, Hydrodynamic and Hydromagnetic Stability, Clarendon Press, Oxford, (1970).
11. R. J. Schmidt and S. W. Milverton, Proc. Roy. Soc., (London), A, 152, (1935), 586.
12. R. Krishnamurti, J. Fluid Mech., 42, (1970), 295.
13. R. Krishnamurti, J. Fluid Mech., 42, (1970), 309.
14. R. Krishnamurti, J. Fluid Mech., 60, (1973), 285.
15. L. N. Howard, in: Proceedings of the Eleventh International Congress on Applied Mechanics, Springer, Berlin, (1966), 1109.
16. F. H. Busse, J. Fluid Mech., 52, (1972), 97.
17. J. E. Fromm, Phys. of Fluids, 8, (1965), 1757.
18. W. L. Heitz and J. W. Westwater, J. Heat Transfer, 93, (1971), 188.

19. M. L. Samuels and S. W. Churchill, A. I. Ch. E. J., 13, (1967), 77.
20. F. Chiesa and R. Guthrie, Met. Trans., 2, (1971), 2833.
21. A. R. Ovchinnikov, J. Appl. Mech. Phys., 8, (1967), 81.
22. E. J. Harp and D. T. J. Hurle, Phil. Mag., 17, (1968), 1033.
23. W. T. Mitchell and J. A. Quinn, A. I. Ch. E. J., 12, (1966), 1116.
24. G. K. Batchelor, Quart. Appl. Math., 12, (1954), 209.
25. G. Poots, Quart. J. Mech. Appl. Math., 11, (1958), 257.
26. J. O. Wilkes and S. W. Churchill, A. I. Ch. E. J., 12, (1966), 161.
27. M. J. Stuart and F. Weinberg, J. Cryst. Growth, 12, (1972), 217.
28. G. S. Cole and W. C. Winegard, J. Inst. Metals, 93, (1964), 153.
29. A. Mueller and M. Willhelm, Z. F. Naturforsch., 19a, (1964), 254.
30. H. P. Utech and M. C. Flemings, in: Crystal Growth, Ed. H. S. Peiser, Pergamon Press, (1967), 651.
31. D. T. J. Hurle, J. Gillman, and E. J. Harp, Phil. Mag., 14, (1966), 205.
32. D. T. J. Hurle, Phil. Mag., 13, (1966), 305.
33. D. T. J. Hurle, E. Jakeman, and C. P. Johnson, J. Fluid Mech., 64, (1974), 565.
34. M. J. Stuart and F. Weinberg, J. Cryst. Growth, 12, (1972), 228.
35. L. C. MacAuley, Ph. D. Thesis, University of British Columbia, (1972).
36. J. R. Carruthers and W. C. Winegard, in: Crystal Growth, Ed. H. S. Peiser, Pergamon Press, (1967), 645.

37. J. R. Carruthers, J. Cryst. Growth, 2, (1968), 1.
38. W. R. Wilcox and L. D. Fulmer, J. Appl. Phys., 36, (1965), 2201.
39. J. C. Brice and P. A. C. Whiffin, Brit. J. Appl. Phys., 18, (1967), 581.
40. B. Cockayne and M. P. Gates, J. Mater. Sci., 2, (1967), 118.
41. B. Cockayne, M. Chesswas, J. G. Plant, and A. W. Vere, J. Mater. Sci., 7, (1969), 565.
42. K. M. Kim, A. F. Witt, and H. C. Gatos, J. Electrochem. Soc., 119, (1972), 1218.
43. J. D. Verhoeven, Phys. Fluids, 12, (1969), 1733.
44. J. C. Brice, O. F. Hill, P. A. C. Whiffin, and J. A. Wilkinson, J. Cryst. Growth, 10, (1971), 133.
45. J. Wenkus, Private Communication.
46. M. Lichtensteiger, A. F. Witt, and H. C. Gatos, J. Electrochem. Soc., 118, (1971), 1013.
47. H. Schlichting, Boundary Layer Theory, McGraw-Hill, New York, (1955).
48. W. H. McAdams, Heat Transmission, McGraw-Hill, New York, (1954).
49. The Omega Temperature Measurement Handbook, Omega Engineering Inc., Stamford, Conn., (1975).
50. D. T. J. Hurle, E. Jakeman, E. R. Pike, J. Cryst. Growth, 3,4, (1968), 633.
51. G. K. Gaule and J. R. Pastore, Metallurgy of Elemental and Compound Semiconductors, Interscience Publisher, New York, (1961), 201.
52. A. F. Witt, Private Communication.
53. H. B. Phillips, Vector Analysis, John Wiley & Sons, Inc., New York, (1949), 38.
54. C. E. Chang and W. R. Wilcox, J. Cryst. Growth, 28, (1975), 8.

55. W. G. Cochran, Proc. Camb. Phil. Soc., 30, (1934), 365.
56. P. F. Tomlan and J. L. Hudson, Chem. Eng. Sci., 26, (1971), 1591.
57. G. D. Lehmkuhl and J. L. Hudson, Chem. Eng. Sci., 26, (1971), 1601.
58. J. R. Carruthers, J. Electrochem. Soc., 114, (1967), 959.
59. J. R. Carruthers and K. Nassau, J. Appl. Phys., 39, (1968), 5205.
60. N. Kobayashi and T. Arizumi, Jap. J. Appl. Phys., 9, (1970), 361.
61. N. Kobayashi and T. Arizumi, Jap. J. Appl. Phys., 9, (1970), 1255.
62. N. Kobayashi and T. Arizumi, J. Cryst. Growth, 30, (1975), 177.
63. P. A. C. Whiffin, T. M. Burton, J. C. Brice, J. Cryst. Growth, 32, (1976), 205.
64. G. P. Williams, J. Fluid Mech., 37, (1969), 727.
65. W. A. Tiller, K. A. Jackson, J. W. Rutter, and B. Chalmers, Acta. Met., 1, (1953), 428.
66. W. G. Pfann, Trans. A. I. M. E., 199, (1952), 747.
67. J. A. Burton, R. C. Prim, and W. P. Slichter, J. Chem Phys., 21, (1953), 1987.
68. D. T. J. Hurle and E. Jakeman, J. Cryst. Growth, 5, (1969), 227.
69. R. N. Hall, Phys. Rev., 88, (1952), 139.
70. A. Trainor and B. E. Bartlett, Solid State Electronics, 2, (1961), 106.
71. J. R. Carruthers, Can. Met. Quart., 5, (1964), 55.
72. J. A. Burton, E. D. Kolb, W. P. Slichter, and J. D. Struthers, J. Chem. Phys., 21, (1953), 1991.

73. J. R. Carruthers and K. E. Benson, Appl. Phys. Lett., 3, (1963), 100.
74. K. E. Benson, Electrochem. Tech., 3, (1965), 332.
75. A. F. Witt and H. C. Gatos, J. Electrochem. Soc., 113, (1966), 808.
76. K. Morizane, A. F. Witt, and H. C. Gatos, J. Electrochem. Soc., 113, (1966), 51.
77. K. Morizane, A. F. Witt, and H. C. Gatos, J. Electrochem. Soc., 114, (1967), 738.
78. A. F. Witt and H. C. Gatos, J. Electrochem Soc., 115, (1968), 70.
79. K. Morizane, A. F. Witt, and H. C. Gatos, J. Electrochem. Soc., 115, (1968), 747.
80. A. F. Witt, M. Lichtensteiger, and H. C. Gatos, J. Electrochem. Soc., 121, (1974), 787.
81. A. Murgai, H. C. Gatos, and A. F. Witt, J. Electrochem. Soc., 123, (1976), 224.
82. A. Murgai, H. C. Gatos, and A. F. Witt, J. Electrochem. Soc., 122, (1975), 1276.
83. A. Murgai, Ph. D. Thesis, Massachusetts Institute of Technology, (1975).
84. R. Resnick, D. Halliday, Physics For Students of Science and Engineering, Part 1, John Wiley & Sons, Inc., New York, (1963).
85. M. Lichtensteiger, Private Communication.
86. A. Murgai, A. F. Witt, H. C. Gatos, J. Electrochem. Soc., 122, (1975), 1276.
87. D. Holmes, Private Communication.
88. F. X. Hassian, C. D. Thurmond, and F. A. Trumbore, J. Phys. Chem., 59, (1955), 1076.
89. V. M. Glazov, S. N. Chizhevskaya, and N. N. Glagoleva, Liquid Semiconductors, Plenum Press, New York, (1969).

90. L. P. Filippov, Int. J. Heat Mass Transfer, 16, (1973), 865-85.
91. F. G. Allen, J. Appl. Phys., 28, (1957), 1510.
92. B. M. Turovskii and I. I. Ivanova, Russ. J. Phys.Chem., 45, (1971), 98.
93. F. A. Trumbore, E. M. Porbauskyy, and A. H. Tartaglia, J. Phys. Chem. Soc., 11, (1959), 239.
94. C. J. Smithells, Metals Reference Book, Plenum Press, New York, (1967).
95. Y. S. Touloukian, Thermophysical Properties of Matter, Vol. 1, Plenum Press, New York, (1970), 107.
96. Y. S. Touloukian, Thermophysical Properties of Matter, Vol. 10, Plenum Press, New York, (1970), 68.
97. D. E. Gray, American Institute of Physics Handbook, McGraw-Hill, New York, (1972), 4-151.
98. F. B. Hildebrand, Finite Difference Equations and Simulations, Prentice-Hall, New Jersey, (1968).
99. D. K. Lilly, Monthly Weather Review, 93, (1965), 11.
100. P. D. Lax and R. D. Richtmyer, Comm. Pure Appl. Math., 9, (1956), 267.
101. O. Buneman, SUIPR Report, 294. Institute for Plasma Research, Stanford Univ.
102. G. P. Williams, J. Atmos. Sci., 24, (1967), 144.
103. R. D. Richtmyer, Difference Methods for Initial Value Problems, Interscience, New York, (1957).